UNIVERSITÀ DEGLI STUDI DI TRIESTE

UNIVERSITÀ DEGLI STUDI DI TRIESTE

XXXVIII CICLO DEL DOTTORATO DI RICERCA IN FISICA

Finanziato dall'Unione europea - NextGenerationEU
Funded by the European Union - NextGenerationEU

Simulations of two-dimensional crystalline and amorphous oxides

Settore scientifico-disciplinare: **FIS/03 FISICA DELLA MATERIA**

DOTTORANDO / A
MARCO DIRINDIN

COORDINATORE
PROF. ANGELO BASSI

SUPERVISORE DI TESI
PROF. DANIELE COSLOVICH

CO-SUPERVISORE DI TESI
PROF. MARIA PERESSI

ANNO ACCADEMICO 2024/2025

Finanziato dall'Unione europea NextGenerationEU | Ministero dell'Università e della Ricerca | Italiadomani | UNIVERSITÀ DEGLI STUDI DI TRIESTE

[...] and all the substantial realities of Flatland itself,
appear no better than the baseless fabric of a dream.

Flatland
E. A. ABBOTT

UNIVERSITY OF TRIESTE
Department of Physics

Abstract

Simulations of two-dimensional crystalline and amorphous oxides

Marco DIRINDIN

Over the last 20 years the study of low-dimensional systems has been extremely prolific, giving rise to new technological applications and new developments for fundamental research. In this context, two-dimensional network-forming oxides represent an intriguing and understudied class of materials, characterized by low-density network structures formed by covalent bonds. So far, only a couple of these systems have been synthesized, such as silica bilayers and boron-oxygen compounds. The physics of their three-dimensional equivalents is extremely rich and still debated, with an intricate interplay between polymorphism, diverse superstructural units and medium-range order. There are inherent difficulties in measuring the structure of these three-dimensional networks and this has significantly hindered our understanding of them. The synthesis of two-dimensional allotropes thus offers a unique opportunity to use standard surface techniques to examine their structure and dynamics, making these materials ideal benchmarks for testing and developing theories on network-forming glasses.

In this thesis, we use a combination of *ab initio* techniques, large-scale classical simulations and rigorous comparison with experiments to describe the structure of two-dimensional crystalline and amorphous oxides at different length scales. Using experimental data, we develop an effective classical potential for the silica bilayer, which is able to reproduce fine structural details of experimental samples. We use this potential to study the glassy behavior of the system at low temperatures and to assess the relationship between structure and dynamics. For a boria monolayer, we devise an algorithm to perform a systematic search for crystalline polymorphs, and we use it to predict from first principles the structure of a recently synthesized boron-oxygen crystal. Using *ab initio* techniques, we characterize the structure, electronic properties and substrate interactions of the synthesized system, achieving an excellent agreement with the experimental data. After characterizing the crystalline monolayer, we focus on the amorphous structure, developing an algorithm to recover the atomic positions from the experimental images. This allows us to provide a first characterization of this new glassy system.

Our results highlight the connection between atomic local environment and network topology, and suggest a strong similarity between different two-dimensional network-forming oxides. We also identify peculiar behaviors in these two-dimensional systems, such as the presence of large transient crystalline domains in the thermodynamically stable low-temperature liquid, which may point to a profound difference between glassy structure in two- and three-dimensions.

Contents

Chapter 1

Introduction

In this chapter we lay the groundwork for the results presented in this thesis. We discuss the general properties of the materials analyzed in this work, paying particular attention to the connection between atomic structure and macroscopic properties (Sec. 1.1). Since all the systems considered in this work can form low-density amorphous structures, we review the phenomenology of glassy physics and provide an historical overview of the different theories proposed to describe their structure (Sec. 1.2). Finally, we review the key differences between the physics of two- and three-dimensional systems, in particular regarding the existence of a stable ordered phase and the melting process (Sec. 1.3).

1.1 Materials

We begin our discussion with an overview of the materials that will be analyzed later in the remainder of this thesis. We present in detail the properties of silica and boria, which are the main materials of interest for this work, but we also briefly discuss the behavior of germania and graphitic carbon nitrades, which play a minor role in this thesis. For most of these materials we present the phase diagram, their atomic structure and its connection to their physical properties, as well as their two-dimensional equivalents.

1.1.1 Silica

Silicon dioxide, or simply silica, is one of the main constituents of the Earth's crust [1, 2]. It is present in both igneous and metamorphic rocks, as well as in sediments and soils [2]. It is one of the first materials mankind ever manufactured: the earliest glaze dates back to around 12000 B.C. in Egypt, while the first object molded in pure glass dates back to around 7000 B.C. [3]. The properties that make this material so ubiquitous in manufacturing, such as its hardness, stability and ease of workability, are due to its unique atomic structure.

As shown in Fig. 1.1, silica can be found in many different crystalline forms. Nevertheless, with the exception of the high pressure stishovite phase where silicons have octahedral coordination, the building block of every silica polymorph is a $Si\emptyset_4$ tetrahedron[1]. This unit has a silicon atom at the center of the tetrahedron with four sp^3 orbitals. Each of these orbitals forms strong σ bond with a $2p$ orbital of each oxygen, which sit at the vertices of the tetrahedron [2]. These oxygens allow the tetrahedra to connect with each other, and different topologies of the resulting network result in different polymorphs [1, 2].

[1] We use the notation $\emptyset$ to indicate a bridging oxygen between two structural units and O to indicate an oxygen within a unit.

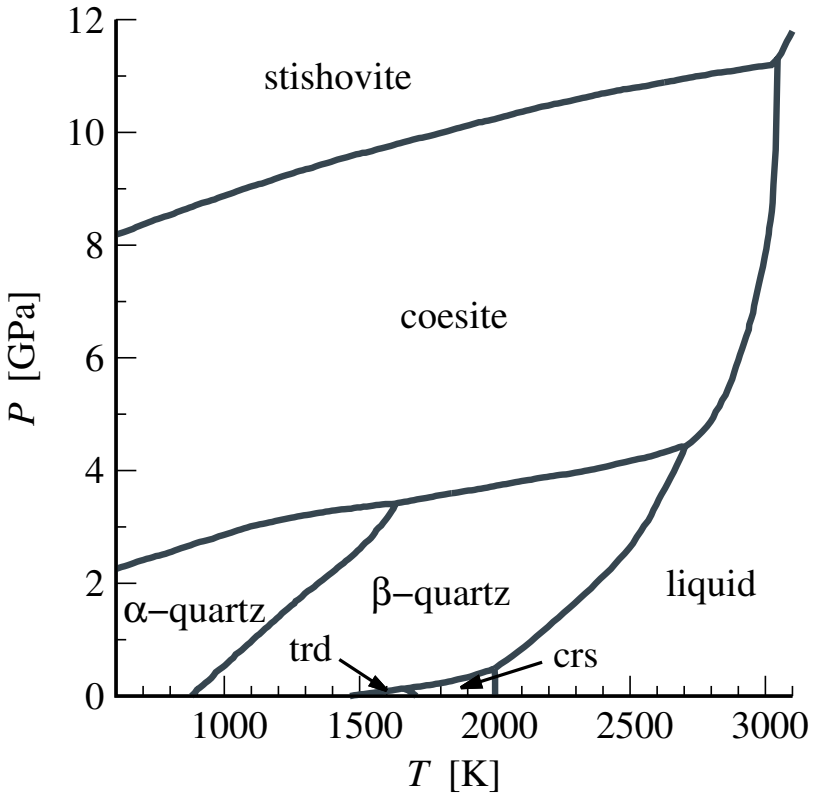

FIGURE 1.1: Phase diagram of the most common silica polymorphs. The acronyms "trd" and "crs" refer to tridymite and cristobalite, respectively. The data have been digitalized from [4].

Silica is also a renowned example of glass-forming system. It is relatively easy to melt at ambient pressure and, if the resulting liquid is then rapidly cooled down, see Sec. 1.2, it turns into an amorphous solid. Liquid silica present some thermodynamic anomalies, such as a density maximum [5–8], which, along with the appearance of a first sharp diffraction peak [9], have been linked with the formation of a disordered but well-defined network structure composed of interconnected tetrahedra [9]. In its vitreous state, silica therefore maintains the same kind of local order of its crystalline phases, see Sec. 1.2.2, with an average *Si-Ø* distance in the $SiØ_4$ tetrahedra of 1.6 Å [10] and an angle between the different tetrahedra, *i.e.* the *Si-Ø-Si* angle, ranging from 120° to 180° degrees, with an average of around $145° - 150°$ [2, 10].

Interest for ultrathin silica films arose in the early 21st century due to their applications in the semiconductor industry [4]. Moreover, the possibility of using standard surface techniques to observe their structure in real space has attracted much attention, as it could resolve a long-lasting quest on the atomic-scale structure of network-forming materials. As we will discuss more in detail in Sec. 1.2.2, there is a long-standing debate about whether a glass is made of crystalline domains embedded in an otherwise disordered matrix or should be regarded as a network of randomly connected rigid units [11]. Experimental measurements on the bulk material are unable to fully resolve this question due to the integrating nature of the standard techniques used [12], such as neutron and X-ray diffraction, and the inability of using surface science techniques on these materials, which are typically large band gap insulators. In this context, a two-dimensional equivalent of bulk amorphous silica allows the use of standard surface imaging techniques to examine both the structure and dynamics of a network-forming glass atom-by-atom, shedding light on this

long-standing controversy.

To the best of our knowledge, only a handful of two-dimensional polymorphs based on the silica tetrahedron have ever been synthesized[2]. The first to be discovered was the silica monolayer [15]. This system consists of a network of corner-sharing SiO_4 tetrahedra, in which one oxygen of each tetrahedron forms a covalent bond with the substrate and the others form bridges with other tetrahedra, resulting in a honeycomb lattice when view from above [15]. The formation of strong bonds with the substrate stabilizes this structure even in the presence of a lattice mismatch between monolayer and substrate, and allows the formation of well-ordered domains on a large scale [16].

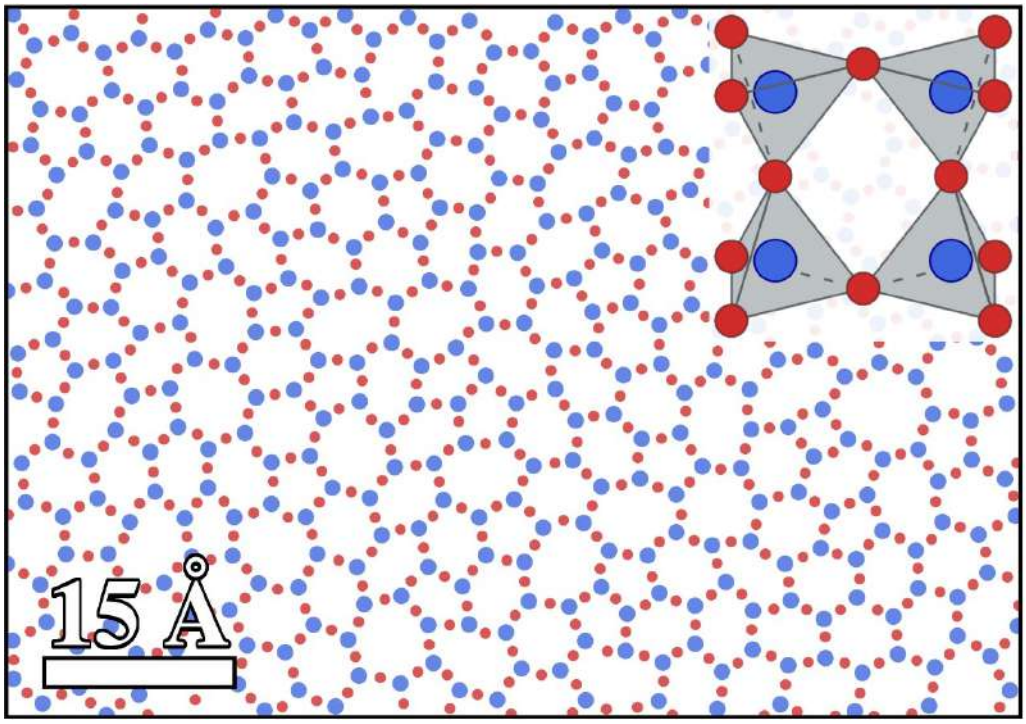

FIGURE 1.2: Top view of the structure produced by our effective model for the silica bilayer (RHH-II model) at lowest investigated temperature ($T = 0.0067$), see Chapter 2. The particles form a well-defined, almost defect-free network. Inset: Three-dimensional scheme of the atoms in the unit cell of the silica bilayer, with their tetrahedral structure highlighted in grey. In both plots, blue and red circles represent silicon and oxygen particles (or atoms, in the inset), respectively.

The second polymorph to be synthesized was the silica bilayer. This material is unique because it can be easily grown with both crystalline [17] and amorphous structures [18, 19]. In both structures, the basic unit consists of two corner-sharing SiO_4 tetrahedra [20], see Fig. 1.2 inset, with a prefect symmetry between the tetrahedra with respect to the plane parallel to the substrate containing the shared oxygen. The presence of this mirror plane was inferred from a comparison of the infrared reflection-absorption spectrum with a Density Functional Theory (DFT) model [17, 19], and is due to a 180° angle between the tetrahedral units. When viewed from

[2]Although these structures are commonly referred in the literature as "silica" phases [4], only the silica bilayer have the stoichiometry SiO_2. The silica monolayer and the "zigzag" phase have stoichiometry $SiO_{5/2}$ and $SiO_{13/6}$, respectively [13]. Other low-dimensional silica structures with strict SiO_2 stoichiometry have been theorized [14], but, to our knowledge, they have not been experimentally detected.

above, these basic units form a hexagonal lattice in the crystalline phase, or a random network of rings of different sizes in the amorphous state, see Fig. 1.2. Due to the absence of direct bonds with the surface, only weak van der Waals interactions bind the bilayer to the substrate [20]. Moreover, this material has no dangling bonds, making it very stable under ambient conditions [18, 20] and even when immersed in water [20]. This stability is such that the system can be easily exfoliated from the surface in which was grown and deposited on another substrate without major changes in its structure [21].

The silica bilayer can be grown using physical vapor deposition on a wide variety of substrates, such as *Ru(0001)* [22], *Pt(111)* [23], *Pd(100)* [24], graphene on *Cu*-foils [18] and *NiPd(111)* alloys [25]. Depending on the lattice mismatch between the bilayer and the surface [20, 25] and the growth conditions [20], the film may have a reticular, an amorphous or a mixed structure [19]. Due to the presence of a metallic substrate, it is possible to use standard surface techniques, like Scanning Tunneling Microscopy (STM) and Transmission Electron Microscopy (TEM), to obtain high-resolution images of the system [18, 26, 27].

The silica bilayer is one of the main materials we focus on in this thesis. In Chapter 2, we will exploit the presence of a mirror plane in its structure to develop a simple strictly two-dimensional model to simulate the system. The structure and dynamics produced by this model will be analyzed in Chapter 3, while in Chapter 4, we will study the structure-dynamics relationship in the model and we will develop a simple effective model to study its interplay with a variety of substrates.

The latest two-dimensional silica polymorph to be discovered is the so called "zigzag" phase [13]. Its structure consists of a complex network of silica tetrahedra with fluctuations both in height and in the plane parallel of the substrate [13]. Two out of the 12 tetrahedra in the unit cell are covalently bonded with the surface, giving this phase an intermediate coupling with the substrate compared to the other two-dimensional silica polymorphs. In experiments, this phase can be easily transformed into a silica bilayer by high-temperature annealing but cannot be converted back. Therefore, it is believed to be a metastable phase under typical experimental conditions [13, 28].

1.1.2 Boria

Diborion trioxide, or simply boria, is the most widely used material after silica in the glass industry, with a wide range of applications in optical systems and glass ceramics [29]. It is also one of the best known glass-formers [29, 30], with an extremely rich and complex physical behavior, largely due to its atomic structure.

The boron atom has three electrons in its valence shell, leading to a sp^2 hybridization of its orbitals and the formation of a planar $B\text{Ø}_3$ equilateral triangle with an average *B-Ø* bond length of 1.372 Å [30]. In this structure, the boron has a vacant p_z orbital perpendicular to the plane of the triangle. Boron orbitals can also have a sp^3 hybridization, which allows them to receive an additional dative bond from one of the oxygen lone-pair orbital, forming a $B\text{Ø}_4$ tetrahedral unit [30, 31]. Due to the different bond types, this unit is distorted, with three *B-Ø* bonds of approximately 1.508 Å and the remaining *B-Ø* bond of 1.373 Å [30].

The planar $B\text{Ø}_3$ triangle and the $B\text{Ø}_4$ tetrahedraon are the building blocks of the only two known crystalline phases of boria, as shown in the phase diagram in Fig. 1.3 (left). At low pressure, the stable crystalline structure is B_2O_3-*I*, which is composed by a set of interconnected ribbons made of corner-sharing $B\text{Ø}_3$ triangles, see Fig. 1.3 (right). At high pressure, instead, the stable phase becomes the B_2O_3-*II*

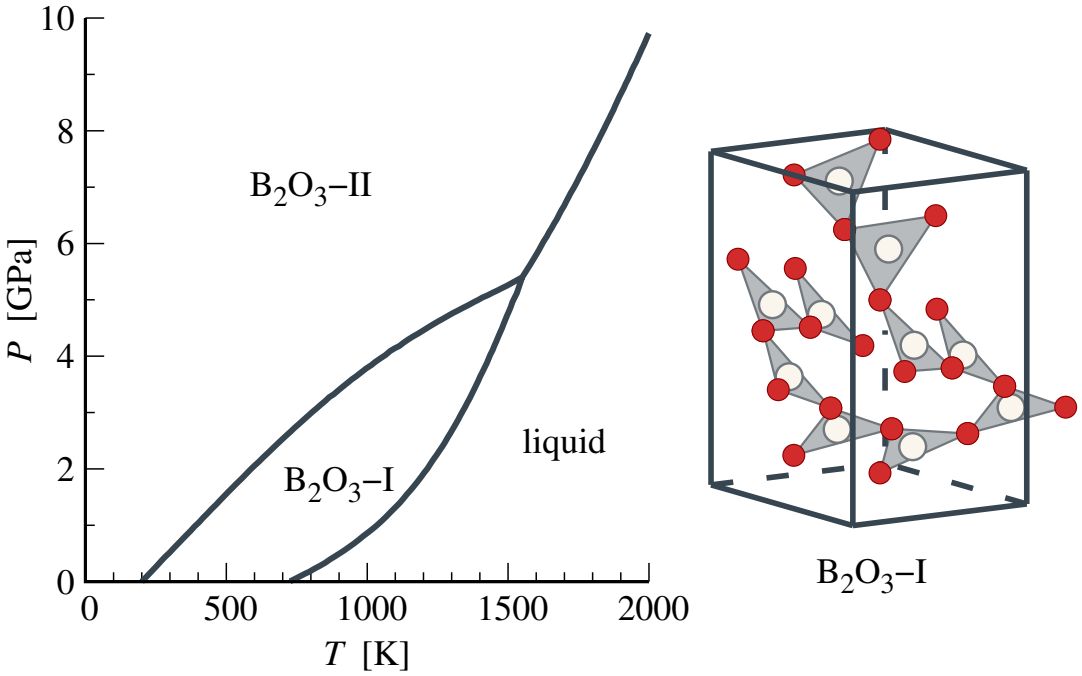

FIGURE 1.3: (Left) Phase diagram of 3*d* B_2O_3 constructed from experimental data and thermodynamic analysis [29]. (Right) Schematic structure of the unit cell of B_2O_3-*I*. The atoms within the unit cell are replicated to highlight the structure of interconnected $B\emptyset_3$ triangles. White and red circles represent boron and oxygen atoms, respectively. The phase diagram has been digitalized from [29].

crystal, whose structure is a three-dimensional network of corner-sharing $B\emptyset_4$ tetrahedra [30]. This structure is approximately 22 % denser than the B_2O_3-*I* crystal [30], which makes the transition between these phases very slow and difficult to measure at low temperatures and pressures [29].

The liquid phase of this material exhibits a rich and peculiar phenomenology. At $T \simeq 1100$ K and ambient pressure the liquid is 64 % less dense than the B_2O_3-*I* crystal [30]. Moreover, at approximately 1470 K and ambient pressure its viscosity is 11 orders of magnitude lower than that of liquid silica, despite the bonds in boria are slightly stronger than those in silica [31]. Moreover, one of the strangest properties of the liquid is its inability to crystallize at ambient pressure. Although the B_2O_3-*I* structure is stable at ambient pressure, no crystallization of the liquid has ever been observed under such conditions, not even when the liquid is seeded with a crystal and allowed to equilibrate for several months at 175 °*C* (448 K) [32–34]. Spontaneous crystallization from the liquid is achieved only when the pressure is increased to $0.4-1.0$ GPa [33, 34], in an enigmatic behavior which has been named "the B_2O_3 crystallization anomaly" [35].

These peculiarities have been linked to the presence of two different building blocks in the low temperature liquid: the $B\emptyset_3$ triangle and a larger $B_3O_3\emptyset_3$ triangle, both shown in Fig. 1.4 (right). The $B_3O_3\emptyset_3$ triangle contains an hexagonal ring composed of alternating boron and oxygen atoms, called the boroxol ring (B_3O_3), and is made up of three connected $B\emptyset_3$ units. This structure is 26.8 kJ/mol more stable than its three constituents $B\emptyset_3$ units [36], making it energetically more favorable at low temperatures. The presence of boroxol groups in the boria glass was first speculated in 1953 [37], but remained a matter of debate for several decades. Nowadays, it is generally accepted that the low-temperature liquid is ruled by the dynamic equilibrium between $B\emptyset_3$ and $B_3O_3\emptyset_3$, with the fraction of boroxol groups

increasing as the temperature decreases. In glassy samples, neutron diffraction [38] and nuclear magnetic resonance experiments [31] estimate that the fraction of boron atoms within boroxol groups is around 75 %, *i.e.* approximately equal number of $B\emptyset_3$ and $B_3O_3\emptyset_3$ superstructural units. Thus, the excellent glass-forming ability of this material is ascribed to the presence of highly stable $B_3O_3\emptyset_3$ units in the liquid, which hamper the crystalline order of the B_2O_3-*I* phase.

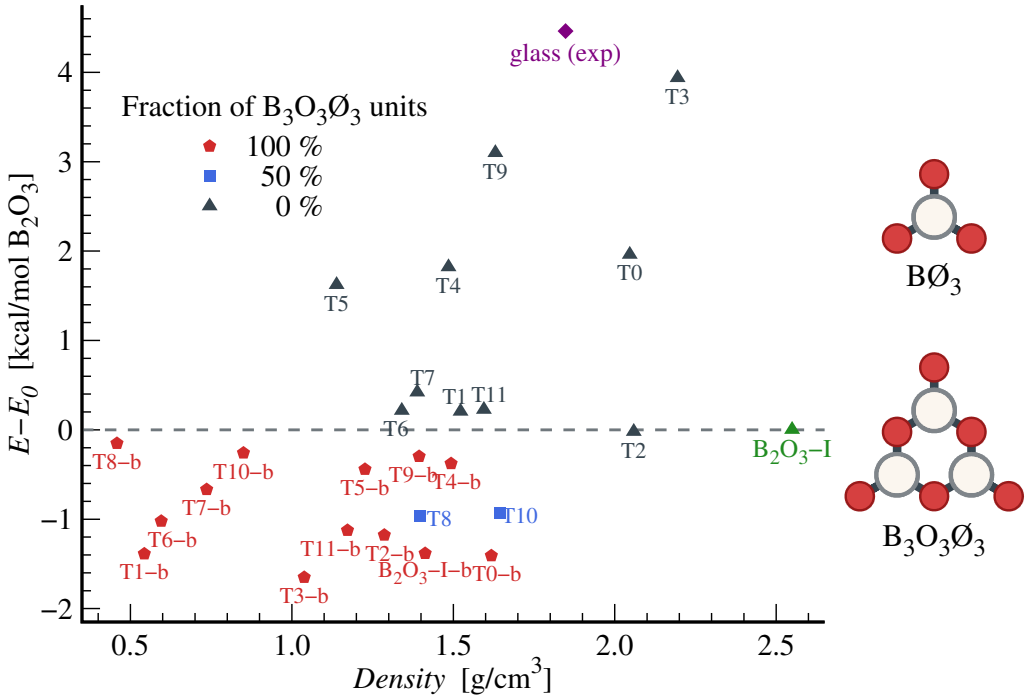

FIGURE 1.4: (left) Energy as a function of density for several theorized polymorphs of 3*d* B_2O_3. The reference energy E_0 is that of the B_2O_3-*I* crystal. Different symbols refer to different fractions of boroxol groups in the structure. The crystalline B_2O_3-*I* structure and the glass are highlighted with a green and a purple symbol, respectively. For the notation, refer to [35], from which the data have been digitalized. (right) Representation of the $B\emptyset_3$ and $B_3O_3\emptyset_3$ units, with the same color scheme as in Fig.1.3 (right).

The high stability of the boroxol groups and their presence in liquid and vitreous structures is puzzling, as no crystal structure of pure boria containing boroxol units has ever been synthesized to date[3]. A possible explanation for this behavior is the presence of a several competing crystalline structures. At low temperatures, the competition between these polymorphs leads to the amorphization of the system, while the application of pressure makes the B_2O_3-*I* crystal the only thermodynamically stable structure. These ideas led Ferlat *et al.* [35] to evaluate the stability of a large number of possible B_2O_3 polymorphs. Such structures are generated starting from a set of sp^2-carbon polymorphs, whose structures are decorated with both $B\emptyset_3$ and $B_3O_3\emptyset_3$ units. The structures were then relaxed using *ab initio* methods. The so-obtained polymorphs were shown to be comparable in energy to the B_2O_3-*I* crystal

[3]Note that crystalline structure of boria with network-modifiers features boroxol-based superstructural units. Moreover, the interplay between these units and the $B\emptyset_4$ tetrahedra has been linked to the rich phenomenology of these materials observed as the concentration of network-modifiers varies [31, 39].

and to have densities similar to that of the glass, as shown in Fig. 1.4 (left), supporting the idea that crystallization is hindered by the presence of numerous energetically degenerate crystalline structures. Further studies on this set of proposed polymorphs highlighted the high degree of flexibility of boroxol-based structures [40] and the crucial role of van der Waals interactions on these systems[4] [41]. Despite this theoretical insight, the absence of experimentally synthesized B_2O_3 polymorphs based on boroxol groups is still puzzling [31].

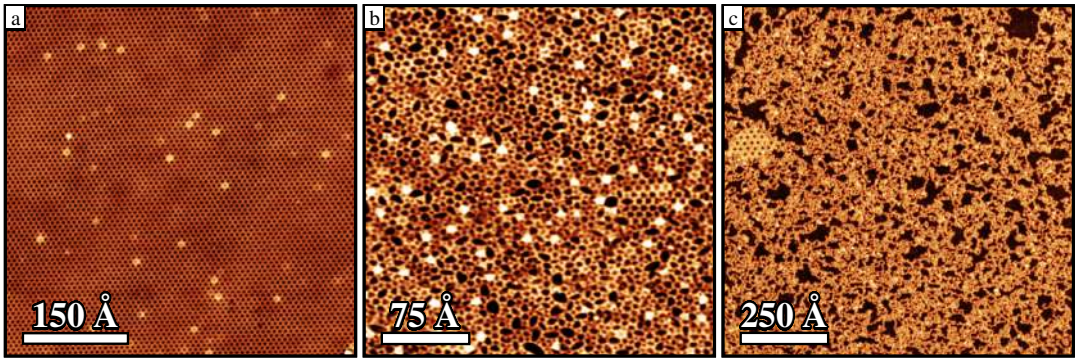

FIGURE 1.5: STM images of the different structures of a boria monolayer obtained after successive flash annealings at 820 K of the crystalline structure. From left to right: (a) crystalline structure, (b) vitreous structure after two flash annealings and, (c) polymeric-like phase and hexagonal crystal obtained after seven flash annealings. The bright spots in panel (a) are due to *Pt* adatoms, as will be shown in Sec. 6.2.1. Experimental images courtesy of Teresa Zio (STRAS laboratory, CNR-IOM, Trieste, Italy).

The synthesis of a two-dimensional boria crystal is very recent, with the first paper on the material published at the end of 2025[5] [43]. The crystal was produced by the STRAS laboratory in Trieste and was analyzed using experimental and *ab initio* methods in collaboration with the authors of this manuscript. Further measurements were also performed in partnership with the University of Innsbruck.

The material was synthesized on $Pt(111)$ and has a crystalline structure composed exclusively of boroxol rings. The system is produced by the deposition of boron atoms in oxygen atmosphere at a substrate temperature of 770 K, followed by a flash annealing at 820 K in ultrahigh vacuum. The resulting structure is an almost perfectly flat monolayer composed of boroxol groups, whose centers are arranged in the sites of a honeycomb lattice with lattice parameters 8.57 Å. Weak van der Waals interactions bind the system to the substrate, and thus the monolayer can form a variety of domains with several orientations with respect to the substrate [43]. Fig. 1.5 (a) shows an STM image of the system, where each bright spot corresponds to a $B_3O_3\emptyset_3$ unit.

[4] A follow-up to the original work on B_2O_3 polymorphs of Ferlat and collaborators showed that including van der Waals interactions in the energy calculation systematically increases the total energy and density of the proposed polymorphs, compared to the original results in [35] (reproduced in Fig. 1.4 (left)). The updated results, presented in Fig. 7 (left) of [41], showed that all the predicted polymorphs have an energy higher than that of the B_2O_3-*I* crystal, and are clustered around the energy and density values of the vitreous system.

[5] A previous work in 2018 reported the synthesis of a two-dimensional compound of boron and oxygen atoms on $Au(111)$ by physical vapor deposition of a precursor molecule [42]. Unfortunately, the lack of clear STM images and the unclear stoichiometry of the compound hindered its precise characterization.

The monolayer structure can be modified with subsequent flash annealings at 820 K [44]. A single flash annealing causes the partial amorphization of the system, which becomes complete after two such annealings. The amorphous structure obtained in this way, shown in Fig. 1.5 (b), bears a striking resemblance to that of an amorphous silica bilayer. Additional flash annealings progressively lead to an amorphous network with a lower density, possibly due to the desorption of some components of the structure [44]. After seven flash annealings, the degradation of the network stops and the system presents two different phases, shown in Fig. 1.5 (c). Most of the system is in a polymeric-like phase, with large interconnected filaments in a disordered arranged, but there are some areas where the system has a crystalline hexagonal symmetry, for example in the left part of Fig. 1.5 (c). This crystal presents large openings of 15 Å in diameter separated by a dense structure, with an overall lattice parameter of approximately 20 Å [44]. Further flash annealings do not qualitatively alter the structure of the system shown in Fig. 1.5 (c), but the layer can be fully decomposed into a polymeric-like phase if the system is annealed at 820 K for more than seven minutes.

The boria monolayer is the one of the materials we focus on in this thesis. In Chapter 5, we will study the properties of a variety of different B_2O_3 monolayer polymorphs, and we will describe the lowest energy structure. In Chapter 6, we will describe the properties of this polymorph on a $Pt(111)$ substrate, and we will show that its structure closely match that of the experimental sample. In Chapter 7 meanwhile, we will describe the properties of the line defects in the system and we provide a preliminary analysis of its amorphous structure, comparing it to that of the silica bilayer.

1.1.3 Germania

Since silicon and germanium atoms belong to the same group of the periodic table, they have the same electron structure in the outer shell, and thus form similar bonds and share many chemical properties [28]. It is therefore not a huge surprise that germania, GeO_2, has a phase diagram similar to that of silica [45]. Both systems form $X\text{Ø}_4$ ($X = Si, Ge$) tetrahedral units at low pressure regime and $X\text{Ø}_6$ octahedral units at high pressure [28]. The phase diagram of germania close to ambient conditions is therefore dominated by an α-quartz-like structure and a stishovite-like structure, which bear a close resemblance to their silica counterparts [45].

The main difference between silica and germania is the different size of germanium and silicon atoms. The larger radius of *Ge* atoms compared to *Si* atoms results in the formation of more distorted tetrahedra and greater sensitivity to pressure [45]. As an example, in the α-quartz-like structure of germania, the *O-Ge-O* angle presents a broader distribution, ranging from 106.2° to 113.1°, compared to the *O-Si-O* angle in α-quartz, which is close to its ideal value of 109.5° [28].

The similarities between silica and germania also extend to their two-dimensional polymorphs. Structures analogous to the silica monolayer [46], zigzag [28] and bilayer [47] have been successfully synthesized using germanium instead of silicon. These low-dimensional germania polymorphs are very similar to their silica counterparts, except for the greater distortion of the tetrahedra and the different substrates on which they form [28].

A particularly interesting case is the germania bilayer, which can be synthesized on *Pt(111)* in both crystalline and amorphous forms [47]. This structure features highly distorted tetrahedra, with *O-Ge-O* angles in the direction perpendicular to

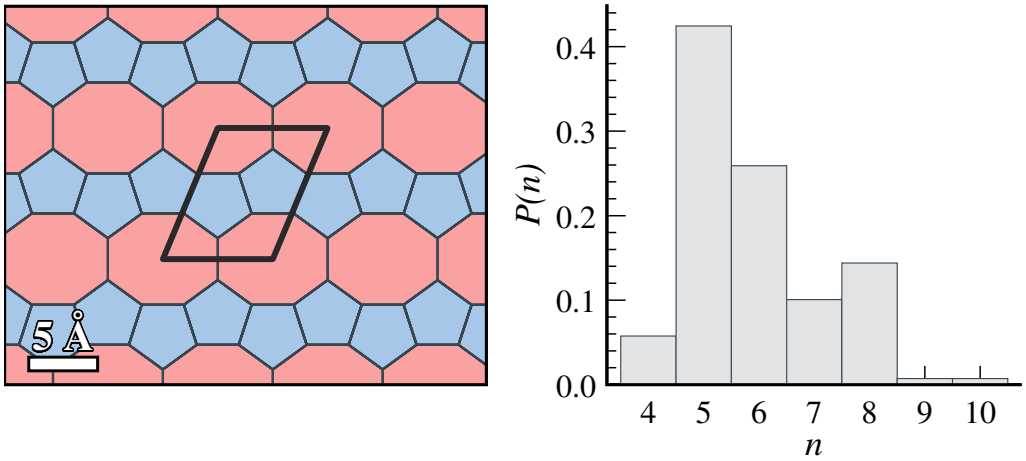

FIGURE 1.6: (Left) Top view of the crystal structure of the germania bilayer on *Pt(111)*, with highlighted the unit cell. Only the bonds are shown and the 5-sided and 8-sided rings are colored in blue and red, respectively. (Right) Ring statistics of an amorphous sample of germania bilayer on *Pt(111)*. The data have been digitalized from [47].

the substrate of around 135° [48] (compared to the 180° for the silica bilayer), resulting in a reduced symmetry due to the absence of a mirror plane between upper and lower layers [28]. Furthermore, when viewed from above, the bilayer's structure is not a regular sequence of hexagonal rings, but rather an ordered string of distorted 8-sided rings connected by stripes of pentagons, see Fig. 1.6 left. This preference for 5- and 8-sided rings is reflected in the amorphous samples, where the ring statistics, *i.e.* the fraction of rings with a given number of sides, is bimodal with two maxima corresponding to the rings present in the crystal. This crystalline structure is a result of the interplay with the substrate, despite this interaction is expected to be weak [28]. Density functional theory calculations for the free-standing bilayer show that the hexagonal structure has an energy 31 meV/Ge lower that the 558 structure observed in the experiment [48]. Nevertheless, when the *Pt(111)* substrate is taken into account the situation reverses, and the 558 structure is 35 meV/Ge lower in energy than the hexagonal one [47]. This behavior highlights that even overlayers that interact weakly with the substrate can be severely affected by its presence, and that the ring structure of such systems presents many different local environments with comparable energies.

1.1.4 Graphitic carbon nitrides

Although the discovery of carbon nitride compounds dates back to 1834 with Liebig's melon structure [49], these materials have attracted significant attention only in recent years. Of particular interest is a class of two-dimensional structures with varying ratios of carbon to nitrogen atoms, known as graphitic carbon nitrides [50, 51]. These crystals tend to have hexagonal symmetry and, depending on the stoichiometry, can exhibit porous structures with openings of more than 2.7 Å in diameter [52–54]. These openings are ideal sites of catalytic activity since they allow adsorbed molecules to interact with the underlying substrate and can be used as a template for hosting single-atom catalysts [55]. Furthermore, these materials are semiconductors with a bandgap ranging from 0.5 to 2.7 eV [52], making them responsive to visible light and thus ideal for applications such as photocatalysis [55–57], gas sensing [52] and use in optoelectronic devices [58, 59].

Much of the interest in these systems is due to the ease with which they can be synthesized on a large scale. Although chemical vapor deposition can be used to precisely control the morphology and stoichiometry of the material [60], the most popular synthesis method is thermal polymerization. This process involves the heating of low-cost precursors, such as melamine or urea, to high temperatures in an inert atmosphere [52, 60]. This method is very cheap and allows for the production of large quantities of material [52], but makes it difficult to precisely control the structure and stoichiometry of the final product.

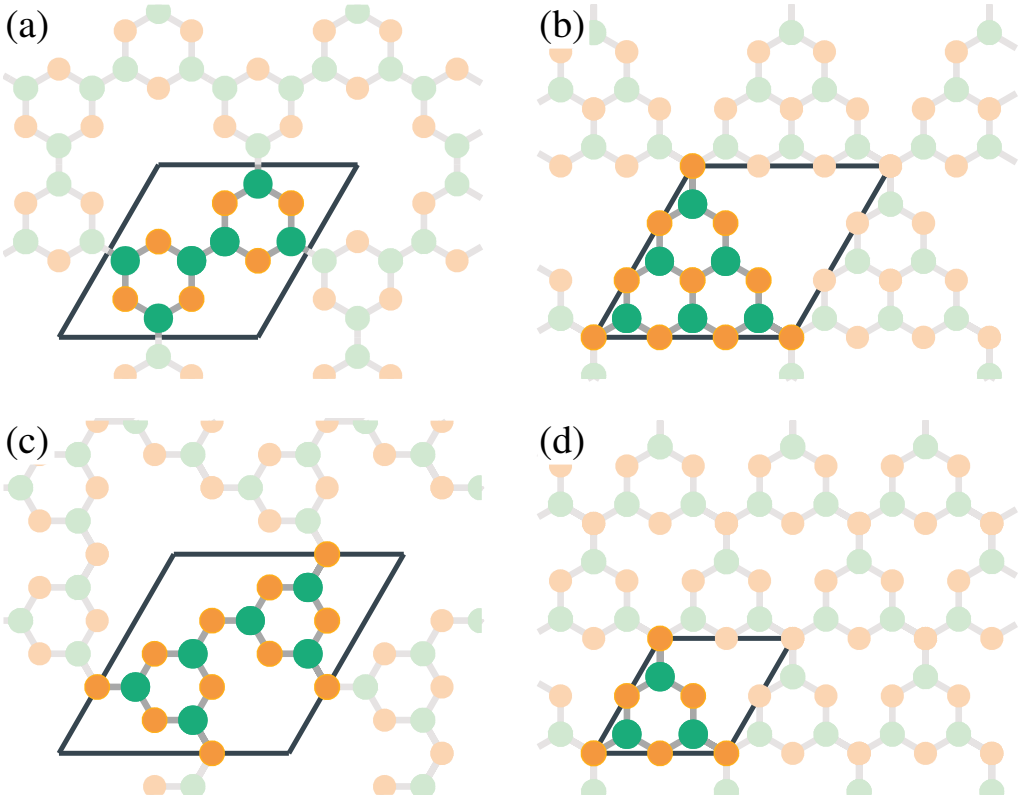

FIGURE 1.7: Sketch of four different graphitic carbon nitride structures proposed in the literature, with stoichiometry (a) CN [61], (b) heptazine-based C_3N_4 [62], (c) triazine-based C_2N_3 [63] and (b) triazine-based C_3N_4 [53]. The unit cell is highlighted in black, while the grey lines identify the bonds between the atoms. Green and orange circles represent carbon and nitrogen atoms, respectively.

Based on the valence of carbon and nitrogen, the ideal stoichiometry of a carbon nitride compound should be C_3N_4. Nevertheless, it is well established that a perfect C_3N_4 composition is difficult to achieve, due to the presence of foreign hydrogens in the final structure or the partial polymerization of the precursors [51]. Thus, numerous different structures have been proposed to explain experimental data [51, 52, 59], see for example Fig. 1.7.

Since the synthesis method involves the polymerization of molecules, the most commonly considered structures are based on triazine and heptazine units, which are present in the molecular precursors used for the synthesis [50]. The triazine unit $C_3N_3\mathcal{N}_3$[6] consists of an hexagonal ring of alternating nitrogen and carbon atoms, with each carbon bonded to an additional nitrogen outside the ring [53]. Heptazine, or tri-s-triazine, consists of three hexagonal C_3N_3 rings fused together, with three

[6] We use the notation $\mathcal{N}$ to indicate a bridging nitrogen between two structural units and N to indicate an nitrogen within a unit.

more nitrogen atoms bonded to the undercoordinated carbons, resulting in the structure $C_6N_7N_3$ [62]. Both units form stable molecules if their nitrogen dangling bonds are saturated with hydrogens [50] and can be used to produce two-dimensional layer with C_3N_4 composition, see Fig. 1.7 (b) and (d) for an heptazine- and triazine-based structures, respectively. From *ab initio* calculations, a heptazine-based framework is expected to be the most stable under ambient conditions [64, 65]. Nevertheless, the synthesis of both structures has been reported [58, 66–68].

Despite the variety of different proposed structures, there is still much uncertainty regarding the possible polymorphs of graphitic carbon nitrides. Experimental conditions and synthesis methods can lead to overlayers with different properties, and our poor understanding of how to control the resulting structure could be detrimental for the application of this promising class of materials.

1.2 Generalities on glassy physics

If a liquid is quenched rapidly enough it is possible to maintain it in metastable equilibrium conditions at temperatures below the melting temperature. In this regime, the dynamics of the system slow down, and if the temperature is further reduced, the material forms a glass. The same process can also occur in some materials above the melting temperature, such as silica and boria. Here, we provide an overview of the general phenomenology of this process and a qualitative classification of glass-forming liquids based on their structure and dynamics (Sec. 1.2.1). We then present an historical account of the different theories proposed to describe the structure of network-forming materials (Sec. 1.2.2), and we compare the merits of the two main theories currently in use (Sec. 1.2.3).

1.2.1 Phenomenology of the glassy systems

Consider a hot liquid in thermal equilibrium and cool it down. Below the melting temperature T_m, the thermodynamically stable phase of a material ceases to be a liquid and becomes a crystal. However, if the system is cooled sufficiently rapidly below T_m, its thermodynamic properties of the liquid can be prolonged at temperatures well below the melting temperature. As the temperature is further decreased, the supercooled liquid becomes increasingly viscous, and the characteristic time required for the system to relax its structure increase sharply. Thus, there is a temperature, called the glass transition temperature T_g, at which the time required for the liquid to properly equilibrate exceeds the time available to make some measurements on the system itself. Therefore, below this temperature the system's structure appears frozen on the observation timescale. The result of this procedure is a glass, an out-of-equilibrium state characterized by the absence of long-range order and yet mechanical properties typical of a solid.

The glass transition temperature is operationally defined as the temperature at which the viscosity η of the system exceeds 10^{12} $Pa{\cdot}s$, that is $\eta(T_g) \simeq 10^{12}$ $Pa{\cdot}s$. Close to T_g, the viscosity of the liquid is thus exceptionally high[7] and corresponds to structural relaxation times on the order of $10^2/10^3$ s [69].

Although the procedure described above is general and applicable to any material, not every material can easily form a glass. The cooling rate required to avoid crystallization of the sample depends strongly on its specific properties. In some

[7] By comparison, for a typical glass-forming system, the viscosity of the liquid near the melting temperature is approximately $\eta(T_m) \sim 10^{-3}/10^{-4}$ $Pa{\cdot}s$ [69].

cases, even cooling rates as high as 10^9 *K/s* may not be enough to prevent crystallization [70].

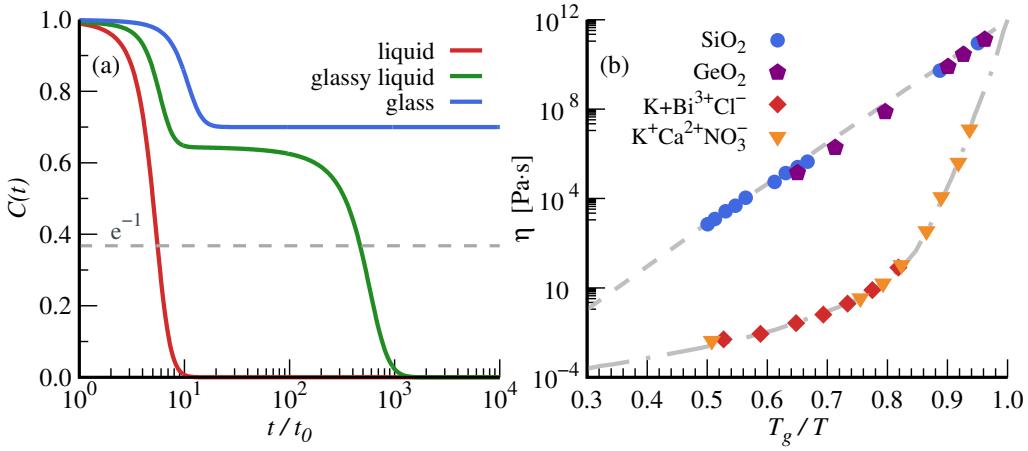

FIGURE 1.8: (a) Schematic behavior of the time-dependent correlation function $C(t)$ for a liquid (red), glassy liquid (green) and glass (blue) system. The horizontal dashed line corresponds to $C(t) = e^{-1}$. (b) Angell plot for two strong glass-formers (SiO_2 and GeO_2) and two fragile glass-formers ($K + Bi^{3+}Cl^-$ and $K^+Ca^{2+}NO_3^-$). The grey curves are a guide for the eyes. The data have been digitalized from [71].

The major difference between a liquid, a supercooled liquid and a glass lies in the decay of their their time-dependent correlation functions over time. In Fig. 1.8 (a), we present the qualitative behavior of one of these correlation functions $C(t)$. In a normal liquid state, $C(t)$ presents a simple exponential decay, which occurs on a relatively short timescale, on the order of picoseconds. Below the onset temperature T_o for the glassy dynamics, *i.e.* the temperature at which the slowing down of the dynamics start to take place, the time-dependent correlation function for the liquid begins to develop a shoulder, which at lower temperatures becomes an intermediate plateau. Thus, for a supercooled liquid, $C(t)$ exhibits a two-step relaxation, with an intermediate plateau stretching over a longer timescale as the temperature decreases. Finally, for a glass, this plateau extends well beyond the time window available for performing measurements on the system, and therefore $C(t)$ shows no decay. From the time-dependent correlation function $C(t)$, it is possible to extract a typical correlation time τ for the system, generally defined by the relation $C(\tau)/C(0) = e^{-1}$. Since the time-dependent correlation function of a glass do not fully decay within the time window t_{obs} available for measurements, its correlation time can only be estimated as $\tau \gg t_{obs}$.

Although the glass transition temperature T_g and the onset temperature T_o for the glassy dynamics are generally lower than the melting temperature T_m, some materials exhibit a slowing down of the dynamics similat to that previously described well above T_m, as is the case for 3*d* silica and boria, see Sec. 1.1.1 and 1.1.2. Thus, a more general term used to describe this behaviour is the *glassy liquids* regime.

Glassy liquids can be qualitatively classified according to their structure and dynamical properties. Regarding their structure, one can distinguish between close-packed and network-forming. Particles in close-packed systems tend to have isotropic interactions and a large number of neighbors, resulting in high number densities for these systems. Materials like metallic alloys and colloids belong to this class, as do popular model systems such as the Kob-Andersen mixture [72]. Network-forming materials are instead characterized by particles with few neighbors and directional bonds, resulting in low densities network structure. In these systems, it is usually

possible to associate different types of particles with the nodes and the edges of the network. Silica, germania and boria are prototypical examples of network-forming materials.

Regarding the dynamical properties, glassy liquids can be differentiated according to the behavior of their viscosity as a function of the ratio T_g/T. This type of data representation, shown in Fig. 1.8 (b) and called Angell plot [73], allows one to distinguish between fragile and strong glass-forming systems. Strong glass-formers exhibit an Arrhenius behavior of the correlation time and viscosity as a function of temperature,

$$\tau = \tau_0 \exp\left(\frac{E}{k_B T}\right) ,$$

where E is a temperature-independent activation energy required to relax the local structure, τ_0 is a temperature-independent characteristic microscopic timescale and k_B is the Boltzmann's constant. Strong glass-formers appear as straight lines in an Angell plot, as shown by the silica and germania data in Fig. 1.8 (b). By contrast, fragile glass-formers display a strong curvature in the Angell plot, with a slope that increases as the temperature decreases, see for example the ionic systems in Fig. 1.8 (b). Since this slope can be interpreted as an apparent activation energy, this behavior is called a super-Arrhenius behavior, and can be fitted with the semi-empirical Vogel-Fulcher-Tamman (VFT) law

$$\tau = \tau_0 \exp\left(\frac{E}{k_B (T - T_0)}\right) ,$$

with τ_0, E and T_0 some material-dependent constants. The VFT law suggests a divergence of the correlation time at a finite temperature T_0, which is reminiscent of the behavior expected for a continuous phase transition at T_0 [74].

Typically, fragile glass-formers are also close-packed systems, while strong glass-formers have a network structure. Recent results, however, suggest that many network-forming systems, such as silica and water, display a fragile behavior at sufficiently high temperatures, which then crosses over to a strong regime at lower temperatures. This fragile-to-strong crossover has been connected to the presence of a low energy cutoff in the potential energy landscape [75]. Moreover, some results suggest that this dynamical behavior is linked to the presence of polyamorphism [76, 77], *i.e.* the existence of two amorphous structures with different density, and might be connected to a liquid-liquid transition in the material [8].

1.2.2 Structure of network-forming systems

We now discuss the different theories developed to describe the structure of a network-forming system. To fully appreciate the similarities and differences between these theories, we present a historical overview of their development.

The structure of network-forming glasses has been subject of much debate over the last century. This is largely due to a long-standing misunderstanding between three different schools of thought[8] [79].

The first theory to be developed was the early crystallite theory. This theory considers a glass to be an agglomeration of discrete nanocrystallites of various sizes,

[8] As will be discussed in this and the following section, all these different "theories" do not provide precise quantitative predictions, and should therefore be regarded as "descriptions" or "frameworks" rather than theories. Nevertheless, in this thesis we will refer to them as theories, for consistency with the literature [11, 78, 79].

separated by some form of "grain boundary", with no atomic bonds crossing the interface between different crystallites [11, 78], see Fig. 1.9 (a). This theory was first proposed by Frankenheim in 1835 [80] to explain the ability of a glassy liquid to flow at temperature much lower than the melting temperature of the crystal. Upon heating, the smallest crystals would melt first, creating a sort of lubrification that allowed the glass to flow [79]. These concepts were later proposed independently by Lebedev in 1921 [81], and were strongly supported by X-rays diffraction data of vitreous silica obtained by Randall *et al.* in 1930 [82–84]. From their diffraction data, they estimated that about 80 % of the volume of the sample was occupied by cristobalite crystallites, with an average diameter of 15 Å [82–84]. The initial appealing aspect of this theory was the similarity of the X-rays diffraction spectra of crystalline and amorphous samples, which indicated a certain correspondence between their structures [11].

Around the same time, the Continuous Random Network Theory (CRNT) began to take shape in western Europe. This theory was based on the idea that the local environment of each atom in a glass should also be similar to the one in a crystal. However, since a glass lacks long-range order, the local environments should be connected randomly, with a wider distribution of the angles between them compared to the crystal [85]. The amorphous network has no broken bonds or under- or over-coordinated particles, making it comparable in energy to the crystal. This results is a continuous (*i.e.* without broken bonds) random network in which the building-blocks (*i.e.* the local environments) are the same as in the corresponding crystal, but unlike the crystal, these units are connected to each other randomly, see Fig. 1.9 (b). It is important to stress that this theory considers only geometric randomness and does not take into account the energy involved in the bonds between the units or the thermodynamic stability of the crystal [11]. The concepts of CRNT were first proposed by Rosenhain in 1927 [86], but the theory gained popularity thanks to a 1932 paper of Zachariasen [85], due in part to his two-dimensional sketch of a A_2O_3 vitreous network [79]. The term continuous random network was later introduced by Warren in 1933 [87].

Among physicists of the Western countries, the random network theory quickly replaced the early crystallite theory [79]. For example, as early as 1933, Randall and collaborators published a paper admitting that they had over-stressed the word *"crystallite"* in their earlier works [88]. The rapid decline in popularity of the early crystallite theory was due to its incompatibility with new experimental data. In particular, X-rays diffraction data of vitreous silica showed that the position of the first peak was expanded by about 6% compared to cristobalite, which was difficult to justify in the crystallite theory. It was also unclear why the first diffraction peak did not get narrower increasing heat treatment, as should be expected by the growth of crystallites upon heating [78, 79]. Moreover, it began to become clear that the surface energy of the crystallites makes the resulting structures much more energetically costly than a random network like the one proposed by Zachariasen [11].

The issues of the early crystallite theory were also discussed by physicists in the Soviet Union and led to the development of the modern crystallite theory, also known as cybotactic theory [78, 79]. In this framework, it is assumed that there are some transient crystalline domains in the liquid, called cybotactic groupings, which fluctuate in size and position. These crystalline domains are then frozen when the system is quenched, becoming embedded in a disordered matrix similar to that described by the CRNT [79, 89]. To accommodate the strain induced by the neighboring disordered structure, the crystalline domains are expected to be highly distorted [89], see Fig. 1.9 (c). This theory thus leads to a continuous random network

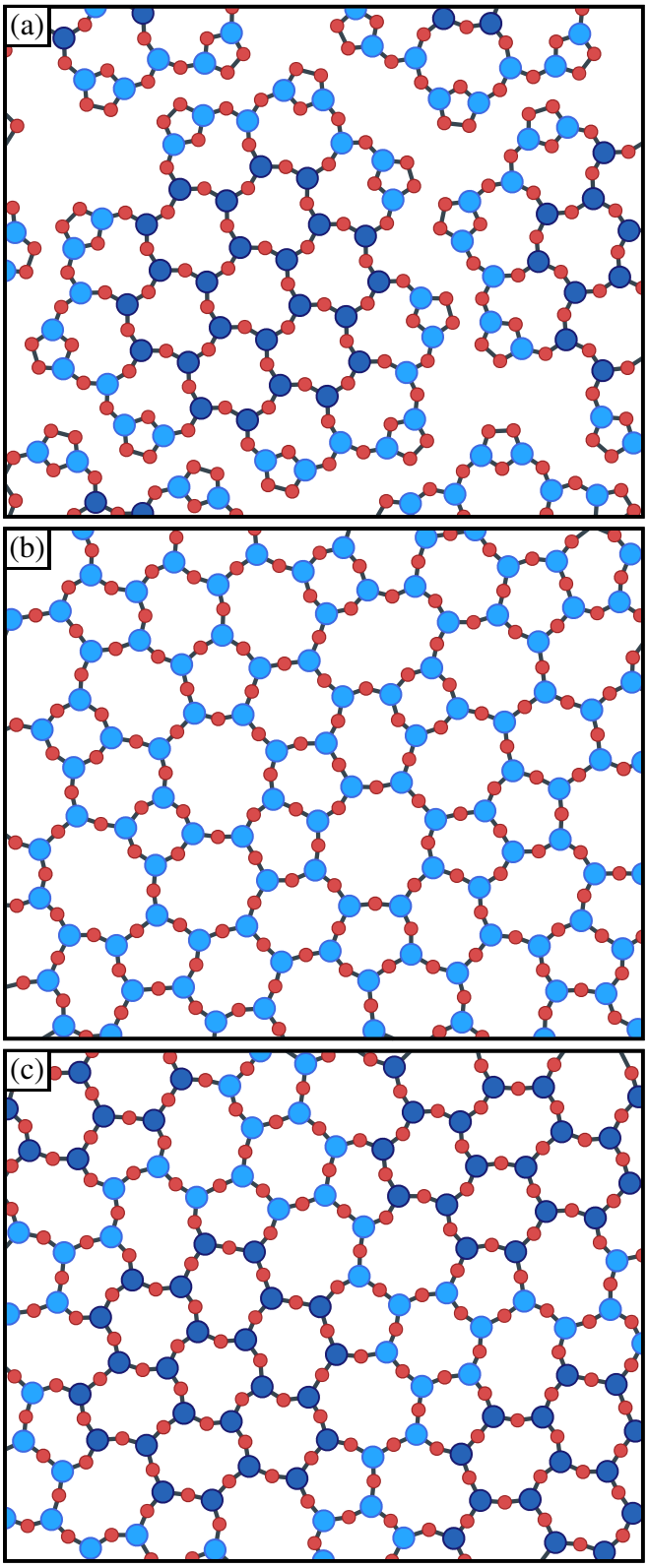

FIGURE 1.9: Two-dimensional schematic diagrams of the structure of vitreous A_2O_3, according to the early crystalline theory (a), continuous random network theory (b) and cybotactic theory (c). Blue and red circles represent A-type and oxygen atoms, respectively. Dark blue circles in (a) and (c) correspond to A-type atoms within a crystalline domain. The images have been digitalized from [11].

like that of the CRNT, but implies that the spatial fluctuations of the degree of structural order are in excess of those expected on a purely statistical ground [11, 89]. The network is thus expected to be nanoheterogeneous [79]. The concept of cybotactic groupings in a liquid was introduced by Stewart in 1927 [90, 91], while the modern crystallite theory was first proposed by Valenkov and Porai-Koshits in 1936[9] [92]. One of the reasons that led them to develop this theory was the drastic structural rearrangement on devitrification predicted by CRNT, which they deemed unrealistic [79].

1.2.3 Comparison of CRNT and cybotactic theory

By the early 1950s, the cybotactic theory began to be accepted by soviet scientists and replaced the early crystallite theory. Nevertheless, this theory was strongly ostracized in the West [79], which firmly favored the CRNT. This was due to several reasons, but the main ones were (i) the unclear distinction between the early crystallite theory and the cybotactic theory, as both theories were originally called "crystallite theory"[10], and (ii) the change of the meaning of the word *"kristallit"* in Russian over time [79].

It was not until the *IV International Congress on Glass*, held in Paris in July 1956, that for the first time the proponents of the two theories met face to face to discuss the merits of the two schools of thought. In that meeting they realized how similar the cybotactic and continuous random network theories were in many aspects, approaching the structure of a network-forming system from two different, but complementary perspectives[11] [79]. The main difference between the two theories regards the homogeneity of the resulting structure. In the framework of CRNT, a glass is statistically homogeneous, while the cybotactic theory predicts that a glass must be nanoheterogeneous [79]. This difference becomes particularly relevant in the case of multicomponent glasses, such as those with network-modifying cations. In this case CRNT predicts that the cations occupy the cages in the original unperturbed network, resulting in a homogeneous distribution of network-modifying cations. The cybotactic theory, instead, envisions that the cations occupy the regions between the cybotactic groupings, resulting in a nanoheterogeneous network where the cations reside in string-like cages [11]. The latter prediction proved accurate, and led Greaves to develop the modified random network theory in 1985 [94]. This latter theory, applicable only to glasses with network-modifying cations, assumes the clustering of the cations and their associated nonbridging oxygens, due to their electrostatic interaction[12]. Thus, the cations actively modify the local structure of the network and at high concentration form one-dimensional channels [11].

In the case of single-component glasses, the question of which theory best describe the structure of a real network-forming system reduces to ask whether the

[9] Valenkov and Porai-Koshits always referred to their theory as crystallite theory, possibly out of respect for Lebedev [79]. This led to much confusion in the field, linking this new theory with the obsolete early crystalline theory.

[10] To the best of the author's knowledge the term *"cybotactic theory"* was first used to describe this theory by Wright around 2014 [79]. The name *"modern crystallite theory"* was instead first used by Urnes in 1960 [93]. Thus, for about 24 years there was no distinction in names between the early crystalline theory and the cybotactic theory, despite their obvious differences.

[11] Kreidl, one of the conference organizers, commented ten years later: *"We found a great difference in the meaning of words in the two languages"* [79].

[12] Note that the electrostatic interactions between cations and nonbridging oxygens is the only type of energy considered in the framework of random network theories [11]. Even in the modified random network theory, no interaction between local environments in the single-component glass is taken into account.

number and size of the crystallites exceed those statistically expected for a random network [11]. Since the structure of a three-dimensional system is notoriously difficult to analyze in real space [20], this information has to be inferred from scattering data. The value of the structure factor $S(k)$ for $k \to 0$ can then be related to the mean square fluctuations of the average number density over a given sampling volume [89]. Thus, simple models based on the different theories can be used to predict the number density fluctuations, allowing for rigorous comparison with the experimental data. This comparison was performed on both silica and germania glasses, but unfortunately proved inconclusive [89]. The theories are in fact highly phenomenological, and thus their corresponding models depend on many parameters, which can always be tuned to reproduce the experimental results.

The inability of scattering data to resolve this controversy over the structure of network-forming systems led to their modelling at the atomic level. By the mid 1960s, doubts began to arise about the feasibility of a three-dimensional network built according to the different theories. This led to the construction of atomic models for such systems. The first ones were hand-built, such as the most famous Bell and Dean's model of 1966 [95], while later models were computer-generated. In particular, the introduction of the WWW algorithm in 1985 by Wooten, Winer and Weaire [96], based on local changes in the network topology, enabled the generation of arbitrarily large structures under periodic boundary conditions with a precise distribution of the structural parameters.

Nowadays, the most widely used theory for describing the structure of network-forming glasses is the continuous random network theory [97]. The cybotactic theory, meanwhile, is regarded as an outdated framework, although it is sporadically revived from time to time [98]. The reason for this is unclear. In our opinion, most of the problems with the cybotactic theory arise from the extensive debate in the literature and the lack of a precise initial distinction between the early crystalline theory and the cybotactic theory, which makes the entire discussion particularly difficult to follow. It should also be stressed that the cybotactic theory lacks precise predictions. For example, it is unclear what the average crystallite size should be, and whether there should be a size distribution of such crystallites. Moreover, the extent of the disordered region between crystallites is not specified, as is the degree of distortions of the crystalline domains. This lack of predictions makes the theory extremely flexible, but it also adds many free parameters that hinder its applicability. In contrast, the continuous random network theory, while not providing accurate predictions by itself, is simpler to apply[13]. Nevertheless, it should be noted that within CRNT framework, the disorder is only geometrical, and no energy between neighboring units is taken into account in the formation of the network. This inevitably makes the CRNT a first-order approximation of the structure of a real network-forming system [78, 79], and leave open the possibility of crystalline domains in the materials.

The synthesis of two-dimensional systems over the past 20 years can shed new light on the structure of network-forming materials [20, 97]. Using standard surface techniques it is possible to resolve the atoms' positions in real space, enabling precise measurements of the angle distributions between atomic units and sizes and frequencies of crystalline domains [19, 20, 26]. It should be noted, however, that the presence of an underlying periodic substrate, see Sec. 4.2, and the peculiarities of the physics of two-dimensional materials, see Sec. 1.3, may make a direct comparison between $2d$ and $3d$ systems difficult.

[13] The concepts of CRNT have proven to be very valuable in this thesis, where they were used to develop an algorithm for generating polymorphs, see Sec. 5.1, and for the reconstruction of the atomic positions from the experimental STM images, see Sec. 7.2.2.

1.3 Peculiarities of two-dimensional systems

Similar systems with diverse dimensionality can have significantly different physical descriptions. This is due to changes of relevance of several effects, such as thermal fluctuations and average number of neighbors. For example, at low dimensionality the thermal fluctuation plays a crucial role in the physics of the systems. Meanwhile, increasing the dimensionality of a system the number of average number of neighbors increases rapidly, making a mean field description increasingly more accurate.

In this section we discuss two peculiarities that distinguish the physics of two-dimensional systems from their three-dimensional counterparts. These effects are related to the thermal instability of a 2d crystal and the melting process in two dimensions, and will be used in this thesis to analyze and frame our data in the context of the theory on 2d systems.

1.3.1 Mermin-Wagner-Hohenberg theorem

In the mid 1960s, the works of Mermin, Wagner and Hohenberg [99–101] demonstrated that in less than three dimensions, a stable ordered phase at finite temperature cannot exist if the system is invariant under a continuous symmetry [99]. In the specific case of a crystalline solid, these results rule out long-range translational order in one and two dimensions for particles interacting with finite-ranged continuous potentials. In this section, we review the main results concerning the instability of a two-dimensional crystal in the harmonic and Debye approximations.

We consider a d-dimensional crystal defined by a set of lattice sites $\{\mathbf{R}\}$. The displacement of the atom at site $\mathbf{R}$ at time t due to thermal fluctuations is $\mathbf{r}(\mathbf{R},t) = \mathbf{R} + \mathbf{u}(\mathbf{R},t)$. Within the harmonic approximation, the displacement field $\mathbf{u}(\mathbf{R},t)$ can be expanded in term of planar waves as

$$\mathbf{u}(\mathbf{R},t) = \left(\frac{L}{2\pi}\right)^d \int \mathbf{u}_k(t)\, e^{i\mathbf{k}\cdot\mathbf{R}}\, d^dk \tag{1.1}$$

where L is the linear length of the system. In this framework, these planar waves or phonons are independent, and the solid can be described as a gas of thermally excited non-interacting phonons [102, 103]. Thus, the equipartition of energy in this gas gives $m\omega_k^2 \left|\mathbf{u}_k\right|^2 = k_B T$, where m is the average particle mass, ω_k is the frequency of the modes with wavenumber $\mathbf{k}$ and T is the temperature. The mean-squared thermal displacement $\langle|\mathbf{u}|^2\rangle$ can then be written as

$$\langle|\mathbf{u}|^2\rangle = \left(\frac{L}{2\pi}\right)^d \int \langle|\mathbf{u}_k|^2\rangle\, d^dk = \frac{dk_BT}{m} \int \frac{g(\omega)}{\omega^2}\, d\omega\,, \tag{1.2}$$

where $g(\omega)$ is the vibrational density of states. In the Debye approximation, the wavelength and frequency are connected by a linear dispersion relation $\omega = ck$, with c the velocity of the phonons, and the vibrational density of states is approximated by $g_D(\omega) \propto \omega^{d-1}\,\Theta(w_D - \omega)$, with ω_D the Debye frequency and $\Theta(x)$ the Heaviside step function [104]. Moreover, in a finite system of linear size L, the integral in Eq. 1.2 has a lower bound equal to $\omega_{min} = \frac{2\pi c}{L}$. Under these assumptions, Eq. 1.2 becomes

$$\langle|\mathbf{u}|^2\rangle \propto k_BT \int_{\frac{2\pi c}{L}}^{\omega_D} \omega^{d-3}\, d\omega\,. \tag{1.3}$$

Thus, in two dimensions (d=2), the previous expression reads

$$\langle |\mathbf{u}|^2 \rangle \propto k_B T \int_{\frac{2\pi c}{L}}^{\omega_D} \frac{1}{\omega} \, d\omega \propto k_B T \ln\left(\frac{L}{\sigma_0}\right) , \tag{1.4}$$

where $\sigma_0 = \frac{2\pi c}{\omega_D} = \sqrt{\frac{2\pi}{\rho}}$ is a characteristic distance and ρ is the number density of the system. This result shows that the mean squared displacement in a two-dimensional crystal diverges logarithmically with the linear length L of the system, meaning that such structure is not stable at any finite temperature in the thermodynamic limit.

The results presented so far show that a two-dimensional crystal is unstable at any finite temperature due to the presence of long-wavelength fluctuations with wavevector $k \simeq \frac{2\pi}{L}$. These fluctuations introduce a system-size dependence in the mean squared displacement, which diverges in the thermodynamic limit. These effects, however, are not exclusive to two-dimensional crystals, but also have an impact on liquids in two spatial dimensions. In particular, the divergence with the system size in Eq. 1.4 arises from the presence of long-wavelength modes and does not depend on the arrangement of its atoms. Thus, any two-dimensional system with acoustic excitations is affected by these fluctuations [105], sometimes called Mermin-Wagner fluctuations.

Atypical behavior in the correlation function of two-dimensional liquids started to be noted around 2015 [106], although it was already known that special care should be taken when analyzing data on $2d$ liquids [107]. In particular, the intermediate plateau, which characterizes the glassy regime, see Sec. 1.2.1, appears to progressively disappear as the system size increases. This behavior was only observed in time-dependent correlation functions related to the translational dynamics, while the orientational dynamics appears unaffected [106]. This effect was later connected to the presence of long-wavelength fluctuations [105], which allow a particle and its neighbors to move together over large distances, contrary to what happen in $3d$ [106]. This atypical behavior was extensively studied with computer simulations [103, 105, 106, 108, 109], but the same effects can also be observed in experiments [110, 111].

Several methods have been used to avoid this system size dependence of the correlation function and to recover the glassy regime. One approach is to rely on the analysis of the orientational dynamics or the bond-breaking correlations [105], which are not affected by long-wavelength fluctuations. The other main technique focuses on the translational dynamics and, instead of the displacement of a particle in the calculations of the translational correlations, uses its cage-relative displacement, defined as its displacement relative to its cage of neighbors[14] [110].

Although these methods allow one to remove the influence of long-wavelength fluctuations from the data, it should be noted that such fluctuations are not spurious effects, but are instead integral part of the physics of the system. Therefore, in our opinion, it is not entirely clear whether glassy dynamics in three and two dimensions are actually ruled by the same physical mechanisms, despite looking similar once cage-relative quantities are used in $d = 2$.

1.3.2 KTHNY theory

The Mermin-Wagner-Hohenberg theorem does not exclude the presence of other types of long-range order, different from translational order, in $2d$ systems at low

[14] This procedure will be discussed in detail in Sec. 3.1.2.

temperatures, as already observed by Mermin [101]. In the mid 1970s, different works by Kosterlitz and Thouless [112, 113], Halperin and Nelson [114, 115], Young [116] and, independently, Berezinsky [117, 118], showed that a novel kind of phase transition can occur in $2d$ systems, ruled by the formation of topological defects. In particular, it was shown that in $2d$ the interaction energy of two topological defects increases with the logarithm of their distance. This interaction is the same as that between two point charges in $2d$ and allows the system to be mapped into a two-dimensional gas of Coulomb charges [119, 120], which is easier to analyze [119, 120].

In the Kosterlitz-Thouless-Halperin-Nelson-Young theory, or simply KTHNY theory, the different phases are characterized by different long-distance behavior of two-point correlation functions. A crystalline system in three dimensions is characterized by long-range order, which means that its translational correlation function does not fully decay at long distances, $G(r) \sim cost.$ for $r \to +\infty$. In two dimensions, a system cannot display long-range translational order due to the Mermin-Wagner-Hohenberg theorem. In this case, a crystal shows a weaker quasi-long-range translational order, with a correlation function between two points that decays algebraically with their distance r, that is $G(r) \sim r^{-\gamma}$ for $r \to +\infty$, with γ a constant. By contrast, a liquid in two or three dimensions is characterized by short-range order, with a space-dependent correlation function that decays exponentially with the distance, $G(r) \sim e^{-r/\xi}$ for $r \to +\infty$, with ξ a characteristic length.

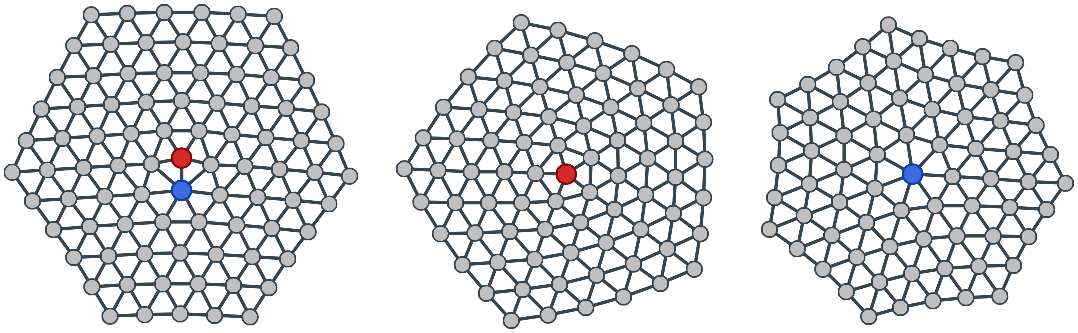

FIGURE 1.10: Topological defects in a system of hard disks: a free dislocation (left) and two types of disclinations (center and right). Red, grey and blue circles represent particles with five, six and seven neighbors, respectively. Black lines identify the neighbors of each particle. Images reproduced from [121].

The KTHNY theory describes the melting of a two-dimensional crystal as follows. In two dimensions, a crystal presents quasi-long-range translational order and long-range orientational order [102]. The typical topological defects in the system are bound pairs of dislocations, which do not significantly alter either the translational or the orientational order. In a system of hard disks, such defects appear as two pairs of adjacent disks with 7 and 5 neighbors, while non-defective particles have 6 neighbors. As the temperature increases, these defects begin to unbind, forming free dislocations in the system, shown on the left of Fig. 1.10. This process destroys the quasi-long-range translational order in the system and leads to the formation of a new phase, called hexatic phase, characterized by short-range translational order and quasi-long-range orientational order. The lack of translational order in the system is due to the presence of free dislocations, which corresponds to the addition or removal of a row of atoms starting from location of the defect. As the temperature increases further, the dislocations break down, forming free disclinations. In a system of hard disks, such defects appear as isolated disks with either 5 or 7 neighbors, as shown in the center and right of Fig. 1.10. The appearance of free

disclinations destroys the residual quasi-long-range orientational order in the system, which becomes a liquid, characterized by both translational and orientational short-range order. In Tab. 1.1, we summarize the extent of order in the different phases in the KTHNY theory.

System	Translational order	Orientational order
Crystal	quasi-long	long
Hexatic	short	quasi-long
Liquid	short	short

TABLE 1.1: Range of different types of order in 2*d* systems in the KTHNY theory.

Therefore, within the KTHNY framework, the melting of a two-dimensional crystal is a two-step process mediated by the unbinding of topological defects. As the temperature increases, the crystal first transitions into a hexatic phase, which later melts into a liquid. The crystal-hexatic transition is continuous, while the hexatic-liquid is first-order [122–124].

The KTHNY theory has been tested mainly in single component close-packed systems. Although some preliminary analyses have been performed on binary systems [125], to the best of our knowledge the melting scenario described by this theory has never been tested for network-forming materials. The presence of strong directional bonds in such systems might alter the energetic cost of the topological defects on which the theory is based, leading to a melting process different from that described in the KTHNY scerario.

Chapter 2

Silica bilayer: effective potential and comparison with experiments

In this chapter we develop a simple interaction model for the silica bilayer. We use a structure-matching approach to reproduce the structural features of the experimental samples and then study the model over a broad range of temperatures using molecular dynamics simulations. We show that even a model with simple isotropic interactions can successfully reproduce the structure of network-forming systems with covalent bonds and that the thermodynamic and dynamic properties of our model broadly resemble those of three-dimensional silica. Interestingly, the system presents a rich glassy dynamics, even well above the melting temperature.

We first describe our strategy to model the silica bilayer (Sec. 2.1). Then, we compare the structural data observed in experiments with those produced by different functional forms for the interaction potential (Sec. 2.2). Finally, we study the thermodynamic and dynamic properties of the best model as a function of temperature (Sec. 3.1). We conclude with a brief description of the melting of the system.

The bulk of this chapter is adapted from Ref. [126], but it also includes new material (Sec. 2.2.4) and additional discussions.

2.1 Development of the interaction potential

Since its first synthesis in 2012 [18, 19], numerous attempts have been made to simulate the full silica bilayer. Many studies used the structure of amorphous graphene as a template to construct the silica bilayer, relaxing the resulting system with Vashishta [127], Watanabe [128, 129] or Tangey-Scandolo potential [130, 131][1]. To the best of the author's knowledge, no classical force field developed for bulk amorphous silica has been used to simulate the full bilayer structure of this new material in thermal equilibrium [133]. This is mainly due to the presence of an atypical angle of 180° between the tetrahedral units, which is far from the angles generally found in three-dimensional silica, which are between $145° - 155°$, see Sec. 1.1.1. Due to these intrinsic difficulties of a fully atomistic description of the system and the presence of this perfect symmetry between upper and lower layer, Roy, Heyde and Heuer (RHH) suggest a simpler, strictly two-dimensional model of this material [133]. In this model, the position of each atom is projected onto the plane of the substrate, resulting in a strictly two-dimensional effective system. The substrate is not included explicitly due to the weak van der Waals interaction with the silica bilayer[2] [20]. The

[1] Surprisingly, in the literature we found no attempts to use the BKS potential [132], which is widely used to simulate $3d$ silica, see Sec. 1.1.1.

[2] We will analyze a simple model to study the interaction between silica bilayer and the substrate in Chapter 4.

resulting system is therefore composed of effective particles confined in a plane, see Fig. 1.2. For simplicity, we will refer to the effective particle consisting of *Si* (upper layer) - *O* (intermediate layer) - *Si* (lower layer) as a silicon (*Si*) particle and the effective particle consisting of *O* (upper layer) - *O* (lower layer) as an oxygen (*O*) particle. Following Ref. [133], we set the mass ratio between the effective oxygen and silicon particles to 0.57. We emphasize that the STM and TEM images obtained in the experiments are effectively a two-dimensional projection of the structure of the real system. Therefore, this strictly two-dimensional model allows for a direct comparison with the experimental structures obtained using these techniques.

2.1.1 Interaction models

To simulate the system, we consider two different types of pairwise isotropic classical potentials. The first potential features a short-range soft sphere repulsion and a longer ranged Yukawa interaction,

$$u_{\alpha\beta}(r) = \epsilon_{\alpha\beta}\left[\left(\frac{\sigma_{\alpha\beta}}{r}\right)^{12} + q_{\alpha\beta}\frac{e^{-\kappa r}}{r}\right]. \tag{2.1}$$

To ensure global charge neutrality, the ratio between the effective charges of *Si* and *O* particles is set to $Si:O=(+1.5):(-1)$. This model was originally introduced by Roy, Heyde and Heuer [133], and we will therefore refer to it as the RHH model. It captures the general structure observed in the experiments, such as the shape of the radial distribution function and the ring statistics, but it also displays some discrepancies, such as a smaller fraction of hexagonal rings and a larger population of rings with more than 10 sides. Furthermore, in the original RHH model [133], the physical meaning of some parameters is not entirely clear: the screening parameter κ scales with the size of the system and has no direct connection to the intrinsic length scales of the system, while the cut-off distance is set to half the side of the simulation cell, which may be excessive. Finally, most of the analysis of the RHH model so far [133, 134] was done on a very small sample of 80 particles, which was claimed to be enough to avoid significant finite-size effects [133]. One of the aims of this work is to provide solid grounds for the choice of the model's parameters and to improve its agreement with experiments. Moreover, we will systematically check for finite-size effects in the simulation to critically test the findings obtained with the original model.

The second potential we consider involves a soft-sphere repulsion between particles of the same species and a Lennard-Jones attraction between particles of different types [135]

$$\begin{aligned} u_{\alpha\alpha}(r) &= \epsilon_{\alpha\alpha}\left(\frac{\sigma_{\alpha\alpha}}{r}\right)^{12} \\ u_{\alpha\beta}(r) &= 4\epsilon_{\alpha\beta}\left[\left(\frac{\sigma_{\alpha\beta}}{r}\right)^{12} - \left(\frac{\sigma_{\alpha\beta}}{r}\right)^{6}\right] \quad for\ \alpha \neq \beta\,. \end{aligned} \tag{2.2}$$

We will refer to this potential as the LJ model. This functional form was used to model $3d$ silica [135] and, despite its simplicity, reproduces some experimental properties quite well. For both interaction models, we used a shifted-force cut-off, which ensures that the energy and the forces go smoothly to zero at the cut-off distance R_{cut}.

We also considered more complex functional forms for both models. For example, we considered different screening parameters for each interaction type, as well as different exponents in the soft-sphere repulsion and in the Lennard-Jones attraction. However, no major improvements were found over the models presented above.

2.1.2 Computational details

In the following, we will use reduced units, taking $r_{unit} = 1$ Å and $m_{unit} = 72\ g/mol$ [133] as the units of length and mass, respectively, while we set the unit of energy e_{unit} equal to ϵ_{SiSi} for each potential[3]. We define the time unit as $t_{unit} = r_{unit}(\frac{m_{unit}}{e_{unit}})^{1/2}$.

We consider systems composed of N particles in a rectangular cell of sides (L_x, L_y) with periodic boundary conditions. We fixed the number density at the experimental value, $\rho = N/(L_x L_y) = 0.2068$ [133]. We set the ratio L_y/L_x to obtain a nearly square cell commensurate with the honeycomb lattice at the chosen chemical composition $x_{Si} = 2/5$. We carried out molecular dynamics simulations using `RUMD` [136], which is particularly efficient for the system sizes of interest, which range from $N = 80$ to 10^5 particles. We performed all our simulations in the NVT ensemble using a Nose-Hoover thermostat with a thermostat relaxation time $\tau_{term} = 1.6381$. The integration timestep was set to 0.045 at $T = 0.015$ and then scaled with the square root of the inverse temperature as $dt(T) = 0.045\sqrt{0.015/T}$.

We performed two kinds of simulations: the first ones to produce out-of-equilibrium glass states and the second ones to simulate liquids at equilibrium conditions. In the first case, the quench protocol consisted of a sequence of simulations at temperatures 0.0200, 0.0125, 0.0100, 0.0075, and 0.0010. These simulations lasted 50000, 50000, 250000, 250000, and 5000 timesteps, respectively. Note that this protocol does not correspond to the experimental one, which is based instead on physical vapor deposition and can be optimized to produce even very stable glasses [137]. It is therefore not obvious at which temperature one should compare the simulation data with the experimental ones. Nonetheless, we will show in Sec. 2.2 that the structure of these rapidly quenched, out-of-equilibrium states can match very well the experimental data. For the equilibrium simulations, we start from a configuration sampled at high temperature and then equilibrate the system at the desired temperature. We anneal the system until the mean square displacement (MSD) of particles of both species exceeds 10^3. We then perform a production run at the same temperature to store configurations, making sure again that the number of steps is such that the final MSD is always at least 10^3.

[3] We have found that is quite difficult to connect the unit of energy e_{unit} of the models with a physical energy scale. To determine the latter, it is not possible to use experimental observables and therefore it is necessary to resort to DFT calculations. However, using the DFT energy of the crystal crystalline bilayer to set this scale results in a much higher energy scale than expected [133]. In particular, following this procedure, structures simulated at very high temperature (rougly 9700 K) are extremely similar with experimental images obtained at low temperature (77 K) [133]. We speculate that using the DFT energy of a large set of crystalline polymorphs and amorphous structures might result in a more reasonable energy scale.

2.1.3 Optimization procedure

To determine the interaction parameters, we used a structure-matching approach [138]. After some preliminary tests, we decided to fit only a limited set of structural features that we deemed dense of information on the medium range order in the material. In particular, we fitted the average nearest-neighbors distance between effective silicon and the experimental ring statistics. We also added a penalty term to avoid the formation of a considerable amount of small (3-sided) or large (more than 10-sided) rings, which were not observed in the experiments [133]. We obtained the nearest-neighbor distance from the position of the first peak of the radial distribution function (RDF) between silicons, $g_{SiSi}(r)$. We use our definition of rings, presented in Appendix C. The ring statistics is then defined as the probability distribution $P(n)$ of rings with a given number of sides n. Empirically, we found that fitting the *Si-Si* distance and the rings statistics is enough to reproduce a larger set of structural features, including the full shape of the RDFs and the bond-angle distributions, see Sec. 2.2.1.

With that in mind, we aim at minimizing the cost function

$$\chi^2(\mathbf{q}) = \chi^2_{RDF}(\mathbf{q}) + \chi^2_{ring}(\mathbf{q}) + \chi^2_{pen.}(\mathbf{q})\,, \tag{2.3}$$

where $\mathbf{q}$ is the vector of interaction parameters and

$$\chi^2_{RDF}(\mathbf{q}) = \omega^{SiSi}_{RDF}\left[r_{SiSi}(\mathbf{q}) - \tilde{r}_{SiSi}\right]^2\,, \tag{2.4}$$

$$\chi^2_{ring}(\mathbf{q}) = \sum_{n=4}^{10} \omega^n_{ring}\left[P(n;\mathbf{q}) - \tilde{P}(n)\right]^2\,, \tag{2.5}$$

$$\chi^2_{pen.}(\mathbf{q}) = \omega^3_{pen.}\,P(3;\mathbf{q})^2 + \omega^{n>10}_{pen.}\,P(n>10;\mathbf{q})^2\,. \tag{2.6}$$

Here, r_{SiSi} is the position of the first maximum in the *Si-Si* RDF, ω^j_i are weights, and the quantities with a tilde on top are those measured experimentally. In particular, $\omega^{SiSi}_{RDF} = 1$, $\omega^n_{ring} = 3.629025 \cdot 10^{-4}/\sigma_n^2$ with σ_n the standard deviation on $\tilde{P}(n)$, and $\omega^3_{pen.} = \omega^{n>10}_{pen.} = 45$. The experimental data are obtained from samples synthesized by different groups on different substrates, and they are discussed in detail in Appendix B. Since these samples show very similar ring statistics, we decided to include all of them in the evaluation of the cost function. Note that all the experimental quantities involved in $\chi^2(\mathbf{q})$ are measured at low temperature, due to the constraints on the STM and TEM techniques used to obtain the atomic positions. Furthermore, despite extensive analysis of this material in the literature [4, 16, 20], publicly available datasets with the experimental atomic positions are scarce.

Some comments about the interaction parameters of the RHH model are in order. In its original formulation, both the cutoff radius R_{cut} and the screening length $l_C = \frac{1}{\kappa}$ scale linearly with the cell side [133]. This results in long-range interactions that become progressively more expensive to compute as the system size increases. To determine the optimal values of these parameters, we proceeded as follows. Since the cost function depends weakly on both κ and R_{cut}, we optimized them separately: we evaluated the cost function by changing one of these parameters at the time, while fixing the others to their values in the original RHH model. We found empirically that fixing $R_{cut} = \frac{1}{\kappa}$ produced overall good results, hence we optimized the screening parameter using this constraint. As shown in Fig. 2.1, the cost function becomes nearly constant when $\kappa < 0.1$, close to the value used by RHH for $N = 80$ ($\kappa_{RHH} = 0.1093$) [133]. We also found that the cost function has two minima,

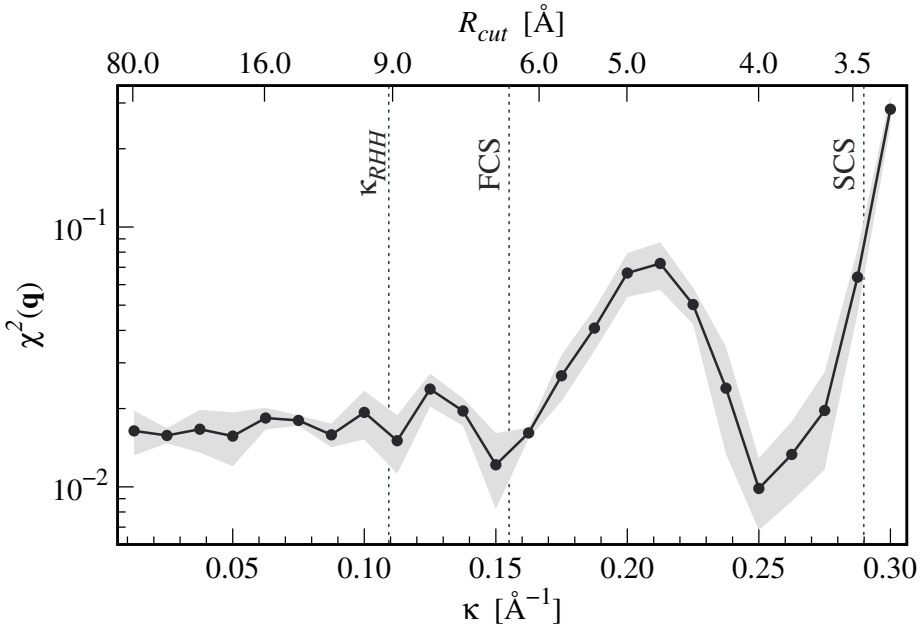

FIGURE 2.1: Dependence of the cost function $\chi^2(\mathbf{q})$ on the screening parameter κ for the original RHH model. The cutoff parameter was set to $R_{cut} = 1/\kappa$. The shaded area is an estimate of the statistical uncertainty. The vertical dashed lines indicate the first coordination shell (FCS) and the second coordination shell (SCS) of $g_{SiSi}(r)$ and the original values of the screening parameter and the cutoff radius used by Roy *et al.* [133] (κ_{RHH}).

which correspond to values of l_C just after the first coordination shell and around the second coordination shell of $g_{SiSi}(r)$, respectively. These results indicate that the network structure depends mainly on interactions up to the second shell of neighbors. Using this information, we reoptimized the parameters of the RHH model fixing $\frac{1}{\kappa}$ and R_{cut} just after the first (4.0 Å) or the second coordination shell (6.0 Å). We will call the corresponding reparametrized models RHH-I and RHH-II, respectively. Finally, we also fixed $\epsilon_{\alpha\beta} = 1$ for the RHH models and $\epsilon_{\alpha\alpha} = 1$ for the LJ model, because we found no significant decrease in the cost function when these parameters are varied. The only parameters to optimize are then $\mathbf{q} = \{\sigma_{SiSi}, \sigma_{SiO}, \sigma_{OO}\}$ for the RHH models and $\mathbf{q} = \{\sigma_{SiSi}, \sigma_{SiO}, \sigma_{OO}, \epsilon_{SiO}\}$ for the LJ model.

The evaluation of the cost function for a given $\mathbf{q}$ was carried out as follows. We started by simulating the original RHH model at high temperature ($T = 0.0200$), well within the liquid phase, and stored N_{conf} independent configurations. Starting from each of these configurations, the liquid was cooled down to the glass state following the procedure described in Sec. 2.1.2. We then computed the RDFs and the ring statistics using all the N_{conf} final configurations we obtained.

To minimize the cost function, we used the Levenberg-Marquardt algorithm implemented in `lmfit` [139]. For the minimization, we used systems of 500 particles and we averaged the ring statistics over $N_{conf} = 10$ configurations. Once a minimum was found, we carried out ten additional minimizations starting from a small random perturbations of the parameters found in the minimum. We then compared the value of the cost functions obtained for this set of minima. For this evaluation, we increased the system size to 7000 particles and we averaged over $N_{conf} = 50$ configurations. We selected the optimal model as the set of parameters with the lowest χ^2 among these refined minimizations. The optimized parameters of each model are summarized in Tab. 2.1.

Model	σ_{SiSi}	σ_{SiO}	σ_{OO}	ϵ_{SiO}	κ	R_{cut}
RHH	2.25	1.075	0.900	–	0.1093	9.1518
RHH-II	2.3015	1.0873	0.9227	–	0.1675	6.00
RHH-I	2.3039	1.0611	0.8899	–	0.2500	4.00
LJ	2.3445	1.3582	1.6913	0.1708	–	$2.5\cdot\sigma_{\alpha\beta}$

TABLE 2.1: Interaction parameters of the models studied in this work. Note that the values of κ e R_{cut} for the RHH model are those used in [133] for $N = 80$ particles.

2.2 Comparison with the experimental glass structure

We now compare the interaction potentials obtained with the experimental data. We first focus on standard two- and three-body structural correlations (Sec. 2.2.1), and we then turn to properties and correlation of the network structure (Sec. 2.2.2). We conclude with a discussion of the computational efficiency of the developed models (Sec. 2.2.3) and the generalizability of the interaction potentials used to simulate other two-dimensional oxides (Sec. 2.2.4).

2.2.1 Radial distribution functions and bond angle distributions

In Fig. 2.2 we compare the partial RDFs $g_{\alpha\beta}(r)$ measured experimentally with those obtained from our interaction models. All the models reproduce the general shape of the experimental RDFs pretty well. In particular, they correctly reproduce the positions of the first peaks in these functions. It should be noted that, contrary of Roy et al. [133], we did not convolute the simulated RDFs with a Gaussian function to emulate the experimental uncertainty on the measured positions. Therefore, the first peaks of $g_{SiSi}(r)$ and $g_{SiO}(r)$ obtained from our models are sharper than those observed in the experiments, but we do not deem this difference relevant to our analysis.

To better characterize the local structure of the system, we turn to the Bond Angle Distributions (BADs), which measure the distribution of angles produced by three neighboring particles. We considered two particles of species α and β neighbors if their distance is less that the position of the first minimum in the corresponding partial $g_{\alpha\beta}(r)$, which equal 3.90 Å, 2.60 Å and 3.50 Å for Si-Si, Si-O and O-O neighbors, respectively. In Fig. 2.3 we compare the BADs for two selected triplets of neighboring particles. We found that the RHH model and its reparametrized variants capture well the essential features of the BADs observed in the experiments: both the distribution of $Si-Si-Si$ and $Si-O-Si$ angles are peaked around 120° and are symmetric about the maximum. The LJ model is instead visibly worse than the other: the distributions are slightly shifted to smaller angles and the distribution of $Si-O-Si$ angles present a spurious peak around 90°, possibly due to an excess of square local arrangement. Nevertheless, from Fig. 2.3 we find no clear distinction between the RHH models, and we can only conclude that the LJ model performs poorly compared to the RHH functional form.

2.2.2 Ring structure

Since traditional structural indicators do not reveal major differences between the RHH models, we turn to many-body properties related to the network structure. We start by analyzing the ring statistics $P(n)$, which is the probability of finding

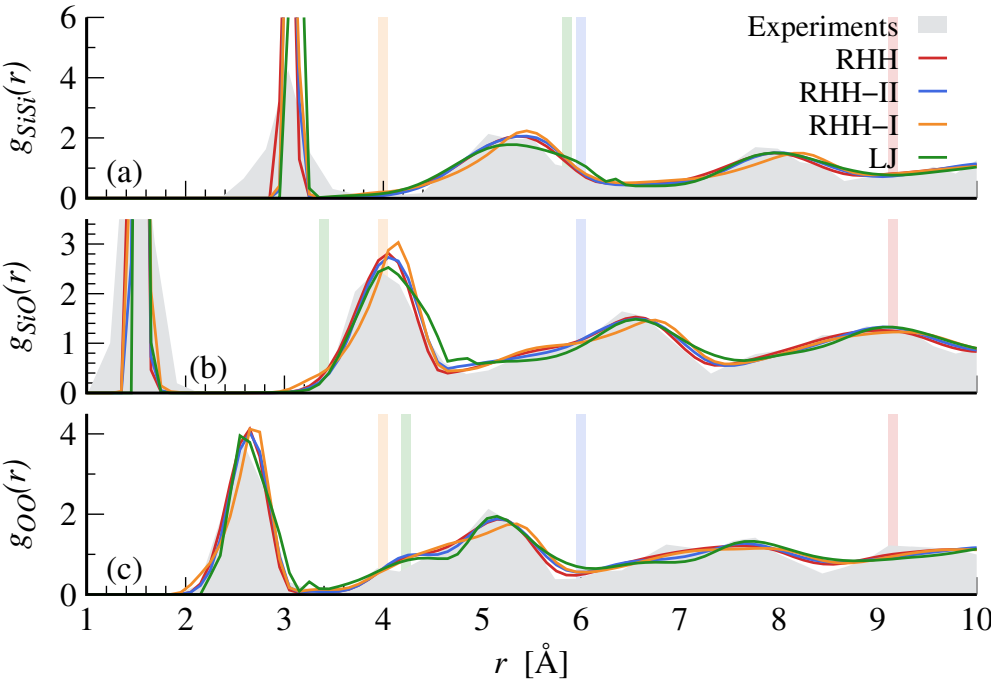

FIGURE 2.2: Comparison between the experimental radial distribution functions and the ones of the models studied in this work: (a) $g_{SiSi}(r)$, (b) $g_{SiO}(r)$, and (c) $g_{OO}(r)$. The experimental data refer to a silica bilayer on Ru(0001), see Appendix B. The vertical bands mark the cutoff radii used for the RHH (red), RHH-II (blue), RHH-I (orange), and LJ (green) models.

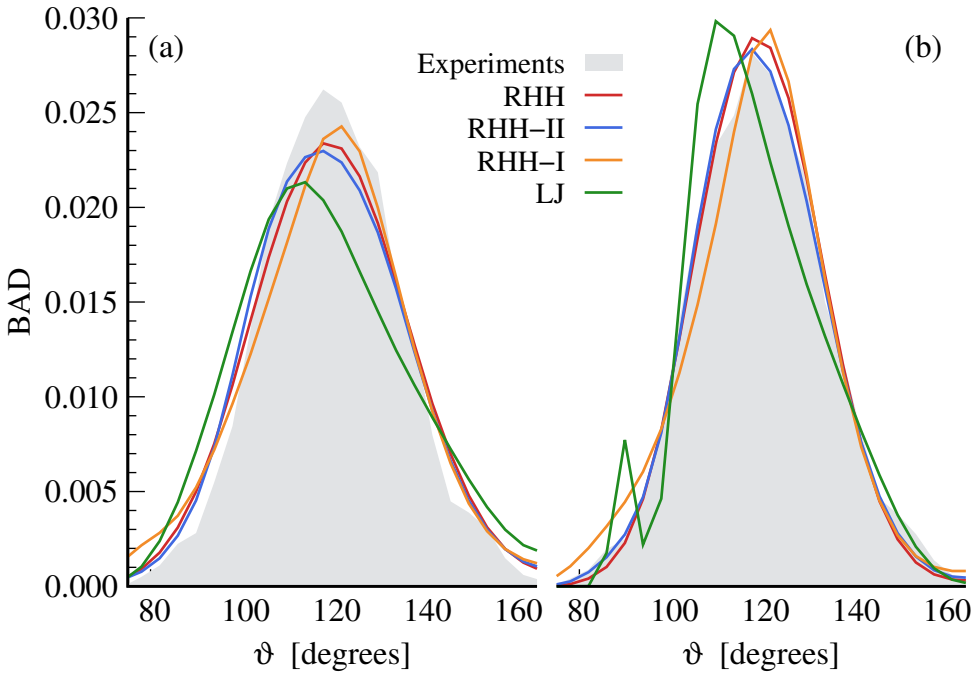

FIGURE 2.3: Comparison between the experimental bond-angle distributions and the ones of the models studied in this work for (a) *Si-Si-Si* (left) and (b) *O-Si-O* angles (right). The experimental data refer to a silica bilayer on Ru(0001), see Appendix B.

a n-sided ring in the system. Following the convention for silica systems without homopolar bonds [140], we define the number of sides of a ring as the number of

silicon particles it contains.

The ring statistics were directly targeted by our structure-matching procedure. We thus expect the reparametrized models to improve the agreement with the experimental data compared to the original RHH model. In Fig. 2.4, we can see that both RHH-I and RHH-II models substantially improve the agreement between experimental and simulated ring statistics. Notably, both models correctly reproduce the high fraction of hexagonal rings in the experiments, which is underestimated by the standard RHH model [133]. The RHH-II model also reduces the fraction of rings with more than 10 sides, as can be appreciated from the inset in Fig. 2.4. Thanks to the large number of indipendent low-temperature structures, our data reveal a clear exponential decay of $P(n)$ for large ring sizes. This feature is hard to detect experimentally, due to the much more limited statistics. We also note that the LJ model fails to capture the precise structure of the ring statistics, underestimating the fraction of hexagonal rings and producing a very fat tail at large n.

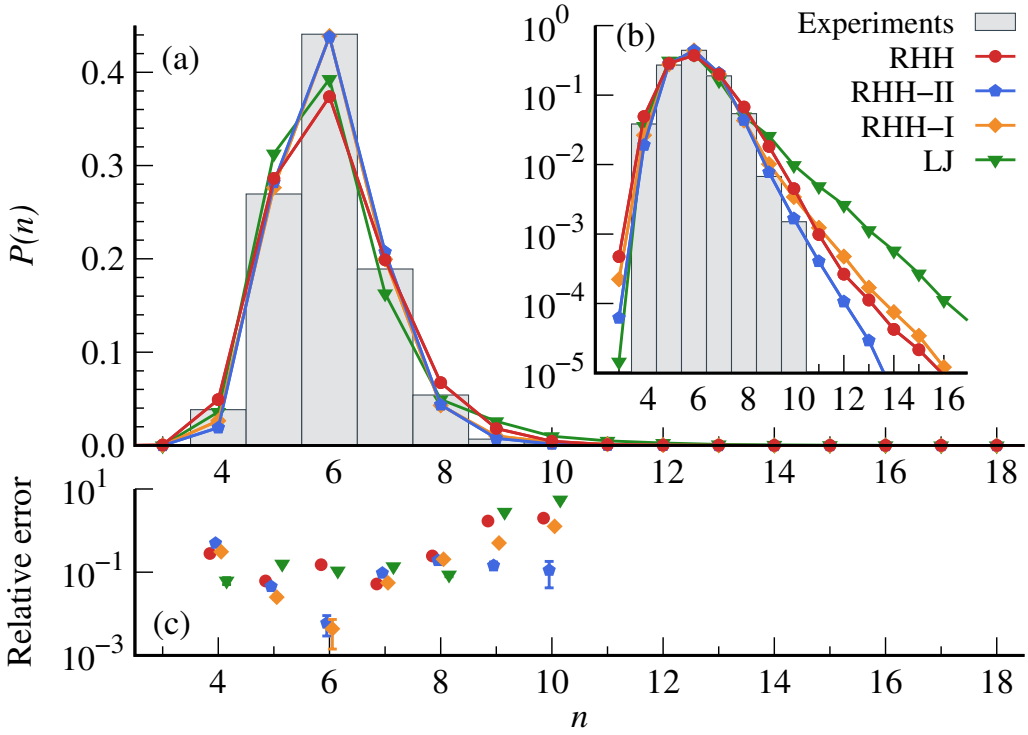

FIGURE 2.4: Comparison between the experimental ring statistics and the ones of the models studied in this work, in (a) linear and (b) semi-logarithmic scales. Note that in panel (a) the data for the RHH-I and RHH-II models are almost superposed on top of each other. (c) Relative errors between the experimental ring statistics and the one of each studied model. The experimental data are the average over several samples grown on different substrates, see Appendix B. Error bars are shown only when larger than the symbol size.

Additional differences between the studied models are revealed by studying the ring correlations in the network. It is well known that for a large number of natural networks, such as polycrystalline grains [141], two-dimensional glasses [133, 142, 143], foams [144] and others, large rings tend to be surrounded by smaller ones [145]. Historically, this anticorrelation is quantified by the empirical Aboav-Weaire law, which affirms that $m_n \sim A + \frac{B}{n}$, where m_n is the average ring size of the neighbors of a ring of size n, while A and B are fitting parameters. For all the models considered

in this work we observe that large rings tend to be connected to smaller ones [126], in agreement with the Aboav-Weaire law.

Despite its remarkable generality, it is difficult to compare different systems using the Aboav-Weaire law and its parameters do not have a clear connection with the network structure [145]. Therefore, we turn to a more mathematically grounded metric of correlations in the network. A standard measure of the correlation between nodes in network theory is the assortativity coefficient, which is a quantity in the range $[-1, +1]$ that measures the likelihood that two connected nodes of the network have similar properties [146]. In particular, this coefficient is $+1$ (-1) if the network has assortative (disassortative) mixing, while it is 0 if the node properties are randomly distributed among the nodes. Here, assortative mixing means that nodes with similar properties tend to be connected together, while dissortative mixing means that the properties of linked nodes have opposite fluctuations with respect to the mean.

We computed the assortativity coefficient by considering the dual of the atomic network, which is a network where the rings are the nodes and two nodes are joined if the corresponding rings share at least one edge. As a node property, we use the number of sides, n, of the ring. The assortativity coefficients obtained for the different models are compared in Table 2.2. All the models have a negative assortativity coefficient, meaning that the ring structures produced by our models have small rings close to large ones, like the experimental sample of silica bilayer [133, 142, 143] and in agreement with the empirical Aboaw-Weaire law. Although the assortativity coefficients are all negative, we observe a general trend in their magnitude: the longer the range of the potential, the more disassortative is the network. However, within statistical uncertainties, both the original and the reparameterized RHH models produce disassortative network structures compatible with experimental data. Interestingly, the assortativity coefficient we obtained by analyzing the experimental structures is appreciably lower than that reported in [145] and is not compatible with it within error bars. We believe this disagreement might be due to different treatment of the boundaries in the calculation of the assortativity coefficient in open boundary conditions. We also emphasize that the assortativity coefficient is a very fine quantity and even in the samples we analyzed in Appendix B we found wide sample-to-sample fluctuations in this quantity. Nevertheless, this discrepancy might suggest that the agreement between network structures produced by the triangle raft algorithm and the two-dimensional silica, observed in [145], may be coincidental.

Model	**Assortativity coefficient**	**Interaction range**
Experiment	$-0.22 \quad \pm 0.06$	$-$
RHH	-0.2185 ± 0.0003	7.4
RHH-II	-0.1610 ± 0.0004	5.1
RHH-I	-0.1323 ± 0.0005	3.6
LJ	-0.0876 ± 0.0006	2.9

TABLE 2.2: Comparison between the assortativity coefficients of the models studied in this work. The interaction range is calculated as the distance at which the potential energy between a silicon and an oxygen particle is 1 % of its value at the minimum.

Model	χ^2	χ^2_{RDF}	χ^2_{ring}	$\chi^2_{pen.}$	Efficiency ratio Forces	Efficiency ratio MD
RHH	1.47	**0.03**	0.97	0.46	1.00	1.00
RHH-II	**0.32**	**0.03**	0.24	**0.04**	2.28	1.64
RHH-I	1.24	**0.03**	**0.19**	1.01	2.52	2.12
LJ	21.24	1.41	2.67	17.17	**2.88**	**2.88**

TABLE 2.3: Comparison between the original RHH model and the ones studied in this work, see text for definitions. The best values for each indicator are shown in bold. For a better comparison of the cost function values, we multiply all values by a factor 10^2.

2.2.3 Averall assessment and computational efficiency

Our structural analysis of the glass states shows that the RHH-II model provides the best overall agreement with the experimental system. It correctly reproduces the behavior of the RDFs, the BADs and the ring statistics. Its network structure also possesses a marked disassortative mixing in ring sizes, as observed experimentally. From a more quantitative point of view, the RHH-II model produced the lowest cost function (χ^2), significantly improves the agreement with the experimental ring statistics compared to the original model (χ^2_{ring}) and produces the smallest fraction of very large and small rings ($\chi^2_{pen.}$), see Tab. 2.3.

We also note that our reparametrization of the RHH model improves its computational efficiency. When using `RUMD`, we found that the RHH-II model is approximately 64% more efficient than the original RHH model due to its smaller cutoff radius. The efficiency ratio that we observe for both reparametrized RHH models is, however, lower than what we can expect from the number of interacting particles computed from the RDFs.A possible explanation is that, due to the small number of interacting particles in the reparametrized model, the computing units of the GPU are not saturated and the computation is not as efficient as it could be. Nevertheless, we observe a speedup of a factor 2.28 in the direct evaluation of forces, which may be valuable when considering the choice of the model.

2.2.4 Generalizability of the models

Given the ability of the RHH-II model to reproduce even the finest properties of the silica bilayer, it is natural to wonder whether the RHH functional form could be parametrized to simulate other two-dimensional glass-forming oxides.

As shown in Sec. 1.1.3, the structure of the germania bilayer looks very similar to the one of the silica bilayer. It has the same building-block made of regular tetrahedra and the same vertical symmetry between the upper and the lower layers, except for a larger tilting of the tetrahedra due to the larger size of germania atoms compared to silicon ones [28]. Moreover, it has the same crystalline polymorphs found in two-dimensional silica and can be grown either crystalline or amorphous, depending on the substrate and the synthesis process. As discussed in Sec. 1.1.1 and Sec. 1.1.3, the main difference between silica and germania bilayers is that the crystalline structure of the germania bilayer consists of 5- and 8-sided rings, see Fig. 1.6 left, while a crystalline silica bilayer is made only of hexagonal rings. This also affects the ring statistics of amorphous germania samples, which present two maxima instead of one, see the right panel of Fig. 1.6.

Since the germania bilayer is so similar to the silica one, it is natural to think that RHH functional form can be easily adapted to reproduce the properties of this system, but we have found this not to be the case. We used the same strictly two-dimensional model and the same experimental properties in the cost function as for the silica bilayer, but despite our efforts, we could never obtain a bimodal ring statistics like the one of the germania bilayer. We think this failure might be due to the excessive simplicity of the RHH functional form. In the case of germania, the interaction potential should stabilize both the small pentagons and the larger octagons, while hindering all intermediate ring sizes in between. This task might be achieved by an effective potential with more than one minimum, but it is out of reach for something as simple as the RHH model.

The B_2O_3 monolayer is, from a certain point of view, the best two-dimensional network-forming system known to date. Like the silica and germania bilayers, the B_2O_3 monolayer interacts very weakly with the substrate. The choice of a strictly two-dimensional model is fully justified in this case, given its monoatomic thickness of the system, see Sec. 1.1.2 and Chapter 6. As we will discuss in Chapter 6, the basic unit of the B_2O_3 monolayer is a boroxol ring, and in the crystalline phase these units form the nodes of a network of slightly distorted hexagons. This network can be amorphized if the system is heated, and there is some evidence that the boroxol rings do not break during the heating process, provided that the temperature is sufficiently is not too high, see Chapter 7. Since a boroxol ring can connect via oxygen bridges to three other boroxols, there is a perfect correspondence between boroxol rings and oxygen bridges with effective silicon and oxygen atoms in the RHH model. This similarity is further highlighted by the ring statistics obtained from the amorphous B_2O_3 monolayer assuming the boroxol rings as effective particles, see Fig. 7.6 (c).

Despite these strong similarities, we were unable to obtain an all-atom interacting potential for the B_2O_3 monolayer by reparametrizing the RHH model. We again used a strictly two-dimensional model, and we employed the RHH functional form to describe the interaction between boron and oxygen atoms. Due to the lack of detailed experimental data for the structure matching approach, we attempted to reproduce the strain-energy curves presented in Fig. 5.6. We were able to reproduce these curves relatively well, but the system was unstable even in low-temperature simulations, breaking up the boroxol rings and forming a high density phase. We think this might be due, once again, to the presence of two very different length scales in the system: one related to the small boroxol ring, and the other linked to the larger hexagons composed by these rings. Moreover, it should be noted that the specific internal structure of the boroxol rings allows them to be connected to only three other boroxols, while our model for the silica bilayer does not have such constrain. We speculate that successful modelling of this material using empirical potentials would require introducing molecular units and angle-dependent terms in the force-field.

2.3 Key results

The key insights we gained in this chapter can be summarized as follows:

- The network structure of the silica bilayer is mainly due to interactions up to the second coordination shell.

- Fine structural indicators, such as the rings statistics, are more sensitive to small changes in interaction potentials than standard two- and three-body structural correlations.
- Although our effective model reproduces the experimental structure of the silica bilayer quite well, more complex functional forms are required to simulate other two-dimensional oxides.

Chapter 3

Silica bilayer: dynamics and elementary relaxations

In this chapter, we study the properties of the model for the silica bilayer developed in the previous chapter as a function of temperature. We carefully characterize the thermodynamics, structure and dynamics of the system as the temperature decreases, paying particular attention to the effects specific to two-dimensional systems, such as Mermin-Wagner fluctuations and the KTHNY theory of melting. We also identify and characterize the elementary relaxations in the system, providing a plausible mechanism for the relaxation of the structure at low temperatures, and we discuss the melting process of the crystal. Our results show that our model for the silica bilayer exhibits strong similarities with 3*d* silica. Both materials feature thermodynamic anomalies at the temperature at which the network starts to form, and the correlation times of both systems follow an Arrhenius law at low temperatures. Moreover, they have similar types of elementary rearrangements, and the dynamics in both systems begin to slow down well above the melting temperature.

We first discuss the thermodynamic, structure and dynamics of the system as the temperature decreases, comparing them to those of 3*d* silica (Sec. 3.1). We then analyze the elementary relaxations of the system, focusing on topological changes in the connectivity of the network (Sec. 3.2). Finally, we estimate the melting temperature of the crystal and we provide a qualitative description of the melting process, comparing it with the KTHNY scenario (Sec. 3.3).

The bulk of this chapter is adapted from Ref. [126], but it also includes new material (Sec. 3.2 and Sec. 3.3.2) and additional discussions.

3.1 Glassy dynamics

In this section, we investigate in detail the structure and dynamics of 2*d* silica, as modeled by the RHH-II potential. Our simulations are performed at equilibrium over a broad range of temperatures, starting from normal liquid states at high temperature down to the highly viscous regime. As we will show in Sec. 3.3, the range of temperatures considered in this section is well above the melting temperature of the crystalline system.

We start by characterizing the thermodynamics and the emergence of the network structure (Sec. 3.1.1). We then carefully analyze the dynamical properties of the system, paying particular attention to the presence of Mermin-Wagner fluctuations (Sec. 3.1.2) and identifying two distinct temperature regimes (Sec. 3.1.3).

3.1.1 Thermodynamic anomalies and network structure

It is well-known that the formation of a random network structure in bulk $3d$ silica is accompanied by thermodynamic anomalies, such as a minimum in pressure (at constant density) and a peak in the specific heat [9, 76, 77]. These anomalous features are common to other network-forming liquids, such as silicon and water, and have been attributed to polyamorphism, i.e., the presence of different liquid phases, as well as to changes in the properties of the potential energy landscape [147, 148].

To check whether $2d$ silica follows similar trends, we collect in Fig. 3.1 several thermodynamic observables as a function of temperature. We first inspect the energy $e_{IS}(T)$ of the underlying inherent structures, i.e., the local minima determined by a local minimization of the potential energy from equilibrium configurations sampled at a given temperature [149]. The inherent structures were obtained using the l-BFGS algorithm [150] as implemented in the `atooms` package [151], with a convergence criterion of 10^{-10} on the mean square force. From Fig. 3.1 (a) we see that e_{IS} is approximately constant at high temperature and drops markedly below $T \approx 0.02$. As found in other $3d$ glass-forming liquids [152], this crossover temperature also marks the onset of glassy dynamics, see Sec. 3.1.3.

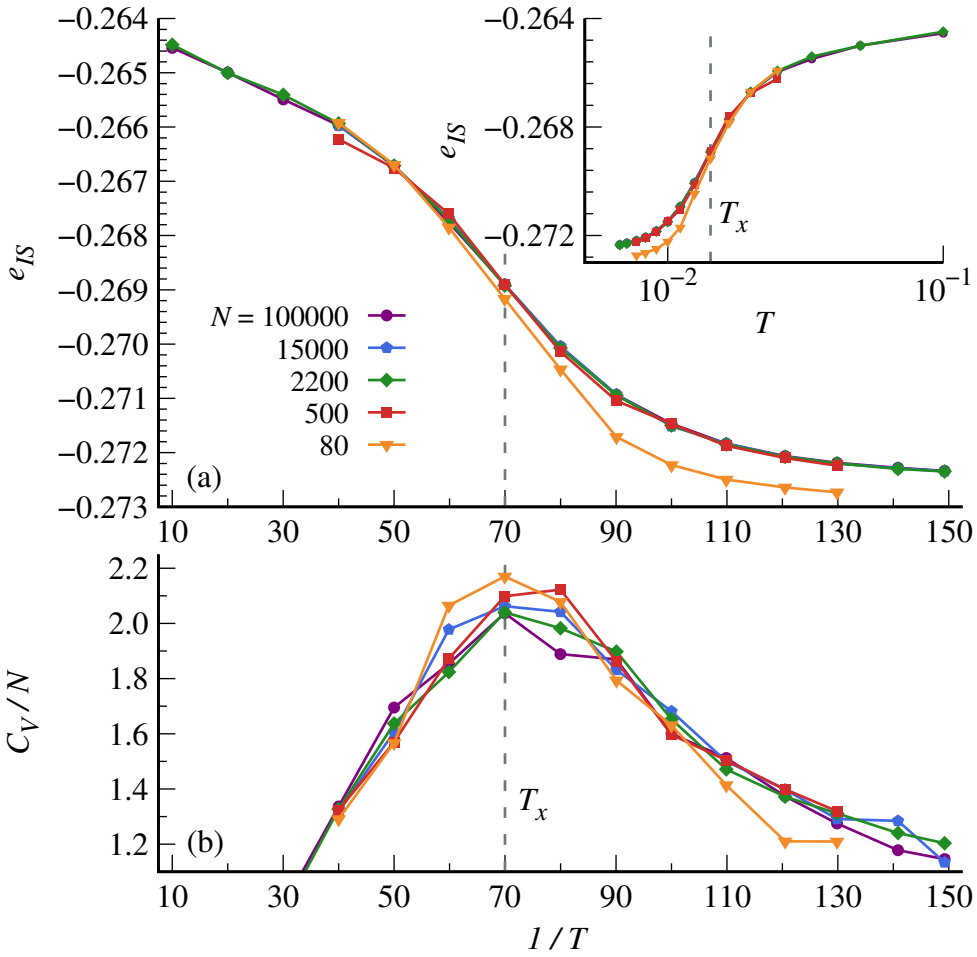

FIGURE 3.1: Temperature dependence of (a) the average potential energy per particle e_{IS} of the inherent structures and (b) excess specific heat per particle C_V / N, for different system sizes, as indicated in the figure. The inset of panel (a) shows e_{IS} versus T in semi-logarithmic scale.

Systems with Gaussian statistics of inherent structures display a simple scaling $e_{IS} \sim 1/T$ below the onset temperature [153]. While models of fragile glass-forming liquids are typically well-described by such Gaussian statistics, in $3d$ silica this regime is very narrow, if existent at all, and e_{IS} saturates rapidly at low temperatures, going through an inflection point. The saturation of e_{IS} below T_x has been interpreted as the approach to the "bottom of the landscape", as evidenced by the presence of a lower bound to the inherent structure energy distribution [134], and has been connected to a fragile-to-strong crossover [75, 134], see Sec. 3.1.3. Our results for the RHH-II model appear qualitatively similar to those of $3d$ silica. In particular, we observe no evidence of an extended linear regime, $e_{IS} \sim 1/T$, and the data feature an inflection point at a crossover temperature $T_x \approx 0.0147$. A similar behavior was observed in the original RHH model [134] using a system of 80 particles. As shown in Fig. 3.1, although such small systems are affected by significant finite-size effects, their qualitative trends are similar to those of larger systems. Our analysis thus puts the findings of Ref. [134] on a firmer basis.

Turning to conventional thermodynamic quantities, Fig. 3.1 (b) shows the excess specific heat per particle $C_V/N = \frac{dU}{dT}\Big|_V$. The specific heat displays a broad peak around $T_x \approx 0.0147$, and the pressure has a minimum at the same temperature [126]. These features appear qualitatively similar to those found at constant density in $3d$ amorphous silica as modeled by the BKS potential [77]. Note that both anomalies occur at the same crossover temperature T_x in the RHH-II model, while a clear discrepancy between the two is found in BKS silica. We do not have clear explanation for this difference, which might be related to the different dimensionality of the two systems.

To connect the thermodynamic anomalies shown in Fig. 3.1 to the evolution of the liquid structure, we show in Fig. 3.2 (a) the structure factor $S_{SiSi}(k)$ between silicon atoms. At high temperature, the $S_{SiSi}(k)$ displays a sharp peak, centered around $k \approx 2$ Å^{-1}, which splits upon cooling into a "first sharp diffraction peak" at $k_1 = 1.375$ Å^{-1} and a main peak at $k_2 = 2.475$ Å^{-1}. These wave-numbers corresponds roughly to the typical length scales of the rings and of the *Si-Si* bonds, respectively, similar to what found in $3d$ silica [9]. Upon cooling, the liquid structure thus crosses over from the one typical of a "normal" liquid to the one of a network liquid. To pinpoint this crossover, we look for an inflection of $S_{SiSi}(k)$ in the range between k_1 and k_2. Remarkably, this inflection starts to develop around the same crossover temperature T_x identified from the thermodynamic analysis. Conversely, in BKS silica the inflection of $S_{SiSi}(k)$ occurs around $T = 6000$ K [9], while the peak of C_V around $T = 4800$ K [76], further showing that, although their thermodynamic behaviors are qualitatively similar, there are quantitative differences between two- and three-dimensional silica.

The formation of a network structure is demonstrated by the probability distributions of the number of *Si*-neighbors of *Si* particles in Fig. 3.2 (b). Above T_x, the distribution of the number of neighbors is broad, suggesting that the network is not well defined yet. Below T_x, instead, the liquid develops a network structure with the characteristic features of $2d$ amorphous silica, *i.e.*, 3-fold local arrangements and 6-membered rings becomes the locally favored structures of the network structure[1] [126]. When the temperature decreases below T_x we also observe a sharp drop in the number of coordination defects, which in our case corresponds to *Si* particle

[1]These properties are typical of the two-dimensional projection of the material. If the out-of-plane direction is taken into account, the arrangment of silicon atoms is tetrahedral, and the rings structure also include 4-membered rings.

with a number of *Si*-neighbors other than three, see the inset of Fig. 3.2 (b). Comparing these results with the experimental data used to match the structure of the RHH-II glass, we observe that the former resembles a liquid equilibrated at around $T \approx 0.0100$ [126], while our lowest equilibrated temperature is about twice lower than that. This suggests that the experimental amorphous samples of $2d$ silica are representative of poorly annealed glass states.

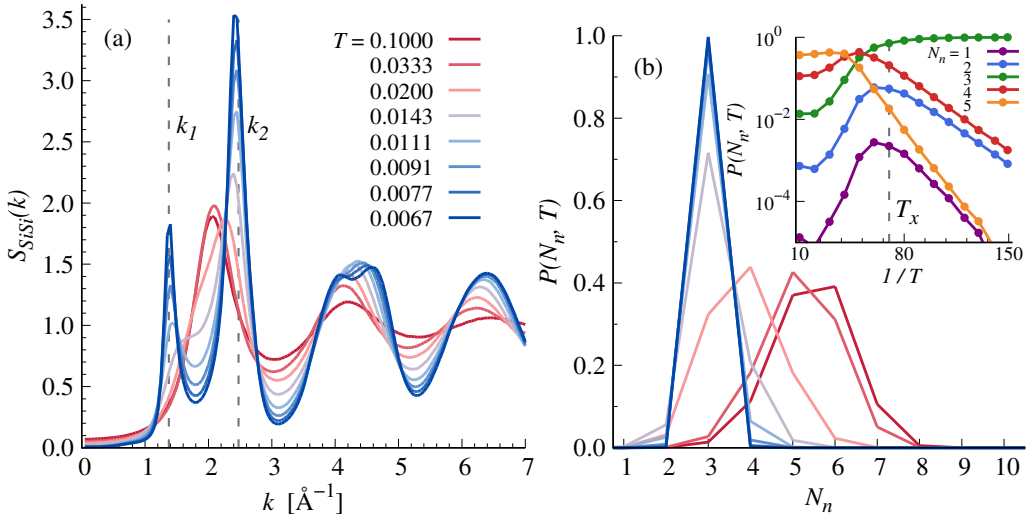

FIGURE 3.2: (a) Structure factor $S_{SiSi}(k)$ and (b) distribution of the number of *Si-Si* neighbors at different temperatures. The inset of panel (b) shows the temperature dependence of distribution of *Si-Si* neighbors. The structure factors and the neighbors distributions are calculated for a system with 10^5 particles.

3.1.2 Mermin-Wagner fluctuations and finite-size effects

We now analyze the dynamical properties of $2d$ silica in equilibrium conditions, from high temperature down to the glassy regime. As discussed in Sec. 1.3.1, it is well-established that the dynamics of $2d$ liquids, as measured by standard time-dependent correlation functions, is severely affected by Mermin-Wagner (MW) fluctuations [105]. Previous analyses of the RHH model have not considered these effects [134]. Thus, the goal of this section is to take them into account, putting the analysis of the dynamics of the RHH-II model on firm grounds.

To extract meaningful information about the dynamics in the glassy regime, it is necessary to remove the effect of MW fluctuations. As discussed in Sec. 1.3.1, this can be done using cage-relative particle displacements in the time-dependent correlation functions [105, 106, 108]. In practice, we first define the displacement of the cage of the i-th particle between the time instants t and $t + t_0$,

$$\Delta\tilde{\mathbf{r}}_i(t, t_0) = \frac{1}{N_i} \sum_{j=1}^{N_i} \left[\mathbf{r}_j(t + t_0) - \mathbf{r}_j(t_0) \right] , \tag{3.1}$$

where the sum runs over the N_i neighbors of the i-th particle. The cage-relative displacement $\mathbf{r}_i(t + t_0) - \mathbf{r}_i(t_0) - \Delta\tilde{\mathbf{r}}_i(t, t_0)$ is then used to define the corresponding cage-relative correlation functions.

Typical results of this procedure are illustrated in Fig. 3.3 (a) from simulations at $T = 0.0100$, slightly below T_x. The correlation function of interest is the self intermediate scattering function, which is calculated both using the raw coordinates of the

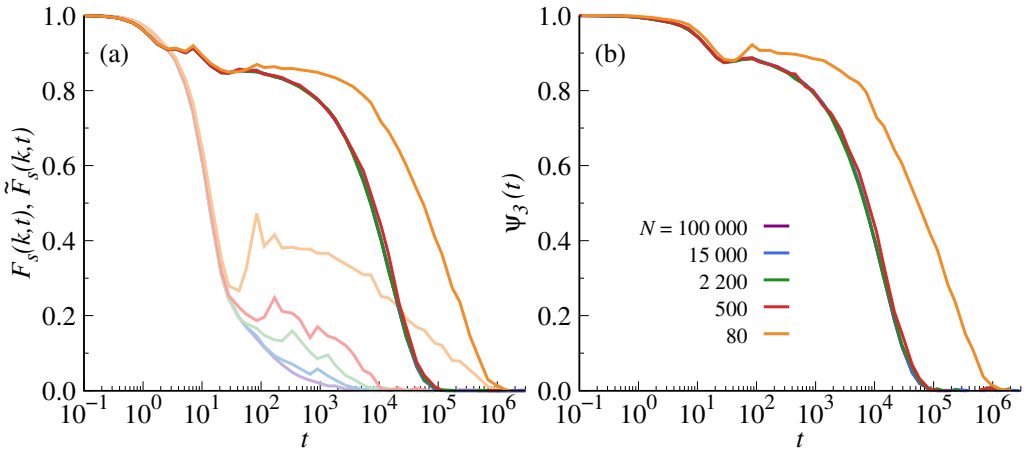

FIGURE 3.3: Effect of the long-wavelength fluctuations on translational (a) and orientational (b) correlation functions for different system sizes N. The translational correlation functions in panel (a) are presented in both standard $F_s(k,t)$ (pastel colors) and cage-relative $\tilde{F}_s(k,t)$ (full colors) versions, and are evaluated at the wavenumber k_2. All the curves in both panels are obtained at temperature $T = 0.0100$.

Si particles

$$F_s(\mathbf{k},t) = \left\langle \frac{1}{N_{Si}} \sum_{j=1}^{N_{Si}} e^{i\mathbf{k}\cdot\left[\mathbf{r}_j(t)-\mathbf{r}_j(0)\right]} \right\rangle , \tag{3.2}$$

and using the cage-relative displacements

$$\tilde{F}_s(\mathbf{k},t) = \left\langle \frac{1}{N_{Si}} \sum_{j=1}^{N_{Si}} e^{i\mathbf{k}\cdot\left[\mathbf{r}_j(t)-\mathbf{r}_j(0)-\Delta\tilde{\mathbf{r}}_j(t,0)\right]} \right\rangle , \tag{3.3}$$

where N_{Si} is the numer of *Si* particles in the system.

As found in close-packed glass-forming liquids [105, 106], the bare $F_s(k,t)$ displays strong finite-size effects and MW fluctuations progressively wash out the glassy dynamics as N increases. Note that the oscillations of $F_s(k,t)$ at intermediate times are not due to statistical noise: the time of the first peak of these oscillation grows with the square root of the number of particles N, as expected for a wave that cross a distance $L \sim \sqrt{N}$ at constant speed. The same behavior is observed in closed-packed liquids in two dimensions [105]. When using cage-relative displacements, instead, finite-size effects almost completely disappear and the correlation function reveals a genuine glassy dynamics, with a well-defined relaxation time $\tau_\alpha(k)$ at $\tilde{F}_s(k,\tau_\alpha(k)) = e^{-1}$. Similar results can be obtained for the mean square displacement (not shown).

Although the use of cage relative quantities removes the effects due to MW fluctuations, standard finite-size effects are still present for very small systems, as shown by the data for $N = 80$ particles in Fig. 3.3 (a). By performing systematic tests for different system sizes, we assess that finite-size effects in the cage-relative correlation functions disappear for systems with more than $N = 200$ particles. This contrasts with the analysis of Roy *et al.* [133], who suggested instead that $N = 80$ would be enough to remove major finite-size effects, as found in $3d$ liquid silica [154]. We tentatively attribute this discrepancy to the fact that Roy *et al.* mostly focused on structural quantities, where finite-size effects are less visible.

As discussed in Sec. 1.3.1, another approach to avoid finite-size effects due to MW fluctuations is to focus on the correlation functions of the orientational degrees

of freedom. Such functions can be constructed defining a complex bond-order parameter for a 3 symmetry of the j-th Si particle as

$$\psi_{3,j}(t) = \frac{1}{3}\sum_{l=1}^{3} e^{3i\phi_{jl}(t)},$$

where $\phi_{jl}(t)$ is the angle between the bond that connects the Si particles j and l at time t and an arbitrary reference line, and the sum runs over the first n nearest neighbors of j. From this local order parameter we can then construct a correlation function of the bond-order parameter between silicon particles as

$$\Psi_3(t) = \frac{\langle \sum_{i=1}^{N_{Si}} \psi_{3,i}(t)\psi^*_{3,i}(0)\rangle}{\langle \sum_{i=1}^{N_{Si}} \psi_{3,i}(0)\psi^*_{3,i}(0)\rangle}.$$

In Fig. 3.3 (b), we show this function for different system sizes at $T = 0.0100$. As expected, $\Psi_3(t)$ shows no major finite-size effects, except for the smallest system size considered ($N = 80$).

3.1.3 Glassy dynamics and dynamic crossover

We now turn our attention to the dynamics of the RHH-II model as a function of temperature. As discussed in the previous section, we remove the effects of MW fluctuations either by using cage-relative displacements or by considering correlation functions that are independent of MW fluctuations by construction, *e.g.*, bond-orientational and bond-breaking correlation functions [109]. We report results for the largest available system size, $N = 10^5$, and over a considerably larger temperature range than previous work [134]. Moreover, we will focus on the correlation times extracted from time-dependent correlation functions. This contrasts with previous works [134] that based their analysis on diffusion coefficients. However, these quantities are ill defined in two-dimensional systems, as they diverge logarithmically with the system size in $2d$ [109].

We start by analyzing the cage-relative self intermediate scattering functions $\tilde{F}_s(k,t)$ evaluated at $k = k_2$, which corresponds to the main peak of the $S_{SiO}(k)$ structure factor. The corresponding length scale is around the typical Si-O bond distance. We show these results for the Si particles in Fig. 3.4 (a). The correlation functions exhibit typical glassy behavior, with structural relaxation taking on longer time scales as T decreases. Note the appearance of a plateau, only slightly masked by short-time vibrational motions, around the onset temperature $T_o \approx 0.2 > T_x$.

The same qualitative behavior can be seen in Fig. 3.4 (b) for the time-dependent correlation function of the 3-fold bond-order parameter between silicon particles $\Psi_3(t)$. Interestingly, the slowing down of translational and orientational degrees of freedom proceeds on the same footing across the whole range of temperatures, and occurs on the same time scale at low temperatures. This behavior contrasts with $2d$ liquids with close-packed local arrangements, for which translational and orientational degrees of freedom tend to be coupled only at low temperature [155].

It is useful to compare these results with correlation functions that measure more directly the dynamics of the bonds. We focus here on bonds between silicon and oxygen particles and compute the probability that such a bond persists up to time t. The corresponding bond-breaking correlation function is shown in Fig. 3.4 (c). Although this function does not show any plateau at intermediate times, its slowing down upon cooling is similar to $\tilde{F}_s(k,t)$.

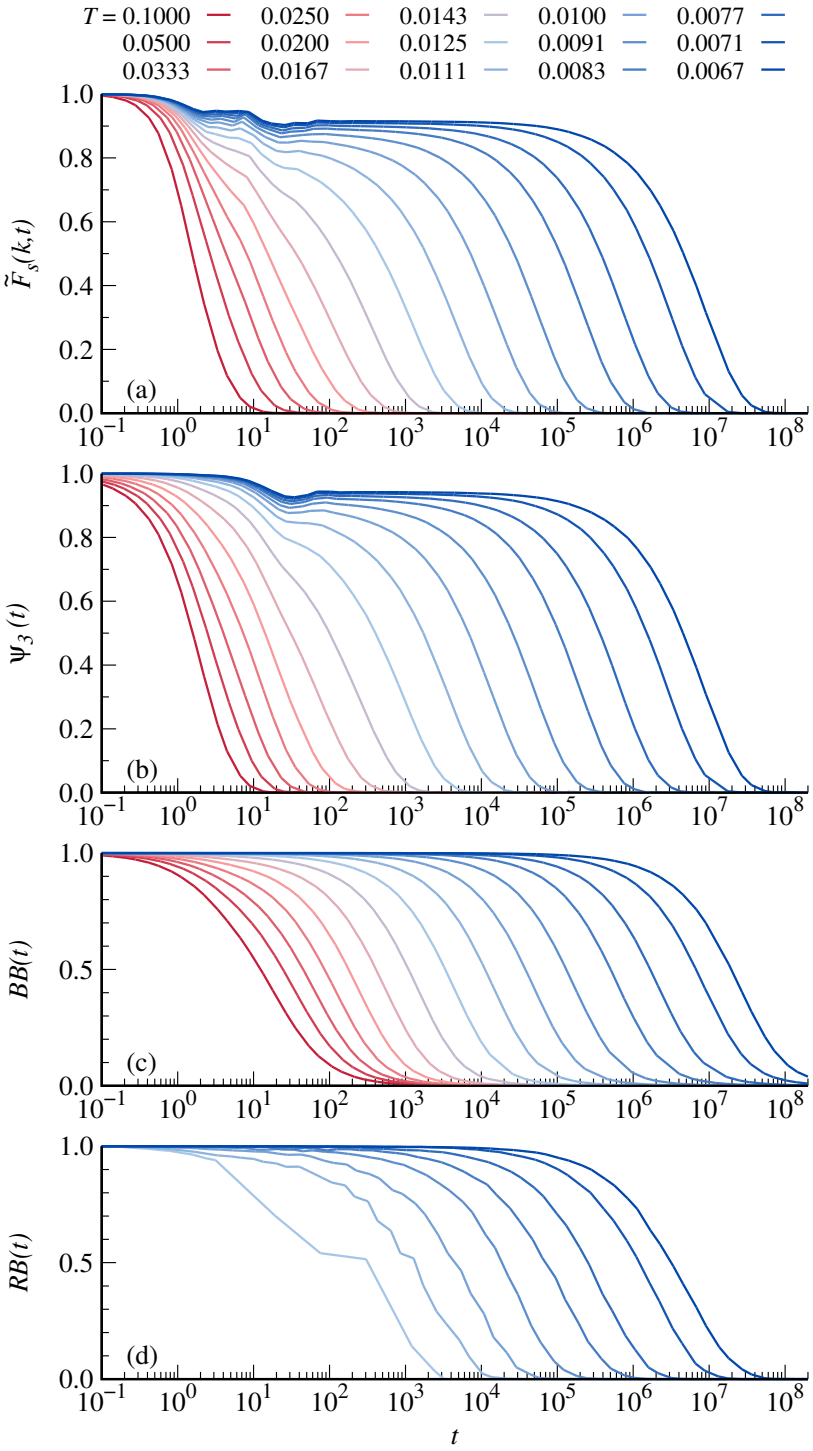

FIGURE 3.4: (a) Cage-relative self intermediate scattering functions (at $k = k_2$), (b) orientational correlation functions for the 3-fold order parameter between *Si-Si* particles, (c) bond breaking correlation functions and (d) ring breaking correlation functions for different temperatures, as indicated in the figure. Note that the ring breaking correlation functions can only be computed for temperatures $T \leq 0.0125$, due to the lack of a well-defined network structure at higher temperatures. The cage-relative self intermediate scattering functions, orientation correlation functions and bond breaking correlation functions are calculated for $N = 10^5$ particles, while the ring breaking correlation functions for $N = 2200$ particles.

Moving on to larger length scales, we analyze the dynamics of rings, which are expected to be a key structural element of 2*d* silica networks. Similarly to the bond-breaking correlation function, we define the ring correlation function as the probability that a ring has not changed its identity, *i.e.*, the ordered sequence of indices of the particles composing the ring, after a time t. As shown in Fig. 3.4 (d), this correlation function is well defined only below the crossover temperature T_x. Apart from this, it shows a similar shape as the bond-breaking correlation function, but it relaxes on a shorter time scale. We found that the two sets of correlation functions can be collapsed onto one another by multiplying the time by about a factor 6 in the ring breaking correlation function (note that 12 *Si-O* bonds are involved in a 6-fold ring).

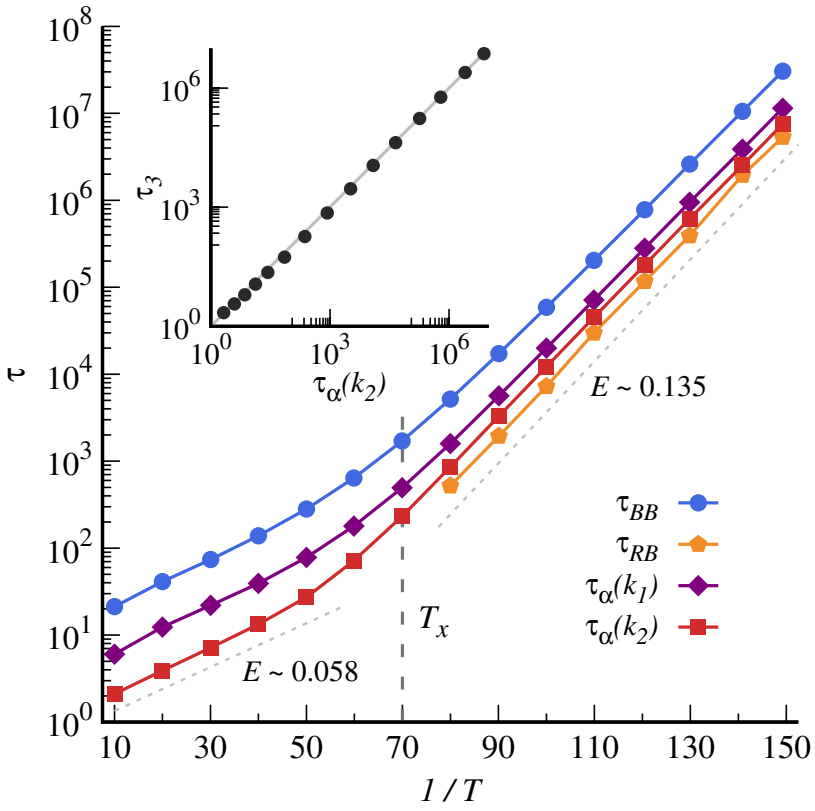

FIGURE 3.5: Correlation times of the bond breaking correlation function (τ_{BB}, circles), of the ring breaking correlation function (τ_{RB}, pentagons) and cage-relative α-relaxation times for silicon atoms, $\tau_\alpha(k_1)$ (diamonds) and $\tau_\alpha(k_2)$ (squares). All quantities are calculated for $N = 10^5$ particles, except the correlation time for the ring breaking correlation functions, for which we use $N = 2200$ particles. The inset shows the orientational relaxation time τ_3 as a function of $\tau_\alpha(k_2)$.

The structural relaxation times extracted from the above correlation functions are gathered in Fig. 3.5 in an Arrhenius representation. We also include in the figure the relaxation times obtained from the $\tilde{F}_s(k,t)$ calculated at $k = k_1$, i.e., close to the first sharp diffraction peak of $S_{SiSi}(k)$, as well as the orientational relaxation times from $\Psi_3(t)$, see inset of Fig. 3.5. All the relaxation times grow hand in hand with decreasing temperature. Three regimes are clearly visible from our data. At both high and low temperatures, the relaxation times are well described by an Arrhenius law, $\tau(T) = \tau_0 \exp(E/T)$. The apparent activation energies are $E \simeq 0.058$ and $E \simeq 0.135$, at high and low temperatures, respectively. Thus, 2*d* silica is a perfect example of strong glass-former in the Angell classification, consistent with the findings of Roy *et al.* [134], which, however, were based on the ill-defined diffusion coefficient and

covered a smaller temperature regime. The presence of two different free energy activation barriers at high and low temperatures might suggest an increase in the typical local energy barrier to overcome to relax the system and/or a decrease in the entropy associated with such process at low temperatures. To assess which of these effects is dominant, a more careful investigation is required [156, 157]. Between the two Arrhenius regimes, there is a crossover regime centered around T_x, over which the liquid behaves as a fragile glass-former. This regime is, however, very narrow and only covers a decade in relaxation times. Moreover, while we clearly observe a strong behavior at low temperature, which extends over at least four decades in relaxation times, we see no evidence for two distinct "fragile" and "mixed" regimes, as discussed in [134]. Overall, our results put the analysis of Roy *et al.* on a firmer basis and clarify the nature of the distinct temperature regimes in liquid $2d$ silica.

3.2 Elementary rearrangements

The low-temperature Arrhenius behavior observed in Fig. 3.5 suggests that, below T_x , structural relaxation is governed by a single elementary process. To identify such process, we turn to the analysis of the elementary rearrangements in our system. We first develop a procedure to identify local rearrangements according to changes in the topology of the network, and we then classify the typical processes occurring at low temperature. Finally, we analyze the proportions of these kinds of relaxations and their characteristic timescale as a function of temperature.

3.2.1 Identification of rearrangements

Computational studies on elementary rearrangements in glass-forming liquids identify them as rapid rearrangements of sets of particles whose displacements exceed a certain threshold [107, 158]. To reduce the influence of short time thermal vibrations, displacements are often evaluated using either the inherent structures or the positions averaged over a small increment of time [107]. In our system, due to the presence of long-wavelength fluctuations, the particles' positions between two different time instants cannot be easily compared, as these fluctuations can displace a particles and its neighbors over large distances without any change in network connectivity[2] [106]. Although using cage relative displacements or averaging the positions over a short period of time can in principle solve this issue, we decide to focus on the topological changes in the network, which we deem more reliable and less affected by thermal fluctuations.

The procedure we use to define the rearrangements is as follows. We consider the network structure of the system at two instants of time $t_0 < t_1$. The connectivity of a network with N nodes can be represented with a $N \times N$ matrix A, such that $A_{ij} = 1$ if nodes i and j are connected and $A_{ij} = 0$ otherwise. The matrix A is called the adjacency matrix of the network, and it is not unique, since its definition rely on a particular enumeration of the nodes [146]. Let $A(t_0)$ and $A(t_1)$ be the adjacency matrices of the system at times t_0 and t_1, respectively. If $A(t_0)$ and $A(t_1)$ are obtained using the same enumeration of the nodes, then their difference $B(t_1, t_0) = A(t_1) -$

[2]To get an idea of the effect of such fluctuations on the system, we present as M3.1 in Appendix E a movie with the trajectory of the system at the lowest temperature considered in our analysis ($T = 0.0067$) and as M3.2 in Appendix E a movie with the same trajectory but with positions averaged over a short period of time to reduce the influence of the thermal fluctuations. The use of averaged positions significantly reduces, but does not eliminate, the effect of long-wavelength fluctuations.

$A(t_0)$ is a $N \times N$ matrix such that

$$B_{ij}(t_1, t_0) = \begin{cases} +1 & \text{if } i \text{ and } j \text{ are not connected at } t_0 \text{ but are connected at } t_1 \\ 0 & \text{if } i \text{ and } j \text{ do not change their connectivity between } t_0 \text{ and } t_1 \\ -1 & \text{if } i \text{ and } j \text{ are connected at } t_0 \text{ but are not connected at } t_1 \end{cases} .$$

Thus, non-zero entries of $B(t_1, t_0)$ correspond to bonds that form or break between the times t_0 and t_1. The matrix $B(t_1, t_0)$ can be rearranged so that it is in block form[3], with each block corresponding to a subset of nodes that change their connections only between themselves. Let us define a rearrangement between two instants of time as a set of particles that change their connectivity only with other particles within the same set and do not alter the connections of the other particles in the network. Then, each block in $B(t_1, t_0)$ identifies a single rearrangement that occurs in the system between t_0 and t_1.

The procedure described above is computationally expensive, as it involves the calculation of several $N \times N$ matrices and the representation of one of them in block form. However, it is possible to perform all the steps defined above without representing the matrices explicitly, but using instead the list of neighbors of each particle at the two instants of times, and checking the neighbors present only at one of the instants considered. In particular, we compile for each particle a list of its neighbors present only at time t_1 (newly formed bonds) and its neighbors present only at time t_0 (old broken bonds). We then use a simple clustering algorithm on these lists to identify the set of particles that change the connections only between themselves.

3.2.2 Classification of elementary rearrangements

In our analysis of the elementary rearrangements, we represent the network structure of the system using *Si* particles as nodes, while *O* particles define the edges between nodes. In particular, two *Si* nodes are connected if they are neighbors of the same *O* particle. Figure 3.6 displays the typical changes in connectivity that occur between two close instants of time at low temperature. Since the time interval is much shorter than the structural relaxation time, most of the particles do not change their neighbors, and are thus not involved in a rearrangement. Meanwhile, particles that do change their neighbors form isolated clusters identified by a series of newly formed and broken bonds connected together.

By visual inspection of the rearrangements occurring at low temperature ($T = 0.0067$) over short time intervals ($t_1 - t_0 \sim 0.0015 \cdot \tau_\alpha(k_1)$), we noticed that most of the rearrangements fall in two different typologies: string-like rearrangements and bond-switch rearrangements. String-like rearrangements are characterized by a single line of successive newly developed and destroyed bonds, with the particles at the beginning and at the end of the chain being coordination defects at t_1 or t_0. Thus, these rearrangements correspond to the motion of a coordination defect along the string, or the formation or annihilation of two opposite coordination defects. These rearrangements can be either small, involving only two or three particles, like those in the bottom right of Fig. 3.6, or quite large, involving several tens of particles, like the one in the left of Fig. 3.6. The appearance of these processes is qualitatively

[3]This representation is possible thanks to the existence of loops of alternating old and new bonds which visit all the atoms involved in a rearrangement [159]. The entire procedure presented here can be seen as a formalization of what was done by Barkema and Mouseeau to describe the elementary rearrangements is 3*d* amorphous silicon [159].

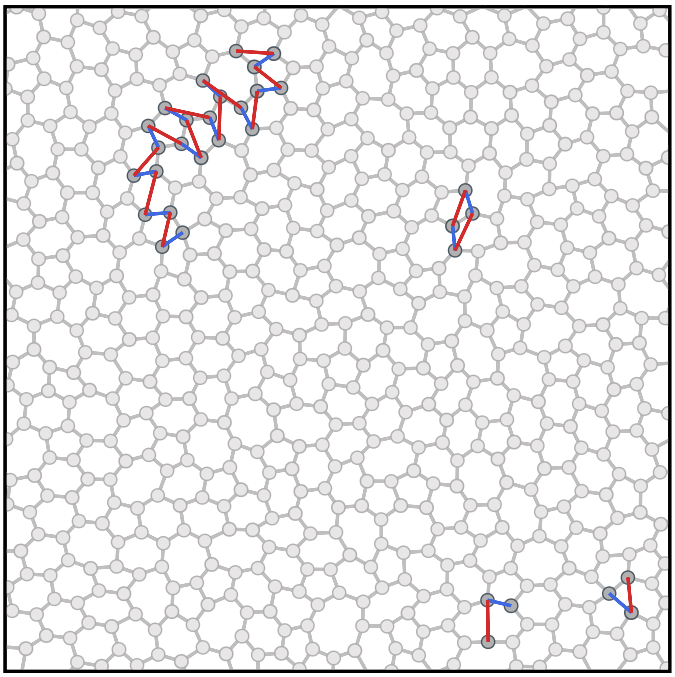

FIGURE 3.6: Snapshot of typical rearrangements in the low temperature network, with a short time interval between the two frames considered. We depict with grey circles the position of the *Si* particles in the first frame, and as lines the connections between the particles. Dark grey circles correspond to *Si* particles that change at least a neighbor in the considered time interval, and red and blue lines represent newly formed and broken bonds, respectively. Light grey circles instead represent *Si* particles which do not change their connectivity between the two frames, and grey lines represent bonds present in both frames. Four rearrangements can be identified in the snapshot: two small t-strings on the bottom right, a larger t-string on the top left and a bond-switch on the top right.

similar to that of string rearrangements observed in close-packed glass-forming liquids [160], where the rearranging particles move along a line and each particle at the end of the rearrangement occupies the position previously occupied by the particle preceding in the string. Due to these similarities, we refer to these local relaxations as *topological-strings* (*t-strings*).

The other typical rearrangement we observe is the bond-switch (BS) rearrangement. This process involves four particles with no coordination defects at either t_0 or t_1. Such a rearrangement is thus localized and preserves the number of bonds in the system. It is also a well-known relaxation used to produce a realistic network structure in the WWW algorithm [96, 161] and has been found to be primary mechanism for non-defect-based diffusion in amorphous silicon [159]. In a perfect $2d$ hexagonal network, this rearrangement produces a Stone-Wales defect, transforming four hexagonal rings into two heptagons and two pentagons [128, 162]. Remarkably, this process can be triggered in the experimental sample of silica bilayer using an electron beam [26] and has been suggested as the main relaxation channel in this system [163].

In our visual representation, a bond-switch appears as a parallelogram with alternating newly developed and broken bonds, as shown in the top right of Fig. 3.6.

Because of its relevance in the literature of network-forming materials, we also consider concatenations of multiple bonds-switches as independent relaxations[4]. Due to the computational cost involved in their evaluation, however, we limit our analysis to concatenation of up to three bond-switches. In particular, our analysis shows that there are 6 inequivalent concatenations of two bond-switches (2 BS) and 40 inequivalent concatenations of three bond-switches (3 BS). Many of the latter involve the formation of very small or large rings in the network, and are thus expected to be very rare, if present at all, in a physical network.

3.2.3 Temperature dependence of elementary rearrangements

We now turn our attention to the statistical properties of the elementary rearrangements as a function of temperature. To this end, we analyze the fraction $P(t, T)$ of Si particles involved in a given type of rearrangement over a time interval t at a given temperature T.

In Fig. 3.7 (a), we present $P(t, T)$ for a system of 15000 particles in thermal equilibrium at $T = 0.0067$, the lowest temperature at which we were able to equilibrate the system. At short times, very few rearrangements occur, and most of them are t-strings, thus involving the motion of coordination defects in the network. At longer times, bond-switch processes start to appear and they become the predominant rearrangements at times just before the structural relaxation time $\tau_\alpha(k_1)$. While a single BS is always the predominant relaxation channel in this regime, there is also a substantial fraction of rearrangements equivalent to concatenations of several bond-switches. These concatenations involve fewer particles overall and exhibit a maximum at later times than the single BS move. The combination of all the rearrangement based on a BS move almost completely account for the rearrangements involving defectless particles. We speculate that including higher order concatenations of BS moves, we would be able to fully account for the defect-less rearrangements in the system. At times comparable to or larger than $\tau_\alpha(k_1)$, the elementary relaxations begin to merge, producing complex rearrangements that do not fit into any of the types previously defined and involve a large number of particles[5].

In Fig. 3.7 (a) we observe that at low temperatures ($T = 0.0067$), t-strings occur on a short time scale and involve a small number of atoms, while most atoms are involved in bond-switch moves at times close to τ_α. We repeat this analysis at different temperatures, to assess how the fraction of particles involved and the characteristic times of a given type of rearrangement change as a function of temperature. To this end, for each type of relaxation we define the time interval $t_{max}(T)$ at which $P(t, T)$ reaches a maximum and $P_{max}(T) = P(t_{max}, T)$ the maximum fraction of particles involved in that type of rearrangements. These quantities, $t_{max}(T)$ and $P_{max}(T)$, thus represent the characteristic timescale over which a rearrangement occurs and the

[4]Clearly, such rearrangements are not elementary modifications of the network. However, they can appear as such if the interval between t_0 and t_1 is much smaller than the typical time required to perform a bond-switch. Moreover, they have already been considered as such in other studies in the literature [159].

[5]With our analysis, it is possible to think of the trajectory of the system as a sequence of rearrangements. These events are ordered in time and two successive events can be connected if they share at least one particle. Thus, we can represent the trajectory as a directed graph or tree, where the nodes are the rearrangements and the direction of the bonds follows the flow of time. In this representation, an example of which is shown in figure F3.1 in the Appendix E, one easily sees how the different rearrangements combine together over time, and how complex rearrangements develop from the combination of simpler ones.

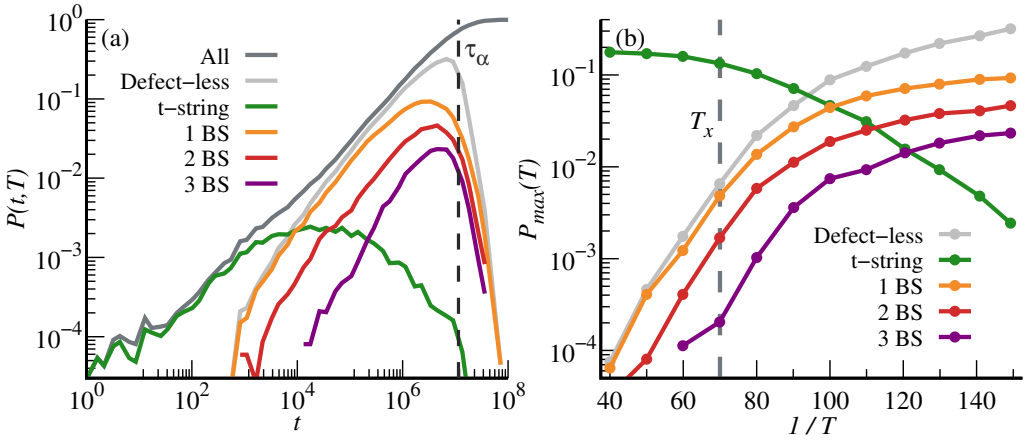

FIGURE 3.7: Properties of different types of rearrangements. (a) Fraction of *Si* particles involved in rearrangements of a given type at temperature $T = 0.0067$ as a function of the time interval between the instants of time considered. (b) Maximum fraction of *Si* particles involved in rearrangements of a given type as a function of temperature. All quantities are calculated for a system of $N = 15000$ particles.

typical fraction of the system that performs such relaxations on that timescale, respectively.

In Fig. 3.7 (b) we show $P_{max}(T)$ as a function of temperature for the different types of rearrangements defined in Sec. 3.2.2. At high temperatures, the main relaxations are t-strings. As the temperature decreases, however, the relevance of this type of rearrangement diminishes, and around the temperature $T \simeq 0.0111$ bond-switches become dominant. A possible explanation for this behavior is the formation of a well-defined network at temperature $T < T_x$, with a decreasing number of coordination defects as the temperature decreases, as shown in Fig. 3.2 (b). Due to the small number of particles with the wrong coordination at low temperatures, t-strings become progressively rarer, while the rearrangements that do not alter the coordination of the particles, such as bond-switches, become prevalent.

From the behavior of $t_{max}(T)$ (not shown), we observe that the characteristic time scale for the occurrence of a t-string rearrangement is always smaller than that of the BS moves. In particular, this time scale is approximately constant and equal to $0.07 \cdot \tau_\alpha(k_1, T)$ at high temperatures, while it begins to decrease around the temperature T_x, reaching $0.001 \cdot \tau_\alpha(k_1, T)$ at $T = 0.0067$. The characteristic time scales for the different concatenations of BS moves appear to be roughly similar, and equal $0.5 \cdot \tau_\alpha(k_1, T)$ for all the temperature considered in this analysis. Since the characteristic time scale for these rearrangements and τ_α scale in the same way with temperature, the bond-switch moves are good candidates for the microscopic processes which that the structure of the system to relax, particularly at low temperatures, when these rearrangements are more prevalent.

Overall, our results show that bond-switch rearrangements are particularly relevant in two-dimensional silica, like in its $3d$ counterpart. This local relaxation is a suitable candidate for the microscopic mechanism that allows the structure of the system to relax at low temperature. In particular, it would be very interesting to evaluate the potential energy barrier required to perform such rearrangements and compare it to free energy barrier obtained from the analysis of the correlation times in Sec. 3.1.3. Moreover, due to their local nature, the BS moves are also ideal candidates for trial moves in Monte Carlo simulations [161], and their use for our model for $2d$ silica might significantly speed up the simulations, allowing the system to be

studied at even lower temperatures. Finally, it would be interesting to frame our results in the context of the theories of dynamic facilitation [107, 164], which are based on the idea that a region of rearranging particles facilitates the relaxation of nearby regions.

3.3 Melting of the crystal

As discussed in Sec. 1.2.1, three-dimensional silica becomes a glassy liquid at temperatures well above its melting temperature. As the silica bilayer shows strong similarities to its $3d$ counterpart, it is reasonable to ask whether the same holds true for our model. We thus estimate the melting temperature of the system, also checking for finite size effects due to Mermin-Wagner fluctuations. We also provide a qualitative description of the melting process in this system, and we compare it with the well-established KTHNY scenario.

3.3.1 Estimation of the melting temperature

The dynamic slowdown of a glassy liquid is sometimes linked with its metastability relative to the corresponding crystal [69, 165, 166]. However, no clear connection has been found yet between the onset of the glassy dynamics and crystallization, as recently shown using a rigorous approach [167]. The lack of a connection between these two temperatures is also evident in systems such as silica and boria, where the onset of glassiness occurs at temperatures well above the melting temperature [168].

To address this issue for the RHH-II model of $2d$ silica, we estimated its melting temperature using brute force simulations. We first heated a crystalline sample to the target temperature T and then annealed it. During the annealing, we monitored the magnitude of a crystalline order parameter, as defined below, and we identified the melting of the crystal by the drop of the order parameter to a negligible value. To describe crystalline order, we used the 6-fold order parameter evaluated on the second coordination shell

$$\psi_{6,j}^{SCS}(t) = \frac{1}{6}\sum_{l=1}^{6} e^{6i\phi_{jl}(t)}\,, \tag{3.4}$$

where $\phi_{jl}(t)$ is the angle between the bond connecting the *Si* particles j and l and an arbitrary reference line, and the sum runs between the fourth and the ninth nearest neighbors of the j-th particles. This definition assumes that the first and the second coordination shells contain the expected number of particles, *i.e.*, three and six, respectively. This assumption is accurate at low temperatures, where the number of coordination defects is small, but becomes imprecise at high temperatures, where their number becomes substantial, as shown in the inset in Fig. 3.2 (b). We are forced to use this coarse local order parameter due to the 3-fold symmetry of the local environment of the silicons. In the crystalline phase, this results in an antiferromagnetic-like ordering of the local order parameters, making their average, *i.e.* the global order parameter, equal to zero in the thermodynamic limit. From the local order parameter in Eq. 3.4, we define a global order parameter

$$\Psi_6^{SCS}(t) = \frac{1}{N}\sum_{j=1}^{N} \psi_{6,j}^{SCS}(t)\,, \tag{3.5}$$

and we use its module as a measure of the degree of crystallinity of the sample.

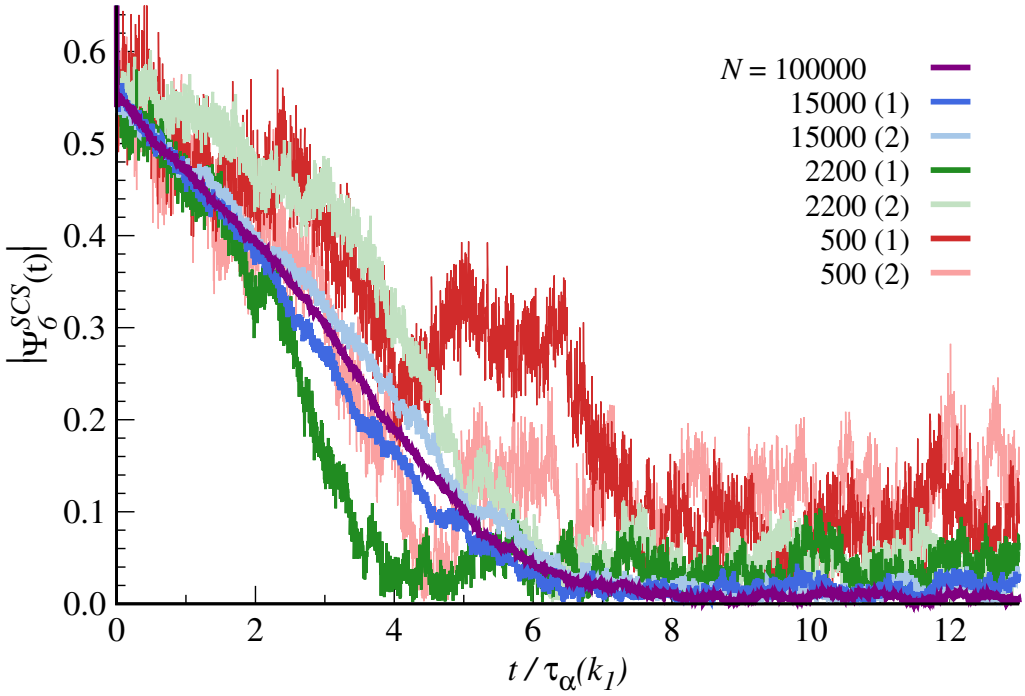

FIGURE 3.8: Evolution of the module of the global order parameter $|\Psi_6^{SCS}(t)|$ over time during the melting of systems of various sizes. During the melting process the temperature was fixed to $T = 0.0091$. Different runs for the same system size are denoted by a number between brackets in the key.

We first test whether the melting process is affected by finite size effects due to long-wavelength fluctuations. As discussed in Sec. 3.1.2 such fluctuations are present in our system and have a profound impact on its translational dynamics. To assess whether they also influence melting, we select a low temperature ($T = 0.0091$) and we study the melting of crystalline systems of different sizes. We present the results of this analysis in Fig. 3.8. No clear finite size effect is observed in the melting curves and increasing the system size only leads to a decrease in the fluctuations of the global order parameter, as expected from its definition in Eq. 3.5.

Having established that the melting kinetics has no significant finite size effects, we proceed to estimate the melting temperature using a system of $N = 2200$ particles. By repeating the above analysis at different temperatures, we found that the crystal melts, within our observation window, at least down to $T = 0.0067$, which is the lowest temperature at which we can equilibrate the liquid. Thus, despite the huge increase in relaxation times observed in this system, see Sec. 3.1.3, the liquid is not metastable with respect to the crystal over the entire range of temperatures we investigated. These results indicate that two-dimensional silica, like its $3d$ counterpart [168], displays glassy dynamics already well above its melting temperature.

3.3.2 Melting process and comparison with the KTHNY scenario

As discussed in Sec. 1.3.2, according to the KTHNY theory, melting of a two-dimensional crystal is a two-step process [102, 114, 115, 120, 169, 170]. The first step involves the unbinding of dislocations, resulting in a hexatic phase with quasi-long-range orientational order but short-range translational order. Later, the unbinding of disclinations results in the loss of quasi-long-range orientational order and the formation of a liquid phase. In a close-packed two-dimensional system, where each particle has

on average six neighbors, dislocations appear as a bound pair of particles with coordination five and seven, while disclinations are isolated particles with five or seven neighbors [102], as shown in Fig. 1.10.

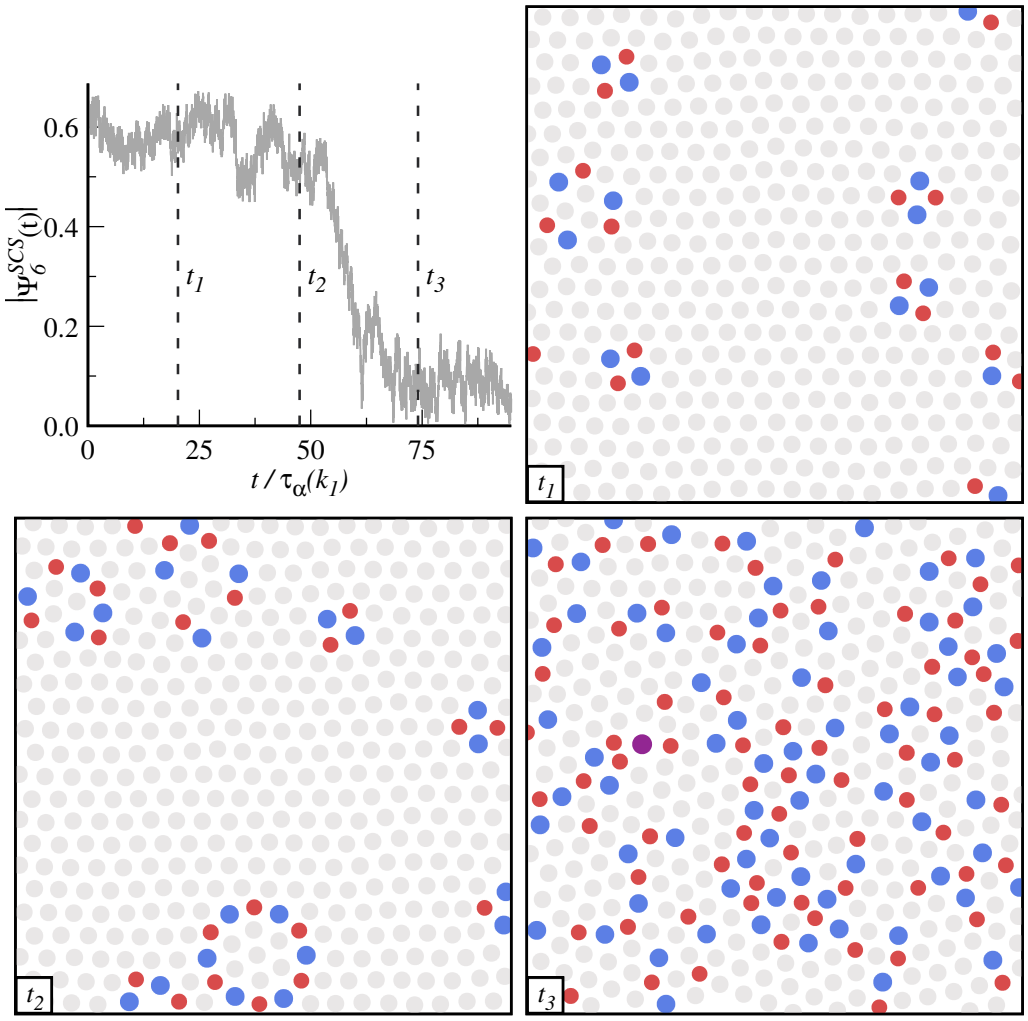

FIGURE 3.9: (top left) Evolution of the module of the global order parameter $|\Psi_6^{SCS}(t)|$ as a function of time during the melting of system at $T = 0.0067$. Three vertical dashed lines indicate the times for which we visualize the system in the remaining panels. In the snapshots, we represent the rings as effective particles, whose position is the center of mass of the corresponding rings. Red, platinum, blue and purple circles represent 5-, 6-, 7- and 8-sided rings.

To the best of our knowledge, these effects have only been assessed numerically for close-packed systems [122, 123, 125, 171, 172]. Thus, it is interesting to examine the melting process of our model of the silica bilayer in the light of the KTHNY scenario. We consider a system of $N = 2200$ particles at $T = 0.0067$, the lowest temperature at which we can equilibrate the liquid. To frame the behavior of $2d$ silica in the KTHNY theory, we consider the dual of the network structure, *i.e.* a new system of effective particles corresponding to the rings of the original system. The position of each effective particle is the center of mass of the corresponding ring. In this picture, the low-temperature system appears as a set of close-packed disks, where the disks have a coordination equal to the number of sides of the underlying rings. Although this mapping provides a formal correspondence to the KTHNY scenario for $2d$ melting, it is important to note that the presence of an underlying

atomic system might have significant effects of the appearance and interaction of topological defects, *i.e.* effective particles with coordination other than six.

In Fig. 3.9, we present three representative snapshots taken during the melting of the system[6]. We draw the snapshots according to the dual description of the system, representing the 5-, 6-, 7- and 8-sided rings as red, platinum, blue and purple circles, respectively. We observe that melting proceeds through a series of steps. Initially, several Stone-Wales defects form, see snapshot t_1 in Fig. 3.9, which in our description appear as two neighboring pairs of red and blue circles. Each of these defects corresponds to a bound pair of dislocations in the KTHNY scenario, see Sec. 1.3.2. In our system, these defects are stable, and are continuously excited and annihilated during the first part of the simulation. When two such defects are close together, they merge and form chains of alternating 5- and 7-sided rings that can have both ends loose or form a closed loop[7], see snapshot t_2 in Fig. 3.9. These chains are stable and enclose crystalline domains rotated relative to the bulk crystal. Finally, these chains begin to interact with each other, forming a nearly percolating cluster of defects, see snapshot t_3 in Fig. 3.9. This step destroys the overall orientational order of the crystal, leading to a liquid.

Interestingly, this melting process appears to be qualitatively different from the KTHNY scenario. For example, disclinations, *i.e.* bound pairs of a 5- and 7-sided rings, generally appear as part of a Stone-Wales defect or a chain of defects, and not as isolated structures. Furthermore, isolated topological defects such as single 5- or 7-sided rings are quite rare, even in the liquid phase. A more systematic investigation of the melting process of the model and its comparison with the KTHNY theory is left to a future study.

3.4 Key results

The key insights we gained in this chapter can be summarized as follows:

- Our model is a strong glass-forming system, with correlation times that follow two Arrhenius laws at both high and low temperatures, and with a sharp crossover between the two centered at the temperature at which the network starts to develop.
- Despite the large structural relaxation times at low temperature, our model is not metastable with respect to the crystal, even at the lowest temperature considered.
- Similarly to $3d$ silica, the bond-switch process is particularly relevant in our model for the silica bilayer and provides a plausible mechanism for the relaxation of the system at low temperatures.
- The melting of the crystal occurs in stages that first involve the formation of Stone-Wales defects and then chains of alternating 5- and 7-sided rings.

[6] The melting of this system using our effective description is available as a movie, see movie M3.3 in Appendix E.

[7] Remarkably, some of these structure are known defects in other two-dimensional atomic networks. For example, the circle of 5- and 7-sided rings at the bottom of snapshot t_2 in Fig. 3.9 is a "flower defect" that can be found in graphene samples [128].

Chapter 4

Silica bilayer: structure-dynamics relation

In this chapter we carefully analyze the relationship between structure and dynamics in our simple model for the silica bilayer. We use a set of bond-order parameters to describe the degree of local order, while the dynamics is characterized using the four-point structure factor and the dynamic propensity evaluated in isoconfigurational ensemble. We study both the free-standing system and the system in the presence of a periodic substrate. One of the key findings in the analysis of the free-standing system is the presence of large transient crystalline domains in the low temperature liquid, even when the latter is not metastable with respect to the crystal. This result is in contrast to the physics of other three-dimensional glassy systems, where such large crystalline domains are not detected. Furthermore, the simulations of the system on a substrate allow us to assess how the structure and dynamics of the overlayer are affected by the presence of a periodic potential. This allows a qualitative classification of the substrates based on their effect on the properties of the overlayer.

We first evaluate the degree of local crystalline order and we compare it with dynamical indicators (Sec. 4.1). We then introduce a new model to simulate a $2d$ system in the presence of a periodic potential that mimics the effect of the substrate and we characterize the structure and dynamics of the overlayer (Sec. 4.2). Finally, we frame our results in the context of different theories on the structure and dynamics of network-forming systems (Sec. 4.3).

The majority of this chapter is unpublished work, with only a subsection (Sec. 4.1.1) adapted from Ref. [126].

4.1 Static and dynamic correlation lengths

In Sec. 3.1.1 we showed that as the temperature drops below T_x, the system starts to form a well-defined network structure, with the emergence of a first sharp diffraction peak in the structure factor and a decrease in the number of coordination defects. We now turn our attention to a local description of the structure of the system, focusing in particular on the low temperature regime. We will then attempt to connect the emergence of this local crystalline order to dynamical heterogeneities by calculating the four-point structure factor and the dynamic propensity in the isoconfigurational ensemble.

4.1.1 Static correlation lengths

The locally favored structure found in the low-temperature liquid is an equilateral triangle centered on a *Si* particle, thus sharing the same local symmetry as the crystal[1]. Therefore, it is natural to wonder whether these structures develop some orientational order beyond the first coordination shell and whether there is any interplay with crystallization. This type of analysis may also shed light on the experimentally observed structures, which show some regions with pronounced local crystalline order [18, 20, 173].

To characterize the bond-orientational order, it is useful to introduce a set of order parameters that quantify the local alignment of bonds with n-fold local symmetry. We define the complex bond-order parameter for an n-fold symmetry of the j-th particle as

$$\psi_{n,j}(t) = \frac{1}{n}\sum_{l=1}^{n} e^{in\phi_{jl}(t)}\,, \tag{4.1}$$

where $\phi_{jl}(t)$ is the angle between the bond connecting particles j and l at time t and an arbitrary reference line, and the sum extends over the first n nearest neighbors of j. In this section, we will focus on the *Si* particles as central particles for the calculation of $\psi_{n,j}$. Due to the 3-fold local antiferromagnetic symmetry around *Si* particles, only $n = 3$ is relevant for correlations within the first coordination shell. The calculation of $\psi_{3,j}(t)$ is the average of three values, each of which is a function of the angle $\phi_{jl}(t)$ between the central particle and one of its neighbors and a reference axis. This causes the local order parameter for a 3-fold symmetry to be strongly affected by the thermal vibration of the particle positions. To smooth out these small-scale spatial fluctuations we thus define a set of coarse-grained local order parameters, averaging $\psi_{3,j}(t)$ over the first or the second *Si*-*Si* coarse-grained coordination shell, $\psi_{3,i}^{cg(m)} = \frac{1}{N_m}\sum_{j=1}^{N_m}\psi_{3,j}$, where N_m is the number of particles in the m-th coarse-grained coordination shell.

We define the first coarse-grained coordination shell as first three neighbors of the considered i-th particle[2], while the second coarse-grained coordination shell is defined as the set of nearest neighbors of the particles in the first coarse-grained coordination shell of the i-th particle, excluding the i-th particle itself. Using these local order parameters, it is possible to construct an even smoother local order parameter as $\tilde{\psi}_{3,i}^{cg(2)} = \frac{1}{3}\left(\psi_{3,i}(t) - \psi_{3,i}^{cg(1)} + \psi_{3,i}^{cg(2)}\right)$, where the change of sign for $\psi_{3,i}^{cg(1)}$ is due to the antiferromagnetic symmetry of the 3-fold order parameter between successive coordination shells in the crystal. We found no major differences between the bare and coarse-grained parameters, except for smoother spatial fluctuations of the latter[3]. We also define a bond-order parameter $\psi_{6,i}^{R}$ for a 6-fold symmetry between the rings, using the centers of mass of the rings as effective coordinates in the equation for the local order parameter. Compared to $\psi_{3,j}$, this local order parameter has a simpler ferromagnetic symmetry in the crystal, but its calculation require a costly evaluation of the rings' structure, which is not well defined at high temperature, as discussed in Sec. 3.1.3.

[1] Note that, according to the Mermin-Wagner theorem [101], the crystalline phase can only display quasi-long range order.

[2] Note that at low temperatures, each *Si* particle tends to have three nearest neighbors, and thus this procedure returns exactly the first coordination shell as defined by the RDF.

[3] Although these local order parameters have similar behavior and produce comparable static correlation lengths, they have different correlations with the dynamic propensity and capture local order on different length scales, as we will see in Sec. 4.1.3.

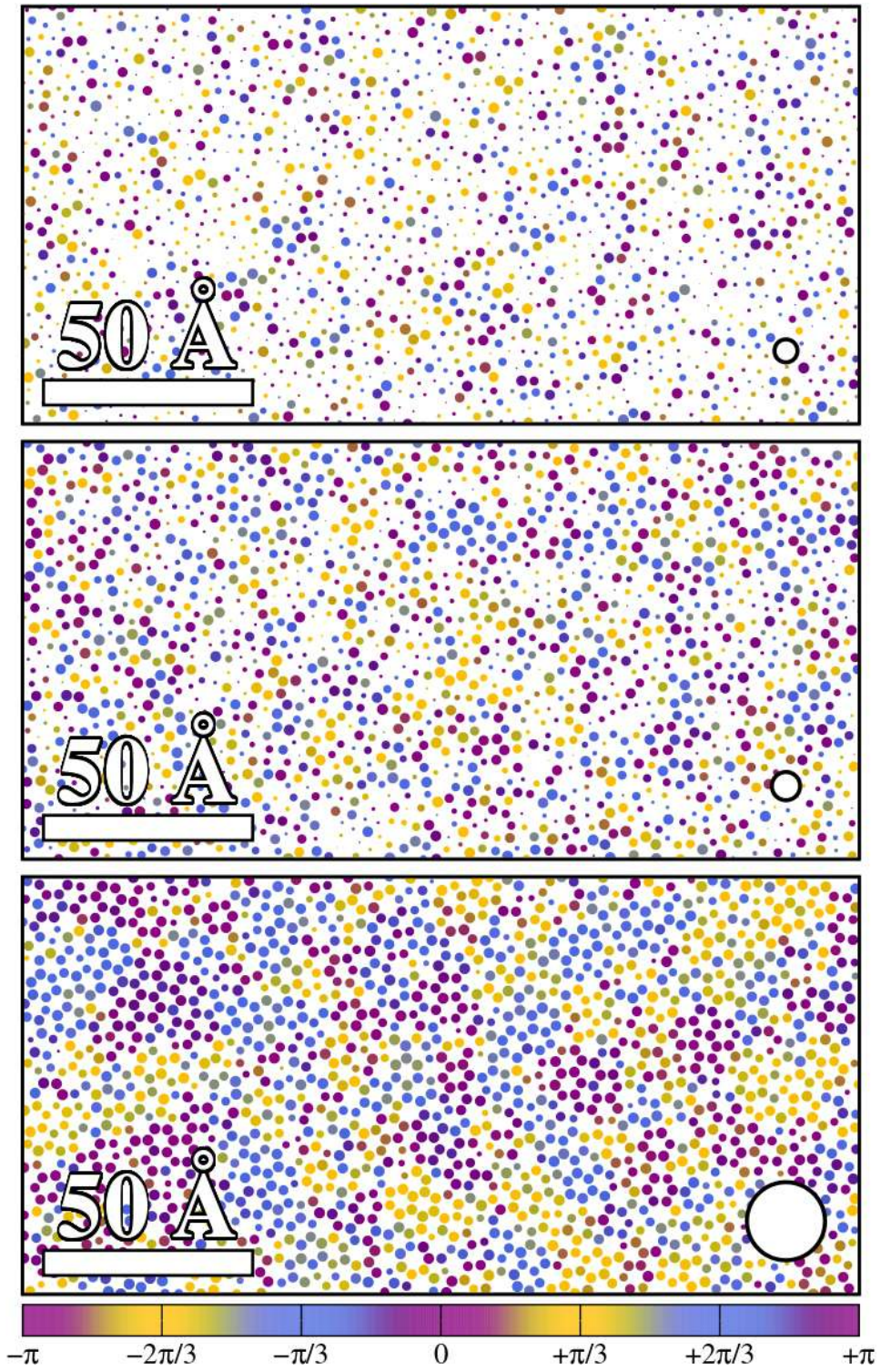

FIGURE 4.1: Snapshots illustrating the development of local crystalline order. The particles are color-coded according to the phase of the complex local order parameter $\psi_{3,i}$, while their size is proportional to $|\psi_{3,i}|$. Only *Si* particles are shown. The configurations are taken at temperature $T = 0.0250, 0.0143 (\approx T_x)$, and 0.0067 (from top to bottom). The white circle in the lower right corner of each configuration has a radius equal to the static correlation length at the corresponding temperature. The palette features repeating colors due to the antiferromagnetic symmetry of $\psi_{3,i}$ in the honeycomb lattice.

Representative snapshots of the spatial distribution of the 3-fold bond-order parameter between silicons are shown in Fig. 4.1, from above the crossover temperature T_x down to the lowest equilibrated temperature[4]. The color-coding is chosen to highlight regions with similar phases of the order parameter, while the radius of the particles is proportional to the amplitude $|\psi_{3,j}|$. We clearly observe patches of particles with similar orientational order, which are visible around the crossover temperature T_x and whose typical size grows appreciably with decreasing temperature. At low temperatures, the system displays numerous crystalline regions of nanometric size and different orientations.

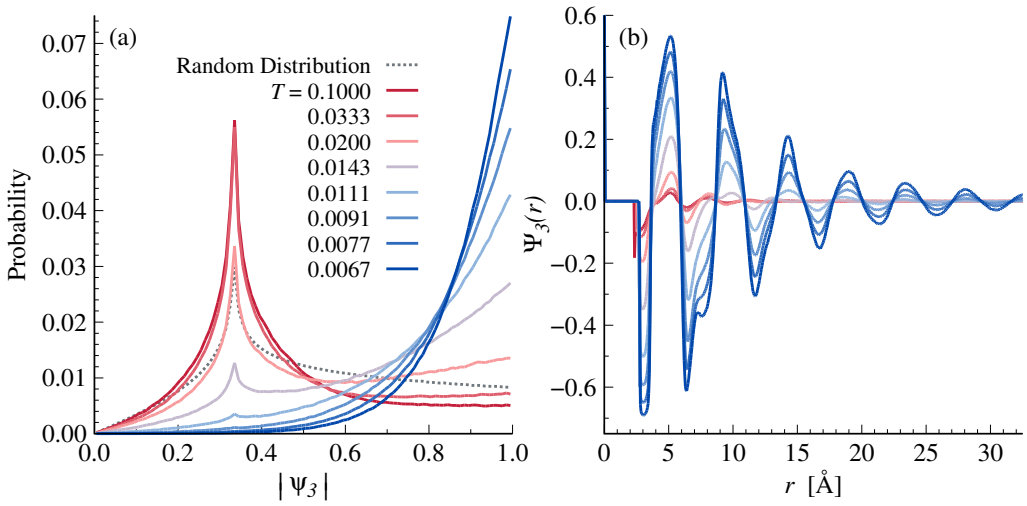

FIGURE 4.2: (a) Distribution of the module of the local order parameter for a 3-fold symmetry between *Si* particles at different temperatures. The dashed distribution corresponds to a random distribution of particles. (b) Spatial correlation function $\Psi_3(r)$ of the local order parameter for a 3-fold symmetry between *Si* particles at different temperatures. The data presented are calculated for a system of $N = 10^5$ particles.

The probability density function $p(|\psi_3|)$ is shown in Fig. 4.2 (a). It shows the progressive crossover from the nearly random arrangements of the closest 3 bonds at high T, to orientationally ordered local arrangements at low T. In particular, as the temperature decreases, the maximum of the distribution shifts from $p(|\psi_3|) \simeq 0.33$, similar to that of a random distribution of particles, to a nearly perfect local 3-fold arrangement ($p(|\psi_3|) \simeq 1.0$). To quantify the spatial extent of the locally ordered domains, we compute the n-fold bond-orientational correlation function

$$\Psi_n(r) = \frac{\langle \sum_{i,j} \psi_{n,i} \psi^*_{n,j} \delta(r - r_{ij}) \rangle}{\langle \sum_{i,j} \delta(r - r_{ij}) \rangle}, \tag{4.2}$$

where $r_{ij} = |\mathbf{r_i} - \mathbf{r_j}|$. Similarly, we define the corresponding correlation functions for the coarse-grained parameters and the bond-order parameters between rings. We show the temperature variation of $\Psi_3(r)$ in Fig. 4.2 (b). The correlation function has alternate negative and positive regions, due to the antiferromagnetic-like order between successive shells of neighbors. Clearly, the absolute value of the correlation progressively increases as T is lowered, confirming the visual impression from Fig. 4.1.

[4]Fig. 4.1 and its equivalent with the spatial distribution of the 6-fold bond-order parameter between rings are available as figures F4.1 and F4.2 in Appendix E.

To extract the associated correlation length ξ_n, we fit the envelope of $|\Psi_n(r)|$ to an exponential decay following the procedure described in Appendix D. We proceed in a similar fashion to compute the correlation lengths, $\xi_3^{cg(1)}$, $\xi_3^{cg(2)}$ and $\tilde{\xi}_3^{cg(2)}$, of the coarse-grained bond-order parameters and the one, ξ_6^R, associated with the bond-order between rings. We also extract a correlation length ξ_{RDF} from the total RDF $g(r)$ by fitting the envelope of $|g(r)-1|$. Figure 4.3 (a) demonstrates the increase of translational order in the RDF as the temperature decreases. This increase appears much more pronounced than that found in the literature for other glassy systems [174].

Remarkably, all the studied static correlation lengths display the same temperature dependence, as shown in Fig. 4.3 (b). All the lengths are nearly constant at high temperature and start growing when T drops below the crossover temperature T_x, at which a well-defined network structure forms. The growth of both translational and orientational order is described by a remarkably simple scaling $\xi \sim 1/T$, which accounts, below T_x, for the T-dependence of all the static correlation lengths. We will further discuss this relationship and its connection to Tanaka's phenomenological theory in Sec. 4.3.2. At the lowest investigated temperature, the correlation lengths reach about one nanometer, but even larger correlated domains are observed in Fig. 4.1.

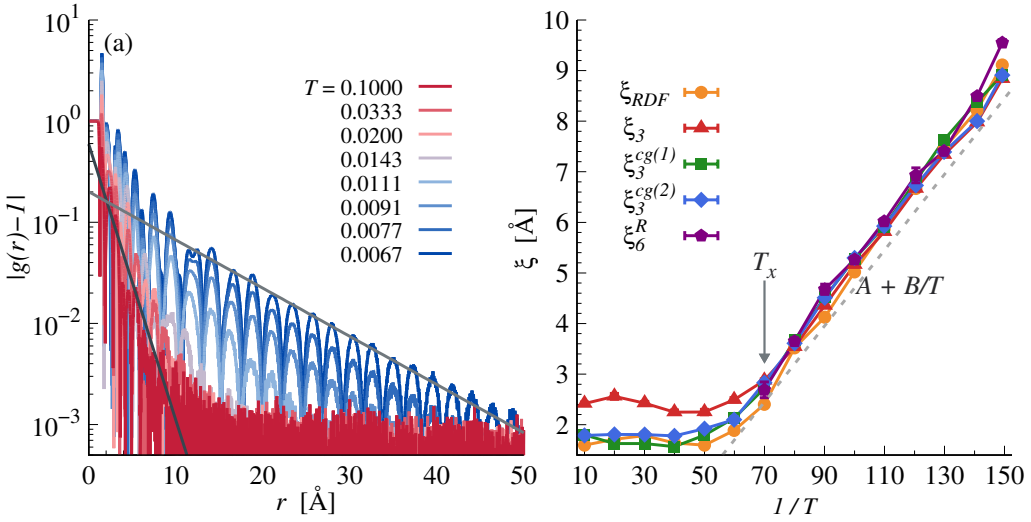

FIGURE 4.3: (a) Decay of the radial distribution function ($g(r)$) at different temperatures. Black and grey lines are fitting function of the form $f(r) = A\,exp(-r/\xi)$ for $T = 0.1000$ and $T = 0.0067$, respectively. The fitting parameters A and ξ are determined with the algorithm described in Appendix D. (b) Static correlation lengths as a function of the inverse temperature. The correlation lengths are extracted form the radial distribution function (ξ_{RDF}, circles) and the spatial correlation functions for the bare 3-fold orientational order parameter (ξ_3, triangles), its coarse-grained version averaged over the first ($\xi_3^{cg(1)}$, squares) and the second ($\xi_3^{cg(2)}$, diamonds) coordination shells, and the 6-fold orientational order parameter between rings (ξ_6^R, pentagons). All quantities are calculated for $N = 10^5$ particles.

One of the striking conclusions from Fig. 4.3 (b) is that the correlation lengths associated to the orientational (ξ_3) and translational (ξ_{RDF}) order grow together as temperature decreases. At first glance, this seems in contrast to what has been found for other two-dimensional systems studied in the literature, where the orientational order extends much further than the translational one [122, 123, 175]. However, it

should be emphasized that such a decoupling between the translational and orientational order is expected only for a hexatic phase, in which the correlation functions of the orientational degrees of freedoms decay polynomially with the distance, while those of the translational degrees of freedoms decay exponentially [102], as discussed in Sec. 1.3.2. On the other hand, for a set of locally ordered domains separated by amorphous regions that dephase both orientational and translational order, both types of order are expected to become decorrelated on the scale of the domains [175], resulting in $\xi_3(T) \sim \xi_{RDF}(T)$, as found in our system. This is further supported by our estimate of the average radius of the locally ordered domains, which increases as $1/T$ as the temperature decreases, like the other static correlation lengths considered in this work. The locally ordered domains in this analysis are defined as set of connected hexagonal rings whose difference in the angle of ψ_6^R does not exceed a given threshold, and their radius is calculated as the square root of their area divided by π [5].

The above results show that local crystalline order grows steadily in $2d$ silica upon cooling below the crossover temperature T_x. Note, however, that we found no signs of irreversible crystallization (in the sense of quasi-long range order): the locally ordered domains break up on the same time scale as the structural relaxation time τ[6], see Sec. 3.1.3, and the system remains an ergodic liquid in the entire temperature range we investigated, as shown in Sec. 3.3. The structure of the system will be discussed in the context of continuous random network theory and the cybotactic description in Sec. 4.3.1.

4.1.2 Dynamic correlation lengths

The dynamics of liquids approaching the glass transition is spatially heterogeneous, with slow and fast rearranging regions whose size increases as temperature decreases [155]. Since our system exhibits transient local crystalline domains, see Sec. 4.1.1, it is natural to wonder whether these structures are related to the spatial inhomogeneities of the dynamics. In particular, we can compare the typical lengths associated with the local crystalline order and dynamical heterogeneities, to assess whether they grow at the same rate as temperature decreases.

Typically, the dynamical heterogeneities are quantified using the four-point structure factor [103, 176]. This quantity involves the displacement of a particle between two instants of time and it is thus strongly affected by long-wavelength fluctuations and finite size effects [103], see Sec. 1.3.1. Therefore, we calculate a cage-relative version of the four-point structure factor [103]. For each particle i, we compute the cage-relative overlap function

$$\tilde{w}_i(t) = \Theta\left(\delta - |\mathbf{r}_i(t) - \mathbf{r}_i(0) - \Delta\tilde{\mathbf{r}}_i(t,0)|\right) , \tag{4.3}$$

where $\Theta(x)$ is Heaviside step function, δ is the displacement threshold and $\Delta\tilde{\mathbf{r}}_i$ is the displacement of the cage of the i-th particle, as defined in Sec. 3.1.2. The cage-relative overlap function measures whether a particle has moved (relative to its cage) a distance greater than δ in a time interval t. Thus, $\tilde{w}_i(t) = 1$ corresponds to "fast"

[5] The data related to the crystallites vary for different values of the threshold used to define them and we have not found a clear-cut criterion for setting this parameter. In our analysis, we fix its value to 45° since the crystallites obtained for this value seems reasonable, but our results do not change for other choices of the parameter. We present as F4.3 in Appendix E a snapshot of the system before and after the identification of the crystalline domains.

[6] We present as M4.1 in Appendix E a video showing the trajectory of the system at low-temperature ($T = 0.0067$) using the same plotting scheme as Fig. 4.1.

rearranging particles, while $\tilde{w}_i(t) = 0$ identifies "slow" rearranging particles which have not yet escaped the cage formed by their neighbors. The displacement threshold δ is generally a fraction of the typical interatomic distance [103, 105, 176]: it should be large enough to be insensitive to fast thermal vibrations, but also small enough to capture the first escape of the particle from the cage formed by its neighbors. We focus on the *Si* particles and we set $\delta = 0.30$ Å, which is roughly 0.2 times the distance between *Si*-*O* particles[7]. We calculate the cage-relative overlap function at time $t = \tau_\alpha(k_2)$[8], when the dynamic heterogeneities are expected to be most pronounced [103].

To provide a visual impression of the degree of the dynamical heterogeneities of the liquid, we show in Fig. 4.4 the dynamical field $\tilde{w}_i(\tau_\alpha)$ for the same three temperatures as in Fig. 4.1. The sizes of the slow and fast rearranging regions increase dramatically as the temperature decreases, and at the lowest temperature they are much larger than the sizes of the local crystalline domains (note that the area in Fig. 4.4 is three times larger than that in Fig. 4.1).

Using the overlap function described above, the cage-relative four-point structure factor $\tilde{S}_4(k,t)$ for the *Si* particles is defined as

$$\tilde{S}_4(k,t) = \left\langle \frac{1}{N_{Si}} \tilde{W}(\mathbf{k},t)\tilde{W}(-\mathbf{k},t) \right\rangle , \tag{4.4}$$

where

$$\tilde{W}(\mathbf{k},t) = \sum_{j=1}^{N_{Si}} \tilde{w}_j(t) e^{-i\mathbf{k}\cdot\mathbf{r}_j(0)} . \tag{4.5}$$

From the cage-relative four-point structure factor we extract a dynamic correlation length ξ_d fitting $\tilde{S}_4(k,\tau_\alpha)$ at small k with a Ornstein-Zernicke function [176]

$$\tilde{S}_4(k,\tau_\alpha) = \frac{S_0}{1+(\xi_d k)^2} . \tag{4.6}$$

The fitting range is $[0; 1.5/\xi_d]$ for $T \leq 0.125$, while for higher temperatures we fix it to $[0; 0.5]$. We also tested more complex fitting functions [176], without significant changes in the final results.

In Fig. 4.5 (a), we present $\tilde{S}_4(k,\tau_\alpha)$ as a function of the temperature. The value of the four-point structure factor as $k \to 0$ increases with decreasing temperature, due to the progressively more heterogeneous dynamics at lower temperatures. In the same figure we also show three examples of the fitting function for the curves at high ($T = 0.0200$), intermediate ($T = 0.0111$) and low ($T = 0.0067$) temperature. Despite the large size of the system considered ($N = 10^5$), which allows us to calculate the structure factor up to small k values, at low temperatures the curves do not present a clear plateau as $k \to 0$, making the fitting procedure potentially inaccurate in this region.

In Fig. 4.5 (b), we compare the evolution with temperature of the dynamic correlation length ξ_d with two static correlation lengths associated to the translational ξ_{RDF} and orientational ξ_3 degrees of freedom, already presented in Sec. 4.1.1. Clearly, the typical length scale of the dynamical regions increases much more rapidly that

[7] A similar analysis was performed focusing on the *O* particles and using $\delta = 0.35$ Å, obtaining results similar to the one discussed in this subsection.

[8] To simplify the notation in this subsection, we will henceforth denote $\tau_\alpha(k_2)$ simply as τ_α.

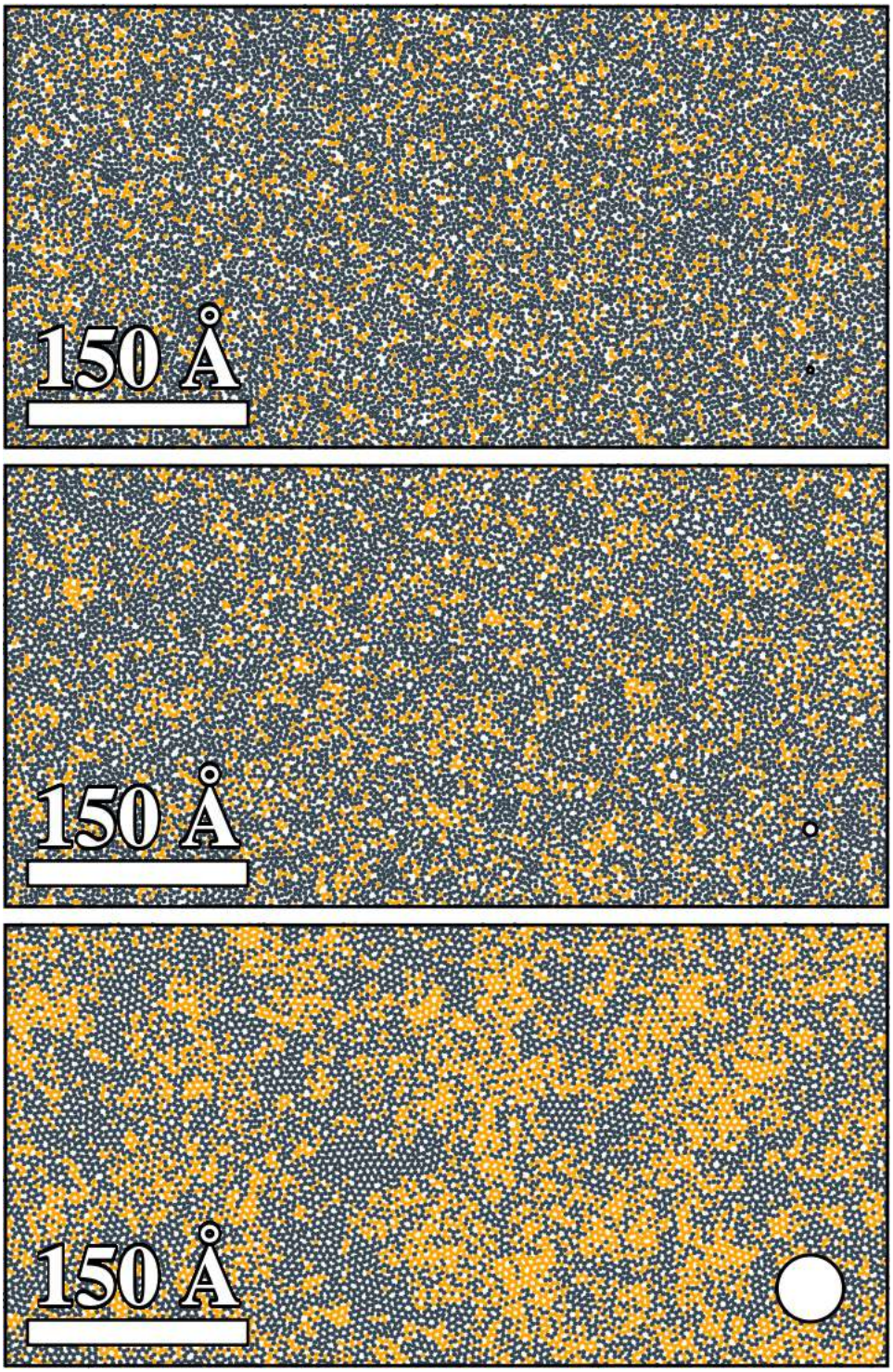

FIGURE 4.4: Snapshots illustrating the development of dynamical heterogeneities. The particles are color-coded according to their value of the cage-relative overlap function evaluated at $t = \tau_\alpha$, with black and orange particles corresponding to slow ($\tilde{w}_i(t) = 0$) and fast ($\tilde{w}_i(t) = 1$) rearranging particles, respectively. Only *Si* particles are shown. The configurations are taken at temperature $T = 0.0250$, 0.0143 ($\approx T_x$), and 0.0067 (from top to bottom). The white circle in the lower right corner of each configuration has a radius equal to the dynamic correlation length at the corresponding temperature. Note that the scale in this figure is three times that of Fig. 4.1.

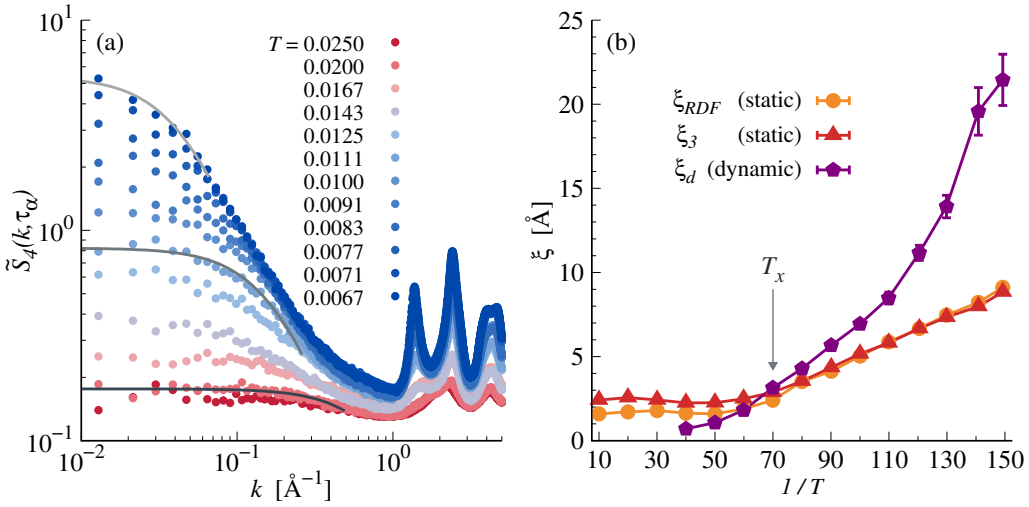

FIGURE 4.5: (a) Four-point structure factor at different temperatures. Black, grey and light grey lines are fit with a Ornstein-Zernicke function for the curves at $T = 0.0200$, $T = 0.0111$ and $T = 0.0067$, respectively. (b) Comparison of static (ξ_{RDf} and ξ_3) and dynamic (ξ_d) correlation lengths at different temperatures. The data presented are calculated for a system of $N = 10^5$ particles.

the static correlation lengths[9], with their ratio exceeding two at the lowest temperature considered. This result implies that crystalline regions cannot be the sole cause of the dynamical heterogeneities in the system. If this were the case, we would expect ξ_d and ξ_3 to scale together as the temperature decreases. However, we cannot fully rule out a relation between crystallites and slow rearranging regions. For example, at low temperatures several neighboring crystallites might behave as a single slow rearranging region. This might be due to a greater stability of the boundaries between different crystallites compared to the more disordered regions[10].

The features of dynamic heterogeneities in 2d silica appear qualitatively different than those of other models of two-dimensional glass-forming liquids, in which the dynamic and orientational correlation lengths grow together with decreasing temperature and much more rapidly than ξ_{RDF} [174, 177]. We have no clear explanation for this behavior, which might be due to the difference in density and average number of neighbors between our system and those previously studied in the literature. Furthermore, as remarked at the end of Sec. 4.1.1, for a set of crystalline domains separated by amorphous regions, orientational and translational order are expected to increase together with decreasing temperature $\xi_3 \sim \xi_{RDF}$ [175]. Our results indicate that network-forming liquids behave differently than close-packed liquids in two dimensions, even more so than than their three-dimensional counterparts [178].

4.1.3 Structure-dynamics correlations in the iso-configurational ensemble

To assess the correlation between structure and dynamics at a microscopic level, we rely on the so-called iso-configurational ensemble [179]. In this approach, an ensemble of N_{sim} trajectories is generated starting from the same atomic configuration, using velocities drawn from the Maxwell-Boltzmann distribution at the appropriate

[9] Our data for ξ_d can be fitted equally well with a function that grows polynomially ($\xi_d \sim T^{-\alpha}$) or exponentially ($\xi_d \sim \exp(\beta/T)$) with temperature. More precise measurements would be required to determine the analytical behavior of this correlation length as a function of temperature.

[10] The microscopic connection between structure and dynamics will be analyzed in the iso-configurational ensemble in Sec. 4.1.3.

temperature. The quantify of interest is the dynamic propensity of a particle $p_i(t)$, defined as the mean square displacement of the particle, averaged over the different N_{sim} trajectories, $p_i(t) = \langle |\Delta \mathbf{r}_i^2| \rangle_{iso}$, where $\langle \cdot \rangle_{iso}$ indicate the average over the ensemble of trajectories. Unlike standard simulations in the NVT ensemble, this approach allows one to precisely assess how much the dynamical heterogeneities at time t is due to the structure of the system at the initial time [179]. For example, the spatial distribution of the propensity of motion can be compared with that of a structural indicator to assess to what extent the two are correlated, as shown in Fig. 4.6. Alternatively, the dynamic propensity can be fitted using a more complex descriptor of the local structure of the system. Interpretable statistical models can then be used to understand which structural property is most strongly associated with fast- or slow-rearranging particles [180].

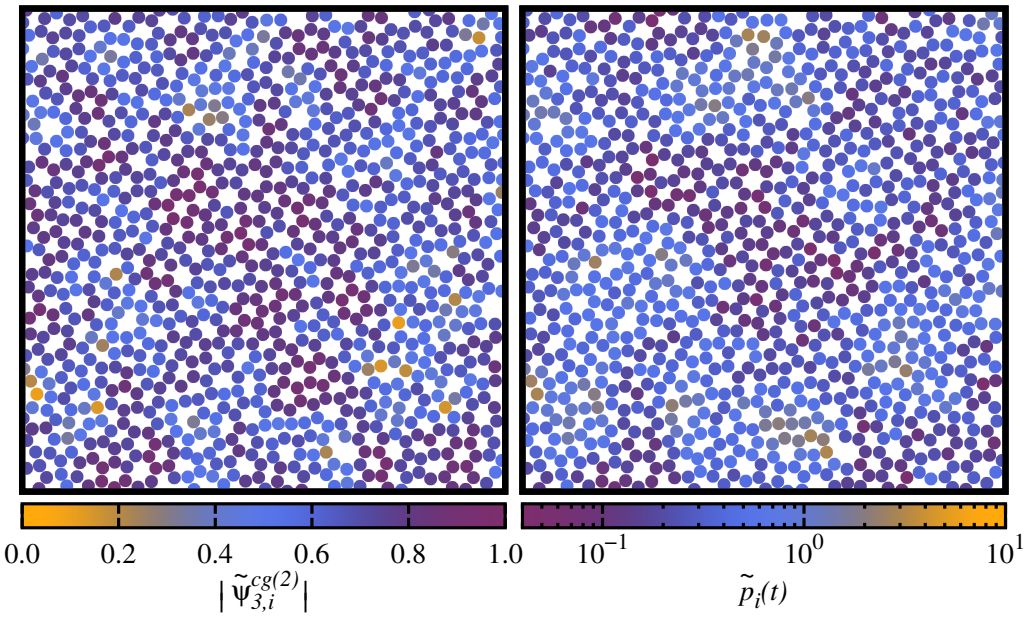

FIGURE 4.6: Snapshots comparing the degree of local crystalline order (left) and the dynamic propensity (right). The degree of local crystalline order is quantified with the module of the local order parameter $\tilde{\psi}_{3,i}^{cg(2)}$, and the cage-relative dynamic propensity $\tilde{p}_i(t)$ evaluated at time $t = 0.09\tau_\alpha$, when the correlation with the structure is strongest, see Fig. 4.7. Only *Si* particles are shown.

Since the calculation of the dynamic propensity involves the displacement of a particle, it is affected by long-wavelength fluctuations, see Sec. 1.3.1. We thus compute the cage-relative version of the dynamic propensity $\tilde{p}_i(t)$, removing from the displacement of the particle the displacement of its neighbors. We evaluate the propensity of motion starting from 10 different configurations of 2880 particles in thermal equilibrium at temperature $T = 0.0100$. For each configuration we generate an set of 100 trajectories in the NVT ensemble[11], over which the iso-configurational average is performed.

In Fig. 4.7 we show the Pearson correlation coefficient [181] between the cage-relative dynamic propensity at time t and several local order parameters, which capture both the local crystalline order (ψ_3, $\psi_3^{cg(1)}$, $\psi_3^{cg(2)}$ and $\tilde{\psi}_3^{cg(2)}$) and typical coordination defects (ψ_4). The two vertical lines identify the start (τ_β) and the end (τ_α) of the intermediate plateau in the MSD, respectively. The time interval between τ_β and

[11] For the computational details on the simulations, refer to Sec. 2.1.2.

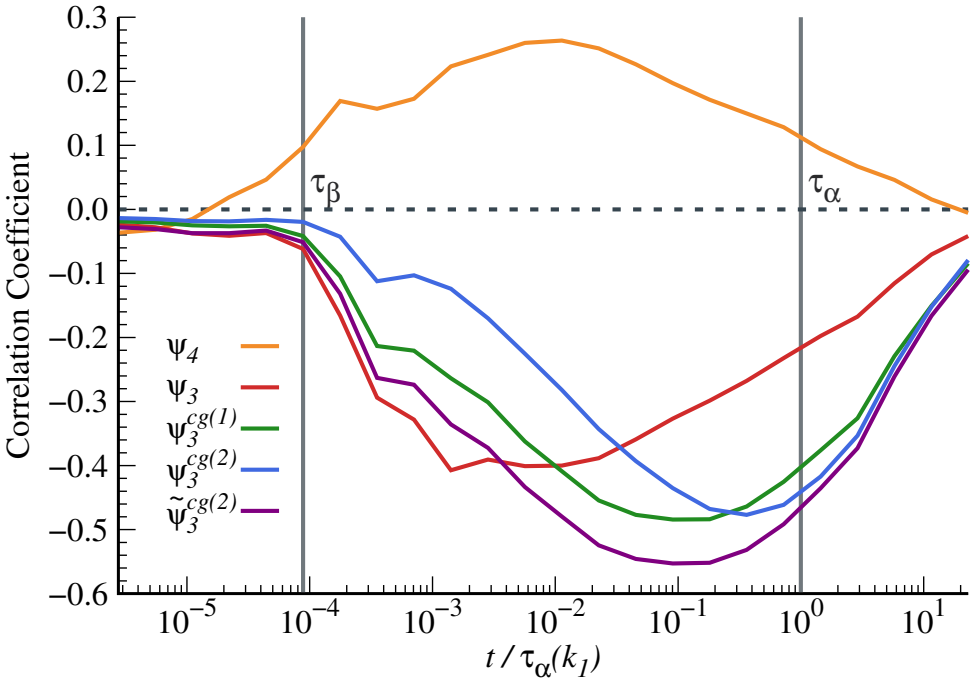

FIGURE 4.7: Correlation coefficient between the cage-relative dynamic propensity and different local orientational order parameters as a function of time. The local order parameters used are sensitive to both the local crystalline order (ψ_3, $\psi_3^{cg(1)}$, $\psi_3^{cg(2)}$ and $\tilde{\psi}_3^{cg(2)}$) and typical coordination defects (ψ_4). Two vertical lines identify the start (τ_β) and the end (τ_α) of the intermediate plateau in the MSD. The curves are the averaged over 10 different configurations of $N = 2880$ particles.

τ_α shows the strongest correlations. Focusing on this regime, we observe a small positive correlation between the propensity and ψ_4, and a clear anticorrelation between the propensity and the local order parameters associated with the local crystalline order. The correlation coefficients with the coarse-grained 3-fold order parameters reach a maximum at later times than the bare one, and exhibit a stronger anticorrelation with the propensity. This effect is observed in particular for $\tilde{\psi}_3^{cg(2)}$, and it is likely due to the larger regions considered in its calculation, which make it more sensitive to the medium-range order. In this regard, the anticorrelation between propensity and coarse-grained order parameters indicates that particles within crystallites tend to be slow rearranging particles in the dynamics. This is expected, since crystalline regions have a lower energy than their disordered surroundings and are thus more stable. However, as depicted in Fig 4.6, the anticorrelation between propensity and local crystalline order is rather modest, reaching at most -0.55[12]. This suggests that, although crystalline domains are slower regions of the dynamics, they cannot fully explain the dynamical slow down, supporting the results of our analysis of the correlation lenghts.

Since individual physically motivated parameters cannot fully describe the behavior of the propensity, we turn to a more systematic set of structural descriptors. We consider a set of orientational order parameters for a n-fold symmetry, with

[12]Note that our analysis is performed at $T = 0.0100$ which is not the lowest temperature at which we can equilibrate our system. At lower temperatures we expect a stronger anticorrelation between the propensity and the local crystalline order.

$n \in [2; 18]$. The order parameters are computed considering all the possible combination of neighbors types. For each raw order parameter ψ_n we obtain the coarse-grained parameters $\psi_n^{cg(1)}$, $\psi_n^{cg(2)}$ and $\psi_n^{cg(3)}$, averaging ψ_n over the first, second and third coarse-grained shell, respectively. Thus, the final set of descriptor contains 138 local order parameters for each atomic species, which capture different local symmetries at various distances. We use this set of descriptors to fit the propensity using an ordinary least square regression [182]. The resulting fitting function is only modestly correlated with the propensity, with a correlation coefficient of 0.57 and 0.44 for *Si* and *O* particles, respectively. The largest weights in the fitting function for silicons are assigned to the 3-fold order parameters averaged over the first and the third coordination shell, while the weights for oxygens show no clear preference for any structural descriptor.

A larger set of orientational descriptors is thus unable to significantly improve the prediction of the dynamic propensity compared to the simple $\tilde{\psi}_3^{cg(2)}$. This might be due to the lack of new information added by the broader set of descriptors compared to the set of 3-fold local order parameters. In fact, for *Si* particles, with the exception of the descriptors based on ψ_3, all other order parameters capture symmetries not present in our system, and thus do not provide any additional information about its local structure. For *O* particles meanwhile, it can be argued that orientational order parameter as defined in Eq. 4.1 cannot properly describe their local environment. In the crystal, the arrangement of *Si* and *O* particles around an oxygen has a rectangular symmetry, with an aspect ratio of $\sqrt{3}$. However, the bond order parameter defined in Eq. 4.1 captures only radially symmetrical arrangements and thus cannot describe asymmetric environments such as those of the oxygens. This is reflected in the absence of dominant weights in the fitting function for the oxygens.

Due to the presence of large crystalline domains and huge correlation times at low temperatures, we expect a strong correlation between structure and dynamics in our system. The results of this section, however, suggest that a small set of simple structural descriptors are unable to fully capture such correlations. We think that the use of more complex and flexible approaches, such as those based on unsupervised learning [183], can significantly improve our results.

4.2 Effect of the substrate on the structure and dynamics

Many two-dimensional systems do not form strong covalent bonds with their substrates. Thus only weak van der Waals forces bind the overlayer and substrate together. It is generally expected that such weak interactions allow the overlayer to be threated as free-standing [43, 126, 128, 130, 133, 184, 185]. This is corroborated by the small variations in the electronic properties and the structure of the free-standing and supported system [126], see for example Sec. 6.1.3. The observation that the deposited material can form crystalline patches with different orientation or produce an amorphous layer [28, 43], further supports the hypothesis that the periodicity of the underlying substrate does not strongly affect the overlayer.

However, the behavior of these systems deposited on a substate is not as simple as it might seem at first glance. For example, *ab initio* calculations have shown that weak van der Waals interactions with the substrate can change the lowest energy structure of a germania bilayer [48] and can significantly reduce the activation energy of elementary rearrangements in the silica bilayer [27, 163]. Furthermore, the same systems can form crystalline, polycrystalline or amorphous layers on the same

substrate using different synthesis procedure [47, 173], or they can produce a similar amorphous structure when deposited on different substrates [28, 126]. Moreover, the growth of specific structures of the overlayer have been correlated with the oxygen affinity, the strain and the adhesion energy of the film to the substrate [20, 25, 28]. Nevertheless, to the best of our knowledge, no simple computational model has been proposed to study these effects in a controlled environment.

4.2.1 Model

Liquids deposited on substrates or confined inside nanochannels can be modelled in several ways. These generally assume the confining walls to be smooth planes [186, 187] or surfaces consisting of pinned point particles [188–190]. We use the latter approach, assuming the substrate particles are frozen in their equilibrium positions and ignoring contributions form out-of-plane forces, thus maintaining a strictly two-dimensional overlayer. This approach allows us to directly compare the properties of the system with and without the substrate, which acts as an external periodic potential.

Since the substrate particles positions are fixed at their respective lattice sites and the out-of-plane forces are ignored, it is too computationally expensive to compute the interaction between each particle of the overlayer and all the substrate particles. A better approach is to describe the interaction with the substrate as an external periodic potential acting on the overlayer particles.

We thus develop a new interaction model for the efficient simulation of a $2d$ system on a substrate. We assume that the interaction between overlayer and substrate is mainly due to the topmost layer of the latter. The set of particle positions in this topmost layer, projected on the $2d$ plane, is

$$Latt(\mathbf{a_1}, \mathbf{a_2}) = \{n\,\mathbf{a_1} + m\,\mathbf{a_2} \mid n, m \in \mathbb{Z}\}\ , \tag{4.7}$$

where $\mathbf{a_1}$ and $\mathbf{a_2}$ are the lattice vectors describing the topmost layer of the substrate. We further assume that the interactions between the overlayer and the substrate are the same for all atomic species and depend only on the distance between the particles of the two systems. In this framework, the addition of a substrate corresponds to the addition of an external field

$$U_{sub}(\mathbf{r}) = A \sum_{\mathbf{R} \in Latt(\mathbf{a_1}, \mathbf{a_2})} e^{-\left(\frac{|\mathbf{r}-\mathbf{R}|}{k}\right)^2}\ , \tag{4.8}$$

where A is the energy scale of the interaction between the overlayer and substrate and k regulates the range of influence of a single substrate lattice site.

Experimental samples of the amorphous silica bilayer have been grown on graphene [18], *Ru(0001)* [22] and *Pt(111)* [23]. The topmost layer of these substrates has an hexagonal symmetry with lattice parameter a of 2.46 Å (graphene), 2.70 Å (*Ru(0001)*) and 2.77 Å (*Pt(111)*) [28] [13]. Thus, the particles of the substrate occupy the sites of a hexagonal lattice described by $Hex(a)$. We assume that the particles of the overlayer tend to be pinned by the atoms in the substrate, *i.e.* $A < 0$. Since we expect a weak interaction between substrate and silica bilayer, we set the energy scale A to a fraction $f < 1$ of the potential energy per particle in the inherent structures of the

[13] Note that the lattice parameter for a free-standing silica bilayer is approximately 5.28 Å [24].

free-standing system $e^0_{IS}(T)$[14]. Therefore, the substrate potential we consider in this work is

$$U_{sub}(\mathbf{r}; a, f, k, T) = -f \cdot e^0_{IS}(T) \cdot \sum_{\mathbf{R} \in Hex(a)} e^{-\left(\frac{|\mathbf{r}-\mathbf{R}|}{k}\right)^2}. \tag{4.9}$$

Since we are mainly interested in changes in the structure and dynamics of the overlayer due to variations in the substrate lattice parameter a and its interaction strength f, we reduce the parameters of the model by fixing $k = \frac{a}{5\sqrt{\ln 2}}$. This value of k is such that the interaction due to a single lattice site at $\mathbf{R}$ is half of its maximum value when $|\mathbf{r} - \mathbf{R}| = a/5$. Thus, this value is appropriate for substrates where the source of interaction with the overlayer is strongly localized to the lattice sites of the substrate. For example, when $|\mathbf{r} - \mathbf{R}| = a/2$ the interaction becomes almost negligible, being ~ 0.013 of its maximum value.

The main advantages of our effective model for the substrate are that it does not require additional degrees of freedom in the simulation and maintains a strict $2d$ geometry for the overlayer. Moreover, the calculation of the substrate field $U_{sub}(\mathbf{r})$ can be implemented efficiently if the particles positions are folded into the substrate unit cell before evaluating energies and forces. Since this process involves only matrix multiplication and floor operations, it is computationally cheap. A possible disadvantage of our approach is that it is difficult to include the thermal motion of the atoms of the substrate. Including this effect could be relevant when studying the synthesis process, but it is beyond the scope of this work.

4.2.2 Classification of the substrates varying the interaction stregth

Let us first focus on how the structure and dynamics of the system change when the interaction strength f between the substrate and the overlayer is varied. We consider a system of 2880 particles in a rectangular box[15], and we consider 12 different hexagonal substrates with lattice parameters in the range $[1.32;\ 5.76]$ Å[16]. For each substrate we consider 10 different interaction strengths in the range $f \in [0.00;\ 0.10]$. Simulations are performed in thermal equilibrium at temperature $T = 0.0100$, see Appendix A for details on the simulation parameters and the equilibration procedure. We have analyzed in detail the structure and dynamics of the overlayer in the presence of a substrate, and below we present a selection of results, which are supported by a more in-depth analysis.

By carefully comparing the structure and dynamics produced by the different substrates, we identified four different types of substrates:

[14] It is doubtful that the interaction between overlayer and substrate has the same temperature variations as $e^0_{IS}(T)$, and a more careful analysis would be needed to understand how this interaction might behave as the temperature varies. In our analysis, however, this assumption is relevant only in Sec. 4.2.3, where we study the glassy dynamics of the systems at different temperatures. Moreover, from preliminary studies, we found that our conclusions do not change if we set the interaction strength between the overlayer and the substrate at a constant value, independent on the temperature and close to $e^0_{IS}(T = 0.0100)$.

[15] Due to periodic boundary conditions, the size of the simulation cell strongly influences the number of commensurate substrates that can be considered. We chose the size of the cell according to the lattice parameter of the overlayer, thus, in this approach, the number of possible commensurate substrates is related to the number of unit cells of the overlayer. We found useful to set the number of overlayer unit cells as the product of two highly composite numbers, to allow the system to be simulated on a large number of possible substrates. For example, a system of 2880 particles (24×24 unit cells) allows 63 different commensurate hexagonal substrates with lattice parameters $a > 1$ Å. Instead, for a system of 2200 particles (20×22 unit cells) there are only 5 different substrates that satisfy the same constraint.

[16] For simplicity of exposition, we will always round the lattice parameters to two decimal digits.

- **Type I: Substrates that strongly affect the overlayer**
  Substrate lattice parameter: $a = 2.64, 5.28$ Å.
  This class consists of substrates which strongly enhance the crystalline order in the overlayer for almost any value of the interaction strength f. Thus, as f increases, these substrates induce a significant increase in relaxation times, and the structure of the overlayer starts to exhibit features similar to those of the crystal. This kind of behavior is exemplified in Fig. 4.8 (a), where, even for small values of f, the RDF develops sharp peaks at the typical distances of the crystal. Furthermore, the sharp appearance of a single preferred direction in the distribution of the local order parameter, as shown in Fig. 4.8 (b), indicates the emergence of a single crystalline domain in the system. Substrates belonging to this class generally have a lattice parameter that divides the lattice parameter of the free-standing system ($a_{2d\,SiO_2} = 5.28$ Å) without any remainder. Thus, these substrates strongly enhance the crystalline order even at small values of f because a crystalline overlayer has a strong overlap with the substrate lattice sites, resulting in a decrease of the total energy. Moreover, since the lattice parameter is a multiple of that of the substrate, there are no internal stresses on the structure of the overlayer induced by the substrate[17].

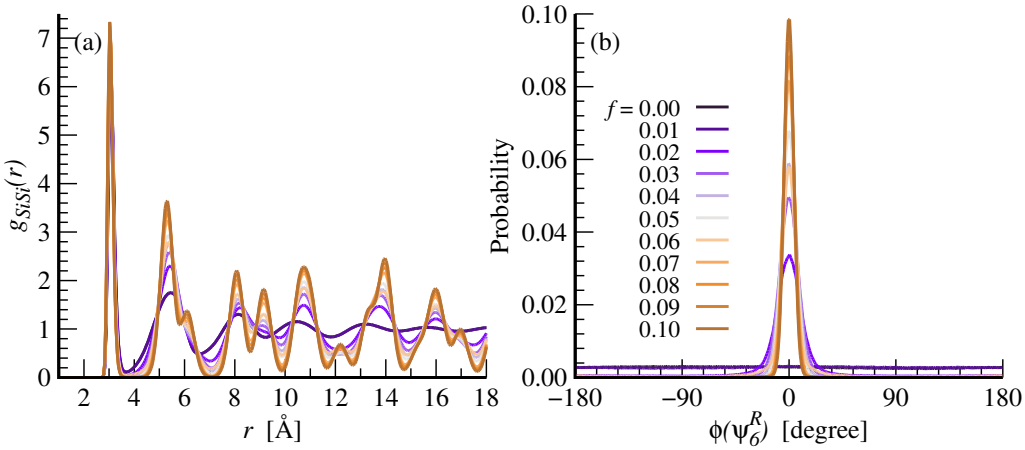

FIGURE 4.8: Structural data for simulations with a type I substrate, with lattice parameter $a = 2.64$ Å. (a) Radial distribution function between *Si-Si* particles as a function of the interaction strength f between overlayer and substrate. (b) Phase distribution of the local order parameter ψ_6^R for a 6-fold symmetry between the rings as a function of f.

- **Type II: Substrates that weakly affect the overlayer up to a threshold strength**
  Substrate lattice parameter: $a = 1.32, 1.35, 2.54, 2.76, 3.02, 5.76$ Å.
  This is the most common class of substrates in our analysis. The substrates in this class weakly affect the structure and dynamics of the overlayer for small values of the interaction strength f, which thus resemble those of the free-standing system. However, when the interaction strength exceeds a certain threshold, these substrates start to strongly influence the properties of the overlayer similarly to the type I substrates, see for example Fig. 4.9 (b). At high values of f, these substrates enhance the local order of the system and induce a substantial slowdown of its dynamics, as shown in Fig. 4.9 (a). Moreover, the phase of the local order parameter shows a single preferred direction for

[17] We present as M4.2 in Appendix E a video showing the out-of-equilibrium trajectory on a substrate in this class.

the local environments in the system, as depicted in Fig. 4.9 (b). We think that the dynamics slowdown at high values of f is due to pinning and stabilization of local crystalline domains induced by the substrate periodic potential. However, since there is a mismatch between the lattice parameter of substrate and overlayer, the formation of large crystalline domains requires the overcome of internal stresses and occurs only if the interaction strength between substrate and overlayer is high enough to make the process energetically favorable[18].

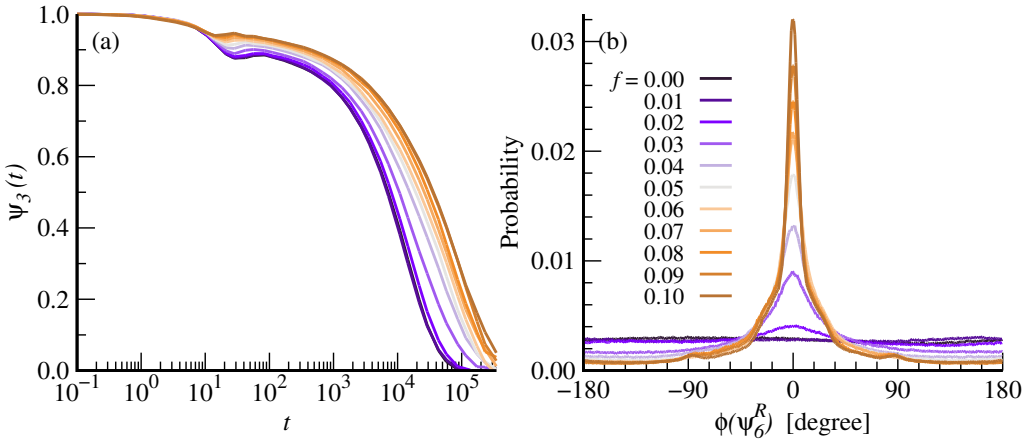

FIGURE 4.9: Structural and dynamical data for simulations with a type II substrate, with lattice parameter $a = 2.76$ Å. (a) Time-dependent correlation function for the orientation degrees of freedom $\Psi_3(t)$ as a function of the interaction strength f between overlayer and substrate. (b) Distribution of the phase of the local order parameter ψ_6^R for a 6-fold symmetry between the rings as a function of f.

- **Type III: Substrates which stabilize multiple crystalline orientations**
  Substrate lattice parameter: $a = 2.11$ Å.
  Substrates in this class induce no major changes in the RDFs or the ring statistics of the overlayer when increasing the interaction strength f. Moreover, increasing f, they display a moderate increase in the correlation times, which are generally lower than those observed for type I and II substrates[19]. The distribution of the module of the local order parameter shows a small increase in the degree of local order, see Fig. 4.10 (a), which is significantly smaller than that of type II substrates. The main feature of these substrates is their ability to stabilize multiple crystalline orientations, as can be observed by the presence of two peaks in the distribution of the phases of ψ_6^R in Fig. 4.10 (b). Thus, we speculate that the slowdown of the system on these substrates is due to the competition between multiple crystalline orientations, rather than pinning of crystalline domains as is the case for type I and II substrates[20].

- **Type IV: Substrates which decrease the local crystalline order**
  Substrate lattice parameter: $a = 2.88, 3.52, 4.23$ Å.
  Substrates in this class have no significant effect on the dynamics of the overlayer, even at the highest interaction strength considered. While their effect

[18] We present as M4.3, M4.4 and M4.5 in Appendix E, three videos showing the trajectories on the substrate $a = 2.76$ Å for different values of the interaction strength f.

[19] The data concerning the dynamics of these systems as a function of f are not shown. However, in Sec. 4.2.3 we will compare the behavior of the correlation times of systems on type II, III and type IV substrates as a function of temperature.

[20] We present as M4.6 in Appendix E a video showing the trajectory on a substrate in this class.

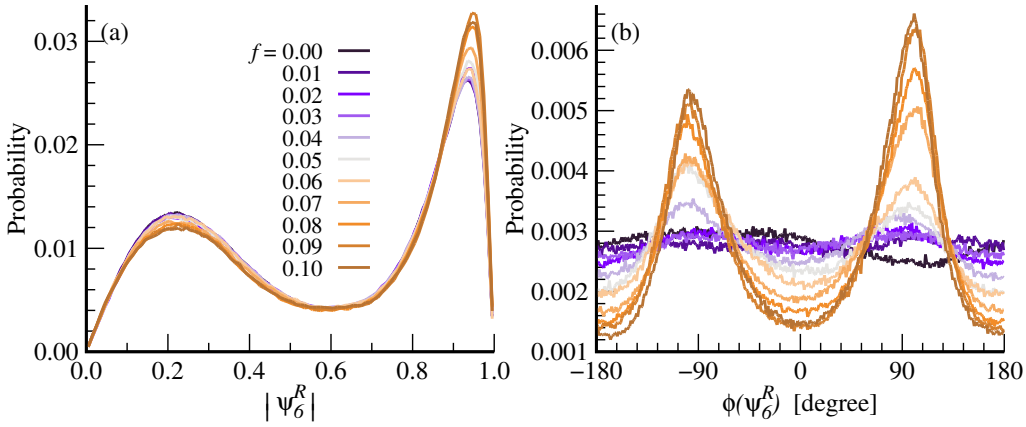

FIGURE 4.10: Structural data for simulations with a type III substrate, with lattice parameter $a = 2.11$ Å. Distribution of the module (a) and phase (b) of the local order parameter ψ_6^R for a 6-fold symmetry between the rings as a function of the interaction strength f between overlayer and substrate.

on the dynamics is negligible, as will be discussed in Sec. 4.2.3, their influence on the structure of the system is subtle but measurable. As f increases, the system displays a decrease in local order. This appears as a decrease in the height of the first peaks in the RDFs and in the fraction of hexagonal rings. Moreover, it is particularly evident in the marked shift of the distribution of the module of the local order parameter toward lower values of the module, as shown in Fig. 4.11 (a). Meanwhile, the phase of the local order parameters displays a single preferred direction, see Fig. 4.11 (b), even though the alignment of the bond-order parameters along that direction is very modest. Thus, the substrates in this class show a surprising trend: *increasing* the interaction strength with the substrate results in a *decrease* in local order, with no apparent impact on the dynamics[21]. This effect might be due to the stabilization of locally favored structures with symmetries different from those of the crystal, but a more detailed analysis is required to fully determine the origin of this behavior[22].

This classification is rather qualitative, and there is some overlap between the different classes. For example, type II substrates may have such a low interaction strength threshold that they behave like type I substrate, which interact strongly for any value of f. It would be ideal to develop a geometric parameter which can be used *a priori* to quantify the overlap between the substrate lattice position and the crystalline structure of the overlayer. However, the different possible translations and rotations of the two lattices make the definition of such parameter non-trivial.

Our analysis shows that even a simple substrate with very weak interaction with the overlayer can significantly influence its structure and dynamics. Moreover, the substrate periodic potential does not simply lead to an increase in order of the overlayer, but can also lead to highly nontrivial effects, such as the stabilization of multiple crystalline orientations or a decrease of local crystalline order. Our results thus

[21] Note that this behavior supports our conclusions of Sec. 4.1, *i.e.* the crystalline domains in the liquid cannot be the sole cause of the dynamic slowdown. Indeed, the system simulated on substrates of this class shows a substantial decrease of local order without major changes in the dynamics.

[22] We present as M4.7 in Appendix E a video showing the trajectory on a substrate in this class.

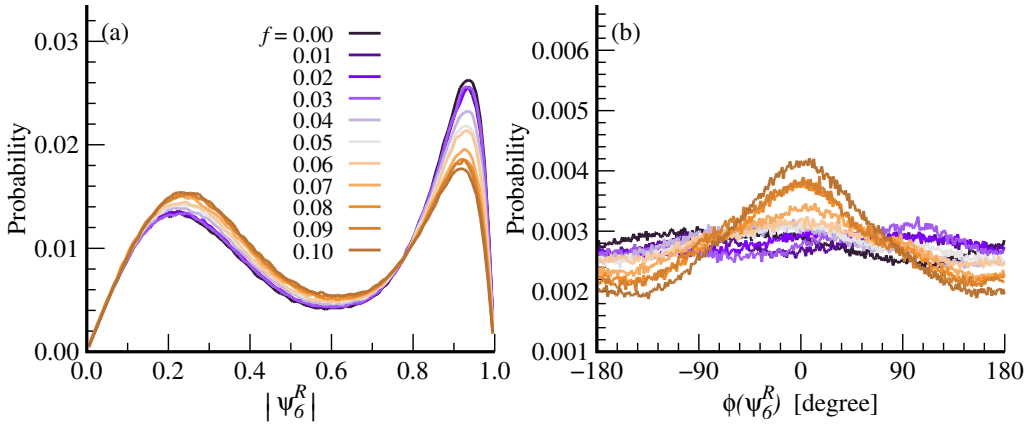

FIGURE 4.11: Structural data for simulations with a type IV substrate, with lattice parameter $a = 4.23$ Å. Distribution of the module (a) and phase (b) of the local order parameter ψ_6^R for a 6-fold symmetry between the rings as a function of the interaction strength f between overlayer and substrate. Note that the ranges in both plots are the same as in Fig. 4.10.

provide a guide to interpret the experimental data, and suggest a more careful analysis of the deposited systems, to assess whether they can indeed be described as free-standing.

4.2.3 Glassy dynamics in the presence of a substrate

We now turn our attention to the glassy dynamics of the 2d silica model on a selected number of substrates. Substrates of type I strongly enhance the crystalline order, thus making it difficult to avoid the crystallization of the overlayer even at high temperature or for low values of the interaction strength f with the substrate. Even if a liquid phase can be stabilized on such substrates, a small decrease in temperature typically causes the complete crystallization of the system. Thus, we decided not to consider these substrates in our analysis. We select instead two substrates of type II, both with lattice parameter $a = 2.76$ Å, using moderate ($f = 0.05$) and high ($f = 0.08$) interaction strengths. We also consider a substrate of type III ($a = 2.11$ Å) and one of type IV ($a = 4.23$ Å), both of which with a relatively high ($f = 0.08$) interaction parameter with the overlayer. For each system, we perform equilibrium NVT simulations with temperatures in the range $T \in [0.1000; 0.0077]$ [23]. For each temperature, we calculate the time-dependent bond-order correlation function $\Psi_3(t)$, as defined in Sec. 3.1.2, from which we extract the correlation time τ_3.

In Fig. 4.12 we show the correlation times of the systems as a function of temperature. Liquids on type II substrates display the greatest difference compared to the free-standing system and exhibit a peculiar dynamic behavior, reminiscent of the fragile-to-strong crossover in water [191]. For such substrates, we can qualitatively identify three different temperature regimes. At high temperatures, the system does not feel the presence of the substrate, since its dynamics is mainly ruled by short-range interactions and collisions between particles, and it thus behaves like a hot liquid. At intermediate temperatures, the system starts to feel the presence

[23] Note that while we menaged to equilibrate the free-standing system down to $T = 0.0067$, we were unable to equilibrate all the systems considered in this subsection below the lowest temperature $T = 0.0077$. This is due to the combination of various effects, such as the higher relaxation times due to the substrate, the higher computational cost of these simulations compared to the free-standing ones and the more limited computational resources available for this study.

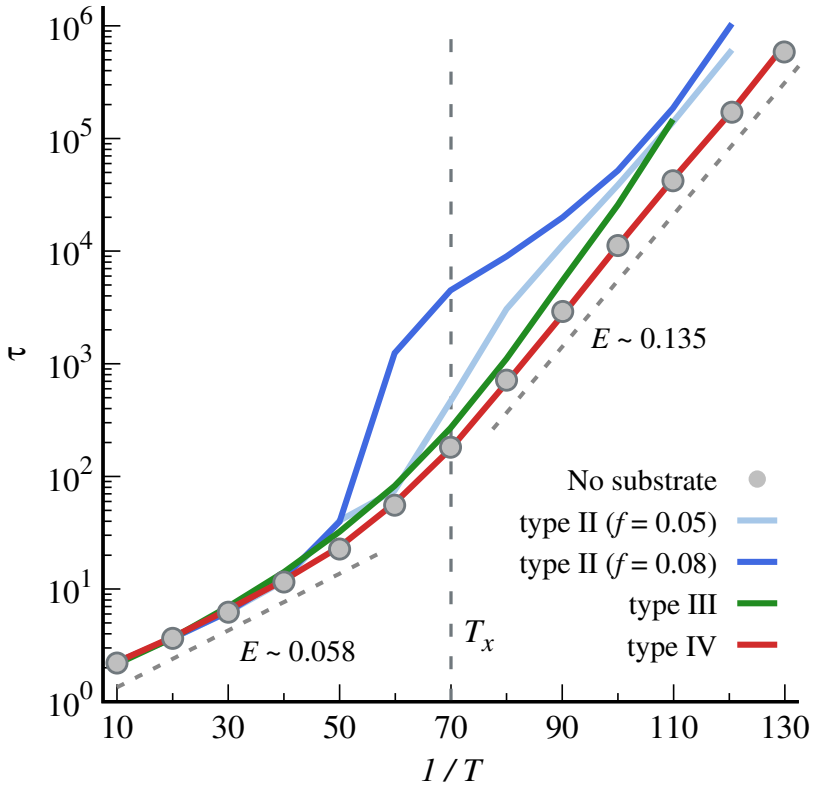

FIGURE 4.12: Correlation times of the bond-order correlation function for different systems with and without substrates. The substrates considered are of type II ($a = 2.76$ Å) both at moderate ($f = 0.05$, pastel blue) and high ($f = 0.08$, blue) interaction parameter, type III ($a = 2.11$ Å, $f = 0.08$, green) and type IV ($a = 4.23$ Å, $f = 0.08$, red). The correlation times for the system without substrate are identified with grey points. Quantities in the presence of a substrate are calculated for $N = 2880$ particles, while those for the free-standing system are evaluated with a $N = 10^5$ particles system.

of the substrate and there is an increase in the degree of local order and correlation times compared to the system without a substrate. This regime is rather broad and roughly coincide with the crossover region between the two Arrhenius behaviors of the free-standing system identified in Sec. 3.1.3. Thus, the system is most affected by the presence of a substrate around the temperature T_x where the network structure starts to form in the liquid. This might be due to the local pinning a small set of particles at the substrate sites, which favors the formation of the network at temperatures higher than that of the free-standing liquid. From Fig. 4.12 we also see that increasing f leads to longer correlation times and a sharper transition to a network liquid, which supports our explanation. Finally, at low temperatures the correlation times in the presence of the substrate appear to follow an Arrhenius law with the same free energy activation barrier as the free-standing case, with no major changes for different values of the interaction strength. This might be an artifact of the small number of data points available in this regime, or it could suggest that the activation energy barrier for the elementary relaxations in the systems are much higher than the interaction strength f between overlayer and substrate.

While the behavior of type II substrates in Fig. 4.12 is very rich, substrates of types III and IV show only a moderate difference from the free-standing case. Simulations with type III substrates produce correlation times with a T-dependence similar to those without the substrate. Still, the dynamics slows down appreciably more

in the presence of the substrate, especially at low temperatures. At low temperatures, the correlation times seems to follow an Arrhenius law with a slightly higher free-energy activation barrier than that of the system without a substrate. As shown in Fig. 4.10 (b), substrates of type III stabilize multiple crystalline orientations. We thus speculate that the elementary relaxations are hindered because they involve the conversion of patches of particles from one crystalline orientation to another. A more careful analysis of the dynamics at low temperatures is required to test this hypothesis.

Finally, we discuss the behavior of the systems on a type IV substrate. Surprisingly, these simulations reproduce the correlation times of the free-standing system almost perfectly, with only a minor increase of τ_3 that never exceeds 15 % of its value in the absence of a substrate. Currently, we do not have a clear explanation as to why the overlayer does not significantly change its properties when simulated on these types of substrates, and a more detailed analysis is required to fully understand this unusual behavior. However, assuming substrates of this type can be realized experimentally, they represent a promising prospect for the synthesis and characterization of amorphous samples, since on them the overlayer behaves as a truly free-standing system.

4.2.4 Structure-dynamics correlations in the presence of a substrate

As discussed in Sec. 4.2.2, the presence of a periodic substrate typically enhances the local crystalline order of the overlayer and generates a set of preferred alignments for the bond-order parameters. To assess whether this increase in local crystalline order has a direct effect on the dynamics of the system, we study a selection of systems on different substrates in the iso-configurational ensemble.

We select systems simulated on three different substrates of type II ($a = 2.76$ Å, $f = 0.05$), III ($a = 2.11$ Å, $f = 0.08$) and IV ($a = 4.23$ Å, $f = 0.08$). Type I substrates are not considered in this analysis since they induce the immediate crystallization of the overlayer. For each system, we evaluate the cage-relative dynamic propensity at temperature $T = 0.0100$ and we calculate its correlation coefficient with a set of structural descriptors as a function of time. The computational details for the calculation of the dynamic propensity are the same as in Sec. 4.1.3. Namely, we consider 10 independent configurations for each system and we average the propensity on an ensemble of 100 trajectories for each configuration. As discussed in Sec. 4.1.3, in the free-standing system the propensity is moderately anticorrelated with the local order parameters for a crystalline ordering ($\tilde{\psi}_3^{cg(2)}$), and weakly correlated with the bond-order parameter for the typical coordination defects (ψ_4). Thus, we use these parameters as structural descriptors. We also calculate the correlation coefficient between the propensity and potential energy due to the interaction with the substrate for both silicons (u_{sub}^{Si}) and oxygens (u_{sub}^{O}) particles. This latter quantity allows us to assess whether the substrate periodic potential tends to pin the overlayer particles to the substrate lattice sites.

In Fig. 4.13 we show the correlation coefficients between the cage-relative propensity at a time t and a set of structural descriptors. Simulations with a type II substrate enhance the correlation between the propensity and local crystalline order parameters. The same holds for the correlation with ψ_4, which quantifies defective local environments. However, all these correlations are still modest, the largest being the one between propensity and local crystalline order, equal to -0.68. Moreover, even if the correlations are stronger for the system with the substrate compared to ones without, their increase is much more modest than what can be expected from the

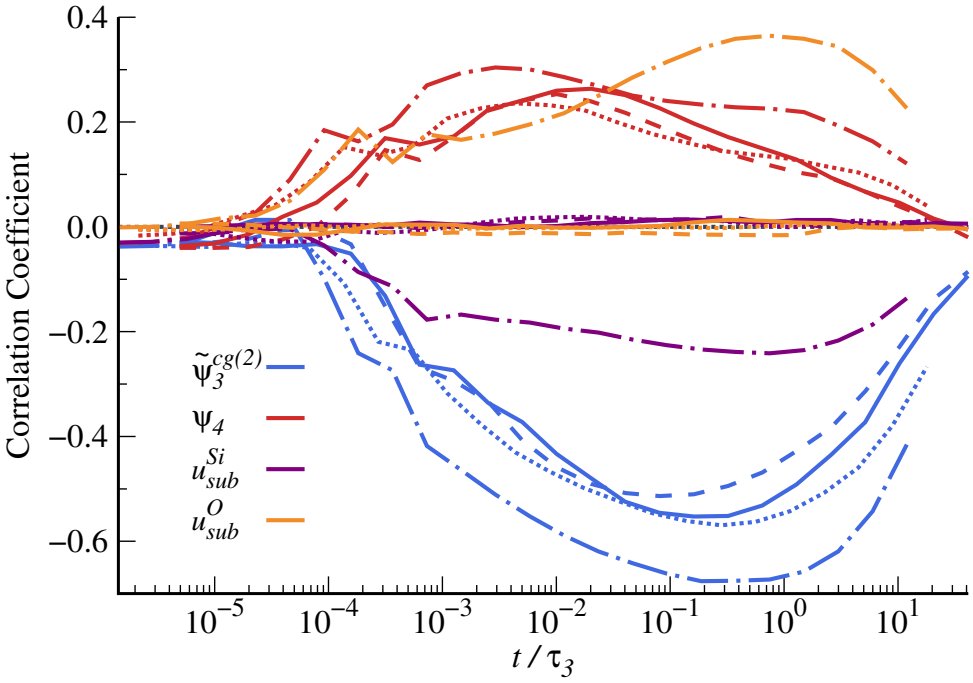

FIGURE 4.13: Correlation coefficient between the cage-relative propensity and different structural parameters as a function of time for systems with and without substrates. The structural parameters used are sensitive to local crystalline order ($\tilde{\psi}_3^{cg(2)}$) and typical coordination defects (ψ_4). We also use as structural indicator the potential energy due to the interaction with the substrate for both silicons (u_{sub}^{Si}) and oxygens (u_{sub}^{O}) particles. The systems considered are without substrate (full curve), or with a substrate of type II ($a = 2.76$ Å, $f = 0.05$, line-dot-line curve), III ($a = 2.11$ Å, $f = 0.08$, dotted curve) or IV ($a = 4.23$ Å, $f = 0.08$, dashed curve). For each system, the time is rescaled with the respective correlation time τ_3 associated to the decay of the orientational degrees of freedom. The curves are the averaged over 10 different configurations of $N = 2880$ particles.

increased dynamic slowdown and the strong increase of local crystalline order observed in Fig. 4.9. This further support our conclusion in Sec. 4.1, *i.e.* the emergence of large crystalline patches is correlated with the dynamic slowdown, but it is not solely responsible of it. In Fig. 4.13 we also observe for the simulations with a type II substrate a weak correlation between propensity and the energy of the *O* particles due to the interactions with the substrate. For the *Si* particles we observe instead a weak anticorrelation. These observations suggest that the overlayer particles are pinned by the potential wells due to the substrate. Since the potential energy induced by the substrate is negative, see Sec. 4.2.1, the positive correlation between propensity and u_{sub}^{O} means that mobile *O* particles tend to be far from the substrate lattice sites. Conversely, the negative correlation between propensity and u_{sub}^{Si} means that mobile *Si* particles tend to reside close to the substrate lattice sites. This apparently bizarre behavior can be rationalized as follows. The lattice parameter of the substrate considered ($a = 2.76$ Å) is close to half the lattice parameter of the free-standing overlayer ($a_{2d\,SiO_2} = 5.28$ Å). The unit cell of silica bilayer projected onto the plane contains many oxygens whose distance is exactly half of the lattice parameter $a_{2d\,SiO_2}$. Thus, when the system is simulated on this substrate, placing the oxygens close to the substrates lattice sites produces a lower energy than placing the silicons close to these sites. Therefore, we expect the *O* particles to reside close to

the substrate lattice sites and to be more affected by the potential wells due to the underlying substrate, in agreement with the data in Fig. 4.13.

While the correlation coefficients for the system on a type II substrate show some differences compared to the free-standing case, simulations with types III and IV substrates do not. Simulations with both substrates display no major changes in the correlation coefficients compared to the ones without a substrate. The only difference we observed is that type IV substrates slightly reduce the anticorrelation between propensity and local crystalline order, in agreement with the data in Fig. 4.11, but this effect can be due to limited statistics. Surprisingly, simulations with both types of substrates show no correlation between propensity and potential energy per particle due to the interaction with the substrate. Thus, the pinning of the overlayer particles to the substrate lattice sites does not affect the mobility of the system in any measurable way. This further highlights the weak effect these substrates have on the overlayer, as discussed in Sec. 4.2.2.

4.3 Comparison with theories

In the previous sections, we have investigated the local structure of the system and its empirical correlations with the dynamical heterogeneities. We now frame our results in the context of the theories of network-forming glassy systems introduced in Sec. 1.2.2. In particular, we assess the relevance of two historical pictures of the structure of network-forming amorphous systems, namely CRNT and the cybotactic description (Sec. 4.3.1). We also critically test the predictions of more recent theoretical models of the structure-dynamics relationship in network-forming liquids (Secs. 4.3.2 and 4.3.3).

4.3.1 Continuous random network theory and cybotactic description

The results of Sec. 4.1.1 demonstrated that, as the temperature is lowered, our model for the silica bilayer accumulates a high degree of local crystalline order. At low temperatures, the crystalline domains are nanometer-sized, but, crucially, their lifetimes are finite. These findings are reminiscent of the cybotactic description of network-forming amorphous systems, see Sec. 1.2.2, that postulated the existence of transient crystallites embedded in a disordered matrix[24]. The spatial extent of these domains is also clearly larger than what can be expected from a network of randomly connected rigid units, as prescribed by the continuous random network theory [131]. Overall, our results for $2d$ silica are thus more compatible with the cybotactic description than the CRNT, contrary to what is generally expected for $3d$ systems [97].

We speculate that the pronounced local crystalline order in 2d silica may be due to the absence of locally favored structures that compete with the crystalline domains [192, 193]. This could be due to the dimensionality of the system. For example, in $3d$ there are two possible ways to pack a maximum number of neighbors around a particle, which is placing them at the vertexes of a dodecahedron or an icosahedron. Since these arrangements maximize the number of neighbors of the central particle, they are expected to be low-energy structures for monoatomic system with isotropic interactions [194]. While the arrangement in a dodecahedron is compatible with long-range order, the disposition of the icosahedron is not, making

[24] See for example M4.1 in Appendix E, a video with the trajectory of the system at low-temperature ($T = 0.0067$) where the crystalline domains are highlighted using the same plotting scheme as Fig. 4.1.

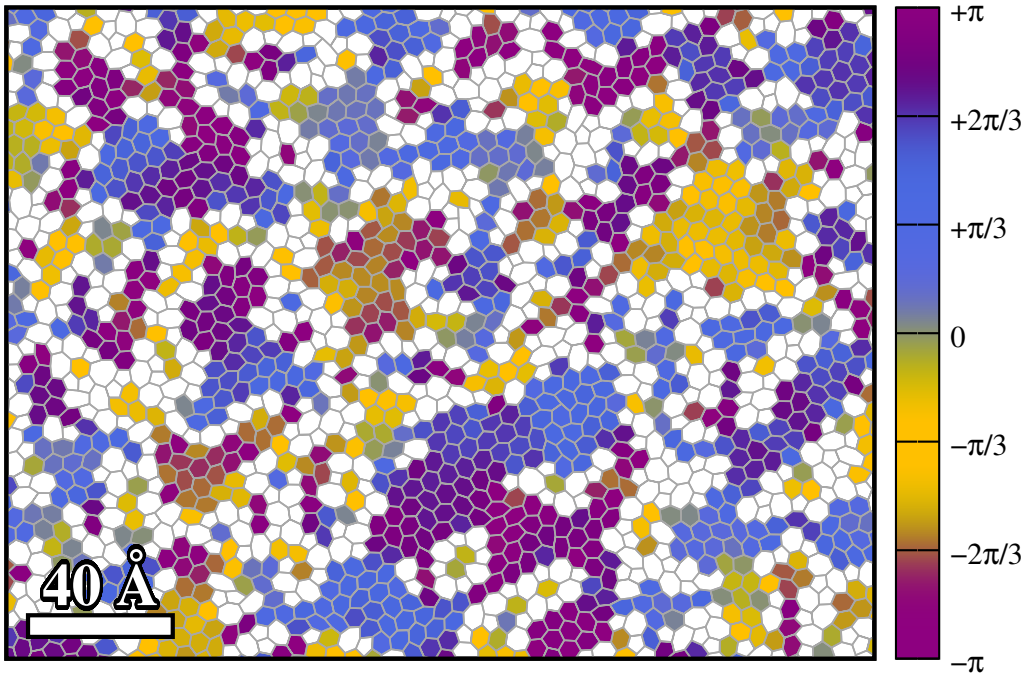

FIGURE 4.14: Snapshot of the ring structure of the system at the lowest temperature at which we menage to equilibrate the liquid ($T = 0.0067$). Only the hexagonal rings are colored and the colors correspond to the phase of the complex local order parameter $\psi^R_{6,i}$.

it an ideal locally favored structure that competes with the crystalline order. In two-dimensions, the situation is different. The only way to pack the maximum number of neighbors around a particle is to place them in a hexagonal arrangement, which is perfectly compatible with long-range order.

Since our model for the silica bilayer is inevitably a $2d$ approximation of the real $3d$ structure of the material, it is natural to wonder whether the experimental systems display large ordered domains and hence whether our low-temperature structures resemble those of the experiments. As shown in Sec. 3.1.1, experimental samples resemble our structures equilibrated at around $T \sim 0.0100$, while our lowest temperature is about twice lower than that ($T = 0.0067$). Nevertheless, even at $T \sim 0.0100$ our system presents large static correlation lengths and crystalline domains, albeit smaller than those at the lowest temperature, see Fig. 4.3. In the experiments, the behavior of the crystalline domains is much less clear. Large crystalline domains up to 50 Å can sometimes be observed in an otherwise disordered sample [18, 173], but it is not known if the system, prior to low-temperature quenching, was a liquid in thermal equilibrium, as expected in the cybotactic description, or was undergoing crystallization. Moreover, as discussed in Sec. 4.2, the presence of an underlying substrate could strongly enhance the formation of large crystallites. On the other side of the argument, experimental data are sometimes analyzed in the context of the CRNT, and any inconsistencies between the data and the theory are discarded[25] [131]. Nevertheless, the CRNT is a first-order approximation to the

[25] As a concrete example, in [131] the structure of an amorphous sample is analyzed in the context of the CRNT. The authors note the presence of several microcystallites composed of 7 hexagonal rings, and explain their appearance as a trivial statistical effect due to large number of hexagonal rings present in the network. However, the authors miss that some "microcystallites" are actually connected to each other, resulting in a cluster of 65 hexagonal rings, which seems difficult to explain as a simple statistical effect.

structure of a real network-forming material [78, 79], and its hypotheses might be wrong. For example, experiments have observed particles with wrong coordination and broken bonds [18], thus the network is not strictly "continuous" as the CRNT predict. Furthermore, the CRNT assumes that the randomness in the network is purely geometrical [11], while in a real system energetic and structural constraints inevitably play a role [78].

Therefore, due to the ambiguity of the sample preparation and the effects of the underlying substrate, it is difficult to assess which theory is more appropriate to describe the structure of the experimental samples. Our model, by contrast, address both issues and could be used as a benchmark for testing and developing new theories on the structure of two-dimensional network-forming systems.

4.3.2 Critical-like scenario

One of the theories developed to describe the dynamic slowdown of a glassy system is the critical-like scenario, developed by Tanaka and collaborators [166]. This phenomenological theory has been successfully tested on several two- and three-dimensional closed-packed systems [174, 195], although it is not widely accepted [74]. In the critical-like scenario, it is postulated that the dynamic slowdown in a glassy liquid is due to the development of orientational order among the particles [166]. In particular, it is assumed that the dynamical heterogeneities are due to fluctuations of this static structural order and regions with high orientational order coincide with slow rearranging regions of the dynamics. The fluctuations of the orientational order are expected to increase with decreasing temperature with critical-like behavior, making the dynamics progressively more heterogeneous and slower at lower temperatures.

According to this theoretical framework, the correlation length ξ for the orientational order is expected to grow with decreasing temperature as $\xi \sim [(T - T_0)/T_0]^{-2/d}$ [166, 196], where d is the dimensionality and T_0 is the critical temperature. Moreover, since the dynamic slowdown is assumed to be a consequence of the development of orientational order, the dynamic correlation length ξ_d is expected to grow as ξ as the temperature decreases ($\xi_d(T) \sim \xi(T)$), and both correlation lengths are expected to grow much faster than the correlation length associated to the translational order $\xi_{RDF}(T)$. Finally, the structural relaxation time is expected to be connected to ξ by the relation $\log(\tau) \sim \xi^{d/2}$ [166, 174].

At first glance, the predictions of the critical-like scenario appear to be in good agreement with our data. The growth of the static correlation lengths discussed in Sec. 4.1.1 ($\xi \sim A + B/T$) corresponds to the first term in the Taylor series of $\xi \sim [(T - T_0)/T_0]^{-2/d}$ in the limit $T_0/T \ll 1$ for $d = 2$. Moreover, combining the behavior of the static correlation lengths with the low-temperature Arrhenius behavior observed in Sec. 3.1.3, we obtain $\log(\tau) \sim \xi$, as expected in this theory [174]. Upon closer inspection, however, several discrepancies emerge between our data and this scenario. As shown in Sec. 4.1.1 and Sec. 4.1.2, the correlation lengths in our system vary with temperatures as $\xi_{RDF} \sim \xi \ll \xi_d$, that is, translational and orientational correlation lengths are similar and scale more slowly with decreasing temperature than the dynamic correlation length. This is different from what is postulated in the critical-like scenario where, as temperature varies, the correlation lengths are expected to satisfy $\xi_{RDF} \ll \xi \sim \xi_d$. It is also clear from our results in Sec. 4.1.3 that the ordered domains are not the sole cause of the dynamics slowdown, as assumed in Tanaka's theory. Moreover, analyzing our data within this theoretical framework, the critical temperature in our system is approximately $T_0 \sim 0$. This result, combined

with the Arrhenius behavior of the correlation times at low temperatures, suggests the absence of a transition at a finite temperature in our system, which is instead implicit in Tanaka's theory. Therefore, we deem the critical-like scenario not appropriate to describe our system.

4.3.3 Two-state model

Several three-dimensional network-forming liquids, such as water and silica, display a fragile-to-strong crossover as the temperature decreases [75–77, 191]. The nature of this crossover has been the subject of a long-standing debate in the literature. In this section, we will focus on one the main theoretical models that describe this behavior, namely the two-state model developed by Tanaka [197], and test its predictions against our simulation data for 2d silica.

In the two-state model, the system is described as an ideal mixture of two liquids with different different local structures: a normal-liquid structure, corresponding to the high-temperature liquid, and a locally favored structure, which is preferred at low temperatures [166]. Assuming that these structures have activation energies of E_1 and E_0, respectively, the relaxation time τ_α can be written as

$$\tau_\alpha(T) = \tau_0 \exp\left(\frac{E_0 s + E_1(1-s)}{k_B T}\right), \tag{4.10}$$

where τ_0 is a microscopic time and $s \in [0; 1]$ is the fraction of normal-liquid structures in the system [197]. This fraction can be calculated from the distribution $p(\psi)$ of a local order parameter. If such distribution is bimodal and it is possible to identify a threshold value $\bar{\psi}$ of the local order parameter which separates the two peaks of the distribution, then $s = \int_{-\infty}^{\bar{\psi}} p(\psi) d\psi$ [5]. In the case of water and three-dimensional silica, for instance, the relevant local order parameter is the distance between the nearest particle in the second coordination shell and the furthest particle in the first coordination shell [5].

One of the underlying hypotheses of the model is that network-forming systems with directional bonding do not form extended ordered domains, as this would result in a significant loss of entropy. Thus, the building blocks of the network are assumed to be structurally independent units, allowing the system to be treated a mixture of two local structures whose sizes do not change with decreasing temperature[26] [166].

Thus, in Tanaka's two-state model, the correlation time of the system is directly linked to its structural order, assuming the system is a mixture of two different structures in dynamical equilibrium. We test this model on our simulation data for the silica bilayer. To discriminate the two different structures in the liquid, we use the module distribution of the local order parameter $\tilde{\psi}_{3,j}^{cg(2)}$, shown in Fig. 4.15 (a). Since this order parameter is linked to the local crystalline order, the two different structures can be identified as (transient) crystalline and disordered structures, respectively. To quantify the fraction of these units, we must introduce a threshold value $\bar{\psi}$. Here, we follow two different approaches. In the first approach, we set the threshold so that the crossover between the more disordered population at high temperature and the more crystalline population at low temperature is as sharp as possible, see

[26] Note that, as discussed in Sec. 1.2.2, the degree of local crystalline order in a network-forming system is still a matter of debate.

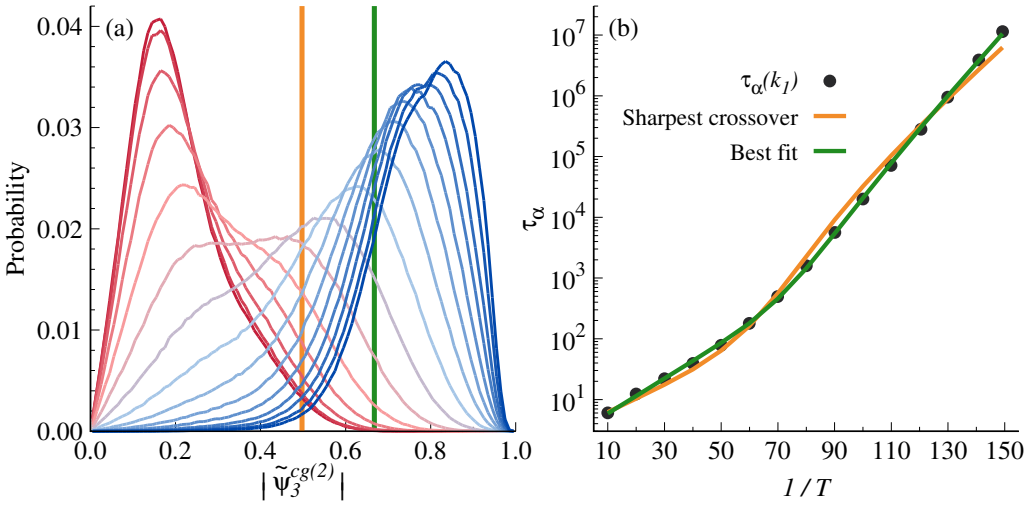

FIGURE 4.15: (a) Distribution of the module of the local order parameter $\tilde{\psi}_3^{cg(2)}$ at different temperatures. The colors of the distributions represent the same temperatures as Fig. 3.4. The vertical lines identify the threshold value used to discriminate between the two structures in the liquid in the "sharpest crossover" (orange) and "best fit" (green) approaches. (b) Comparison between the measured structural correlation times (black dot) and that predicted by the two-state model using the "sharpest crossover" (orange) and "best fit" (green) approaches to set the threshold value for the local order parameter.

the orange line in Fig. 4.15 [27]. In the second approach, we treat the threshold $\bar{\psi}$ as a mere fitting parameter in Eq. 4.10. The resulting threshold value is shown as a green vertical line in Fig. 4.15.

In Fig. 4.15 (b), we compare the fit of the correlation times $\tau_\alpha(k_1)$ obtained from the two-state model using the two different threshold parameters. As expected, using $\bar{\psi}$ as a fitting parameter produces the best fit. However, as shown in Fig. 4.15 (a), the fitted threshold value cuts off a large part of the low temperature distribution of the order parameter, and has no clear physical interpretation. Conversely, choosing $\bar{\psi}$ so that the crossover between the two populations is sharpest leads to a neat separation of ordeered and disordered structures, see Fig. 4.15, but yields a poor fit of the correlation times, with residuals 23 times larger than those of the previous approach. We report the threshold values used, the fitting parameters and the sum of the residuals of both approaches in Tab. 4.1.

Therefore, although the two-state model can fit our data well, using $\bar{\psi}$ as a fitting parameter, there are obvious physical inconsistencies in its description of our system. The best fit is obtained for a threshold $\bar{\psi}$ which has no clear physical meaning, as shown by the position of the vertical green bar in Fig. 4.15 (a). Furthermore, from a conceptual point of view, it is not even clear whether the two-state model can be applied to our system. The model assumes that the directional bonding in a network-forming liquid limits the local order to the nearest neighbors. This is clearly not the case in our system, where locally ordered domain of few nanometers can be found in the low temperature liquid, as discussed in Sec. 4.1.1. Thus, we conclude

[27] To be precise, if $s(T, \bar{\psi})$ is the fraction of disordered structures at temperature T using as threshold $\bar{\psi}$, the sharpest crossover between the populations is obtained by maximizing $\max_T \frac{\partial s(T,\bar{\psi})}{\partial(1/T)}$ with respect to $\bar{\psi}$. That is, we set the threshold to maximize the maximum derivative of $s(T, \bar{\psi})$ as a function of temperature.

Parameters	Sharpest crossover	Best fit
$\bar{\psi}$	0.4975	0.6675
τ_0	3.72	3.05
E_0	0.097	0.107
E_1	0.050	0.066
Residuals	1.45	0.066

TABLE 4.1: Fitting parameters of the two-state model using two different approaches to determine the threshold $\bar{\psi}$.

that the two-state model cannot be successfully used to describe our results on the silica bilayer.

4.4 Key results

The key insights we gained in this chapter can be summarized as follows:

- Decreasing the temperature, our model accumulates a high degree of local crystalline order, leading to the formation of large transient crystalline domains in the liquid.
- Although crystalline regions are slower regions of the dynamics, they cannot fully explain the dynamics slowdown of the system.
- The influence of a weak periodic substrate can lead to highly non-trivial changes in the structure and dynamics of the overlayer.
- The descriptions of the structure and dynamics provided by the different theories considered here fail to fully describe the behavior of our system, making it an ideal, if somewhat peculiar, test bench for future theories.

Chapter 5

B_2O_3 monolayer: models for polymorphs and extensions

In this chapter we use physically motivated concepts borrowed from continuous random network theory to develop a simple algorithm for the systematic search of $2d$ crystalline polymorphs. The algorithm does not rely on any prior knowledge of the system's structure or stoichiometry and predicts possible structures that can be studied by first principles and compared with experiments. We demonstrate the richness of the structures discovered by the algorithm and its flexibility by considering two different systems, with diverse compositions and connectivities.

We first describe the generalities of the algorithm (Sec. 5.1). We then apply it to a B_2O_3 monolayer, focusing on the lowest energy polymorphs and their comparison with experiments (Sec. 5.2). Finally, we consider the two-dimensional polymorphs of the C_xN_y compound, whose composition in the experimental samples may vary (Sec. 5.3).

The majority of this chapter is unpublished work, with only small sections (Sec. 5.2.2 and Sec. 5.2.3) already presented in Ref. [43]. The results for the C_xN_y monolayer (Sec. 5.3) were obtained by Francesca Cucchiaro for her master's thesis [54], where I acted as co-supervisor.

5.1 Algorithm

We present here the algorithm we developed to perform a systematic search for two-dimensional polymorphs of a given compound. The algorithm can be divided into two main steps. The first concerns the generation of possible structures that satisfy a set of physically motivated constraints. Since many structures equivalent by translation or rotation can be obtained, the second step involves filtering such structures to select the inequivalent ones.

5.1.1 Motivation

In his seminal paper in 1932, Zachariasen presented some general arguments to describe the structure of a network-forming material [85]. Assuming that the main interactions between atoms in a crystal and in the corresponding glass are the same, he deduced that the local environment around each atom should also be similar in the two systems. However, since a glass, unlike a crystal, lacks long-range order, there should be some broadening in the angle between neighboring units [85]. This interplay between quasi-rigid local structures and geometric randomness in which these structures are connected on a larger scale is the core of the original continuous random network theory, see Sec. 1.2.2.

In this framework, the requirement that the local environments of a glass and a crystal are similar is crucial for the existence of amorphous structures with an energy comparable to the crystalline ones [85]. Although the original formulation of these concepts was strongly focused on amorphous structures, these ideas can be also used to produce crystalline polymorphs in a controlled manner. The set of resulting polymorphs can then be analyzed to find structures with low formation energy to be compared with those observed in experiments, see Sec. 5.2 and Sec. 5.3, or to identify polymorphs with ideal structures for specific applications, such as atomic sieving or catalysis.

5.1.2 Generation of the structures

For simplicity, we will describe the algorithm we developed for generating polymorphs of a B_2O_3 monolayer as an example. Extending the algorithm to three-dimensional systems, different materials or stoichiometries is conceptually straightforward, although it introduces technical difficulties, see Sec. 5.3.1 and 5.4.

As described in Sec. 1.1.2, the structure of 3*d* amorphous B_2O_3 is a combination of $B\emptyset_3$ and $B_3O_3\emptyset_3$ equilateral triangles, while the only known low-density crystalline phase (B_2O_3-*I*) is composed only of $B\emptyset_3$ units. There is a long-standing controversy over whether B_2O_3-*I* is the stable structure under ambient conditions and whether a crystalline structure containing $B_3O_3\emptyset_3$ units can exist [31, 43]. This led Ferlat *et al.* to propose a set of possible polymorphs for this material, decorating three-dimensional framework produced by sp^2-carbon with the structural units observed in the amorphous B_2O_3 [35]. The resulting polymorphs have been shown to have comparable energy to that of the known stable crystal and to have a density close to that of the glass, see Fig. 1.4, highlighting the roughness of the energy landscape of such material.

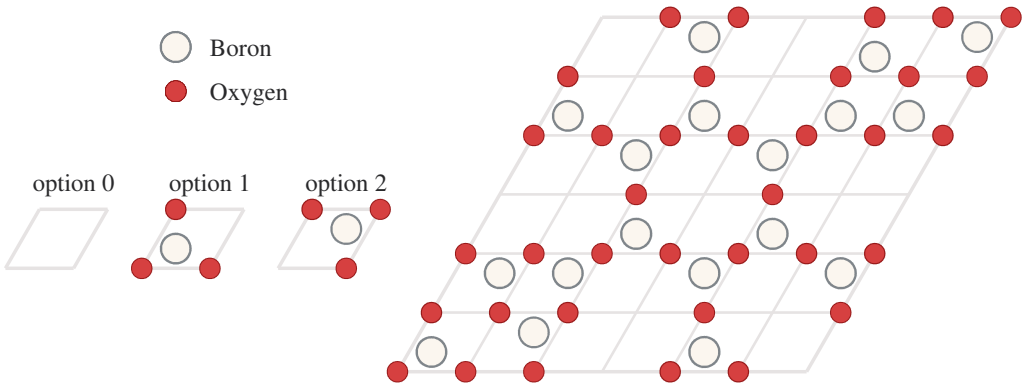

FIGURE 5.1: Sketch of the algorithm developed to produce polymorphs. We define a cell with three possible occupation options (left) and we use N^2 such cells to construct a supercell (right). The resulting structure is accepted or rejected according to constraints on the number of bonds formed by each atom, its stoichiometry and its symmetry. An example of the resulting structure (left) shows a combination of $B\emptyset_3$ and $B_3O_3\emptyset_3$ unit. White and red circles represent boron and oxygen atoms, respectively.

Here, we use a different approach to generate polymorphs that does not rely on previously known structures and allow us to identify polymorphs with a low formation energy. Noting that the $B_3O_3\emptyset_3$ unit can be broken up into three $B\emptyset_3$ equilateral triangle, we use these as building blocks. We consider three different cells of equal size, which can be empty or have an upward or downward pointing

$B\emptyset_3$ triangle. The size of these cells is set such that the distances between the atoms in the $B\emptyset_3$ unit are equal to their equilibrium value. From these elementary units, we construct a larger $N \times N$ hexagonal supercell. The individual cells within the supercells are filled using three different occupation options, as shown in Fig. 5.1. We then generate all the possible fillings of the supercell and we discard the ones that do not satisfy constraints on the number of bonds formed by each atom (considering periodic boundary conditions), the stoichiometry and the symmetry of the system.

We begin the discussion with the constraints on the number of bonds. Our non-empty options for filling the cells have a boron atom inside the cell and three oxygen atoms at its corners. By construction, the boron saturates all its bonds, while the oxygens must be shared between two different cells to do so. However, not all combinations of adjacent cells can be accepted. If two cells share two oxygens, as can be achieved by filling two successive cells along the x axis with options 2 and 1, the borons in the cells will be too close to each other. Since both borons have their electronic shells completely filled, there is a strong repulsion between the two, which increases the energy of the corresponding structure. Since the aim of this procedure is to generate polymorphs with low formation energies, this placing has thus to be discarded. Therefore, we can summarize the constraints on the number of bonds with the rule that each oxygen must be shared between two cells and that adjacent cells cannot share more than one oxygen[1]. It is important to emphasize that these constraints on the number of bonds significantly reduce the number of accepted structures and are the core of the algorithm itself. Moreover, these constraints are borrowed from Zachariasen's original work, since the rules we derived can be restated as the saturation of the bonds of each atom, as originally stated by Zachariasen [85].

The other constraints we can enforce during the polymorph generations concern the cell's stoichiometry and symmetry. The former limits the number of non-empty cells to be placed[2], while the latter forces the system to possess particular symmetries. In this work we force the supercell to be symmetrical with respect to its main diagonal. This reduces the number of cells to be independently filled, speeding up the algorithm. However, this assumption is arbitrary and can be applied if suggested by experiments, as in case of B_2O_3.

5.1.3 Filtering of the structures

The algorithm accepts or rejects a supercell based only on the occupancy of its constituting cells, without checking whether an equivalent configuration has already been found. This makes the resulting structures highly redundant, since supercells equivalent by translation or equivalent under symmetry operations are considered distinct. We address this problem as follows. Due to the large number of polymorphs produced by the algorithm, see Sec. 5.4, a one-to-one check to verify whether two structures are equivalent is computationally infeasible. Therefore, we divide the produced polymorphs in subsets based on the number of particles and the number of neighbors at different distances[3] [54]. A one-to-one equivalence check is then performed only for structures within the same subset.

[1] In Sec. 5.3 we will consider a system composed of carbon and nitrogen atoms. In this system, nitrogen will play the role of oxygen in the previous discussion. However, since nitrogen can form two or three bonds, see Sec. 1.1.4, we will allow a nitrogen to be shared between two or three cells.

[2] This constraints will be relaxed in Sec. 5.3 when we consider C_xN_y compounds.

[3] This computation is relatively simple, due to the discrete nature of the structures produced by the algorithm, which require the evaluation of the neighbors only at specific distances.

The result of this process is the complete set of all the possible inequivalent structures that can be accommodated in the original cell satisfying the imposed constraints. Since only geometric rules are used to construct these polymorphs, the resulting structures are rigid and, it is useful to perform a final structural optimization step with empirical force fields or *ab initio* methods to minimize the total energy of the system[4].

5.2 Predicted two-dimensional B_2O_3 polymorphs

We employ the algorithm described in Sec. 5.1 to perform a first-principles analysis of the polymorphs of a B_2O_3 monolayer. We consider a supercell composed of up to 6 cells along each crystalline axis and use the same 3 occupancy options as in Fig. 5.1. The constraints we impose during the cell generation are a strict B_2O_3 stoichiometry and the symmetry about the major diagonal. Moreover, we force each oxygen to be shared between two cells and adjacent cells cannot share more than one oxygen. We then perform a final variable-cell relaxation (vc-relax) step[5], to optimize the structure of the resulting systems. In this final step we maintain a strict two-dimensional geometry. Since we fix the number N^2 of cells used to construct the supercell and use the above constraints, the generated polymorphs will have different densities within a certain range.

5.2.1 Properties

In Fig. 5.2 and 5.3 we present some examples of the structures generated by the algorithm, along with the corresponding simulated STM images. We can clearly see that the algorithm produces structures with varying densities and composed of different structural units, ranging from simple $B\emptyset_3$ triangles, to boroxine rings to larger units, see Fig. 5.2. These structures, composed of two triangular units in the unit cell connected by an oxygen hinge, are particularly relevant to the following discussion. We classify them using the notation T_nH_m, where n and m are the number of $B\emptyset_3$ (T) and $B_3O_3\emptyset_3$ (H) units present in their unit cell, respectively. Conversely, the structures presented in Fig. 5.3 are identified using the notation S_i, with i a sequential index. In Fig. 5.2 and Fig. 5.3, we can also observe the effect of the final vc-relax step on the structures. As an example, the structure presented in Fig. 5.1 and the structure S_1 in Fig. 5.3 are the same polymorph before and after this relaxation step, respectively.

A natural question is whether these polymorphs resemble the structures synthesized in the experiments, since the substrate periodicity and the anisotropy of the out-of-plane environment can severely influence the structure of the overlayer. Remarkably, some of the simulated STM images we obtain are qualitatively similar to those observed in experiments. For instance, as we will discuss in detail in Chapter 6, the crystal obtained after the deposition of boron atoms on a *Pt(111)* substrate in an oxygen atmosphere and a flash annealing at 820 K [43], shown in Fig. 1.5 (a), corresponds to the structure T_0H_2 in Fig. 5.2. We also observe similarities between our polymorphs and the structures obtained after subsequent annealing cycles of

[4]Since the polymorphs produced by the algorithm are highly symmetric, it is advisable to slightly perturb the atomic positions before this minimization procedure to allow the system to reach deeper energy minima.

[5]The variable-cell relaxation is a structural optimization in which both the atomic positions and the lattice constants can be varied to reduce the total energy of the system. In this work, this step is performed through the `vc-relax` routine of the `Quantum ESPRESSO` code [198, 199]. For the computational details of our *ab initio* calculations refer to Appendix A.

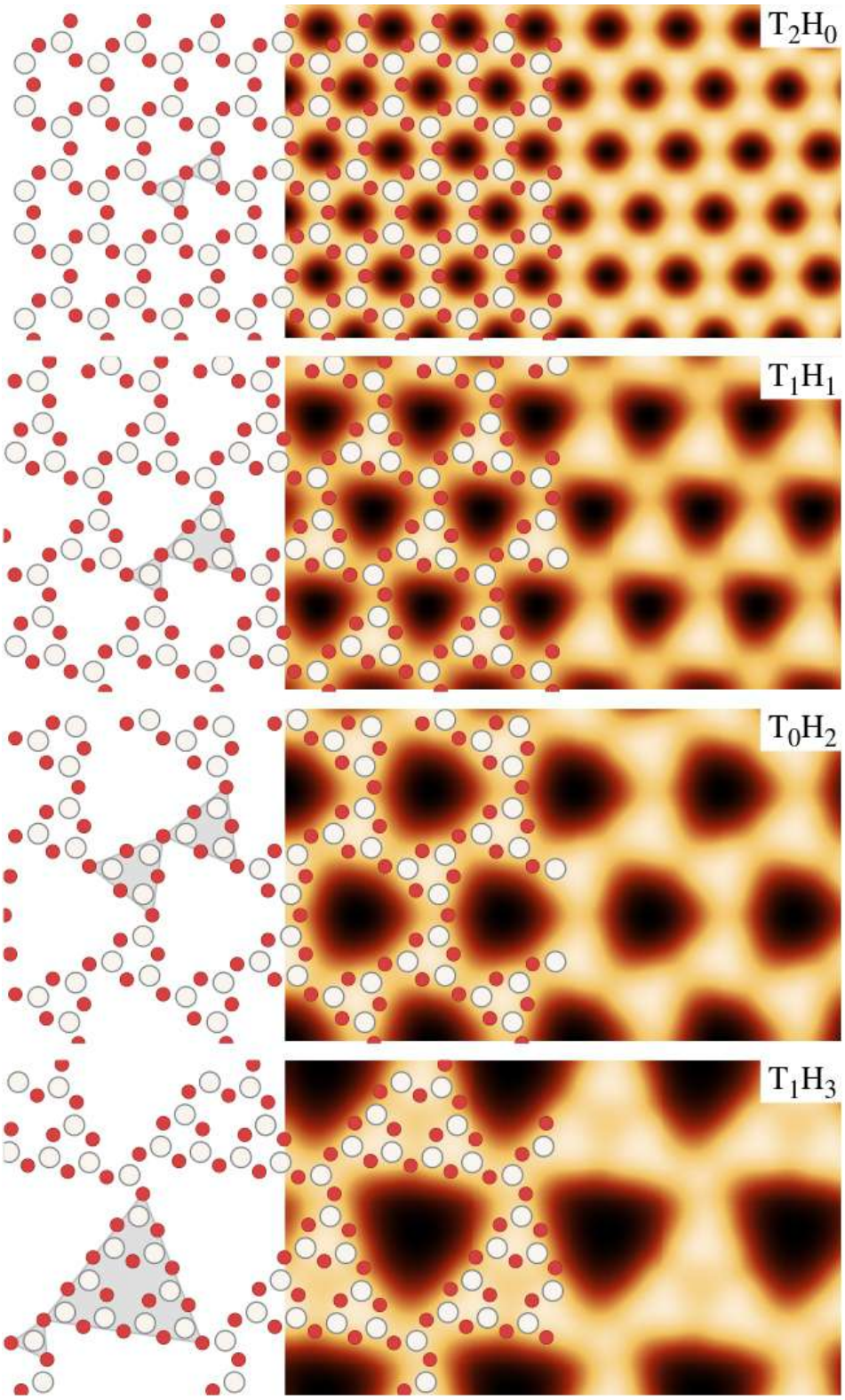

FIGURE 5.2: Structure and simulated STM images of selected polymorphs, all characterized by the presence of two triangular superstructural units in the cell, highlighted in grey. As will be shown in Fig. 5.4, the T_0H_2 polymorph is the lowest energy structure found by the algorithm. Each panel is 50 Å$\times$ 20 Å. For the notation, refer to the text. The color scheme of the atomic models is the same as in Fig. 5.1.

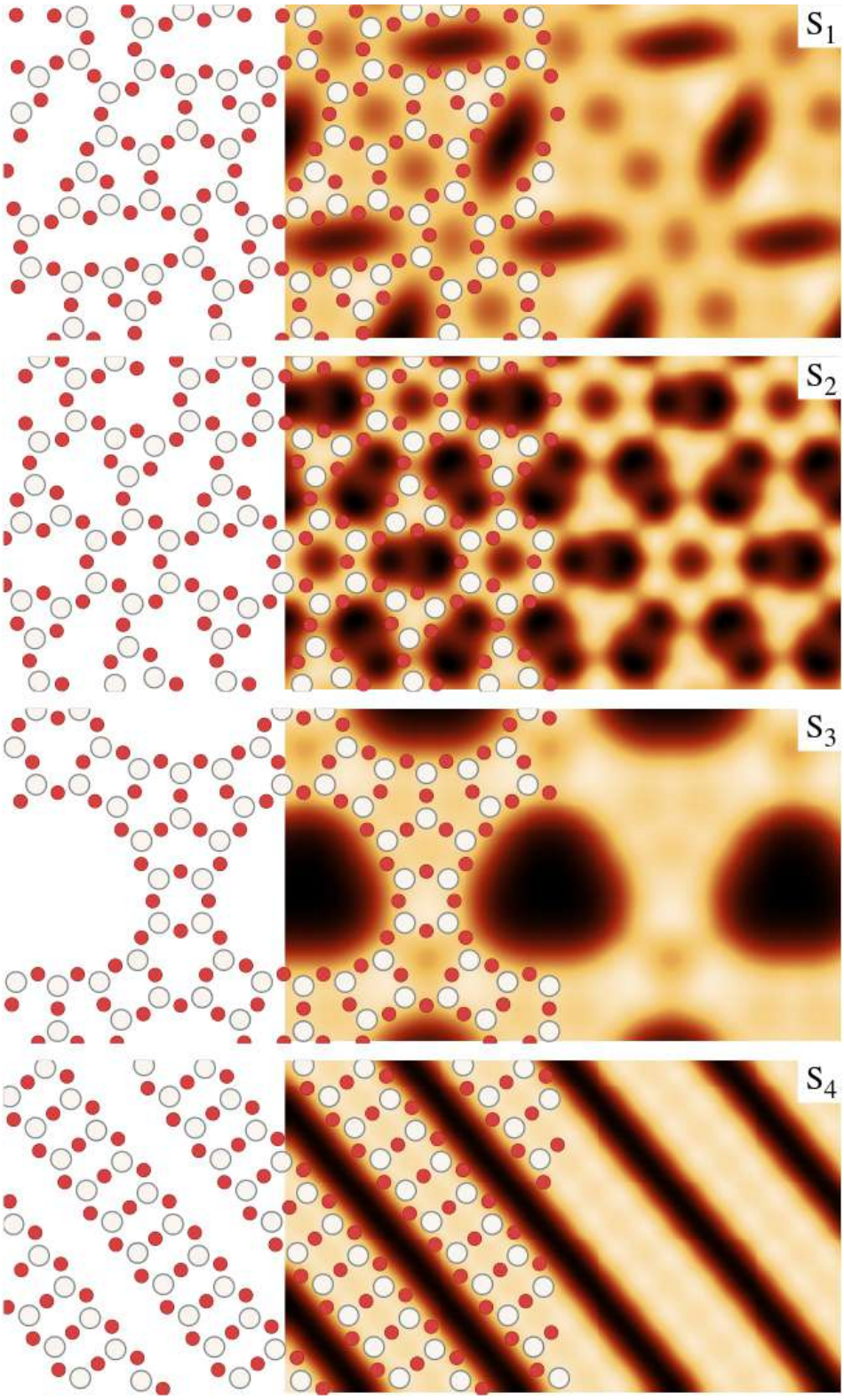

FIGURE 5.3: Structure and simulated STM images of selected polymorphs generated by the algorithm. Each panel is 50 Å× 20 Å. For the color scheme of the atomic models, refer to Fig. 5.1.

the boria monolayer. As an example, Fig. 1.5 (c) is the result of 7 annealing cycles at 550 K after deposition, which results in the appearance of an hexagonal crystal with pores of approximately 15 Å and string-like structures [44]. These structures

bear a close resemblance to the S_3 and S_4 polymorphs presented in Fig. 5.3. Since a thorough analysis of these experimental structures has yet to take place, and the lattice parameter of the S_3 structure is 14.7 Å, thus smaller than that observed in the structure of Fig. 1.5 (which is about 20 Å [44]), this agreement is only qualitive. Nevertheless, we argue that our polymorphs, produced in a controlled manner and with complex bonding of superstructural units, are a good starting point for developing a structural model for the systems studied in the experiments.

To predict the low-temperature ($T = 0$ K) phase of the B_2O_3 monolayer, we compare in Fig. 5.4 the energies per formula unit of the different polymorphs obtained by the algorithm. In contrast to Ferlat *et al.* [35], our scheme produces polymorphs with a mixture of $B\emptyset_3$ and $B_3O_3\emptyset_3$ units, as can be seen by comparing the color scale in Fig. 5.4 with Fig. 1.4. We also note that most polymorphs tend to have a higher fraction of $B\emptyset_3$ than $B_3O_3\emptyset_3$. This leads to more compact structures, with densities in the range of $0.24-0.31$ atoms/Å^2.

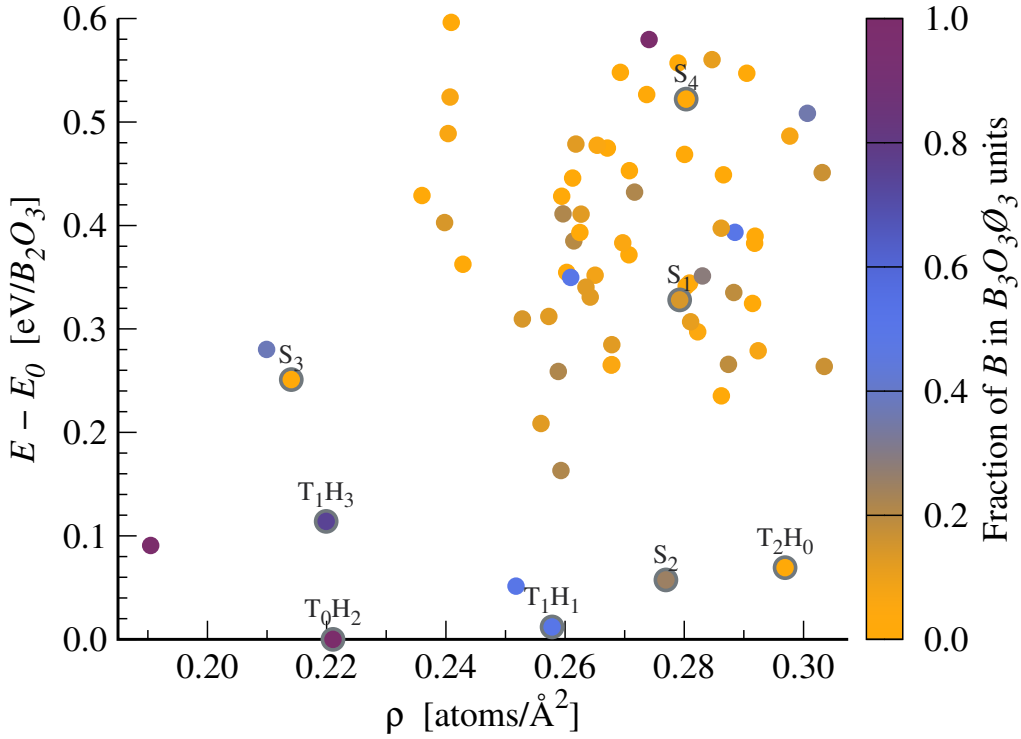

FIGURE 5.4: Scatter plot of the energies and densities of the different B_2O_3 polymorphs after the structural optimization. The palette represents the fraction of boron atoms inside boroxol B_3O_3 rings and the reference energy E_0 is the lowest energy, obtained for the T_0H_2 structure. The structures presented in Fig. 5.2 and 5.3 are highlighted with a grey outline and a corresponding code. For the T_nH_m notation refer to the text.

Close inspection of Fig. 5.4 reveals a set of polymorphs in a narrow energy range (0.1 eV/B_2O_3) close to the most stable one. These low-energy systems span the entire density range, and the lowest energy polymorph (T_0H_2) is significantly less dense than the average. Upon visual inspection, most of these low-energy systems belong to the T_nH_m class of polymorphs, with a unit cell composed of two connected triangular units, see Fig. 5.2. These units can be $B\emptyset_3$ or $B_3O_3\emptyset_3$ triangles, but they can also correspond to complex superstructural units made by a combination of the latter two, see for example the T_1H_3 structure in Fig. 5.2. Moreover, as shown in

Fig. 5.2, the connections between units in the T_nH_m class of polymorphs tend to be non-straight, resulting in pores with a triangular shape.

5.2.2 Rigid and flexible models

We now focus our attention on the structure of the T_nH_m class of polymorphs. These systems are characterized by the presence of two connected triangular units in the unit cell, with an angle between their centers and the shared oxygen atom that can be different, in general, from 180°. By construction, during the generation process, the angle between the unit is straight, *i.e.* 180°, but during the structural optimization the systems reach a deeper energy minimum by rotating in opposite way the triangular units with respect to their centers, reducing the lattice constant.

To study this mechanism, we start from the structure with straight bonds between the units, and we consider two different models leading to compressed systems. In the first (*rigid*) model, we fix the relative coordinates of the atoms inside the unit cell and we vary its lattice parameter. This procedure results in an isotropic deformation, with a parabolic shape of the energy as a function of the lattice constant, as indicated by the dashed lines in Fig. 5.6. In the *rigid* model the angle between the triangular units is thus fixed at 180°. We relax this constraint in the second (*flexible*) model, where we fix the bond lengths and the internal angles within the triangular units, and we accommodate the compression of the system by rotating the triangular units in opposite directions.

Using simple algebra, we derive for this model the relation

$$s = \frac{\sqrt{1 + r^2 - 2r\cos(\theta)}}{1 + r}, \tag{5.1}$$

which links the angle θ described joining the common oxygen between two triangular units with their centers, the ratio $s = a(\theta)/a_0$ of the lattice parameter before (a_0) and after ($a(\theta)$) compression, and the ratio $r = L_2/L_1$ of the sides of the two units. These geometric parameters are shown in Fig. 5.5 for the T_1H_1 polymorph. If these units have the same side, such as the T_2H_0 and T_0H_2 structures, this relation simplifies to

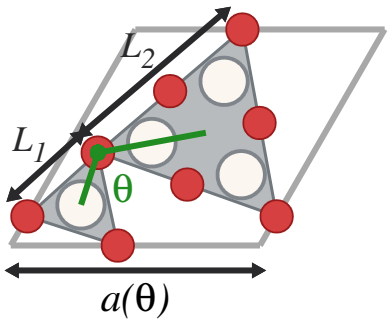

FIGURE 5.5: Scheme of the *flexible* model for the T_1H_1 polymorph.

$$s = \sin\left(\frac{\theta}{2}\right). \tag{5.2}$$

Since rotating the units can only decrease the lattice parameter, this *flexible* model can only be used to describe the compression of the system, see the solid lines in Fig. 5.6.

We employ the *rigid* and *flexible* models to study the behavior of the structures presented in Fig. 5.2 as the lattice parameter varies[6]. In particular, we compare structures with a specific lattice constant and we calculate their energy with a self-consistent calculation. We present the results in Fig. 5.6. For all the structures considered, the *flexible* model allows the system to reach a deeper energy minimum than the *rigid* model. Moreover, the energy minimum obtained for the *flexible* model is remarkably close to the energy obtained after the vc-relax step. It is worth noting

[6]We present two structures of the T_0H_2 polymorphs produced using the *rigid* and *flexible* models, along with their respective energy-strain curves, in figure F5.1 in the Appendix E.

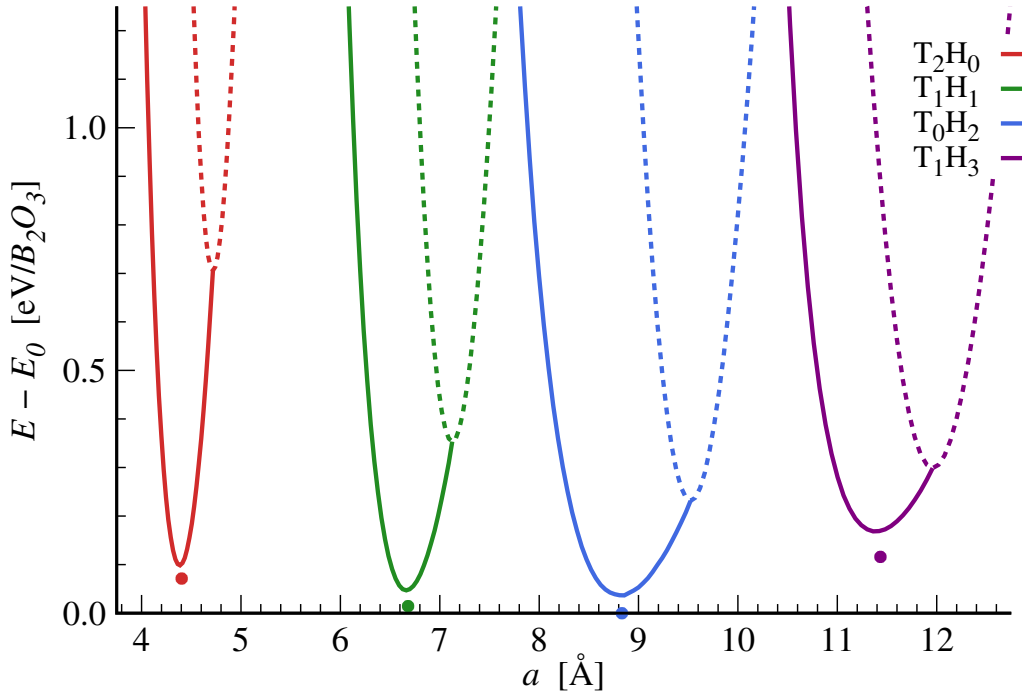

FIGURE 5.6: Energy as a function of the lattice parameter a for different T_nH_m polymorphs. Dashed and solid lines refer to the *rigid* and *flexible* models, respectively. The points correspond to the equilibrium structures after the vc-relax step applied to the *flexible* model. The reference energy E_0 is the lowest energy, obtained for the relaxed T_0H_2 structure. For the T_nH_m notation refer to the text.

that the *flexible* model bears many similarities with the original ideas of Zachariasen on the structure of a network-forming glass [85]. In both schemes, there is an interplay between the rigidity of local units and the flexibility of the connections between them, see Sec. 1.2.2. We also stress that the *flexible* model relies on the presence of a hinge between two units. In the presence of multiple connections between the units, this model cannot be used and the system will be much more rigid, see Sec. 5.3.3.

From the curves of the *flexible* model in Fig. 5.6 we can extract an estimate[7] of the 2*d* Young's modulus Y using the relation [200]

$$Y = \left.\frac{\partial^2 \Delta e}{\partial s^2}\right|_0 , \tag{5.3}$$

where the index 0 identifies the properties of the equilibrium configuration, Δe is the energy per unit area relative to the equilibrium configuration and s is the strain.

The 2*d* Young's modulus, shown in Tab. 5.1, is remarkably low for all the structures considered. In particular, the structure with the lowest energy (T_0H_2) is also the most flexible one, with a 2*d* Young's modulus of ~ 60 *Pa·m*. This value is approximately 5 times lower than the values obtained for other 2*d* materials, like graphene (~ 340 *Pa·m* [200–202]) and *h-BN* (~ 280 *Pa·m* [203, 204]), making this system one the softest one-atom-thick material simulated so far. The stiffness is comparable to that

[7] We stress that the curves in Fig. 5.6 are obtained by fixing the position of the atoms according to our models, whereas in the typical calculations of the Young's modulus only the lattice constant is fixed and the atomic positions are relaxed before calculating the energy. Furthermore, much more care should be taken to accurately evaluate the elastic constants [200]. Thus, our results should be interpreted only as a rough estimate of the true 2*d* Young's modulus.

Structure	Lattice constant [Å]	Angle [degrees]	Energy [eV/B_2O_3]	2d Young's modulus [$Pa \cdot m$]
T_2H_0	4.40	135.1°	0.069	238.9
T_1H_1	6.68	135.6°	0.012	138.9
T_0H_2	8.83	135.7°	0	59.4
T_1H_3	11.44	140.0°	0.114	100.0
T_0H_4	13.49	137.0°	0.091	–
T_5H_3	13.88	137.2°	0.280	–

TABLE 5.1: Structural properties of the T_nH_m polymorphs identified by the algorithm. The lattice constant, the angle θ between the units and the energy refer to the structure after the vc-relax step, while the 2d Young's modulus is calculated from the solid curves in Fig. 5.6 using Eq. 5.3. We use the energy of the polymorph T_0H_2 as reference energy. The structures T_0H_4 and T_5H_3 are shown in figure F5.2 in the Appendix E.

of thicker 2d materials, such as black phosphorus ($\sim 20-50$ $Pa \cdot m$) and transition-metal dichalcogenides (~ 110 $Pa \cdot m$ for WSe_2 and $MoSe_2$) [205]. The high flexibility of the T_nH_m polymorphs could allow their growth on different substrates, as their structures can easily adjust to match the substrate's lattice parameter without major changes in their energy.

5.2.3 The most stable B_2O_3 polymorph

We now focus on the lowest energy structure found by the algorithm: the T_0H_2 polymorph. As will be discussed in detail in Chapter 6, this structure is observed in experiments upon deposition of boron and oxygen on a *Pt(111)* surface, followed by a high temperature annealing cycle.

The unit cell of this system consists of two B_3O_3 boroxol rings connected by an oxygen bridge. The nearest neighbors distance is approximately 1.39 Å between borons and oxygens forming the boroxol rings, and 1.37 Å between borons and the bridging oxygens[8]. The internal angles within the boroxol rings are very close to 120°, making these rings very regular, while the angle connecting the bridging oxygen with its two boron neighbors is approximately 133°[9]. The unit cell contains 15 atoms and its lattice parameter is 8.83 Å, which results in a structure with relatively low density. The system features large triangular openings of 5.45 Å in diameter, as can be appreciated from its simulated STM image, see structure T_0H_2 in Fig. 5.2.

We now turn our attention to the electronic properties of this material. In Fig. 5.7, we present its band structure and density of states (DOS). The system is a wide band gap insulator with a band gap of approximately 6.55 eV[10]. The band gap is indirect, with the highest occupied (HOMO) and lowest unoccupied (LUMO) level at K and Γ, respectively. The bands close to the highest occupied level are rather flat, suggesting the presence of strongly localized electrons [104]. As shown in Fig. 5.7 (right), projecting the DOS onto atomic orbitals, we observe that the bands near the HOMO

[8]Note that this difference between the nearest neighbors distances, albeit small, was not accounted for in the flexible model in Sec. 5.2.2.

[9]Note that this angle between the bridging oxygen and its two boron neighbors is different from those reported in Tab. 5.1, which instead refers to the angle between the bridging oxygen and the center of the triangular units, *i.e.* the boroxol rings in this structure.

[10]This band gap can be easily tuned by changing the lattice parameter, see movie M5.1 in Appendix E.

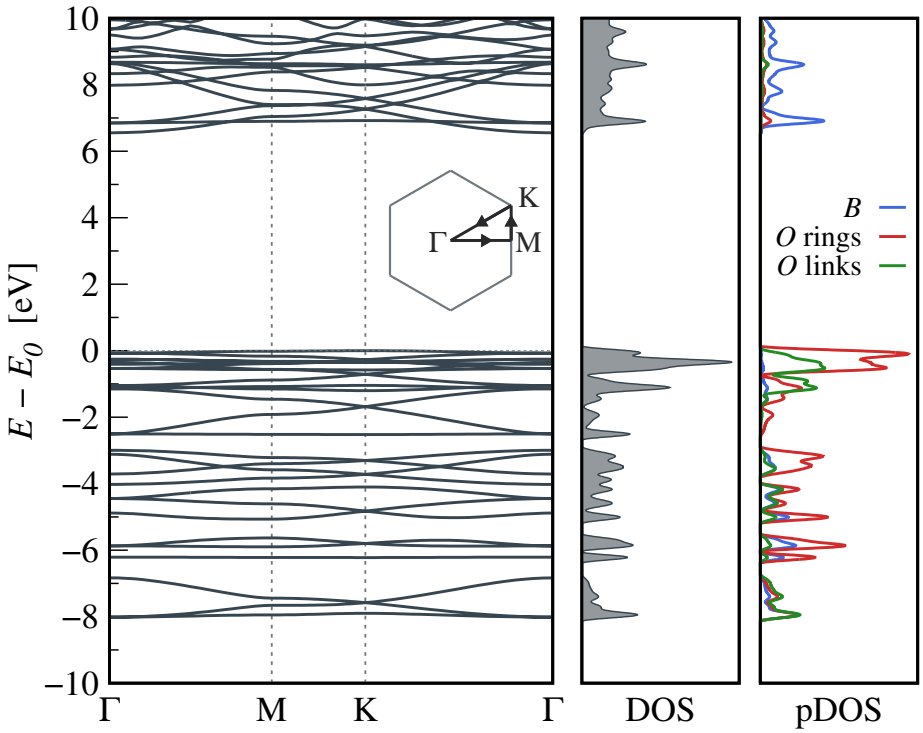

FIGURE 5.7: Band structure (left), density of states (DOS, center) and projected density of states on the atomic orbitals (pDOS, right) of the optimized T_0H_2 structure. The band structure is calculated along the path in the first Brillouin zone presented in the inset and the zero energy E_0 is set to the highest occupied electronic state. In the pDOS, blue, red and green lines represent the density of states of boron atoms, oxygen atoms within a B_3O_3 ring and oxygen atoms between different B_3O_3 rings, respectively. The horizontal axis of the DOS and pDOS plots is in arbitrary units.

are populated mainly by electrons from the oxygens within the boroxol rings, while the LUMO is mainly due to electrons from the borons. In the band structure, we also observe a variety of Dirac cones [206], which are the result of the hexagonal symmetry of the system.

5.3 Two-dimensional C_xN_y polymorphs

Given the similarities between the B_2O_3 polymorphs obtained in Sec. 5.2 and the structures proposed for a C_xN_y monolayer, see Fig. 1.7, we performed a similar study for this new compound. We generate the polymorphs with the same procedure used for the B_2O_3 system, see Sec. 5.2, using supercells made of 6 unit-cells along each crystalline direction and using the same three occupation options as in Fig. 5.1, with boron and oxygen replaced by carbon and nitrogen, respectively. The only difference in the generation procedure for this set of polymorphs concerns the constraints on stoichiometry and the number of bonds. Due to the synthesis methods, there is considerable uncertainty regarding the carbon to nitrogen ratio of the final compound, see Sec. 1.1.4. Thus, we do not enforce any constraint on the stoichiometry of the final structures. Moreover, since nitrogen can form two or three bonds, we modify the constraint on the number of bonds accordingly, allowing each nitrogen to be shared between two or three cells. As before, we forbid adjacent cells to share more than one oxygen to avoid interactions between carbon atoms. By construction, our polymorphs contain only heterogeneous bonds, and thus we cannot generate all

the possible structures proposed in the literature, see for example Fig. 1.7 (a). Since the set of polymorphs produced by the algorithm is too large to systematically perform a vc-relax step on each structure as we did for the B_2O_3 system, we select only a subset of low energy structures to analyze in detail.

5.3.1 Properties

Despite the small changes in the constraints used in the generation process, the number of C_xN_y polymorphs produced by the algorithm is two orders of magnitude larger than the number of B_2O_3 structures studied in Sec. 5.2. In Fig. 5.8 we present the distribution of carbon to nitrogen ratios for all the inequivalent C_xN_y polymorphs. The algorithm produces structures with C/N ratios ranging from 2/3 to 1, with most structures in the interval [0.700; 0.825]. Although we do not impose any constraints on the stoichiometry during the generation process, some stoichiometries are overrepresented in Fig. 5.8, resulting in bins that are more populated than their surrounding ones. Surprisingly, the most populated bin corresponds to the C_3N_4 stoichiometry, which is the ideal stoichiometry for graphitic carbon nitrides, see Sec. 1.1.4). The opposite holds for the C_4N_5 stoichiometry, which has less inequivalent structures than the neighboring $C_{29}N_{36}$ stoichiometry. We deem these effects representative of the atoms connectivity and the constraints on the number of neighbors of each atom.

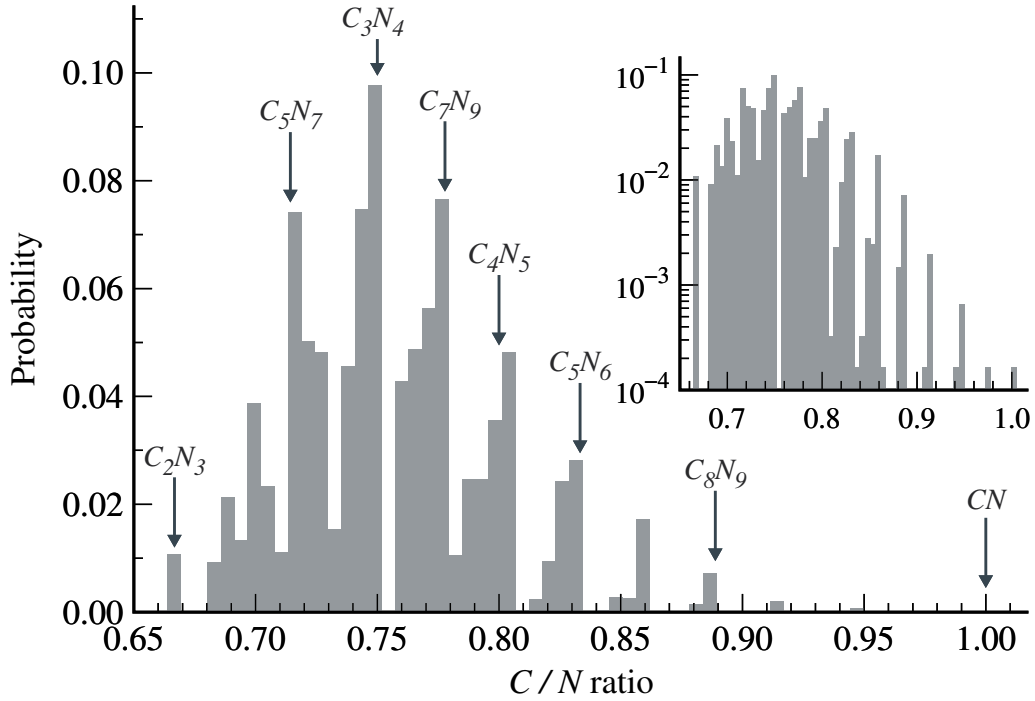

FIGURE 5.8: Distribution of carbon to nitrogen ratio in the generated C_xN_y polymorphs. The arrows indicate specific simple stoichiometries, while the inset presents the same data on a semi-logarithmic scale.

Due to the large number of inequivalent structures obtained using the algorithm and the high computational cost of DFT calculations, we are unable to perform the same systematic analysis as for B_2O_3 in Sec. 5.2. Therefore, we focus on a representative subset of 3200 polymorphs. We start with an evaluation of their energies, before

the vc-relax step. Since the structures have different stoichiometries, it is not possible to compare them using their total energy[11]. Thus, for each structure we calculate its cohesion energy per atom e_{coh}, defined as

$$e_{coh} = \frac{1}{N_{at}} \left(E_{tot} - \sum_X N_X E_X^{isol} \right) , \tag{5.4}$$

where E_{tot} and N_{at} are the total energy and the number of atoms of the system, respectively, E_X^{isol} is the energy of an isolated atom of type X and N_X is the total number of X-type atoms, with $X = C$ or N. This quantity defines how stable a given structure is relative to its isolated atoms, with negative values indicating that the system is more stable than its isolated constituents.

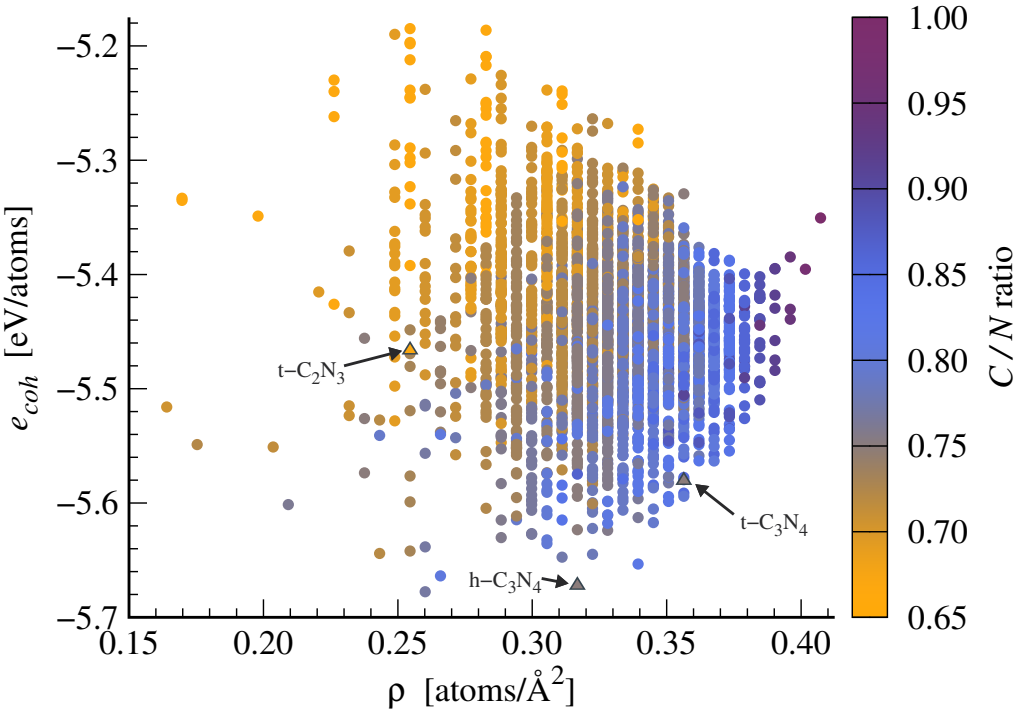

FIGURE 5.9: Cohesion energy per atom as a function of density for a subset of C_xN_y polymorphs. The palette represents the carbon to nitrogen ratio. Triangles and labels identify the three polymorphs known in the literature that satisfy the constraints imposed during the generation process. Namely, these structures are triazine-based C_2N_3 (t-C_2N_3), triazine-based C_3N_4 (t-C_3N_4) and heptazine-based C_3N_4 (h-C_3N_4), see Sec. 1.1.4.

We present in Fig. 5.9 the cohesion energies for the subset of studied polymorphs[12]. All the structures we considered have negative cohesion energy, making them energetically stable. Most of the structures have densities in the range of $0.27-0.37$ atoms/Å^2, while systems with lower densities are quite rare, as found in Sec. 5.2.1. We also note a direct correlation between the density and the C/N ratio. This is due

[11] The main contribution to the system's energy is the energy of its constituent atoms. Therefore, the total energy is almost a linear function of the number of particles [54], making a comparison of the total energies meaningless.

[12] Fig. 5.9 is an analogue of Fig. 5.4 for the polymorphs of the B_2O_3 monolayer, with the difference that the data for the C_xN_y polymorphs refer to structures before the structural optimization, while those for the B_2O_3 system are obtained for the relaxed structures.

to the number of bonds that nitrogen atoms can form: structures with a higher fraction of three-coordinated nitrogens have a higher C/N ratio, since the nitrogens are shared between more carbon atoms. Furthermore, the presence of 3-fold coordinated nitrogens makes the entire structure more compact, resulting in denser systems.

5.3.2 Low energy structures

According to literature, a heptazine-based framework (h-C_3N_4), see Fig. 1.7 (b), has the lowest energy among graphitic carbon nitrides [64, 65], see Sec. 1.1.4. To the best of the author's knowledge, however, no systematic study of these C_xN_y polymorphs has ever been conducted, and the structures considered in the literature were developed based on chemical intuition and the researcher's ingenuity. Thus, more complex structures with lower energy than the heptazine-based framework may exist. Since our algorithm yields the complete set of inequivalent polymorphs satisfying certain physically motivated constraints, we can assess the stability of h-C_3N_4 compared to all the other structures generated by the algorithm.

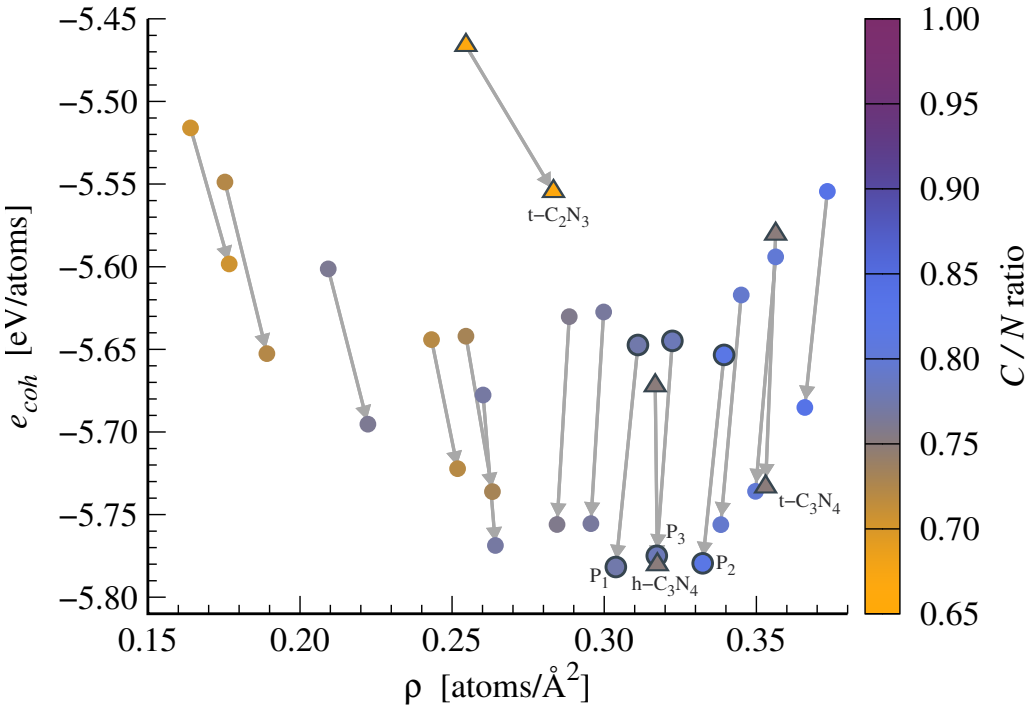

FIGURE 5.10: Cohesion energy per atom for a selected subset of low energy C_xN_y polymorphs before and after the relaxation of the atomic positions. Each arrow connects the initial structure with the relaxed one. The palette and the labels are the same as in Fig. 5.9. We also label as P_n three additional structures with the lowest cohesion energy after the vc-relax step. In order of increasing cohesion energy, these low energy structures are P_1, h-C_3N_4, P_2 and P_3.

To do so, we group the polymorphs with similar densities and for each group we select the polymorph with the lowest cohesion energy. We then perform a vc-relax calculation to optimize the structure of the selected systems. In Fig. 5.10 we show the cohesion energy of the resulting structures. After the relaxation step, four polymorphs with low energy stand out. These structures have nearly the same density of $0.30 - 0.33$ atoms/Å^2 and are almost degenerate in energy, with the maximum energy difference between them of 0.007 eV/atom. Except for h-C_3N_4, which has the second lowest cohesion energy, 0.002 eV/atom higher than the lowest, none of the

other polymorphs match any of the structures discussed in the literature. We present these polymorphs in Fig. 5.11. They feature openings of different sizes arranged in various patterns. The largest opening for each structure always has a diameter of 4.8−5.5 Å, which indicates a greater stability of these medium-size pores compared to smaller or larger ones [54].

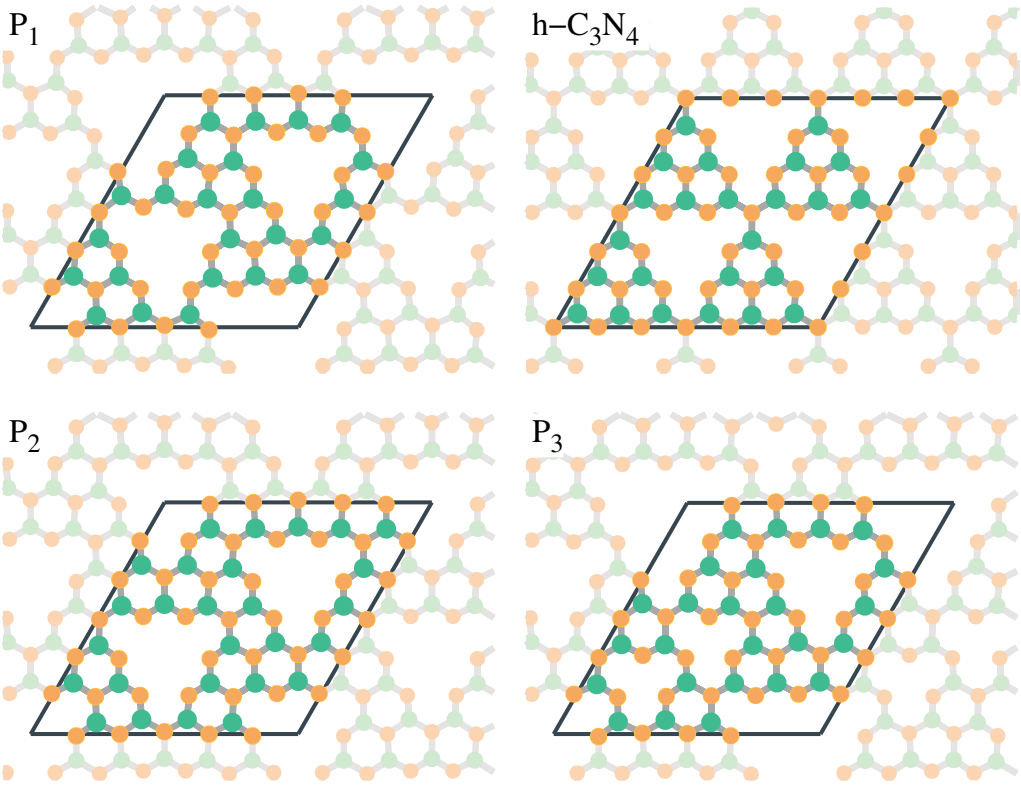

FIGURE 5.11: Structure of the polymorphs with the lowest cohesion energy after the relaxation of the atomic positions. The names of the structures are the same as in Fig. 5.10. In order of increasing cohesion energy, these low energy structures are P_1, h-C_3N_4, P_2 and P_3. The unit cell is highlighted in black, while the grey lines identify the bonds between the atoms. Green and orange circles represent carbon and nitrogen atoms, respectively, as in Fig. 1.7.

Despite the inherent limitations of our calculations, see Sec. 5.4, we deem the existence of a set of nearly degenerate polymorphs relevant for experiments. The typical synthesis method for graphitic carbon nitrides is thermal polymerization, see Sec. 1.1.4. This procedure does not allow precise control over the structure or stoichiometry of the final product. Thus, the presence of a set of nearly degenerate polymorphs suggests a more critical assessment of the experimental samples. These structures are also interesting from a technological standpoint. According to preliminary calculations [54], their large rings are ideal adsorption sites for single-atom catalysts, such as nickel and cobalt.

5.3.3 Rigidity

One of most striking results revealed by Fig. 5.10 is the small change in density following the vc-relax step. For most polymorphs, the change in density is less than 2.5 % of its original value. This contrasts with what we found in B_2O_3, where energy minimization was crucial to optimize the structure, see for example Fig. 5.6, and the vast majority of polymorphs exhibits density variations ranging from 5 % to 12

% of its original value, with only one structure exceeding 27 %. Clearly, the C_xN_y compounds are much more rigid than the B_2O_3 structures. To explain this behavior, we focus on the connectivity of the atoms.

In 1983, Thorpe suggested that in a covalently bonded random network, increasing the average coordination of the atoms result in a transition of the system from floppy to rigid behavior [207]. This effect was quantified by calculating the number of zero-frequency modes, equal to the difference between the number of degrees of freedom of the system and the number of linearly independent constraints. According to this picture, the system becomes rigid when the number of zero-frequency mode is less than zero, *i.e.* the system is over-constrained. Assuming that small vibrations around the equilibrium structure are described by an interaction potential which depends only on the distances between the nearest neighbors and the angles between them, Thorpe derived, in a mean field approach, that the onset of rigidity in a $3d$ system occurs at an average coordination number $\langle z \rangle > 2.4$ [207].

We perform a similar calculation for a two-dimensional C_xN_y compound. The number of degrees of freedom is $2N_{at}$, with N_{at} the number of atoms in the system. Since we do not expect major changes in the connectivity between the neighboring atoms during the vc-relax procedure, the constraints in the system concern the bonds and angles between neighboring atoms. Our polymorphs contain only heterogeneous bonds between atoms, and each carbon atom is three-fold coordinated. Therefore, the total number of bonds in the system is $3N_C$, with N_C the number of carbons. The angular constraints can be calculated similarly, focusing on the carbon atoms and realizing that only two angles need to be specified for each carbon, resulting in $2N_C$ additional constraints. As a result, the condition for a rigid network corresponds to

$$2N_{at} - (3N_C + 2N_C) < 0 \quad \Longleftrightarrow \quad \frac{N_C}{N_{at}} > \frac{2}{5}\,. \tag{5.5}$$

Therefore, from this rough estimate, we expect that all the structures with a carbon to nitrogen ratio greater than $\frac{2}{3}$ are much stiffer than the others, in agreement with our empirical findings comparing the polymorphs of C_xN_y and B_2O_3. It is also noteworthy that the polymorph with the greatest density variation in Fig. 5.10 is isostructural to the T_0H_2 structure in Sec. 5.2.2, with stoichiometry C_2N_3.

5.4 Advantages and limitations of the algorithm

The algorithm presented in this chapter has both advantages and disadvantages. The main advantages are its simplicity and the ability to systematically search for polymorphs that satisfy a set of physically motivated constraints. Moreover, since it requires minimal information about the symmetry of the cell and the atoms it contains, the algorithm could be a valuable tool for predicting the experimental structures on a theoretical basis. We have successfully used this algorithm to determine the structure of an experimentally synthesized B_2O_3 monolayer [43].

The procedure described, however, has some major drawbacks. The first one is the computational complexity of the algorithm. If we consider a d-dimensional supercell composed of n cells along each crystalline axis and consider M different occupancy options for each cells, the number of different possible occupations to be checked is on the order of $\mathcal{O}\left(M^{n^d}\right) = \mathcal{O}\left(e^{n^d \ln(M)}\right)$. Although it is possible to make minor optimizations to the generation, such as fixing the value of the first cell or

forcing a particular symmetry, this scaling cannot be improved. For the largest cell considered in this work ($n = 6$, $d = 2$ and $M = 3$), the generation process required about 24 hours on a single core of a Xeon Gold 6354 CPU, a time we deemed acceptable[13]. Another drawback of the algorithm is the large number of polymorphs it produces. Except for simple systems with fixed stoichiometry, where the number of structures is manageable, see Tab. 5.2, the vast amount of generated polymorphs require further filtering based on the desired structures or properties, see Sec. 5.3 and [54]. We speculate that more physically-based methods could reduce the number of structures to be analyzed.

Number of cells	Number of structures B_2O_3	C_xN_y
2×2	1	3
3×3	2	9
4×4	4	47
5×5	9	432
6×6	58	6129

TABLE 5.2: Number of inequivalent polymorphs obtained for the B_2O_3 monolayer and the C_xN_y compound for various cell subdivisions.

Finally, a comment regarding the comparison with experiments. The polymorphs produced by the process described above constitute the complete set of all the structures that satisfy the constraints used in the generation process. However, the fact that a structure satisfies these constraints does not necessarily mean that it is physically observable. In particular, the low energy polymorphs obtained by the algorithm might be hard to observe due to the kinetics of the synthesis process, or the interaction with the substrate may change the energetic order of the structures. Moreover, it should be noted that the experiments are performed at a low but finite temperature, while our calculations refer to $T = 0$ K. Finally, structural instabilities, such as out-of-plane bending and phonons with imaginary frequencies, must be checked to verify the stability of the resulting structures.

Despite the issues discussed above, we believe this algorithm is quite valuable. It allows us to make general predictions of low energy structures, which might be observed in experiments, and to investigate the local structure of a compound to extract general and meaningful trends, see for example Sec. 5.2.2 and 5.3.3.

5.5 Key results

The key insights we gained in this chapter can be summarized as follows:

- Using a set of physically motivated rules, it is possible to assess from first principles the stability of different compounds at $T = 0$ K, without any prior knowledge of their stoichiometry or structure.
- The high flexibility of T_nH_m-type boria polymorphs allows them to increase their stability by counter-rotating the two building blocks in the unit cell.

[13] Our implementation of the algorithm rely on filling a matrix and checking its structure, more advanced computational methods can clearly speed-up the code, at the cost of increased complexity.

- The T_0H_2 boria structure is one of the softest two-dimensional materials, presenting a wide band gap and large pores of 5.45 Å in diameter.
- The presence of a set of C_xN_y polymorphs nearly degenerate in energy suggests that the experimental samples of carbon nitrides may contain domains with different structures.

Chapter 6

B_2O_3 monolayer: equilibrium crystalline structure

In this chapter we use the lowest energy B_2O_3 polymorph obtained in the previous chapter as a candidate for the structure of a recently synthesized boron oxide monolayer on *Pt(111)*. We study the properties of the polymorph on the *Pt(111)* substrate, obtaining a remarkable agreement with experimental measurements. These results allow us to identify the newly synthesized material as a boria monolayer composed solely of boroxol rings, a structure long predicted but never observed, which can help to understand the unique properties of 3*d* boria.

We begin our discussion by analyzing the influence of the *Pt(111)* substrate on the structural and electronic properties of the boria monolayer (Sec. 6.1). We then describe the typical localized defects in the monolayer, focusing on the defective structures observed in the experiments (Sec. 6.2).

The work presented in this chapter is the result of a fruitful collaboration with the STRAS laboratory in Trieste, which synthesized the material and performed the experimental analysis. In particular, I worked closely with Teresa Zio, a PhD student who performed most of the syntheses and measurements on the boria monolayer. The bulk of this chapter is adapted from Ref. [43], but it also includes new material (Sec. 6.1.4, 6.2.2 and 6.2.3) and additional discussions.

6.1 Structure and electronic properties of $B_2O_3/Pt(111)$

As discussed in Sec. 5.4, the lowest energy polymorph obtained by the algorithm presented in the previous chapter does not necessarily correspond to the structure observed in experiments. However, such structure could be a good starting point for describing the experimental system. In this section, we will use the T_0H_2 polymorph, *i.e.* the lowest energy structure of a boria monolayer, as a candidate for the structure of a two-dimensional compound of boron and oxygen atoms synthesized on *Pt(111)*. We first review the experimental properties of the system relevant to our analysis, and then develop and characterize an atomic model for the monolayer on the substrate.

6.1.1 Experiments on two-dimensional B_2O_3

The first synthesis and characterization of a two-dimensional compound of boron and oxygen atoms is very recent [43]. The system can be synthesized on $Pt(111)$ using two different approaches. The first one is based on the deposition of boron atoms in ultrahigh vacuum (UHV) and a subsequent exposure to oxygen, both performed at a substrate temperature of 770 K, followed by a final flash annealing at 820 K in

UHV [43, 44]. *B* atoms can dissolve in platinum and recent studies have shown that the lowest-energy position of the boron atom is the interstitial sites between the first and the second platinum layers [208]. Moreover, boron atoms can easily diffuse in platinum at typical growth temperatures [208]. Thus, the deposition of boron atoms leads to their segregation in platinum, while subsequent exposure to oxygen at high temperatures allows the O_2 molecule to split on the *Pt* surface and to combine with the highly mobile *B* atoms on the surface. The second synthesis procedure involves the deposition of boron atoms in an oxygen atmosphere at a substrate temperature of 770 K, followed by a flash annealing at 820 K in UHV [43]. This second approach produces layers with higher coverage and more ordered structures, and is thus generally preferred [44].

The synthesized structure is analyzed using a combination of different techniques. The *B/O* ratio is estimated using μ-XPS measurements, which return a value of 0.60 ± 0.15, compatible with a B_2O_3 stoichiometry [43]. This result is further supported by NEXAFS measurements, which showed typical features of *B* atoms bonded to three oxygens [44].

The structure of the layer is analyzed with both STM imaging and microspot Low-Energy Electron Diffraction (μLEED). The measured lattice constant of the layer obtained with both approaches is 8.57 ± 0.03 Å. Moreover, the analyses show the presence of a variety of moiré patterns and crystalline domains with multiple orientations. The STM images further suggest that the layer is atomically thin and has a honeycomb structure with slightly triangular pores.

6.1.2 Structure

The extensive computational analysis presented in Chapter 6 has shown that the T_0H_2 structure is the polymorph of the B_2O_3 monolayer with the lowest energy. The unit cell of this polymorph features two connected $B_3O_3\text{Ø}_3$ units, with an angle between their centers and the shared oxygen of approximately 136°. This results in a honeycomb structure with slightly triangular pores, see the T_0H_2 structure in Fig. 5.2. Moreover, the equilibrium lattice parameter for this system is 8.83 Å, slightly larger than the measured lattice constant[1] (8.57 ± 0.03 Å). These results make the T_0H_2 structure an ideal candidate for the experimentally observed monolayer.

To assess whether this structure is stable on the platinum surface and reproduces the experimentally observed properties, we consider a commensurate supercell for the T_0H_2 structure on *Pt(111)*, obtained as follows. Given two $2d$ lattices, commensurate supercells can be identified by the ratio of the two lattice parameters and the angle of rotation θ between the two lattices, see Appendix D. If we limit the size of the supercell, we obtain a finite set of commensurate supercells which can be easily identified. We developed an algorithm that, given the symmetries of two $2d$ lattices with lattice parameters a and b, and a maximum supercell size, generates the set of all the possible b/a ratios and relative rotations θ of the two lattices that produce a commensurate supercell. We describe this algorithm in detail in Appendix D. Since both the top layer of the *Pt(111)* surface and the T_0H_2 structure have hexagonal symmetry, we use this process to identify possible commensurate supercells of two hexagonal lattices. To identify the supercell that best reproduces the experimental properties, we relax the positions of a selected set of structures using Density Functional Theory (DFT) calculations. We consider three *Pt* layers and a slab geometry,

[1] Note that this difference in the lattice parameter could be reduced by the presence of an underlying substrate. Moreover, as shown in Sec. 5.2.2, this structure is very flexible and can thus be easily compressed without major changes in its energy.

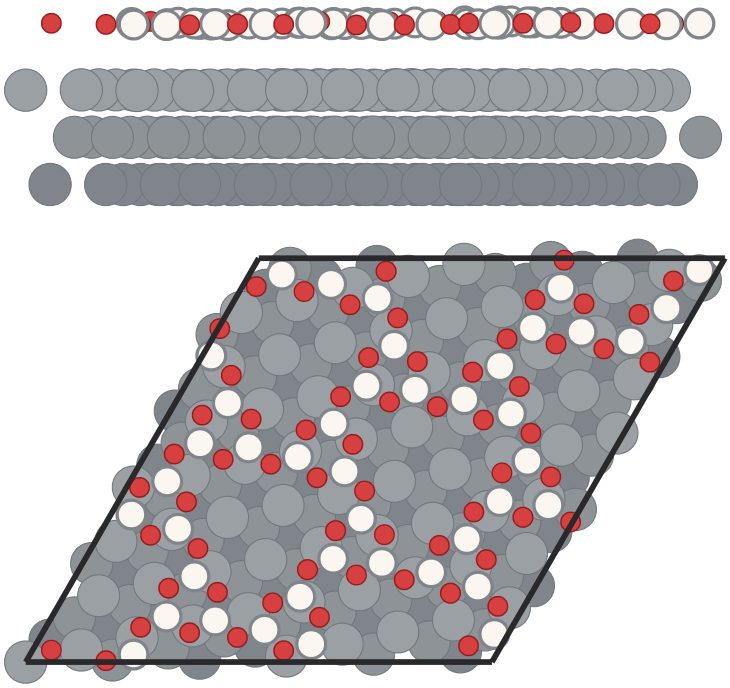

FIGURE 6.1: Supercell for B_2O_3/*Pt(111)* that best match the experimentally measured lattice parameter of the overlayer. The supercell is shown in both side (top) and top (bottom) views. Black lines identify the cell, which has hexagonal symmetry and lattice parameter of 22.79 Å. White and red circles represent boron and oxygen atoms, respectively. Platinum atoms are represented with a grey scale based on their distance from the surface. Note that the overlayer has the same structure as the T_0H_2 polymorph discussed in Sec. 5.2.3, except for a small contraction of the lattice parameter.

while the selected set of supercells contains all structures with less than 350 atoms and a lattice parameter of the overlayer in the range $a \in [8.31; 8.83]$[2].

In Fig. 6.1 we present the supercell obtained using this procedure and which best matches the experimental lattice parameter. In this supercell, the T_0H_2 structure is slightly compressed, with a lattice parameter of 8.615 Å, very close to that measured in experiments (8.57 ± 0.03 Å). There is a rotation of 6.89° between the lattices of the overlayer and the substrate, and the *Pt* lattice is rotated by about 13° relative to the basis vector of the supercell. The moiré supercell has a lattice parameter of 22.79 Å and contains 306 atoms, of which 105 atoms of the overlayer and 67 *Pt* atoms for each of the three layers of the substrate.

The optimize structure features a rather flat configuration of the boria monolayer, with very small buckling of only 0.20 Å. The overlayer is detached from the surface, with an average distance between the two of 3.26 Å. The compression of the T_0H_2 structure induced by the overlayer slightly modifies the structural properties of the system. For example, reducing the angle between the boroxol groups from 135.7° in the free-standing structure to 127.8° in the supported system. However, we observe no major changes in the structure of the overlayer induced by the *Pt* surface. We present in Fig. 6.2, the simulated STM image of the system, obtained by

[2]Commensurate supercells are identified by the ratio b/a of the lattice parameters of overlayer and substrate and their relative rotations. In this analysis, we set the lattice parameter of the *Pt(111)* surface according to the equilibrium distance between *Pt* atoms in the bulk, $b = 2.784$ Å, obtained via DFT calculations. This value is very similar to the one measured in experiments ($b = 2.77$ Å [28]), being only 0.5 % larger.

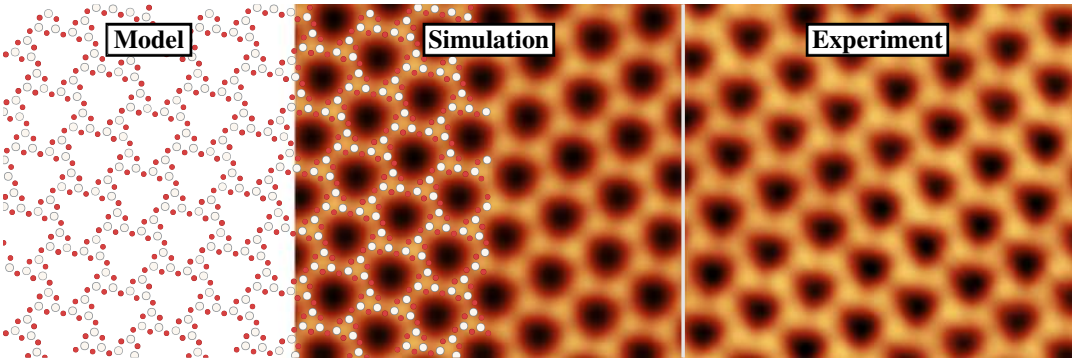

FIGURE 6.2: Comparison between the simulated and experimental STM images. From left to right, atomic model, simulated STM image and experimental STM image. The atomic model refers to the supercell in Fig. 6.1, but for clarity, only B and O atoms are shown. The color scheme of the atomic models is the same as in Fig. 6.1. The vertical side of the image corresponds to 50 Å. Experimental image courtesy of Teresa Zio (STRAS laboratory, CNR-IOM, Trieste, Italy).

Tersoff-Hamann rendering [209] of the DFT calculation, smoothed by a mild gaussian broadening. The simulated STM image matches the experimental structure very well, and correctly reproduces the triangular shape of the pores[3]. In particular, we can identify the bright spots in the experimental STM images with boroxol groups, an hypothesis later confirmed by accurate dI/dV conductance map measurements performed at 8.5 K, which allowed us to resolve the positions of individual O atoms in the layer [43, 44].

The excellent agreement between simulation and experimental data allows us to identify the T_0H_2 polymorphs and the supercell shown in Fig. 6.1 as the structure of the experimental system. This is particularly noteworthy, since it is the first reported synthesis of a structure containing boroxol units [43]. As discussed in Sec. 1.1.2, these units are present in the liquid and amorphous phase, but their absence in the known crystalline structures of boria has been a long-standing issue [31]. The discovery of a system composed exclusively of these units opens exciting new prospects on the physics of boria. For example, it is not known why the synthesis of a boroxol-based crystal is relatively simple in $2d$ but not in $3d$, or whether it is possible to produce crystalline structures with a mixture of $B\emptyset_3$ and $B_3O_3\emptyset_3$ units. We thus believe that the use of two-dimensional systems, with the ability to image their structure and dynamics in real space using standard surface techniques, can shed light on the peculiar behavior of three-dimensional boria.

6.1.3 Interaction with the substrate

The relatively large distance between overlayer and substrate (3.26 Å) and the absence of direct bonds between them, as shown in Fig. 6.1, suggest a weak interaction between the two subsystems. This is further supported by the presence of numerous B_2O_3 crystalline domains with multiple orientations relative to the substrate in the experimental samples.

[3] In the following, we will need to distinguish between the B_3O_3 rings, which are the building block of the system, and the larger ring structures corresponding to the pores. To avoid confusion, in this thesis we will always refer to the latter as "pores", and we will assign to such structures a number of side equal to the number of boroxol groups that define its perimeter. For example, the crystalline structure discussed in this section and shown in Fig. 6.1 has hexagonal pores, as each opening is surrounded by six B_3O_3 rings.

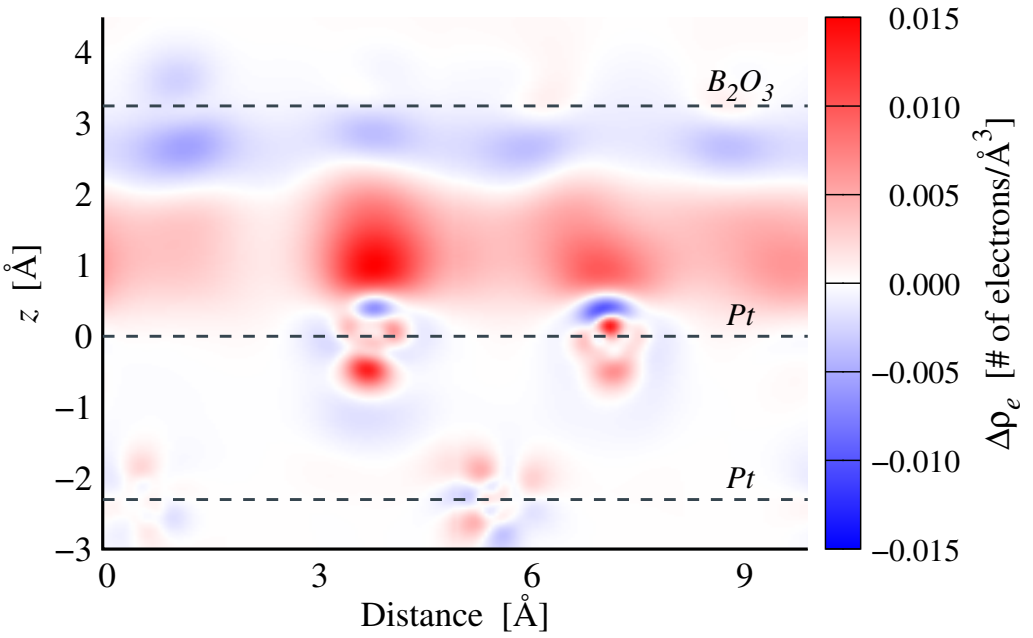

FIGURE 6.3: Electron charge density difference $\Delta\rho_e$ for the $B_2O_3/Pt(111)$ system in Fig. 6.1 along a path connecting the centers of three B_3O_3 rings. The electron charge density difference is computed as the difference in density of electron between the entire system ($B_2O_3/Pt(111)$) and the sum of its components (*Pt(111)* substrate and B_2O_3 overlayer). The vertical axis represents the distance from the topmost layer of the substrate and horizontal dashed lines identify the average position of the B_2O_3 overlayer and the two topmost layers of *Pt(111)*.

To assess the interaction between overlayer and substrate, we calculate the charge transfer between the two systems. We use the commensurate supercell presented in Sec. 6.1.2 as the basis for our calculations. In Fig. 6.3 we present the differential electron density distribution, *i.e.* the difference between the electron density in the entire system and the sum of the densities in the two constituent subsystems (free-standing boria and *Pt* substrate). As can be inferred from the magnitude of the values in the colorbar, there is no significant charge transfer between the overlayer and substrate, with only a small polarization occurring at the interface.

We also evaluate the adhesion energy of the overlayer to the substrate, defined as the difference between the total energy of the system and the sum of its two separate components (free-standing boria and *Pt* substrate). This calculation returns a very small value,

$$E_{adh} = -0.41 \frac{\text{eV}}{B_2O_3 \; formula \; unit} = -0.019 \, \text{eV/Å}^2 , \tag{6.1}$$

which further supports the presence of weak interactions between the overlayer and the substrate. The adhesion energy of $B_2O_3/Pt(111)$ is intermediate between those of germania (-0.0271 eV/Å^2) and silica (-0.0134 eV/Å^2) bilayers on the same substrate, and is very close to that of the silica bilayer on *Ru(0001)* (-0.0176 eV/Å^2) [28], which can withstand mechanical exfoliation and transfer to a new support [21]. Thus, these results show that the boria monolayer on *Pt(111)* presents interactions similar to those of other amorphous 2*d* network-forming systems, and suggest that mechanical exfoliation of the monolayer from the substrate could be feasible[4].

[4]Experimental attempts at mechanical exfoliation are underway, and the preliminary results are promising, though not conclusive [44].

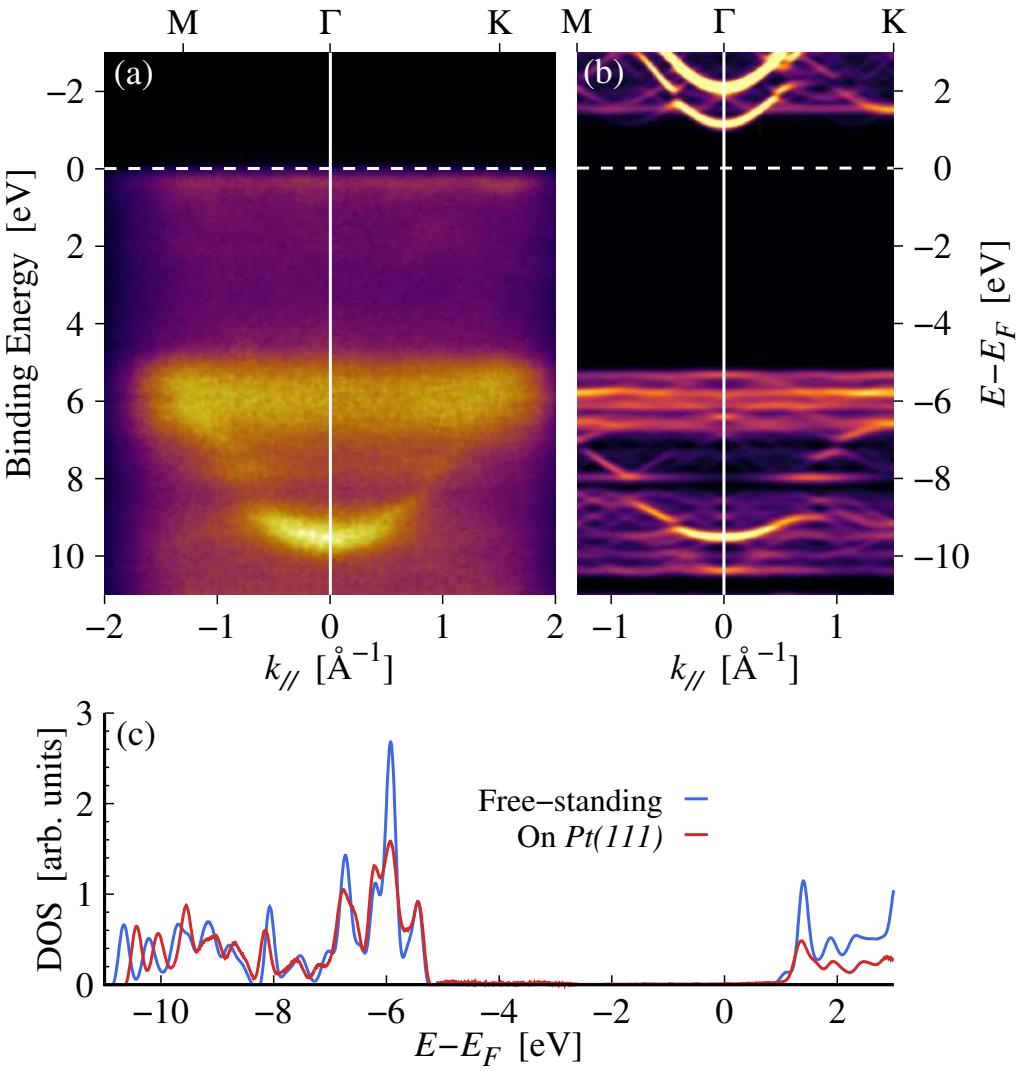

FIGURE 6.4: Comparison of the electronic structure of the free-standing and supported B_2O_3 monolayer. (a) ARPES measurements of the bands structure of B_2O_3/*Pt(111)*. (b) Simulated band structure of the free-standing B_2O_3 monolayer unfolded on the first Brillouin zone of *Pt(111)*. The color represents the spectral weight, which quantifies the overlap between the electronic states of the supercell and those of the unit cell [210]. Specifically, the color map ranges from black, representing no overlap, to bright yellow, which represents high overlap. (c) Comparison of the electronic density of states (DOS) of the free-standing (blue) and supported (red) B_2O_3 monolayer. The DOS for the supported system is obtained by projecting the full DOS onto the atoms of the monolayer. The unfolded band structure was calculated with the `unfold-x` code [210, 211]. Experimental image courtesy of Teresa Zio (STRAS laboratory, CNR-IOM, Trieste, Italy).

Due to the weak interaction between substrate and overlayer, the electronic properties of the latter resemble those of the free-standing system presented in Sec. 5.2.3. In particular, the projected density of states of the overlayer on *Pt* matches well with that of the unsupported system, as shown in Fig. 6.4 (c). We also obtain a good agreement between the band structure obtained by angle-resolved photoemission spectroscopy (ARPES) (Fig. 6.4 (a)) and that of the free-standing monolayer unfolded

on the first Brillouin zone of Pt(111) (Fig. 6.4 (b))[5]. The calculation correctly reproduces both the low-dispersion region at binding energies between 5 eV and 7 eV and the larger dispersion at a binding energy of approximately 9 eV.

6.1.4 Alternative structural model

Previous analyses in the literature on boron-oxygen monolayers have focused on a structural model with two boroxol rings B_3O_3 in the unit cell, connected by a *B-B* bond [42, 212, 213]. This results in a system with *BO* stoichiometry qualitatively similar to our T_0H_2 model for the overlayer, except for the absence of oxygen bridges between the boroxol rings. Although this structure can easily be discarded due to its *B/O* ratio (1.00), which is incompatible to that observed in the experiments (0.60 ± 0.15), we nevertheless decide to test the structure and the stability of this system on *Pt(111)*.

The building block of the *BO* monolayer is the boroxol ring B_3O_3, *i.e.* a hexagonal ring of alternating boron and oxygen atoms. In the free-standing equilibrium structures, the *B-O* distance within the rings is 1.39 Å and the rings are perfect hexagons, exactly as those in the T_0H_2 model. The boroxol rings are connected via a *B-B* bond of length 1.72 Å, and unlike the relaxed T_0H_2 structure, the two boroxol rings are not rotated relative to each other. The relaxed structure features a hexagonal cell with lattice parameter of 7.82 Å, and its repetition produces large hexagonal pores, whose vertices are occupied by B_3O_3 units, as shown in Fig. 6.5. These large pores are nearly perfect hexagons, contrary to the T_0H_2 model where the presence of an oxygen hinge between the two units produced slightly triangular pores. Regarding the electronic properties, the *BO* monolayer is an insulator with a band gap of approximately 3.62 eV. The band gap is indirect, with the HOMO and LUMO levels at Γ and *K*, respectively.

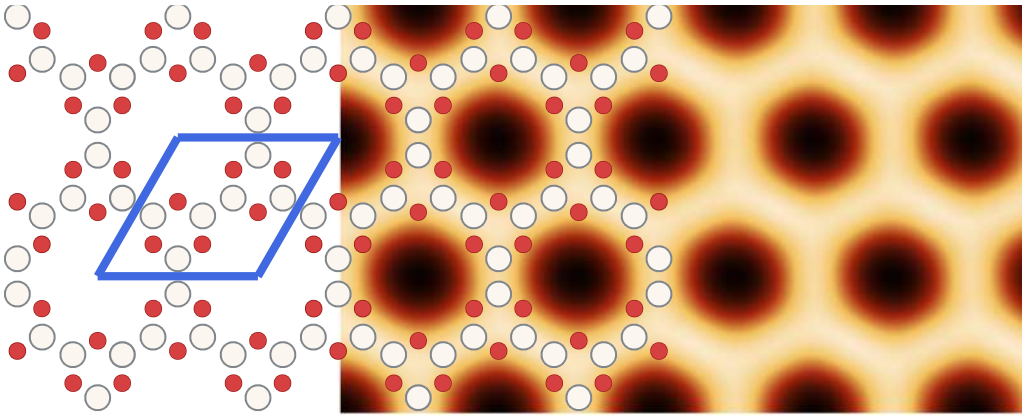

FIGURE 6.5: Structure and simulated STM images of the free-standing *BO* monolayer. The unit cell of the system is highlighted in blue and the vertical side of the image is 20 Å. The color scheme of the atomic models is the same as in Fig. 6.1.

The experimentally measured lattice parameter for the boron oxygen compound is 8.57 ± 0.03 Å. This is 14% higher than that of the free-standing *BO* monolayer, which is an exceedingly high strain value for a supported system [28]. Nonetheless, we construct several commensurate supercells for the *BO* monolayer on *Pt(111)*. We

[5] To align the experimental and simulated band structures we vertically shift the latter. The vertical shift is equal to the value required to match the position of the first peak of the projected density of states below Fermi.

use the approach described in Sec. 6.1.2, considering lattice parameters for the supported system in the range [6.9; 8.4] Å. Once properly relaxed, most supercells fail to produce a flat continuous monolayer like the one observed in the experiment. Typically, strong compression or expansion of the overlayer lattice parameter causes the *B-B* bonds between the boroxol units to break, and these rings to tilt toward the substrate to saturate the resulting dangling bonds. This also occurs for the supercell equivalent to the one presented in Fig. 6.1, which has an overlayer lattice parameter closest to the experimental value. When the strain forced on the *BO* by the substrate is small enough to stabilize a flat connected monolayer[6], the simulated STM images are generally much more complex than the experimental ones and, in any case, lack the characteristic triangular openings.

These results allow us to completely rule out the *BO* system as a possible structure to describe the experimental sample.

6.2 Points defects in supported B_2O_3 monolayer and other network modifications

The B_2O_3 monolayer on *Pt(111)* can easily form large coherent crystalline domains, such as the one shown in Fig. 1.5 (a). However, when observed with the STM, this material sometimes presents some localized features inconsistent with any periodic pattern, such as hexagonal pores with a higher density of states that their surroundings or drops of intensity in the expected location of a $B_3O_3Ø_3$ unit. These features are localized defects in the system, and can be traced back to the presence of adatoms at the surface or the removal of specific units from the overlayer. The analysis of these defects highlights some properties of this monolayer, particularly its interaction with the substrate and the constraints on its network structure due to the internal structure of the boroxol units.

6.2.1 Filling pores by *Pt* adatoms

Regions with higher intensity in the STM image could be due to a shorter distance between the tip and the sample, or to a higher density of states localized in these regions [209]. In the case of B_2O_3/*Pt(111)*, the regions of higher intensity are generally located in the center of the pores formed by six $B_3O_3Ø_3$ units. Since these pores are rather large ($\sim$ 5.5 Å in diameter), this increased intensity is likely due to the presence of additional atoms inside the pore. Possible candidates are *Pt* adatoms. Although the *Pt(111)* surface is cleaned by a cycle of sputtering with Ar^+ atoms and high temperature annealing [44] before the synthesis process, the presence of *Pt* adatoms on the surface cannot be excluded.

To assess this hypothesis, we consider supercells of B_2O_3/*Pt(111)* with the addition of up to 4 *Pt* adatoms onto the *Pt(111)* surface. The supercell used is presented in Fig. 6.1, with an angle of approximately 7° between the basis vector of the *Pt* surface and the overlayer. Due to this relative orientation of the two lattices, there are several non-equivalent positions where the *Pt* adatoms can be placed. In this analysis, we mainly consider sites for the adatoms close to the center of the pore, but in the experimental sample we expect a greater variety of relative positions of the adatoms and the overlayer, also due to the large number of possible orientations between B_2O_3 and *Pt* surface, as shown in Appendix D. For each considered system,

[6] This occurs for lattice parameters of the overlayer in the range [7.3; 8.3] Å.

we relax the particle positions and generate a simulated STM image using the same methods as in Sec. 6.1.2.

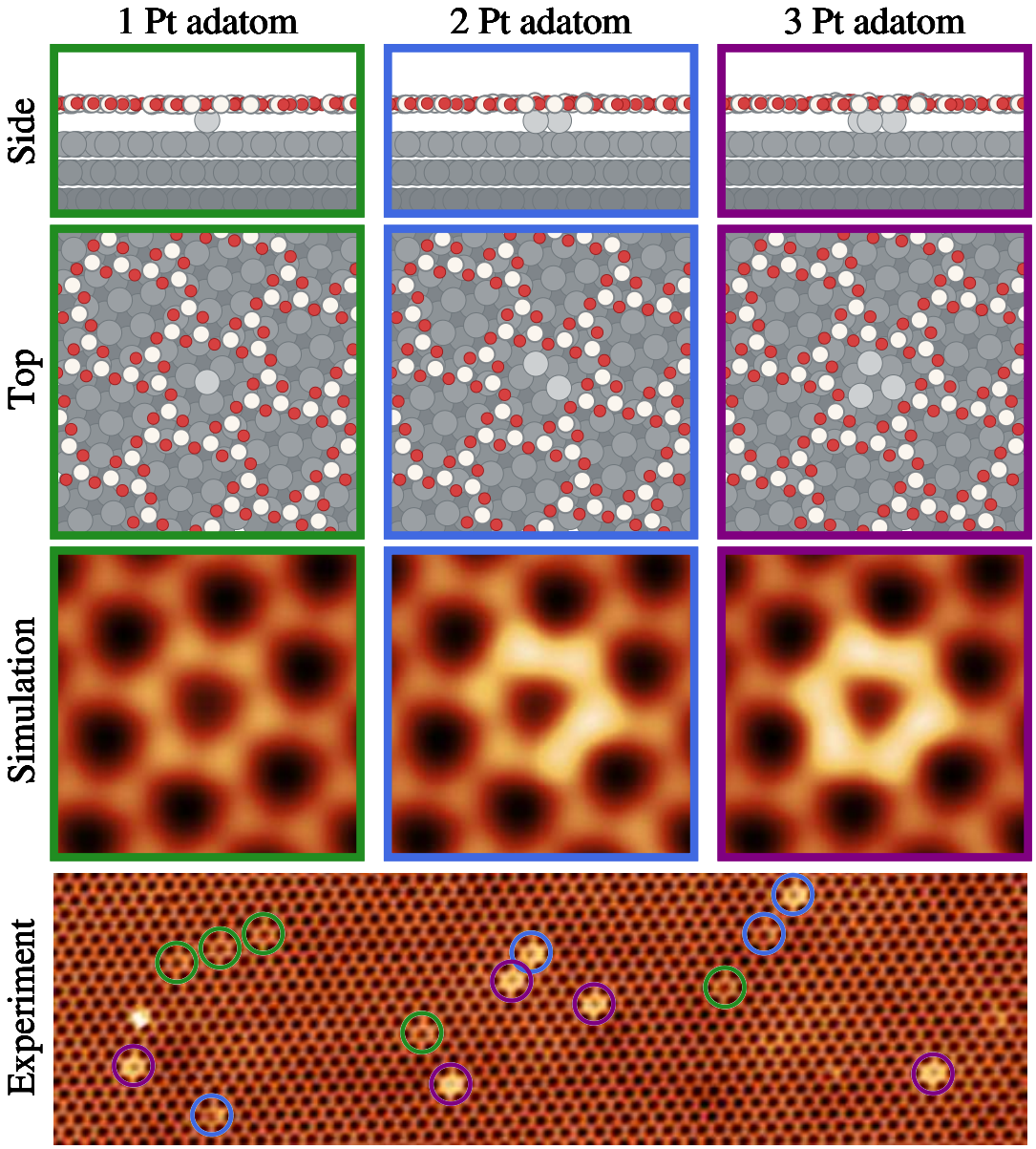

FIGURE 6.6: Comparison of the experimental STM image of a defective crystal (bottom) with those produced by three different structural models, which involve the addition of one (green), two (blue) or three (purple) *Pt* adatoms to the supercell of B_2O_3/*Pt(111)* presented in Fig. 6.1. Each structural model is presented in both side (top) and top (center) views, while its simulated STM image is shown at the bottom. In the experimental STM image, point defects are highlighted with a circle, the color of which corresponds to the structural model that produces the most similar simulated STM image. The size of the square panels is 25 Å$\times$ 25 Å, while the panel with the experimental image is 450 Å$\times$ 125 Å. The color scheme of the atomic models is the same as in Fig. 6.1. Experimental image courtesy of Teresa Zio (STRAS laboratory, CNR-IOM, Trieste, Italy).

We present the results for supercells with up to three *Pt* adatoms in Fig. 6.6. Due to the relative orientation of the overlayer compared to the substrate, in the system with a single adatom, the additional *Pt* is placed at a Hexagonal Close-Packed (HCP) position, while in the systems with two or three adatoms the additional *Pt* are placed

at Face-Centered Cubic (FCC) sites. As can be seen in the top panels of Fig. 6.6, the addition of *Pt* adatoms does not buckle the overlayer, which remains almost perfectly flat even when a pyramid of 4 adatoms is placed inside the pore. This is likely due to the saturation of all the chemical bonds in the overlayer, which determines its high stability. Although the adatoms do not significantly alter the structure of B_2O_3, they locally increase the density of states near the pore in which they are placed, producing structures similar to those observed in the experiments. Increasing the number of adatoms results in a local increase in intensity in the simulated STM images compared to the surrounding environment, and the asymmetric arrangements of the adatoms within the pore lead to a higher intensity of the $B_3O_3Ø_3$ units closer to the *Pt* atoms, as is the case with supercell with two neighboring adatoms. We tentatively assign the bright spots in the experimental image to our simulated systems in the bottom panel of Fig. 6.6.

Although the most common point defects are those shown in Fig. 6.6, we also tried placing *Pt* adatoms in other positions than those shown in the figure. In particular, placing a 4 adatom pyramid inside a pore of the overlayer does not produce significant changes compared the three adatoms presented in Fig. 6.6, except for a hexagonally shaped bright spot in the simulated STM image. Instead, placing a *Pt* adatom exactly under the center of a B_3O_3 rings raises the units by approximately 1.1 Å above the flat overlayer, producing a simulated STM image with three bright dots. Similar features can be observed in the experimental images, but they are quite rare.

6.2.2 Vacancies

In the STM images of the experimental sample, the position occupied by a boroxol group sometimes seems to be empty, leading to the fusion of adjacent pores into a three-lobed structure. Although these vacancy defects are very rare in the synthesized monolayer, they can be produced in large quantities by the desorption of *CO* molecules previously intercalated between the oxide film and the *Pt* substrate [44], as shown in the bottom panel of Fig. 6.7. A possible cause for the formation of these defects during the *CO* desorption is the Mars-van-Krevelen mechanism, in which an adsorbate is oxidized by oxygen taken directly from the oxide film [44, 214]. If the vacancies produced in the overlayer are close to each other, they can merge, causing a localized degradation of the network.

To describe the vacancies observed in the experiment, we simulate configurations with a selected number of boron and oxygen atoms removed. We use the supercell already presented in Fig. 6.1 as template, and we fully relax the atomic positions after the removal of the selected atoms. In Fig. 6.7; we present the results for three different systems obtained after the removal of one *B* atom, one BO_3 unit and one entire boroxol B_3O_3 rings. In all cases, the removal of atoms creates unsaturated bonds in the overlayer, which are passivated by the *Pt* substrate. Despite the different amount of material removed in the three cases in Fig. 6.7, the simulated STM images are strikingly similar, with a three-lobed pore. Such structure appears even when residual material from the missing $B_3O_3Ø_3$ unit is present in the center of the pore. The lack of signature due to leftover material in the simulated image can be due to its greater distance from the tip, as this region is closer to the substrate, or to a lower local density of states due to the connection with the metallic substrate[7].

[7]Despite their appearance, these three-lobed pores present some small variations in intensity within them, which can be detected by looking at changes in concavity of the image intensity. For example,

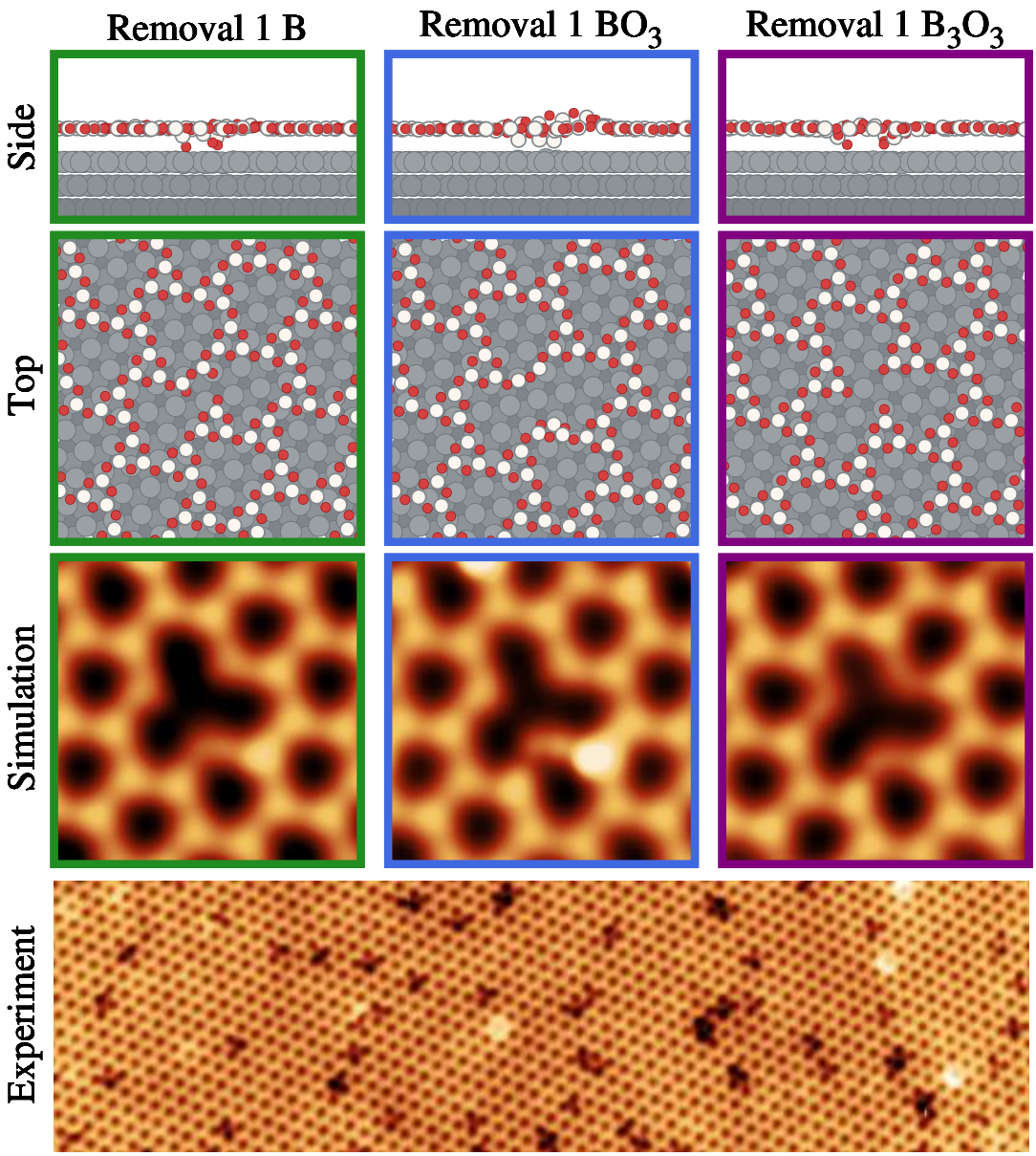

FIGURE 6.7: Comparison of the experimental STM image of a defective crystal after the desorption *CO* molecules (bottom) with those produced by three different structural models, which involve the removal of one B atom (green), one BO_3 unit (blue) or a boroxol B_3O_3 ring (purple) to the supercell of *B_2O_3/Pt(111)* presented in Fig. 6.1. Each structural model is presented in both side (top) and top (center) views, while its simulated STM image is shown at the bottom. The size of the square panels is 30 Å× 30 Å, while the panel with the experimental image is 450 Å× 125 Å. The color scheme of the atomic models is the same as in Fig. 6.1. Experimental image courtesy of Teresa Zio (STRAS laboratory, CNR-IOM, Trieste, Italy).

Since all the vacancy types considered above result in a stronger bonding between monolayer and substrate, we expect different relative orientations of film and substrate, and different positions of the removed atoms, to produce slightly different structures. For example, consider the central panel of Fig. 6.7, corresponding to the removal of a *BO_3* unit. In that case, the unsaturated boroxol ring just below the

in Fig. 7.5, the three-lobed structure in the top right of panel (a) is detected in the panel (b) as three circular pores, two of similar size and a larger one.

removed unit in the top view panel, bonds to its nearest *Pt* atoms of the substrate. However, due to the particular orientation and position of both the substrate and the overlayer, this connection to the substrate makes one of its remaining bridging oxygens to be raised approximately 1.6 Å above the average height of the monolayer. This causes the bridging oxygen and its neighboring borons to be much closer to the tip of the STM than the remaining monolayer, and thus these atoms appear as a bright protrusion just below the vacancy defect. Since this effect is mainly due to the relative position of the unsaturated bonds and their nearest *Pt* atoms, different registries can result in defects with slightly different appearances.

All the models presented in Fig. 6.7 produce simulated STM images similar to each other and to the experimental images. Due to such strong similarity, it is not possible to discern the precise atomistic structure of the vacancy in the experimental sample. The synthesized material likely features different types of vacancy, which, however, appear similar under the STM imaging. The experimental image presented at the bottom of Fig. 6.7 shows the presence of a large number of structures, which are more complex than the single vacancy-like defect discussed above. These structures can be produced by multiple vacancies, and we expect them to feature the same characteristics as the single vacancies discussed above, namely, the formation of bonds between overlayer and substrate and the presence of filaments of residual materials within the pores, which are hard to resolve with the STM.

6.2.3 Stone-Wales defect

Most of the defects observed in the experimental system can be linked to the presence of *Pt* adatoms within the pores or vacancies in the overlayer. One type of defect that is not observed in the experimental sample is the Stone-Wales defect. As discussed in Sec. 3.2.2, this defect results from a bond-switch move which transforms a set of four hexagonal pores into two pentagonal and two heptagonal pores. Stone-Wales defects are found in several 2*d* materials, such as graphene [162] and silica bilayer [26], where they are expected to play a crucial role in the relaxation of the structure and the formation of an amorphous layer [163]. These defects are related to the hexagonal symmetry of the system, and thus should be a general feature of two-dimensional hexagonal materials [128]. We notice, however, that B_2O_3, although having an underlying hexagonal Bravais lattice, does not have the full hexagonal point group symmetry of graphene and therefore we may expect some differences.

We address the absence of observed Stone-Wales defects in the B_2O_3 by analyzing a structural model for the defect using *ab initio* methods. Since we are simulating the system under periodic boundary conditions, the simulation cell has to be large enough to minimize the interaction between a defect and its periodic images. We select a cell with 375 atoms of the overlayer and a lattice parameter of approximately 44.4 Å. Due to the size of the cell and the weak influence of the substrate on the structure of the monolayer, we simulate the overlayer without the *Pt* substrate to reduce the complexity of the calculation.

Since we expect large distortions in the network when a bond-switch move is performed, the preparation of the cell requires special care. We construct the system as follows. We start with a monocomponent crystalline system with a hexagonal lattice and we perform a bond-switch move, introducing a Stone-Wales defect. We connect the particles with springs and we relax the resulting structure with the classical Keating potential [161]. We then replace each particle with a B_3O_3 ring, with an orientation equal to the phase of the 3-fold local order parameter calculated in the monocomponent system, and we place a oxygen at the midpoint between two

neighboring boroxol rings. The resulting system is then relaxed using DFT. To understand the stability of the structure against buckling, the final relaxation step is performed in two different ways. In the first case, we force the atoms to maintain a strict planar geometry; in the second case, before the relaxation, we introduce a small perturbation in the z coordinates of the atoms, allowing for out-of-plane distortion of the network.

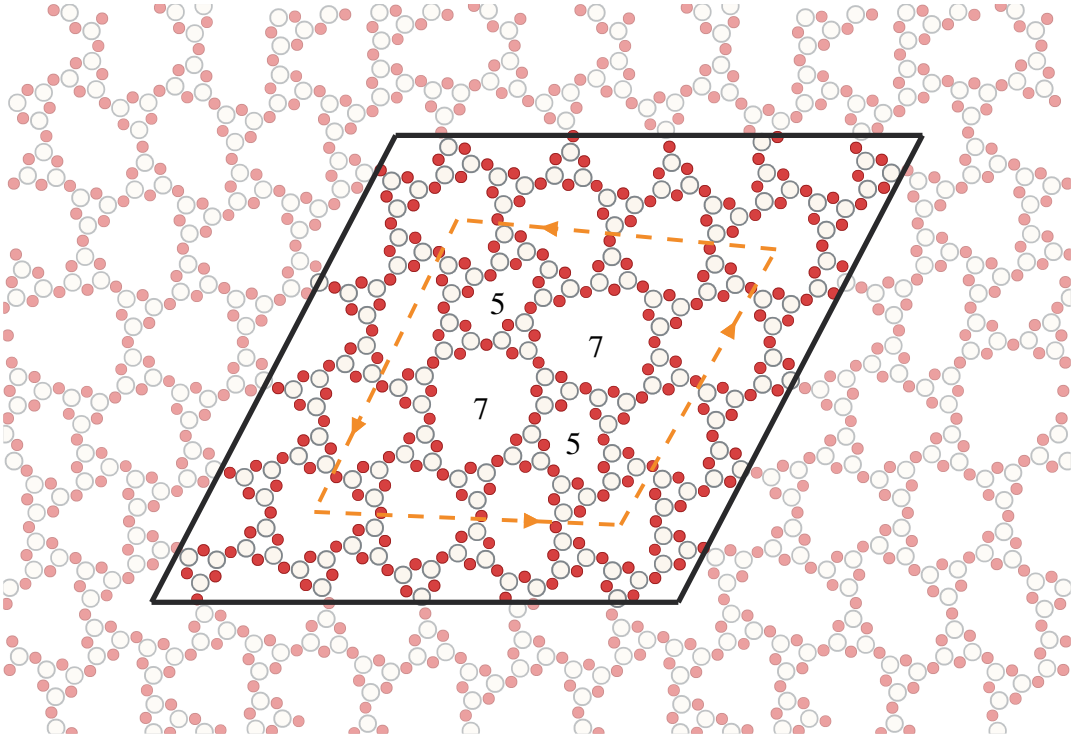

FIGURE 6.8: Relaxed structure of a Stone-Wales defect in a free-standing B_2O_3 monolayer. The out-of-plane coordinate of each atom is fixed to zero. For clarity, the non-hexagonal pores are highlighted with a number in their center, which represent the number of boroxol B_3O_3 rings defining them. The solid black line represents the unit cell, while periodic images of the system are shown with greater transparency. The orange dashed path highlights the change in direction of the hexagonal pores, with the arrow pointing in the same direction as the hexagonal pores. The color scheme of the atomic models is the same as in Fig. 6.1.

In Fig. 6.8 we present the relaxed structure of a Stone-Wales defect when the atoms are fixed to the plane $z = 0$. The defect introduces large distortions into the network and strongly alters the shape of the hexagonal pores in the cell. This effect is likely due to the non-straight bond between neighboring $B_3O_3Ø_3$ units. As discussed in Sec. 5.2.2, the equilibrium angle between two boroxol groups and their shared oxygen is approximately 136° for the free-standing structure. Due to the hexagonal symmetry of the B_3O_3 ring, these bent bonds between the boroxol groups are all clockwise or counterclockwise within the same unit, and neighboring units always have opposite rotations. Thus, under these constraints, the sum of rotations of the boroxol groups in a closed path along the perimeter of a pore should be zero. While this is the case for pores with an even number of sides, like the hexagonal pores in the crystalline layer, it is not possible for pores with an odd number of sides, such as the pentagon and the heptagons involved in a Stone-Wales defect. This forces some angles between the boroxol groups to be straight, such as the edge connecting the two heptagonal rings in Fig. 6.8, increasing the energy of the system

and introducing a distortion into the network. Unlike graphene, where the impact of Stone-Wales defects is short-range [215], in the B_2O_3 monolayer these defects distort the network on larger length scales. For example, the hexagonal pores enclosing the central defect always point counterclockwise, as depicted by the orange dashed lines in Fig. 6.8. As we will discuss in Sec. 7.1, it is not possible to join two crystalline regions with different orientations of the pores without using line defects. Therefore, the presence of different pore orientations near the Stone-Wales defect suggests that its effects are not local, but extend to large length scales[8]. Simulations on larger cells are required to fully describe the behavior of the Stone-Wales defect and the line defects associated with its presence in the network.

The estimated formation energy of the Stone-Wales defect shown in Fig. 6.8 is 7.74 eV[9], relative to the free-standing crystalline system. This value is higher than that found for other two-dimensional hexagonal systems, such as free-standing graphene ($4.5 - 5.3$ eV [128, 162]) and silica bilayer on *Ru(0001)* (4.3 eV [163]), likely due to the long-range distortions induced in the B_2O_3 by the defect and the presence of straight bonds between the $B_3O_3\emptyset_3$ units.

The defect formation energy can be reduced by allowing the overlayer to relax in the out-of-plane direction. Indeed, the presence of straight connections between the units in Fig. 6.8 is due to the strict two-dimensionality of the system. In a non-strictly planar system, these bonds can bend in the out-of-plane direction, reducing their angle and decreasing the energy of the structure. Relaxing the structure of a Stone-Wales defects with small out-of-plane perturbations significantly reduces the energy of the structure, which becomes similar (~ 0.53 eV) to that of the crystalline layer, but introduces a large out-of-plane buckling of approximately 8 Å. These fluctuations are the results of the large distortion of the network already observed in Fig. 6.8 for the strictly planar model.

According to our results, we deem unlikely that Stone-Wales defects are present in the experimental sample or that they play a significant role in the transition to an amorphous layer. In this material, these defects induce the formation of line defects and thus introduce long-range distortions in the network structure. As anticipated before, the difference in behavior between the Stone-Wales defects in the B_2O_3 compared to graphene or silica bilayer is due to the more complex internal structure of the unit in the former. The structure of the boroxol groups and the equilibrium bond angle between these units introduce additional constraints for the formation of a low energy network, and penalize the formation of pores with an odd number of sides, making it a unique case among the $2d$ network-forming materials known so far.

6.3 Key results

The key insights we gained in this chapter can be summarized as follows:

- We obtain a remarkable agreement between the data produced by our model and the experimental sample, which allow us to identify the newly synthesized material as a boria monolayer composed solely of boroxol rings. To date, this is the first crystal composed of these units to be discovered, and its study can shed light on the unique properties of $3d$ boria.

[8] The flattened hexagonal pores in Fig. 6.8 are very similar to the glide line defects discussed in Sec. 7.1, supporting our hypothesis.

[9] Note that this is only an estimate of the energy associated with a Stone-Wales defect. Simulations with larger cells are required to adequately reduce the local distortions in the network at large distances from the defect and provide an accurate energetic cost.

- The boria monolayer interacts very weakly with the *Pt(111)* substrate, resulting is small changes of the structural and electronic properties compared to the free-standing structure.
- The analysis of the point defects in the monolayer shows that in the absence of broken bonds the overlayer is remarkably inert, while vacancy defects lead to bonding between the boria and the substrate.
- The structure of the boroxol $B_2O_3\emptyset_3$ unit and the non-straight bond between these units hinder the formation of pores with an odd number of sides. This significantly increases the energetic cost of Stone-Wales defects, which are not observed in the experimental sample, unlike in other two-dimensional systems as graphene and silica bilayer.

Chapter 7

B_2O_3 monolayer: from extended defects to amorphous structure

In this chapter we study the line defects and the amorphous structures observed in the B_2O_3 monolayer. In both cases, we carefully compare our structural models with the features observed in the experimental STM images and we develop algorithms for the automated analysis of these images. Our results suggest that the amorphous monolayer is composed mainly of boroxol groups, like the crystal, and bears a strong resemblance to the network structure of the silica bilayer.

We begin our discussion with the analysis of the line defects in the system (Sec. 7.1), and we then turn to its amorphous structure, providing the first characterization of the amorphous network produced with this novel material (Sec. 7.2).

The work presented in this chapter is the continuation of our collaboration with the STRAS laboratory in Trieste, where the material was synthesized and analyzed. In particular, also for this part I closely with Teresa Zio, a PhD student who performed most of the syntheses and measurements on the crystalline and amorphous boria monolayer. I'm also grateful to the STRAS laboratory for their hospitality, which allowed me to test directly the algorithms for the automated analysis of freshly acquired STM images. The entirety of this chapter is unpublished work. The results for the analysis of the *CO*-functionalized STM images (Sec. 7.2.2) were obtained by Cecilia Bertolini for her bachelor's thesis [216], where I acted as co-supervisor together with Teresa Zio. In particular, Cecilia performed the experimental measurements with the aid of Teresa and developed the code to analyze the data with my aid.

7.1 Line defects in the B_2O_3 monolayer

When the B_2O_3 overlayer is grown using the procedures described in Sec. 6.1.1, the formation of the crystal begins almost simultaneously at different locations on the substrate. Crystalline domains may have different orientations and offsets relative to the substrate and, as they grow, they come into contact with each other. If there is a mismatch between two adjacent domains an extended line of defects is formed at the connection.

The experimental STM images reveal two different types of line defects. One consists of a chain of highly distorted hexagonal pores, while the other consists of a sequence of large and small pores, as shown in the bottom panel of Fig. 7.1. In both cases, the line defects do not feature a higher intensity in the STM image than their surroundings. These observations suggest that the structure of the line defects is flat and composed of the same $B_3O_3\varnothing_3$ unit as the crystalline system, see Sec. 6.1.2. Moreover, as discussed in Sec. 6.1.3, the interaction between substrate and overlayer

is weak, and does not significantly affect the structure of the latter. Therefore, we develop structural models for the line defects of the free-standing B_2O_3, ignoring the effect of the substrate.

To reduce the interaction between a line defect and its periodically repeated images, or between two defects in the same cell, we consider supercells with at least 3 unit cell of the perfect crystal surrounding the defect. Moreover, to assess whether the defective structure is planar or features strong height distortions, we fully relax the structure and simulate the STM image of the resulting system[1].

We present in Fig. 7.1 the atomic model and the simulated STM image for the three types of line defects we analyzed. The simplest one is the glide defect, shown in the top panel of Fig. 7.1. It consists of a line of distorted hexagonal pores and separates two crystalline regions of opposite orientation (the separation line is parallel to the domain orientations). Thus, by aligning the line defect with the x axis and crossing it, the orientation of the triangular pores in the crystal changes[2] from left to right (or vice versa), as shown by the grey triangles in the first panel of Fig. 7.1. These defects can be simulated in pair in a supercell with periodic boundary conditions; two line defects with opposite orientations have to be present in the cell. The relaxed configuration of this system retains an almost perfectly flat configuration, with a buckling of just 0.09 Å.

As the glide defect involves only hexagonal holes, its formation does not require the breaking of any bonds but only rotations around the oxygen atoms bridging the hexagonal units. Therefore, in principle it can occur in a perfectly ordered crystalline domain through thermally induced distortions. The formation energy of a glide defect can be estimated as the energy barrier required for the transition between the two degenerate configurations with opposite orientation. Due to symmetry, the transition state corresponds to a configuration in which the angle between the bridging oxygen and the boroxol centers is exactly 180°. Moreover, since we expect this type of line defect to occur within a crystalline region, we can assume that the lattice parameter of the system remains constant during the transition between the two energy minima. Thus, using the data from the *rigid* and *flexible* models for the T_0H_2 structure in Fig. 5.6, we estimate the energy difference between the transition state and the ground states to be 1.16 eV/B_2O_3 [3]. This energy barrier can be lowered if we allow the transition state to have height variations in the out-of-plane direction[4], resulting in a value of 0.64 eV/B_2O_3. We think that the use of larger cells, with the simultaneous presence of two opposite glide defects or with more gentle out-of-plane variations, can further reduce this energy barrier. However, we have to keep in mind that this barrier refers to a B_2O_3 unit only, and must be multiplied by the number of units involved in the change of orientation, *i.e.*, the total energy barrier for this glide line defect formation is extensive and goes linearly with the area of the involved domain.

The simulated STM image of the glide defects, shown in the first panel of Fig. 7.1,

[1] For the technical details of the simulation, refer to Appendix A.

[2] In this section, when discussing of the orientation of the crystalline pores, we will refer to them as "triangular pores". However, it would be more accurate to describe them as "hexagonal pores with a triangular shape", as they are surrounded by six $B_3O_3\emptyset_3$ units. We avoid using this term to ease the discussion.

[3] Note that this energy difference is evaluated on a single B_2O_3 unit cell, and should thus be considered a rough estimate of the true energy barrier associated with the formation of a glide defect.

[4] To maintain constant the atomic distances between the nearest neighbors, the transition state requires only a moderate buckling of 0.87 Å.

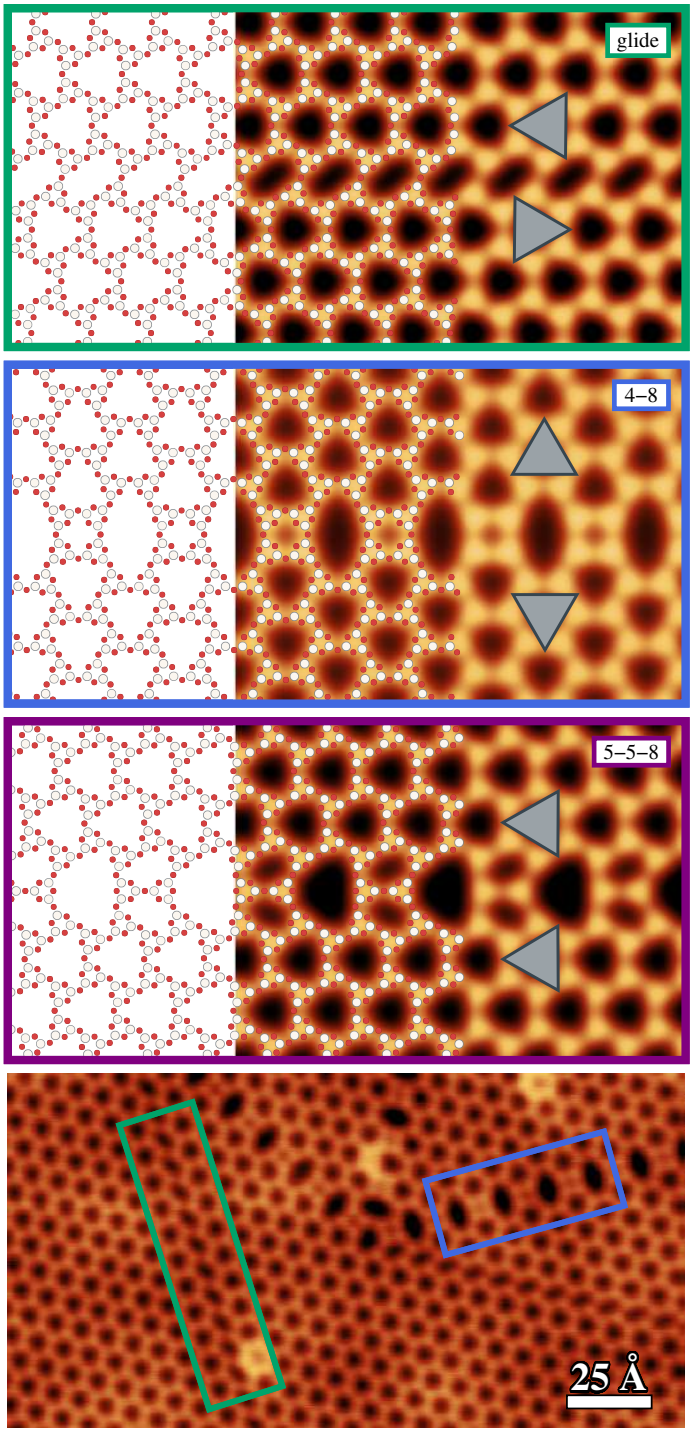

FIGURE 7.1: Atomic model and simulated STM images of different line defects (top three panels) and experimental STM image of the system (bottom panel), featuring several extended defects. The models for the line defects are the glide defect (green), the 4-8 line defect (blue) and the 5-5-8 line defect (purple). In the simulated STM images, grey triangles highlight the orientation of the triangular pores in the crystal below and above the line defect. In the experimental STM image, green and blue rectangles highlight glide and 4-8 line defect, respectively. The vertical side of the top three panels is 50 Å, while in the bottom panel a white bar set the physical length scale. The color scheme of the atomic models is the same as in Fig. 6.1. Experimental image courtesy of Teresa Zio (STRAS laboratory, Trieste).

matches pretty well to one type of line defect observed in the sample, see for example the green rectangle of the bottom panel of Fig. 7.1. The other line defect that frequently appears in the experimental images is an alternating line of 4- and 8-sided pores, shown in the blue rectangle in the bottom panel of Fig. 7.1. We call this structure a 4-8 line defect, and we present it in the second panel of Fig. 7.1. This defect is highly symmetric and also connects two different crystalline domains with different orientations of the triangular pores perpendicular to the line defect, as shown by the grey triangles in the second panel of Fig. 7.1. Because of this change in orientation, it is not possible to create a rectangular cell with only this type of defect[5] and we must simulate this structure on a ribbon, saturating the dangling bonds with hydrogen atoms. The relaxed structure of this defect is remarkably flat, with a maximum difference in the out-of-plane positions of only 0.009 Å. The absence of buckling is likely due to the lack of distorted local environments for this structure. Since this structure contains only pores with an even number of sides, it does not require the presence of straight bonds, and all the angles defined by a bridging oxygen and its two boroxol neighbors are close to those of the crystal.

There are also other line defects that do not necessarily connect crystalline regions with different orientation of the pores. An example of this is a 5-5-8 line defect, shown in the third panel of Fig. 7.1. This structure consists of the repetition of one 8-sided pore and two 5-sided pores, and the orientation of the triangular pores does not change when the line defect is crossed, as shown by the grey triangles in the third panel of Fig. 7.1. This defect has a very small buckling of 0.036 Å in the out-of-plane direction and has never been detected in the experimental samples.

A common line defect in other 2*d* network-forming materials with hexagonal symmetry is the 5-7 line defect, consisting of alternating 5- and 7-sided rings [128]. We develop a structural model for this defect in the B_2O_3 monolayer, but, as for the Stone-Wales defect discussed in Sec. 6.2.3, the planar configuration of system is unstable in presence of small out-of-plane fluctuations. During the optimization of the atomic coordinates, these small fluctuations are amplified, and lead to the crumpling of the monolayer (not shown). These effects are likely due, as discussed for the Stone-Wales defect in Sec. 6.2.3, to the presence of straight bonds between boroxol groups in this structure.

The results in this section thus show how the presence of superstructural units, which can only connect in specific orientations, imposes additional constraints on the boria network, making stable only specific line defects. Moreover, these line defects tend to connect crystalline patches with different orientations of the triangular pores, a feature that appears to be specific of this material that, at variance with other hexagonal 2*d* materials, exhibits lower point group symmetry due to the atomic pattern in the unit cell.

7.2 Amorphous structure

The crystalline overlayer described in Chapter 6 can be amorphized if successive flash annealings at 820 K are performed. After one flash annealing, the crystalline structure partially breaks down, resulting in a mixture of crystalline and amorphous

[5] It is possible to construct a cell periodic in two directions containing a 4-8 defect and another line defect, not presented in this manuscript, consisting of nearly perfect 8-sided pores and distorted 5-sided pores. However, preliminary calculations of this line defect suggest it is not flat. In addition, such structures have never been observed in experiments.

regions [44]. After two flash annealings, the degradation of the crystal is complete, and the sample features an amorphous structure without long-range order.

Since the crystalline B_2O_3 monolayer itself is a very recent material, very little is known about its amorphous counterpart. In this section, we focus on the structure of this latter system, characterizing specific features in the STM images (Sec. 7.2.1), identifying the building block of the network (Sec. 7.2.2) and developing an automated algorithm to analyze and characterize the amorphous structure (Sec. 7.2.3). This analysis allows us to provide a first quantitative characterization of this new amorphous system, and to compare its structure to that of other two-dimensional network-forming materials (Sec. 7.2.4).

7.2.1 Typical structures in the amorphous layer

In the bottom panel of Fig. 7.2, we present a small-scale STM image of the amorphous layer. The system features a complex network structure, with pores of various shapes and sizes, and different intensity variations. Most pores appear relatively regular and similar in size or smaller than the pores in the crystalline layer, while the large pores tend to be highly distorted.

Although at first glance the system bears no resemblance to the crystal, upon closer inspection, several structures typical of the original B_2O_3 monolayer can be identified. For example, in the top right corner of the bottom panel of Fig. 7.2 there is a crystalline patch of 10 hexagonal pores that closely resemble those of the crystalline system. The presence of such crystalline patches in the amorphous sample is not unusual, as discussed in Sec. 4.3.1 for the experimental samples of silica bilayer. Moreover, some large distorted pores in the experimental image match in shape and size to the 8-sided pores made of $B_3O_3\emptyset_3$ units, and are typically adjacent to smaller square pores. These structures are thus very similar to portions of the 4-8 line defect shown in the second panel of Fig. 7.1.

The bright spots in the experimental images can also be tentatively assigned to structures identified earlier in this thesis. Most of these bright spots have a triangular shape, with the sides bulging inward or outward, and are slightly larger than the typical hexagonal pores in the crystal. We identified two different structures of the overlayer that, at least qualitatively, match these characteristics.

The left panels of Fig. 7.2 show the structure of the T_0H_4 monolayer. Such system was obtained during the analysis of 2*d* B_2O_3 polymorphs in Sec. 5.2, and features a unit cell with two triangular units connected by an oxygen hinge. One of these units is $B_3O_3\emptyset_3$, which is the building block of the crystalline monolayer, while the other consists of three boroxol groups connected to form a larger unit with a small 3-sided pore within it. The simulated STM image for this free-standing structure is shown in the third green panel from the top in Fig. 7.2. In the STM image, the larger triangular unit in the structure appears as a large equilateral triangle with sides that bulge slightly inward. Additionally, it features a slight decrease of intensity in the proximity of its center, due to the presence of the small 3-sided pore. In the experimental STM image in the bottom panel of Fig. 7.2, we highlight with green circles the structures that qualitatively match the appearance of the large triangular unit of the T_0H_4 polymorph.

The central panels of Fig. 7.2 show a crystalline layer of B_2O_3 on a *Pt* substrate.

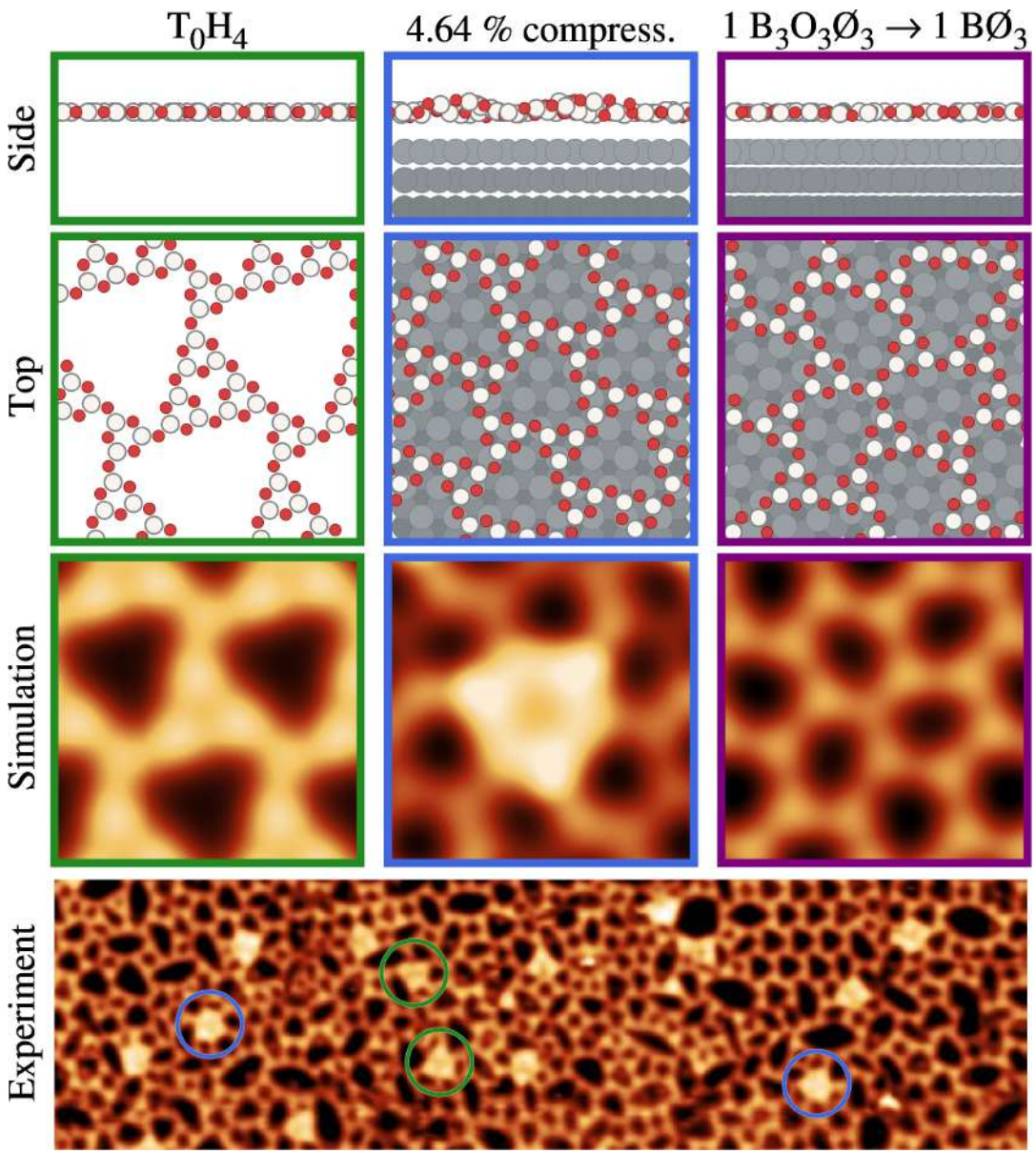

FIGURE 7.2: Comparison of the experimental STM image of the amorphous sample (bottom) with those produced by three different structural models. The models considered are a free-standing polymorph of the boria monolayer (T_0H_4, green), the most stable crystalline system on *Pt(111)* whose lattice parameter is compressed by 4.64 % (blue) and the same crystalline system on *Pt(111)* as Fig. 6.1, where one boroxol group $B_3O_3Ø_3$ is replaced with a $BØ_3$ unit (purple). Each structural model is presented in both side (top) and top (center) views, while its simulated STM image is shown at the bottom. In the experimental STM image, green and blue circles highlight structures similar to the T_0H_4 and the crystalline layer compressed by 4.64 %, respectively. The size of the square panels is 25 Å× 25 Å, while the panel with the experimental image is 270 Å× 75 Å. The color scheme of the atomic models is the same as in Fig. 6.1. Experimental image courtesy of Teresa Zio (STRAS laboratory, CNR-IOM, Trieste, Italy).

The supercell we use in this case for overlayer and substrate [6] imposes a compression of 4.64 % on the B_2O_3 monolayer compared to its free-standing lattice parameter. This strain is relatively large for a two-dimensional system [28], being almost

[6] This specific structure was obtained during the analysis in Sec. 6.1.2 using the algorithm described in Appendix D.

double that of the crystalline structure used in Chapter 6 (2.43 %). To accommodate the compression, the overlayer crumples, with a change in height of up to 1.35 Å. This crumpling results in some hexagonal pores in which half of the boroxol groups are tilted upwards relative to the plane of the monolayer, producing some bright triangular structures in the simulated STM image, with sides that bulge slightly outward and a small decrease in intensity near the center of the pore. These features match relatively well some bright spot in the experimental STM image, which we highlight with blue circles in the bottom panel of Fig. 7.2. It is also likely that the formation of an amorphous network induces some localized strain in the overlayer, giving rise to structures similar to those shown in the central panels of Fig. 7.2.

The boroxol group $B_3O_3\emptyset_3$ is the only building block of the structures presented so far. We thus assess whether it is possible to replace this unit with a smaller $B\emptyset_3$ unit in the overlayer on *Pt(111)*, and whether such a substitution can be detected in the STM images. We use the supercell presented in Fig. 6.1 as a template for this structure. We then replace a boroxol group with a $B\emptyset_3$ unit and we relax the resulting structure, which is shown in the right panels of Fig. 7.2. Remarkably, the monolayer is weakly affected, with no change in the average distance from the substrate (3.26 Å) and only a very small increase in buckling, equal to 0.44 Å compared to 0.20 Å for the original system in Fig. 6.1. The $B\emptyset_3$ unit is half of the size of a boroxol group, however, due to the high flexibility of the system, the network can easily adapt to the new unit without breaking any bonds. Unlike the Stone-Wales defect discussed in Sec. 6.2.3, the effect of this substitution is very localized, and only the openings that include the $B\emptyset_3$ unit are substantially distorted. The simulated STM image of this structure does not differ significantly from that of the crystalline monolayer presented in Fig. 6.2, with no major changes in intensity and a small distortion of the three openings containing the substituted unit. These results thus suggest that the substitution $B_3O_3\emptyset_3 \rightarrow B\emptyset_3$ is possible in the B_2O_3 monolayer, and cannot be easily detected in the STM images. In particular, in the STM images of the amorphous structure, where distortions of the shape of the pores are common, the presence of $B\emptyset_3$ units in the network cannot be discarded.

Although qualitative, our results suggest that the structure of the amorphous monolayer bears some similarities with the crystalline structure, its line defects and its polymorphs. The building block of these systems is the boroxol group $B_3O_3\emptyset_3$, although the presence of $B\emptyset_3$ units cannot be ruled out a priori.

7.2.2 Reconstruction of the atomic positions from the functionalized STM images

Standard STM images alone cannot provide a detailed understanding of the local structures of the amorphous B_2O_3 sample. As discussed in Sec. 6.2, using this technique it is not possible to resolve the internal structure of a boroxol group, which appears as a single bright spot in the image.

Higher resolution can be achieved by performing STM measurements with a *CO*-functionalized tip, and applying a Laplace filter to the resulting image to enhance its edges [44]. In Fig. 7.3 (a) we present the result of this procedure for a crystalline monolayer. The dark triangles in the image correspond to the dark pores in the original STM image, while the lighter triangles are $B_3O_3\emptyset_3$ units. Within these triangles, the positions of the oxygen atoms are defined by six bright spots, while the boron atoms cannot be resolved [44]. Thus, using this technique, atomic resolution of the overlayer can be achieved, allowing for a clear identification of the structures in the amorphous samples.

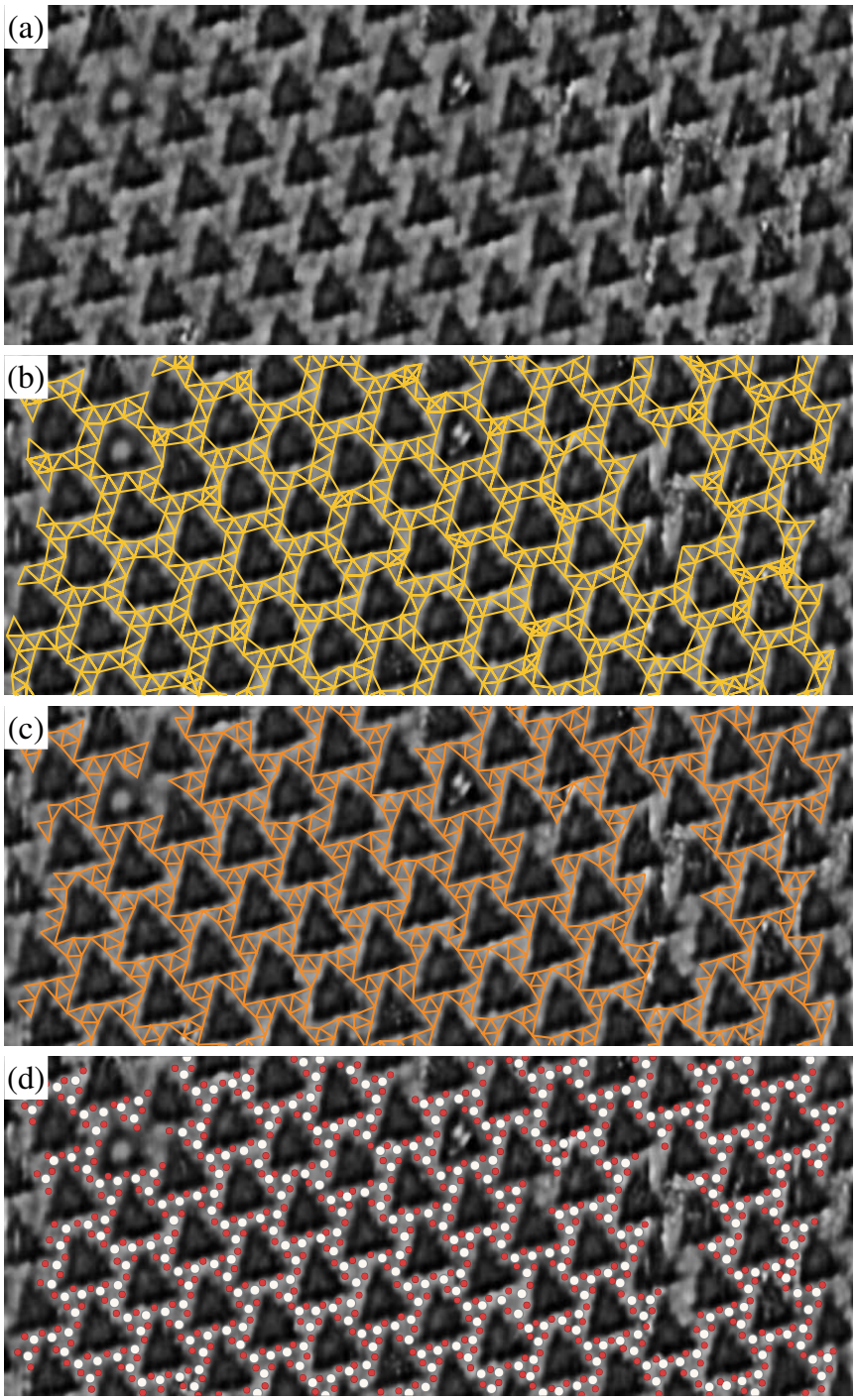

FIGURE 7.3: Schematic procedure of the algorithm developed to recover the atomic positions from the *CO*-functionalized STM images. (a) Experimental image. Black triangles correspond to pores, while light grey triangles are boroxol $B_3O_3Ø_3$ groups. The bright spots within the grey triangles identify the positions of the oxygen atoms. (b) Network produced by connecting all the adjacent oxygens. (c) Refined network obtained by deleting all the triangles that do not satisfy a set of physically motivated constraints (see text). (d) Experimental image with superimposed the atomic positions recovered by the algorithm using the refined network in (c). The color scheme of the atomic models is the same as in Fig. 6.1. The size of each panel is 112.8 Å$\times$ 45.1 Å. Experimental image courtesy of Teresa Zio (STRAS laboratory, CNR-IOM, Trieste, Italy).

We thus develop a semi-automated algorithm to reconstruct the atomic positions of boron and oxygen atoms from the functionalized STM images. In our analysis, we assume that the overlayer is nearly flat and we do not consider any bonding between monolayer and substrate, although, as discussed in Sec. 6.2.2 the existence of unsaturated bonds in the overlayer that can be passivated by the substrate is possible. Since only the oxygen positions can be localized in the functionalized STM images, to recover the position of boron atoms it is necessary to postulate the structure of their local environment. In the continuous random network theory, the local environment of the atoms in an amorphous material is assumed to be similar to that of the corresponding crystal. Thus, within this framework, each B atom is located at the geometric center of a (nearly) equilateral triangle with oxygens at its vertices, that is, a $B\emptyset_3$ unit. If two of these units share a side, the boron atoms at their centers will be close to each other. Since the borons have a closed shell configuration in such units, this will result in a strong repulsion between them, which increases the energy of the system. A key assumption of the CRNT is that a glass has an energy as low as possible, to be competitive with the corresponding crystal, as discussed in Sec. 1.2.2. Thus, configurations in which two $B\emptyset_3$ units share a side have to be avoided.

Having specified the assumptions of our algorithm, we now describe how it works. First, we identify the positions of the oxygen atoms in the experimental image. We tried several approaches for this task, such as identifying the local intensity maximum or locally fitting the intensity of the image with a gaussian function. However, due to the little contrast between the bright spots we want to detect and the noisy background, these approaches proved unsatisfactory. Although more advanced methods, like pattern recognition and convolutional neural networks [217, 218], could solve these issues, due to time constraints we decided to manually acquire the oxygen positions using online tools to digitalize the image [219]. Although this procedure inevitably introduces some errors in the atomic coordinates, we deem the result adequate for a preliminary analysis of the amorphous samples.

From the oxygen positions we calculate the RDF in open boundary conditions, and we use the position of its first minimum as threshold for the definition of first neighbors between O atoms. With this choice of neighbors, we identify the vertices of each $B\emptyset_3$ unit as a set of three distinct oxygen atoms that are all neighbors to each other. For ease of discussion, we will refer to these sets of three oxygen atoms as triangles.

In Fig. 7.3 (b) we show as yellow lines the triangles obtained with the procedure defined above. These triangles cannot be directly used to recover the boron positions and, as we can see for the figure, they are much more than one might expect for the $B\emptyset_3$ units in crystalline B_2O_3. Due to experimental noise, difficulties in performing the measurements and in acquiring the oxygen positions, many triangles are far from regular, and the edges of some triangles intersect those of other triangles. To fix these issues, we proceed as follows. We check whether two edges intersect, and if so, we remove the longer one. We repeat this process until no edge crossing remains. This process has a minor effect on the images of the crystalline sample, which are highly ordered, but yields a significant improvement in the images of the amorphous layer, where edge crossing between different triangles is common.

To identify the more distorted triangles, for each triangle we calculate the index

$$a_i = \frac{4\sqrt{3}}{3} \frac{A_i}{\langle l_i \rangle^2}, \tag{7.1}$$

where A_i is the area of the i-th triangle and $\langle l_i \rangle$ is the average length of its sides.

The index $a_i \in [0; 1]$ is a measure of the regularity of the i-th triangle, with a perfect equilateral triangle having $a_i = 1$ and highly distorted triangles having $a_i \sim 0$. The distribution $P(a_i)$ in the experimental images tends to be heavily shifted to $a_i \sim 1$, as expected due to the regularity of the $B\emptyset_3$ units, but a tail toward lower values of a_i is also present. Thus, to remove the more distorted triangles, we fix a threshold $\tilde{a}$, and we delete all the triangles with values of the index lower than the threshold[7].

The procedure described so far allows us to obtain $B\emptyset_3$ units that are nearly regular, but it imposes no constraints on the number of sides shared between different triangles. To enforce this physically motivated constraint, we progressively discard all the triangles that share three, two and one edges. This process has to be performed in steps, first deleting all the triangles that share three edges, then those that share two sides and finally the ones that share only one edge. The number of edges shared for each triangle has to be re-evaluated at the beginning of each step. This procedure is required due to the presence of spurious triangles formed by a hinging oxygen and its two closest oxygens in the adjacent $B\emptyset_3$ units. Since most of the angles between the $B\emptyset_3$ units are close to 130°, as is the case for the B_2O_3 polymorphs discussed in Sec. 5.2.2, these triangles are very regular, and can be removed only on the basis that they share one or more sides with other units. The triangles obtained with this procedure are shown as orange lines in Fig. 7.3 (c).

Finally, we place a boron atom at the geometric center of each triangle, and an oxygen atom at each of its vertices. To make the images clearer, we discard all the oxygens that were initially detected but are not part of any final triangles. The result of this process for a crystalline sample is presented in Fig. 7.3 (d), where we clearly see that the algorithm successfully recovers the position of both boron and oxygen atoms in the sample. The resulting structure closely matches that obtained in Sec. 6.1.2, and the only assumptions used by the algorithm are the coplanarity of the atoms in the overlayer and the use of $B\emptyset_3$ units as building block. In the figure we can also see that the overlayer appears to be broken in some regions, where we were unable to clearly locate the oxygen atoms.

We now apply our algorithm to the structure of the amorphous layer. In Fig. 7.4 we present a functionalized STM image of the amorphous sample, along with the reconstructed positions of the atoms in the overlayer using the algorithm described above. The sample in the image features a crystalline region on the right, with the same triangular pores as in Fig. 7.3, and a disordered region on the left. The algorithm clearly works better in the crystalline region than in the amorphous one, where the identification of the oxygen positions becomes ambiguous in some areas. Nevertheless, the reconstructed atomic positions allow us to clearly identify some structures in the amorphous network. For example, in the bottom left corner of Fig. 7.4, we can see a 4-, 5-, 7- and 7-sided pores consisting almost exclusively of boroxol groups. In general, in the regions where the network appears continuous and all the oxygen atoms can be detected, the network seems exclusively composed of boroxol groups $B_2O_3\emptyset_3$, as in the crystal. The smaller $B\emptyset_3$ unit, by contrast, never forms continuous structures. Despite the limitations of our algorithm in the correct identification of all the possible structural units, these findings suggest that most of the amorphous network is composed of boroxol groups. For example, in the crystalline region of the top panel of Fig. 7.4, we can see these groups appearing as regular triangles. The amorphous region in the same figure is composed mainly of distorted triangles, which are comparable in size to those in the crystalline region,

[7] The threshold used for this analysis varies from image to image. In general, we set its value close to $\tilde{a} \sim 0.85$, so that most of the distribution is above the threshold.

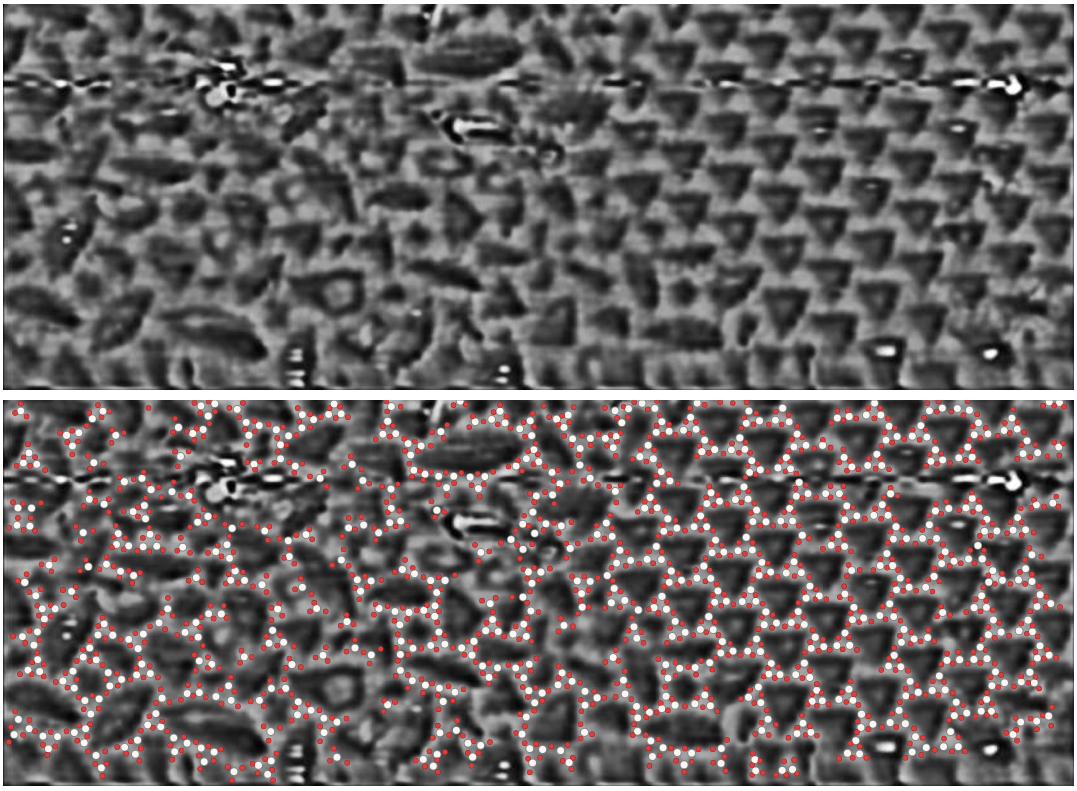

FIGURE 7.4: *CO*-functionalized STM image of the amorphous sample, in its original form (top) and with the atomic positions recovered by the algorithm superimposed (bottom). The color scheme of the atomic models is the same as in Fig. 6.1. The size of each panel is 177.6 Å $\times$ 63.8 Å. Experimental image courtesy of Teresa Zio (STRAS laboratory, CNR-IOM, Trieste, Italy).

while the $B\emptyset_3$ unit, being half the size of a $B_2O_3\emptyset_3$ group, would instead appear as a visibly smaller triangle. This observation, however, does not completely rule out the presence of $B\emptyset_3$ groups in the disordered network. A more refined algorithm and a larger number of experimental images to analyze are needed to validate and put our conclusions on a firmer basis.

7.2.3 Automated analysis of experimental STM images

The functionalized STM images of the overlayer, combined with automated methods for detecting the oxygen positions, can provide a detailed understanding of the structure of the amorphous layer. However, there are intrinsic limits to the usefulness of this technique in understanding the network structure of the system at large scales. From an experimental standpoint, the STM imaging with functionalized tip is not a simple technique, since the bonding of a *CO* molecule to the tip cannot be precisely controlled. Even when observing a small region, the oxygen positions are difficult to pinpoint and the difficulty increases when performing these measurements over larger areas of the sample, where it would be extremely difficult to identify the atoms' positions. This last point is particularly crucial in the case of the B_2O_3, since this system has two characteristic length scales: one connected to the typical size of the building block and another related to the pores formed by these units. While functionalized STM images can help in understanding the former, they cannot produce sufficient statistics to accurately describe the correlation between the pores or the typical size of the crystalline domains in the amorphous sample.

We therefore turn to the analysis of (standard) STM images, which are relatively easy to acquire also over regions larger than 150 nm in length. However, as discussed in Sec. 6.1.2, a critical issue is that each bright spot in the experimental image corresponds to a single building block. Moreover, these spots are very broad and their positions cannot be easily pinpointed. As shown in Fig. 7.5 (a), the problem is further complicated by the presence of *Pt* adatoms, which locally change the density of states of the system and give rise to rings with a higher intensity than the surrounding ones. Due to these issues, we developed an algorithm for the automated analysis of the experimental STM images, which focuses on the pores and from these recovers the position of the building blocks. Since the experimental STM images cannot resolve the internal structure of these building blocks, the algorithm assumes that they are all of the same kind and they contribute equally to the network structure.

We describe the algorithm using as example Fig. 7.5 (a), which is an experimental STM image of the crystalline monolayer with several glide and 4-8 line defects. The first step of the algorithm is the pores' detection. In the B_2O_3 monolayer, pores appear as dark spots in the image, however, they are not always the same. This makes it impossible to detect these regions using a simple intensity threshold. We thus identify the pores as regions whose intensity is lower than their surroundings. In particular, we convert the STM image to grayscale, and for each pixel in the image, we numerically evaluate the second derivative of the intensity $I(x, y)$, using a finite difference method [220]. For example, the numerical estimate for the second derivative of the intensity in the pixel $(x_0; y_0)$ with respect to the x axis is

$$\left.\frac{\partial^2 I(x,y)}{\partial x^2}\right|_{(x_0;y_0)} \simeq \frac{I(x_0+\delta, y_0) + I(x_0-\delta, y_0) - 2I(x_0, y_0)}{\delta^2}\,, \tag{7.2}$$

where δ is a parameter which controls the accuracy of the derivative evaluation. This parameter should be small enough to return an accurate value of the second derivative, but large enough to be insensitive to small random changes in intensity due to noise. In our work, we have found that $\delta \simeq 0.2$ Å produces good results overall, but it is usually better to slightly tweak this parameter to improve the pore detection on the specific image under analysis. After evaluating the derivatives of each pixel, we create a new image in which a pixel is black if the intensity profile around it is convex, *i.e.* both of its second derivatives with respect to the x and y axis are positive. The result of this procedure is a black-and-white image as that shown in Fig. 7.5 (b).

In the images of the amorphous layer, bright spots with a high value of intensity are sometimes present. These regions can be relatively small and similar to the structures shown in Fig. 7.2, or they can be rather large, with a linear dimension equal to several hexagonal pores, and with an irregular boundary, as can be seen on the right border of Fig. 7.5 (a). These latter structures are likely disordered aggregates of material left over from the synthesis. In our algorithm, we assume that each of these bright spots represents a single pore, regardless of its size, as we found that this improves the reconstructed network structure in their vicinity. To detect these structures, we fix an intensity threshold t_I and we select all the pixels in the image with an intensity above the threshold[8]. The pixels selected in this way are colored in black and added to the black-and-white image obtained after evaluating the derivatives, as shown in Fig. 7.5 (b).

[8] In our analysis, where an intensity of 1 means pure white, we use $t_I \simeq 0.95$. However, it is usually better to test several values of this threshold on the specific image being analyzed.

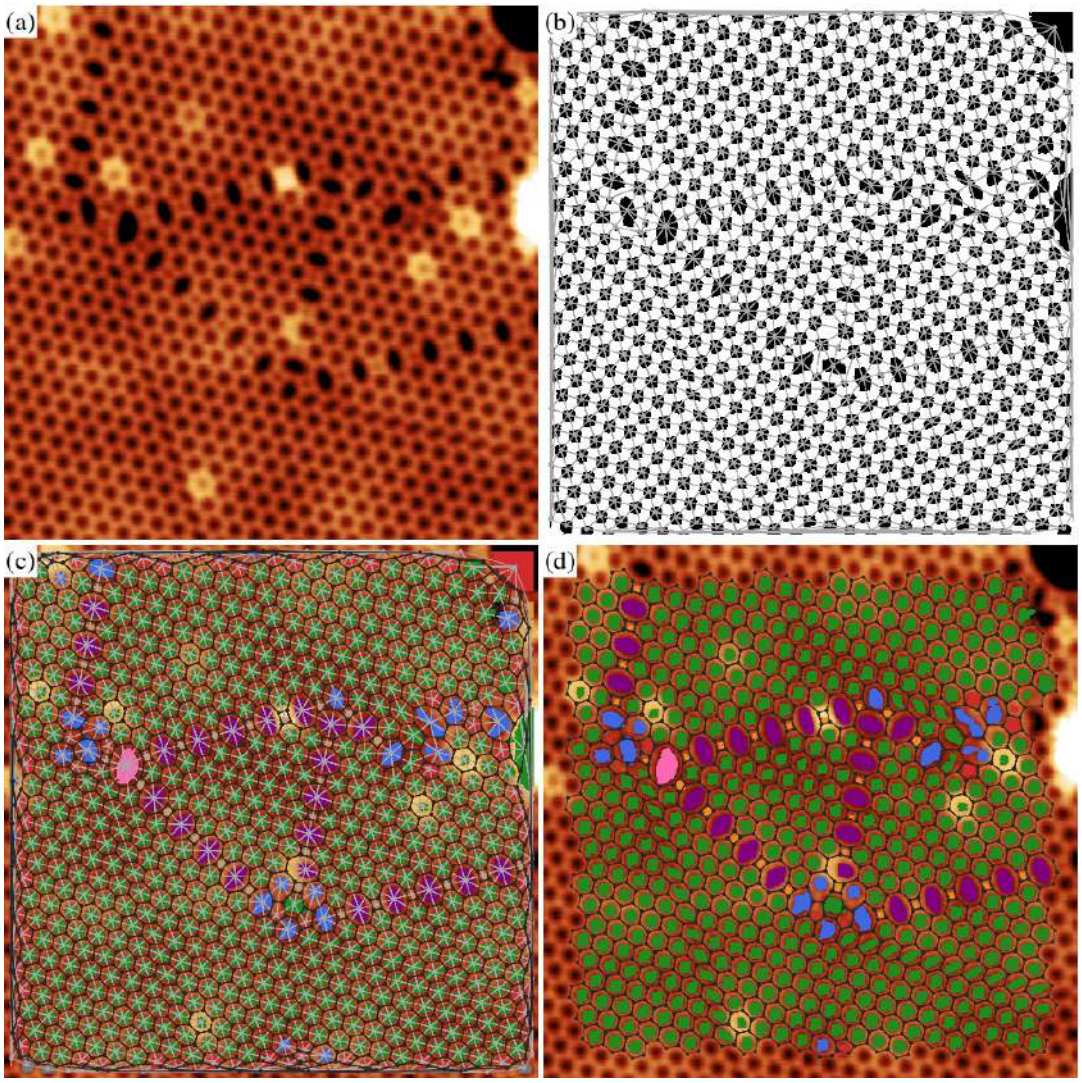

FIGURE 7.5: Schematic procedure of the algorithm developed to analyze the network in the STM images. (a) Experimental image of the crystalline overlayer. (b) Black-and-white image in which only the pixels with a locally convex intensity profile or an intensity above a certain threshold are colored in black. Grey dots are the geometric centers of the identified pores, and the grey lines are the result of a Delaunay triangulation of that set of points. (c) Experimental image, with overlay of the Delaunay triangulation (grey) and the network produced by the build blocks (black). The pores with 4, 5, 6, 7, 8 and 10 sides are colored in yellow, red, green, blue, purple and pink, respectively. (d) Refined network structure, in which the pores in the convex hull and their neighbors have been removed. The black mesh and the colors of the pores are the same as (c) The size of each panel is 20 nm $\times$ 20 nm. Experimental image courtesy of Teresa Zio (STRAS laboratory, Trieste).

From the black-and-white image, we identify all the regions of connected black pixels using a flood filling algorithm. Each of these areas corresponds to a single pore in the original image, and for each pore thus defined, we identify its geometric center by averaging the coordinates of its pixels, shown with grey dots in Fig. 7.5 (b). Areas below a certain threshold, typically around 10 pixels[9], are deemed artifacts due to noise and are removed.

[9]The STM images used in this analysis are typically images of 600$\times$600 pixels, representing an area of approximately 50 Å$\times$50 Å. Therefore, one pixel corresponds roughly to 0.007 Å^2.

We now need a way to identify neighboring pores. Since the distance between the geometric centers of two adjacent pores depends on their number of sides, it is not possible to identify the neighbors using the RDF, as was done in Sec. 7.2.2. Thus, to identify neighboring pores, we perform a Delaunay triangulation of the set of geometric centers of the pores [221]. This triangulation has several properties that makes it ideal for this task, but the most important one is that it maximizes the minimum angle between three connected points [222]. The triangles produced with this procedure therefore tend to be very regular, except at the border of the image. In this work, the Delaunay triangulation was performed using the `scipy` library [223], and the result of the triangulation is shown as grey lines in Fig. 7.5 (b).

Using the Delaunay triangulation, it is possible to assign to each pore an estimated number of sides, equal to the number of its neighbors. In Fig. 7.5 (c) we colored each pore according to its number of sides, with yellow, red, green, blue, purple and pink representing 4-, 5-, 6-, 7-, 8- and 10-sided pores. We found that this way of determining the pores' sizes is more reliable than the use of structural information about the size and shape of the pores. The latter quantities are sensitive to the scale of the image and rely on the definition of precise boundaries between the properties of pores of different sizes, which are not well defined. By contrast, our scheme does not depend on external parameters and relies on the connectivity between the pores, which makes their identification much more reliable.

Using the network produced by the Delaunay triangulation, it is possible to recover the position of the building blocks in the system. In particular, we place a building block in the center of each triangle obtained from the triangulation. The center of the triangle can be defined by the average positions of its vertices, but we deem more accurate to use a weighted average of their positions. Since large pores tend to have their center farther from their edges than smaller pores, it is useful to weight the position of a pore with a function that depends on the number of its sides, so that large pores have a lower weight. In this work, we use as weight for the i-th pore $\omega_i = \sin(\pi/n_i)$, where n_i is the estimated number of sides of that pore. This formula is based on the relation between the radius of the circle inscribing a regular polygon of n_i sides and the length of its sides. Once the positions of the building blocks are defined, we connect them assuming that two building blocks are neighbors if their respective triangles share a side. Since the triangulation produces a set of triangles, the building blocks by definition always have three neighbors. Moreover, their local environment generally has a near-perfect 3-fold symmetry, as the Delaunay triangulation produces very regular triangles far from the edges of the image. In Fig. 7.5 (c) we show the result of this process. The grey mesh is the Delaunay triangulation, while the black mesh corresponds to the recovered positions of the building blocks of the network. As can be see in the image, the reconstructed network automatically identifies the 4-8 line defects, assigning the correct number of sides to their pores.

Since the identification of the number of sides of the pores in our algorithm relies on the local topology of the network, and in particular on the number of neighbors of each pores, it fails on the edges of the image, where not all the neighbors of a pores can be observed. As shown in Fig. 7.5 (c), this results in heavily distorted triangles and pores with the incorrect number of sides. To refine the resulting network, we thus identify the pores at the edge of the image and their neighbors, and we remove the building blocks computed using these pores. We define as boundary pore all the pores in the convex hull of the triangulation, *i.e.* the smallest convex set of points than encloses all the other points in the triangulation, and we compute them using the `scipy` library [223]. In Fig. 7.5 (d) we present the final result of this procedure,

where we overlay the reconstructed network produced by the building blocks onto the original image, and we color each pore according to its number of sides.

In conclusion, we developed an algorithm for the automated analysis of experimental STM images that depends on a small set of parameters and relies on a limited number of assumptions, such as the presence of a single building block in the system. The algorithm allows us to estimate the number of sides of each pore in the image and can recover a reasonable network structure, which can then be further analyzed using standard techniques such as those presented in Chapter 4.

7.2.4 Application of the algorithm for the analysis of the experimental STM images

Using the algorithm described in the previous section on an experimental STM image, it is possible to obtain the positions of both the building blocks and the pore centers, as well as an estimate of the number of sides of each pore. These quantities are the starting point for the analysis presented in Chapter 2 and Sec. 4.1.1, where we characterized the structure and the local order in our model for the silica bilayer. Thus, using the algorithm presented in Sec. 7.2.3, a similar analysis can be performed on the experimental samples, evaluating quantities such as the ring statistics and the correlation lengths for the translational and orientational order, or the distribution of the module of the local order parameters. The algorithm can also be used in the laboratory to quickly assess the quality of the sample, as crystalline patches and line defects can be easily detected. In our tests, the algorithm was able to correctly identify most of the pores in an image of 584×584 pixels representing an area of 150 nm $\times$ 150 nm, with a crystalline system spanning three platinum terraces. However, the algorithm works best on images of linear dimensions between 20 nm and 75 nm, while the number of pixel per nm^2 does not appear to be too crucial for the pore detection[10].

As a case study for the algorithm, we analyze the amorphous structure shown in Fig. 7.6 (a). This sample was obtained after two flash annealings at 820 K of the crystalline sample; the image is also particularly clean, which improves the pores detection. Although the cooling rate of the experimental samples after the flash annealing cannot be accurately controlled, and thus some differences in the structure can be expected when different cooling rates are employed, it should be noted that even the amorphous configurations of silica bilayer lack this accuracy in the sample preparation. Moreover, contrary to the data available in the literature for the silica bilayer, the image shown in Fig. 7.6 (a) is rather large, having a linear size of 50 nm. Due to the large area represented in the image, our algorithm detects 5 184 pores in Fig. 7.6 (a), which is approximately 4 times the number of rings in the experimental configurations available in the literature for the amorphous silica bilayer, see Appendix B.

We start our analysis with the identification of the crystalline regions within the amorphous sample. Since the network structure is reconstructed from the pores positions in the image, we deem the centers of the pores more accurate than the positions of the building blocks. Thus, we focus on the pores' geometric centers and we calculate the local order parameter for a 6-fold symmetry between pores ψ_6^P, as defined in Eq. 4.1. As shown in Sec. 4.1.1, we expect pores in a crystalline environment to have a high value of the module of ψ_6^P. Therefore, to identify the crystalline

[10] In our tests, we primarily used experimental images with 600×600 pixels.

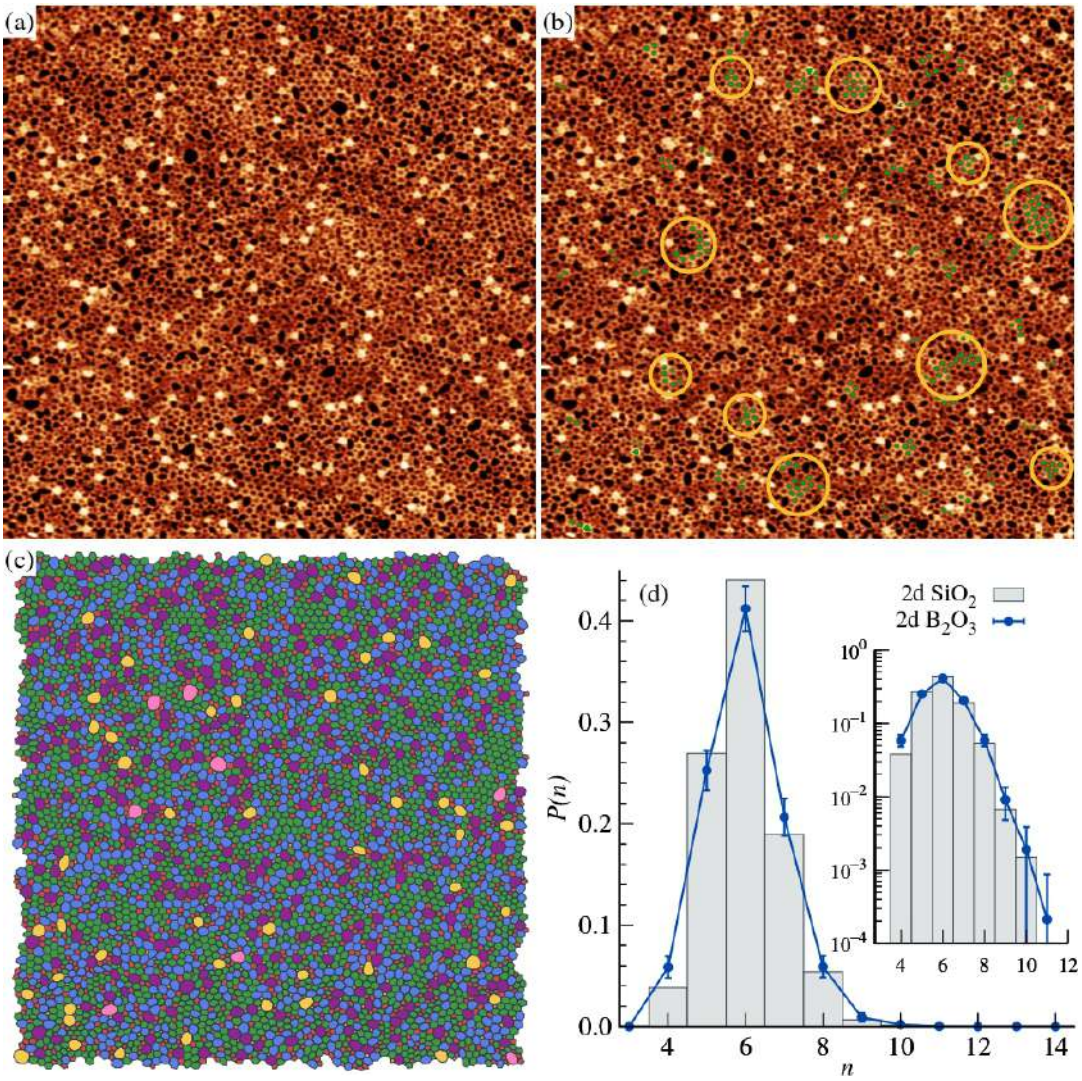

FIGURE 7.6: Analysis of the network structure of an amorphous B_2O_3 sample. (a) Experimental image. (b) Experimental image with pores in a locally crystalline environment colored in green. The larger crystalline patches are highlighted with yellow circles. (c) Network structure recovered from the image presented in (a). The pores with 4, 5, 6, 7, 8, 9 and 10 or more sides are colored in orange, red, green, blue, purple, yellow and pink, respectively. (d) Comparison of the pore statistics of the boria monolayer in panel (c) (blue line) with the ring statistics for the silica bilayer (grey bins), obtained from experimental data available in the literature, see Appendix B. In the inset, the ring/pore statistics are presented in semilogarithmic scale to highlight their decay as the number of sides of the ring/pore increases. The size of the experimental image is 50 nm $\times$ 50 nm. Experimental image courtesy of Teresa Zio (STRAS laboratory, Trieste).

domains, we set a relatively high threshold for the module of the local order parameter, equal to 0.8, and we color all the pores with a module of ψ_6^P above this threshold. The result of this procedure is shown in Fig. 7.6 (b), where we clearly see the presence of several small crystalline domains embedded in the amorphous matrix. Although these domains are much smaller than those we obtained in the low temperatures simulations of our model for the silica bilayer, as shown in Fig. 4.14, they are comparable to those observed for the experimental samples of silica bilayer, see for example Fig. 2 in [142]. In particular, the typical domain contains approximately

10 pores, while the largest one, on the right of the figure, contains 19 pores.

In Fig. 7.6 (c) we present the recovered network structure of the sample, where the lines identify the connections between the building blocks and each pores is colored according to its estimated number of sides[11]. Although the algorithm clearly requires some refinement, as it tends to compress the smaller rings and expand the larger ones, the topology of the network is overall reasonable. In particular, all the bonds between neighboring building blocks have similar lengths, as expected for such a physical network, where the edges correspond to covalent bonds between structural units.

Since the network structure identified by the algorithm is reasonable, we proceed with a first analysis of the network structure of this novel material. We present in Fig. 7.6 (d) a comparison between the pore statistics of the amorphous samples of B_2O_3 (blue line) and the experimental ring statistics of the silica bilayer (grey bins), calculated from the data available in the literature, as described in Appendix B. The two statistics are very similar, with a maximum for hexagonal pores/rings and an exponentially decaying tails for large pores/rings. Remarkably, the data for the two systems are very close to each other, and are compatible within the error bars when the errors in the silica data are also considered, see Appendix B.

This analysis, albeit preliminary, highlights the similarities between 2*d* amorphous silica and boria. Their samples contain several crystalline domains, whose size exceeds the one commonly expected in the continuous random network theory [131], and their pores/rings statistics is remarkably similar. These results, if confirmed by more precise analyses, suggest a certain degree of universality in the physics of these two-dimensional network-forming oxides.

7.3 Key results

The key insights we gained in this chapter can be summarized as follows:

- The line defects typically separate two different regions of the sample with different orientations of the triangular-shaped pores.
- Within the amorphous structure of the B_2O_3 monolayer it is possible to identify local structures that closely resemble the structural units present in the most stable crystal, its line defects and its polymorphs.
- Using *CO*-functionalized STM measurements, we established that the main building block of the amorphous structure is the boroxol group, as in the crystal.
- The network structures of the amorphous samples of both the silica bilayer and the boria monolayer bear some striking similarities, suggesting some degree of universality in this class of materials.

[11] An enlarged version of Fig. 7.6 (c) is available as figure F7.1 in the Appendix E.

Conclusions

The aim of this work was to study the physical properties of two-dimensional crystalline and amorphous oxides. To characterize these materials at different length scales, we used a combination of computational geometry and modelling, *ab initio* techniques, large-scale classical simulations and rigorous comparisons with experiments. We focused on two specific systems, the silica bilayer and a newly synthesized B_2O_3 monolayer, for which we performed the first analysis of both the crystalline and amorphous structures.

In the first part of the thesis (Chapters 2 to 4), we used an effective classical interaction potential to study the properties of the silica bilayer. Using experimental data available in the literature, we reparametrized a simple interaction model to simulate a $2d$ projection of the material. The structural properties of the model match very well those of the experimental samples. Moreover, our model is more efficient than the earlier model of Roy, Heide, and Heuer in the simulation of this system.

We used this reparametrized potential to study the glassy dynamics of the system at low temperatures, paying particular attention to the peculiarities of $2d$ physics, such as Mermin-Wagner fluctuations, and establishing connections with the available theoretical frameworks. Our model of the $2d$ silica shares several features with its $3d$ counterpart. In the liquid phase, the system exhibits several thermodynamic anomalies around the crossover temperature T_x at which the network structure starts to develop. The correlation times follows two different Arrhenius behaviors at high and low temperatures, with an intermediate crossover region centered around the temperature T_x. Interestingly, as in 3d silica, glassy dynamics appear upon cooling well above the melting temperature. We also characterized the elementary rearrangements occurring deep in the glassy regime, providing a plausible mechanism for the relaxation of the structure at low temperatures. This analysis paves the way to a comprehensive characterization of the dynamics, which will be subject of a future work.

We then focused on the local structure of the system and its correlation with the dynamics. Using a combination of several local orientational order parameters, we showed that, as temperature decreases, our model accumulates a high degree of local crystalline order, leading to the formation of transient crystalline domains in the liquid in thermal equilibrium. This is in contrast to what is generally expected for $3d$ network-forming materials, and bears instead a striking resemblance to the cybotactic description of the structure of such systems. Interestingly, although at low temperatures the liquid features both glassy dynamics and transient crystalline domains, the two effects are only partially correlated. In particular, while the crystalline regions relax slower than the bulk, they cannot fully explain the dynamic heterogeneity of the system, as determined within the iso-configurational ensemble. We then assessed the effect of a periodic substrate on our model. We found that, for specific choices of the lattice parameters, even a weak interaction with the substrate can produce non-trivial changes in the structure and dynamics of the overlayer. We attempted to frame our results in the context of the available theoretical descriptions of network-forming glasses, without reaching a satisfactory agreement with their

predictions. Our model for the silica bilayer thus represents a challenge and ideal test bench for future theoretical analyses.

In the second part of the thesis (Chapters 5 to 7), we used a combination of original algorithms and well-established *ab initio* techniques to characterize a novel boron oxygen compound recently synthesized by our experimental collaborators at the STRAS laboratory. In particular, we developed an algorithm to generate polymorphs that satisfy a set of physically motivated constraints, and we used it to discover and characterize the low energy structures of a free-standing B_2O_3 monolayer.

The lowest energy polymorph we found was used as candidate for the structure of the compound synthesized on *Pt(111)*, obtaining a remarkable agreement between the simulation and the experimental data. These results allowed us to identify the newly synthesized material as a boria monolayer composed exclusively of boroxol groups. The discovery of this material is particularly significant, since, until now, no known crystalline phase of boria contained these units: they were only found in liquid and amorphous samples. The presence of these groups in the low temperature liquid has been linked to several peculiar properties of the material, such as its exceptional glass-forming ability. Therefore, the synthesis of this new 2*d* allotrope and the ability of surface science techniques to analyze its structure and dynamics opens new perspectives in understanding the physics of 3*d* boria. Beyond its interest in fundamental research, this new material also features several unique properties that make it ideal for future technological applications. It is extremely flexible, thanks to the interplay between rigid building blocks and flexible bonds, and features large pores of approximately 5.5 Å in diameter, which are ideal for its functionalization. It is also a wide band gap insulator and interacts very weakly with the *Pt(111)* substrate, retaining an almost perfect planar geometry. Moreover, its low adhesion energy on the substrate makes it an ideal candidate for mechanical exfoliation.

After the characterization of the crystalline system, we focused on the analysis of its point and line defects. This analysis highlighted the resilience of the material when all the bonds are saturated and the profound effect of the non straight angle between the building blocks on the network structure of the defective system. We then turned to the analysis of the amorphous overlayer, developing algorithms to analyze both standard and *CO*-functionalized STM images. These algorithms allowed us to provide a first characterization of the amorphous samples, which are mainly composed of boroxol units, like the crystal. This analysis also revealed some striking similarities between the amorphous structures of the silica bilayer and the B_2O_3 monolayer: both materials display a pronounced local crystalline order and similar ring statistics.

Overall, our results for the silica bilayer and the boria monolayer highlight the unique and intriguing features of this class of two-dimensional network-forming oxides. The presence of large transient crystalline domains in the thermally equilibrated liquid phase of silica is in stark contrast with what is found in the 3*d* counterpart, and might suggest a profound difference between the glassy dynamics of two- and three-dimensional network-forming systems. Moreover, the similarity between the structural properties of the systems studied in this work points to a certain degree of universality in this class of network-forming materials.

Acknowledgements

We thank the whole staff of the STRAS laboratory led by Cristina Africh, and in particular Alessandro Sala and Teresa Zio for performing the experimental synthesis and characterization of the boria monolayer, and the close collaboration. We also thank Lorenzo Costigliola, Thomas B. Schrøder, Antimo Marrazzo and Davide Bidoggia for fruitful discussions.

We acknowledge support from the Fondazione ICSC "Italian Research Center on High-Performance Computing, Big Data, and Quantum Computing" - Spoke 7, Materials and Molecular Sciences - National Recovery and Resilience Plan (PNRR) - funded by MUR Missione 4 - Componente 2 - Investimento 1.4 - Next Generation EU (NGEU).

We acknowledge CINECA for the computational resources provided through ISCRA initiative and the agreement with the University of Trieste. We also acknowledge the Glass and Time group of Roskilde University for a generous allocation of computational resources on their GPU cluster.

Appendix A

Computational details

Molecular dynamics for silica bilayer

We considered systems composed of N particles in a rectangular cell of sides (L_x, L_y) with periodic boundary conditions. We fixed the number density at the experimental value for a silica bilayer projected onto the substrate, $\rho = N/(L_x L_y) = 0.2068$ [133]. We set the ratio L_y/L_x to obtain a nearly square cell commensurate with the honeycomb lattice at the chosen chemical composition $x_{Si} = 2/5$. We considered system sizes which range from $N = 80$ to 10^5 particles. We performed all our simulations in the NVT ensemble using a Nose-Hoover thermostat with a thermostat relaxation time $\tau_{term} = 1.6381$. The integration timestep was set to 0.045 at $T = 0.015$ and then scaled with the square root of the inverse temperature as $dt(T) = 0.045\sqrt{0.015/T}$.

We performed two kinds of simulations: the first ones to produce out-of-equilibrium glass states and the second ones to simulate liquids at equilibrium conditions. In the first case, the quench protocol consisted of a sequence of simulations at temperatures 0.0200, 0.0125, 0.0100, 0.0075, and 0.0010. These simulations lasted 50000, 50000, 250000, 250000, and 5000 timesteps, respectively. For the equilibrium simulations, we start from a configuration sampled at high temperature and then equilibrate the system at the desired temperature. We anneal the system until the mean square displacement (MSD)[1] of particles of both species exceeds 10^3. We then perform a production run at the same temperature to store configurations, making sure again that the number of steps is such that the final MSD is always at least 10^3.

Density functional theory

Calculations were performed using the `Quantum ESPRESSO` code [198, 199] based on DFT and plane waves. For the boria system, we used Perdew-Burke-Ernzerhof exchange correlation functional [224] within the generalized gradient approximation method. Vanderbilt ultrasoft pseudopotentials [225] from the PSlibrary [226] were employed, with plane-wave cutoffs of 45 and 225 Ry for the wave function and the charge density, respectively. For the occupation of electronic states, the Marzari-Vanderbilt-DeVitaPayne [227] smearing scheme was used with a smearing parameter of 0.02 Ry. Van der Waals interactions are considered using semiempirical Grimme's DFT-D3 corrections [228]. Geometrical optimizations were performed using the Broyden-Fletcher-Goldfarb-Shanno algorithm with energy and force convergence thresholds of 10^{-4} Ry for the whole cell and 10^{-3} a.u. for each atomic force

[1] Due to the presence of long-wavelength fluctuations, see Sec. 3.3, it would be more appropriate to use the cage relative MSD instead of the standard MSD. Nevertheless, the main difference between the two appear in the plateau region at intermediate times, and we deemed their difference in the diffusion regime negligible for the equilibration purpouse.

component, respectively. For each perfectly symmetric structure, small random displacements of the atomic positions are performed to break the symmetry, allowing non vanishing forces to perform the optimization of the internal degrees of freedom. We employed cells and supercells with slab geometries with in-plane hexagonal periodicity and sufficient height to separate adjacent images along the vertical direction. For the freestanding B_2O_3 model the cell height was 11 Å. For the overlayers on *Pt(111)* substrate we used supercells with 3-layer slab geometries with a lattice parameter of 22.79 Å and height of 18 Å. Our DFT equilibrium lattice parameter for bulk platinum is very similar to the experimental one (only slightly larger by 0.5%). We keep the position of the lowest Pt layer fixed. For the reciprocal space sampling, Γ-centered grids of $2\times2\times1$ and $6\times6\times1$ k-points were employed, respectively, for self-consistent field (SCF) and non-self-consistent field (NSCF) calculations for the supercell. For the elementary unit cell of the boria layer, instead, grids of $6\times6\times1$ and $12\times12\times1$ k-points were used for SCF and NSCF calculations. The simulated STM images were obtained by Tersoff-Hamann approach [209] in the framework of the DFT calculation, smoothed by a mild gaussian broadening. To obtain the B_2O_3 band structure referred to the *Pt(111)* first Brillouin zone, we performed an unfolding procedure using the `unfold-x` code [210, 211].

In the analysis of the graphitic carbon nitrates polymorphs we used Projector-Augmented Wave (PAW) pseudopotentials [229], with plane-wave cutoffs of 45 and 180 Ry for the wave function and the charge density, respectively. Gaussian smearing scheme was used for the occupation of electronic states, with a smearing parameter of 0.02 Ry. Van der Waals interactions were not taken into account during these calculations. We use the same convergence thresholds as the boria system. We employed cells and supercells with slab geometries and in-plane hexagonal periodicity, with at least 15 Å of vacuum in the out-of-plane direction to separate adjacent images along the vertical direction. We used Γ-centered grids of $6\times6\times1$ for the reciprocal space sampling.

We also performed a few DFT calculations on a silica bilayer system, for example to identify an energy scale in our effective model for such system, see Sec. 2.1.2. For these calculations we used the same parameters used for boria, the only difference being the plane-wave cutoffs, which were set to 45 and 125 Ry for the wave function and the charge density, respectively.

For all the systems considered, we verified the convergence of the reciprocal space sampling and both plane-wave cutoffs. In detail, we verified that the changes in both the total energy and the lattice parameter using a more accurate calculation, were less than 10^{-2} of their original values.

Appendix B

Experimental data on the silica bilayer

Although silica bilayers were synthesized as early as in 2012 [18, 22], only a handful of experimental configurations have been made publicly available. Moreover, the information is scattered over several papers, which may lead to some uncertainty when computing the statistical properties of amorphous 2*d* silica.

To bring some order, we present in Table B.1 the list of the experimental configurations we used to determine the reference experimental data in this paper. To the best of our knowledge, these are the only amorphous experimental configurations for which the atoms' positions are available or can be easily extracted. For each configuration, we also report the ring statistics and the assortativity, in order to provide the reader with the complete set of raw data. Of the five configurations we used, only three of them explicitly report the atoms' coordinates and can be used for the calculation of the RDFs and the BADs. The other two configurations are available as figures with colored rings. For these last two configurations, we digitized the positions of each ring vertex, *i.e.*, the positions of the *Si* particles, and we scaled those coordinates so that the average *Si-Si* distance equals the experimental one. Given the somewhat arbitrary procedure used to obtain these coordinates, we did not use them for the RDFs and BADs calculations.

Sample	Reference	Type	Substrate	Appearing also as
A	Tab. S3 in Ref. [12]	AC	Ru(0001)	Fig. 2c in Ref. [142]
B	Tab. S4 in Ref. [12]	AC	Ru(0001)	Fig. 2d in Ref. [142]
C	Tab. S2 in Ref. [173]	AC	Ru(0001)	Fig. 2b in Ref. [142]
D	Fig. 2a in Ref. [142]	RS	Graphene on Cu foil	–
E	Fig. 2e in Ref. [142]	RS	Graphene on Cu foil	–

TABLE B.1: Experimental samples used in this work. AC and RS stands for Atomic Coordinates and Ring Structure, respectively

In Table B.2 and B.3, we provide the raw data we used for the calculation of the experimental ring statistics and assortativity. Each quantity is calculated as a weighted average over the configurations, using as weights the total number of rings in each configuration for the average ring statistics and the total number of rings not touching the outer edge for the average assortativity. We provide both sets of weights in their respective tables.

Sample	Number of rings with n sides							Total
	$n=4$	$n=5$	$n=6$	$n=7$	$n=8$	$n=9$	$n=10$	
A	3	23	39	9	8	0	0	82
B	5	17	28	13	2	2	0	67
C	11	80	130	46	21	2	0	290
D	17	121	186	94	22	3	1	444
E	15	118	204	90	19	2	1	449
Ring statistics								
Mean	0.0383	0.2695	0.4407	0.1892	0.0541	0.0068	0.0015	
Std. dev.	0.0043	0.0034	0.0091	0.0142	0.0083	0.0028	0.0005	

TABLE B.2: Experimental ring statistics for the different experimental samples used in this work.

Sample	Assortativity	Weight
A	-0.663	74
B	$+0.066$	58
C	-0.256	281
D	-0.218	434
E	-0.167	439
Average	-0.2216 ± 0.0637	

TABLE B.3: Assortativity coefficients for the different experimental samples used in this work.

Appendix C

Library developed for the analysis of the ring structure

In silica, a ring is typically defined as an ordered set of silicon atoms satisfying appropriate topological rules [140]. The oxygens are only used to define the connectivity between the silicon atoms, and play no role in the ring analysis. Many different definitions of ring have been proposed over the years [140]. These typically build on the presence of a shortest path between particles, such as in Guttman's [230] or shortest path [231, 232] rings, or on the decomposition of larger rings into more fundamental ones, such as strong [233], irreducible [234] or primitive [235] rings. It should be emphasized that these ring definitions are not equivalent [140] and the use of different definitions may led to different conclusions on the same set of data [236]. The presence of many nonequivalent ring definitions is mainly due to the inherent difficulty of three-dimensional networks and the absence of clear intuitive examples of rings in such systems. In this work, we propose a definition of rings that has its roots in graph theory and has a clear intuitive meaning.

Given a system of silicon and oxygen particles, we can define a graph in which the nodes represent silicon particles, while the oxygens define the connections between the nodes. A graph can always be drawn in a planar representation, i.e. without edge-crossing, on a surface of appropriate genus g [237]. The nodes and edges in a planar representation naturally divide the surface in different regions called faces [237]. Since the faces are always well defined and are bounded by an ordered set of nodes, we identify the rings in the system with the faces of the underlying graph.

This definition of rings is very intuitive in a two-dimensional network like the one considered here. At sufficiently low temperatures, the neighbors of each particles are well defined, and therefore the representation of the system in a rectangular cell with periodic boundary conditions is already a planar representation of the corresponding graph. A rectangular cell with periodic boundary conditions is isomorphic to the surface of a torus, i.e. a surface of genus $g = 1$. Therefore, the voids we observe in a given configuration of the system are exactly equal to the faces and every set of particles surrounding one of these regions is a ring according to our definition. In principle, this definition can also be used for three-dimensional systems, if one of their planar representation can be obtained. We implemented an algorithm to identify the rings as described above in the library `l2dr` [238], which we used to analyze the network structure in this work.

Appendix D

Other algorithms

Calculation of the correlation length

To extract the correlation length ξ_n associated to n-fold bond-orientational order, we fitted the whole $|\Psi_n(r)|$ to an exponential function $A \exp -r/\xi_n$, but giving more weight to the points above the fitting function than those below. This procedure, which captures the trend of the envelope very well, is illustrated in Fig. D.1, More precisely, we minimized the cost function given by

$$\chi^2(A, \xi_n) = \sum_{r \in [r_{min}; r_{max}]} \omega(r) \left(-\frac{r}{\xi_n} + \log A - \log |\Psi_n(r)| \right) , \tag{D.1}$$

where $[r_{min}; r_{max}]$ is the interval over which the fit is carried out and

$$\omega(r) = \begin{cases} 1, & \text{if } A\, e^{-r/\xi_n} \geq \Psi_n(r) \\ -\eta, & \text{otherwise} \end{cases} . \tag{D.2}$$

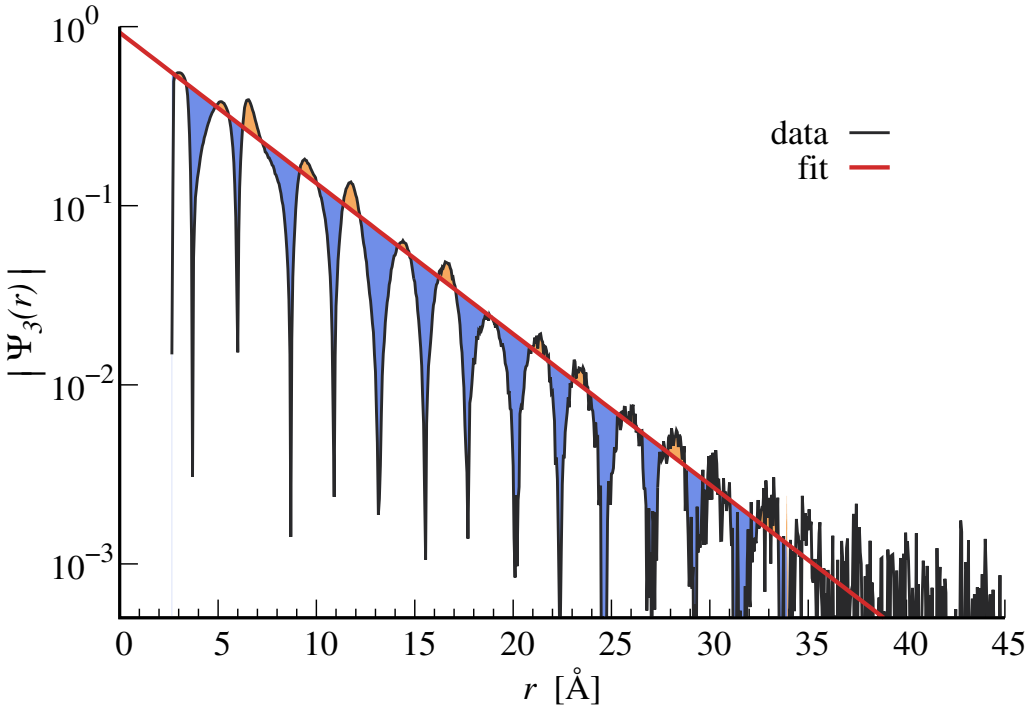

FIGURE D.1: Example of the fitting procedure used to extract the correlation length from the curves in the main text (a). Here $r_{max} = 34$ and the cost function is the sum of twice ($\eta = 2$) the area of the orange regions plus the area of the blue regions.

The minimum distance was fixed to the first non-zero value of $\Psi_n(r)$ for the 3-fold correlations between *Si-Si* and *Si-O* particles and $r_{min} \simeq 4.0$ for the 6-fold correlations between rings, while the maximum one was adjusted depending on temperature so as to remove the noisy part of the correlation function at large r. The weighting function $\omega(r)$ allows one to fine tune the relative weight of points above the fitting line compared with the ones below. We chose $\eta = 2$, since we found the results to be independent of η above this value. Note that even $\eta = 1$ would give the same qualitatively similar trends as a function of T.

Search of commensurate supercells

When a two-dimensional material is grown on a surface, there can be a mismatch between the lattice parameters of overlayer and substrate and a rotation of the overlayer basis with respect to that of the substrate. These effects give rise to different supercells for the system formed by the overlayer and the surface. Different supercells have different symmetries and contain different number of atoms, which can make their study computationally cheaper. Moreover, it might be interesting to check whether a given two-dimensional material is stable on a surface only for a specific relative orientation or how much its lattice parameter can be stretched or compressed to match that of the substrate.

For these reasons we develop an algorithm that finds the commensurate supercells produced by two $2d$ lattices. Our algorithm requires no prior knowledge of the two systems, except for their symmetries. We consider two lattices $\mathcal{A}$ and $\mathcal{B}$ with lattice vectors

$$\begin{aligned} \mathcal{A}&: \{a\mathbf{u_1},\, a\mathbf{u_2}\} \\ \mathcal{B}&: \{b\mathbf{v_1},\, b\mathbf{v_2}\}\ , \end{aligned}$$

where a and b are the moduli of the unit vectors $\mathbf{u_1}$ and $\mathbf{v_1}$, respectively. To produce a commensurate supercell with basis vectors $\{\mathbf{W_1}, \mathbf{W_2}\}$, each basis vectors $\mathbf{W_i}$ has to be written as a linear combination with integer coefficients of the basis vectors of the lattice $\mathcal{A}$ and $\mathcal{B}$. Therefore, if lattice $\mathcal{B}$ is rotated by an angle θ with respect to lattice $\mathcal{A}$, via the rotational matrix $\mathbf{R}(\theta)$, a commensurate supercell has to satisfy

$$\begin{aligned} \mathbf{W_1}&: n_{11}a\mathbf{u_1} + n_{12}a\mathbf{u_2} = \mathbf{R}(\theta)\left[m_{11}b\mathbf{v_1} + m_{12}b\mathbf{v_2}\right] \\ \mathbf{W_2}&: n_{21}a\mathbf{u_1} + n_{22}a\mathbf{u_2} = \mathbf{R}(\theta)\left[m_{21}b\mathbf{v_1} + m_{22}b\mathbf{v_2}\right]\ , \end{aligned} \tag{D.3}$$

where $n_{ij}, m_{ij} \in \mathbb{Z}$. Moreover, to produce a non-degenerate cell, the integer coefficients n_{ij} and m_{ij} have to satisfy

$$\begin{aligned} |n_{11}n_{22} - n_{12}n_{21}| &\neq 0 \\ |m_{11}m_{22} - m_{12}m_{21}| &\neq 0\,. \end{aligned} \tag{D.4}$$

The equations Eq. D.3 and Eq. D.4 define a set of constraints that the integer coefficients have to satisfy to result in a commensurate supercell, assuming that b/a and θ are given, but we can also reason in the opposite way, considering b/a and θ as a function of n_{ij} and m_{ij}. For example, if $\mathcal{A}$ and $\mathcal{B}$ are both hexagonal lattices, with

some simple algebra we have:

$$\frac{b}{a} = \sqrt{\frac{n_{i1}^2 + n_{i1}n_{i2} + n_{i2}^2}{m_{i1}^2 + m_{i1}m_{i2} + m_{i2}^2}} \tag{D.5}$$

$$\theta = \arctan\left(\frac{\sqrt{3}(n_{i2}m_{i1} - n_{i1}m_{i2})}{2n_{i1}m_{i1} + n_{i1}m_{i2} + n_{i2}m_{i1} + 2n_{i2}m_{i2}}\right). \tag{D.6}$$

Therefore, starting from a positive integer N_{max} and generating a set of 8 integers n_{ij} and m_{ij}, each one in the range $[-N_{max}; N_{max}]$, it is possible to find all the commensurate supercells generated by that set of integers. For each supercell it is possible to calculate the ratio between the lattice parameters and the relative rotation of the two basic lattices. In Fig. D.2 we show the set of lattice parameters ratio and relative rotation for two hexagonal lattices. Due to the symmetry of the systems, only the inequivalent part of the graph is represented. In particular, the plot is symmetric with respect to rotation of 30° and periodic with period of 60°. Moreover, due to the symmetry of the x axis, the interval $[1; +\text{inf}]$ is equivalent to the interval $[0; 1]$. The colorscale in Fig. D.2 represents the sum of the number of cells of the two lattices for a given supercell, as an indication of the size of the supercell. The plot shows some small, highly symmetric supercells, such as the point $(b/a, \theta) = (1, 0°)$, surrounded and progressively approached by supercells of increasingly larger sizes. This is to be expected, since small variations in the lattice parameters ratio or the rotations used to obtain a highly symmetrical supercell result in supercells with similar properties, but of much larger sizes.

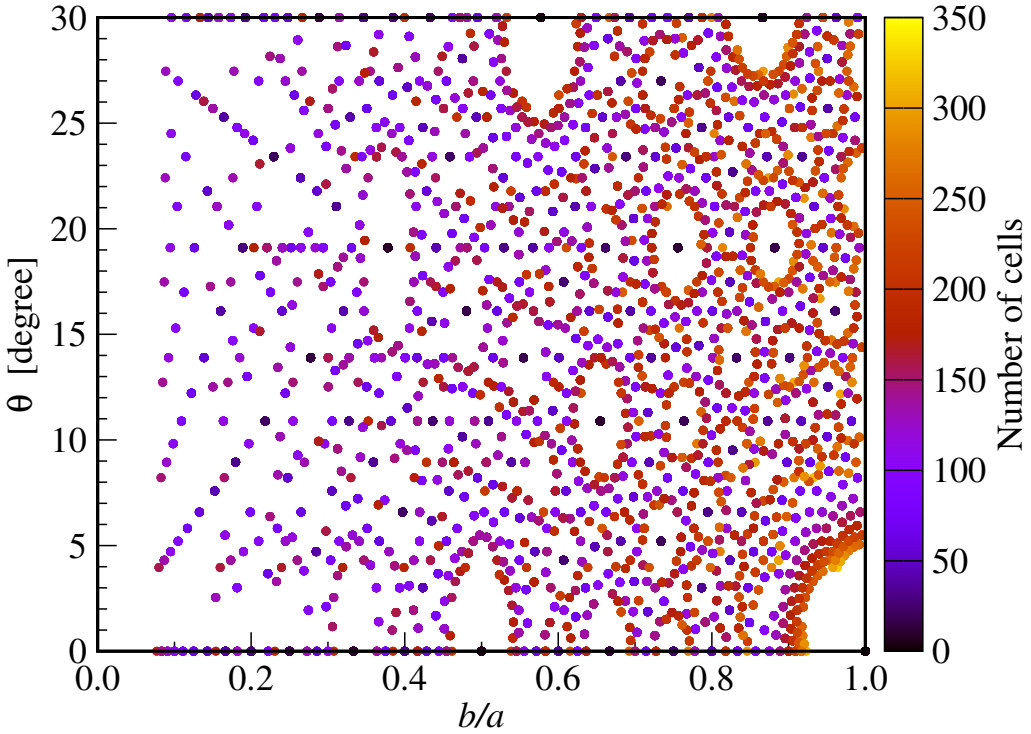

FIGURE D.2: Scatter plot showing the combinations of lattice parameters ratio and relative rotation of two hexagonal lattices required to generate a commensurate supercell. Each point is colored according to the sum of the number of cells of the two elementary lattices, as an indication of the supercell size. Only the inequivalent portion of the graph is shown.

We use the data in Fig. D.2 to check the possible combination of strains and rotations of B_2O_3 and B_3O_3 monolayers on $Pt(111)$. In particular, we fix b to the in-plane lattice parameter of a $Pt(111)$ surface and we study all the supercells within a certain window of values of a, centered around the equilibrium lattice parameter for the free-standing system or the experimentally measured lattice parameter. Due to the large number of particles involved in the supercell and the computational cost of simulating large systems, we limit our study to supercells with less than 350 atoms in total and 3 layers of the substrate. The results of this analysis are presented in Chapter 6.

Appendix E

Additional figures and movies

To support our work, we have prepared a set of figures and movies than can be visualized on this web page[1]. In the following, we provide a brief description of each figure and video.

Figure F3.1 - silica.relaxations_graph.pdf

This figure represents the trajectory of a low temperature system ($T = 0.0067$), shown as a series of successive rearrangements. Each dot represents a single rearrangement, and two rearrangements are connected if they are subsequent and share at least one particle. Green, orange, red, purple and grey dots represent t-string, single bond-switch (1 BS), concatenation of two (2 BS) and three bond-switches (3 BS), and an unidentified rearrangement, respectively. Black dots represents rearrangements which, evaluated between the first frame of the trajectory and the frame at which the relaxation is represented, appear as several separate clusters. The vertical axis represents the instant of time at which a given rearrangement appears, and it is measured in frames of the trajectory, with one frame equal to $10^{-4} \cdot \tau_\alpha(k_1)$.

In the figure we represent both the rearrangements identified between two successive frames and the rearrangement obtained over longer time intervals, starting from the first frame of the trajectory up to the frame at which the rearrangement is placed. These latter rearrangements can be viewed as the concatenation of subsequent individual relaxations identified between two successive frames. Therefore, horizontal lines connect the individual rearrangements to the more complex ones, which are also connected vertically between themselves.

For example, on the left, around time 1000 a single bond-switch (orange dot) appears in the trajectory. Around time 2000, another single bond-switch appears nearby, and when observing the system between time $t_0 = 0$ and $t_1 = 2000$, that set of rearranging particles appears as a concatenation of two bond-switches (red dot). Close to time 2500, another concatenation of 2 BS appears close to the relaxation, and we are unable to correctly classify the resulting rearrangement (grey dot), but at later time several t-strings (green circles) occurs, causing the rearrangement to again appear as 2 BS. Then, close to time 3000, a 1 BS appears nearby, and the overall rearrangement appears as the concatenation of three bond-switches, and so on. In this figure we only plot the data for the largest group of rearrangements in the trajectory.

This representation highlights the complexity of rearrangements in the systems, and allows us to fully describe the trajectory as a tree or directed graph, using the rearrangements as nodes.

[1] https://doi.org/10.5281/zenodo.18669108

Movie M3.1 - dynamics_raw.T0.0067.mp4

This movie shows the trajectory of a system of $N = 15000$ particles at $T = 0.0067$, the lowest temperature at which we can equilibrate the liquid. Blu and red circles represent effective silicons and oxygens, respectively, while the horizontal bar is 20 Å in length. The time interval between two following frames is approximately $0.05\tau_\alpha(k_1)$. The ratio between the time elapsed from the start of the video and $\tau_\alpha(k_1)$ is displayed at the top of the movie. This video highlights the presence of strong thermal fluctuations on a short timescale compared to the relaxation time, even at this low temperature.

Movie M3.2 - dynamics_averaged.T0.0067.mp4

This video shows the same data as the M4.1, with the only difference being the position of the particles in each frame, which are now averaged over 10 successive frames. This averaging procedure significantly reduces the thermal fluctuations observed in M4.1, making the dynamics much clearer. However, since the positions in each frame are the result of an averaging procedure, the movie sometimes shows particles passing through each other.

Movie M3.3 - melting.T0.0067.mp4

The video shows the out-of-equilibrium trajectory of a system of $N = 2200$ particles at $T = 0.0067$. At the start of the simulation the system is a perfect crystal. In the video we plot the dual of the original network, *i.e.* instead of plotting the positions of the particles, we plot the geometric center of the corresponding rings. This procedure significantly reduces the thermal fluctuations of the particles and allows for a direct comparison with the KTHNY theory. Orange, red, grey, blue and purple circles represent 4-, 5-, 6-, 7- and 8-sided rings, respectively.

Figure F4.1 - snapshots.loop.psi3.jpg

This figure is equivalent to Fig. 4.1. It shows the development of local crystalline order in the system. The three panels correspond to configuration taken at temperature $T = 0.0250$, 0.0143 ($\approx T_x$), and 0.0067 (from left to right). The particles are color-coded according to the phase of the complex local order parameter $\psi_{3,i}$, while their size is proportional to $|\psi_{3,i}|$. Only *Si* particles are shown. The white circle in the lower right corner of each configuration has a radius equal to the static correlation length at the corresponding temperature. The palette features repeating colors due to the antiferromagnetic symmetry of $\psi_{3,i}$ in the honeycomb lattice.

Figure F4.2 - snapshots.loop.psi6_rings.jpg

This figure shows the same data as Fig. F4.1, but instead of the local order parameter $\psi_{3,i}$ for a 3-fold symmetry between *Si* particles, it shows the local order parameter $\psi^R_{6,i}$ for a 6-fold symmetry between the geometric centers of the rings. The plotting scheme and the white circles have the same meaning as in Fig. F4.1. The grey mesh represents the ring structure.

Figure F4.3 - snapshots.crystalline_domains.pdf

This figure shows the result of the algorithm that identifies crystalline clusters according to the local order parameter $\psi^R_{6,i}$ for a 6-fold symmetry between the rings, applied to the snapshot of a configuration at $T = 0.0067$. The grey mesh represents the ring structure, and only the hexagonal rings are colored. In the left panel, each hexagonal rings is colored according to the phase of the respective $\psi^R_{6,i}$, as in Fig. 4.2., while in the right panel the rings in the same crystalline cluster (as identified by the algorithm) have the same color, equal to the average phase of $\psi^R_{6,i}$ for the rings within the cluster.

Movie M4.1 - dynamics_loop.T0.0067.mp4

This video shows the evolution of the crystalline domains in the equilibrium simulation of the system at low temperature ($T = 0.0067$). The video uses the same trajectory as movies M3.1 and M3.2, and the positions are averaged as in movie M3.2. Only the *Si* particles are shown, and the plotting scheme is the same as Fig. 4.1 and Fig. F4.1, namely, we plot each particle with a circle, whose radius is linked to the module of $\psi_{3,i}$ and whose color is related to the phase of $\psi_{3,i}$. The video show how the crystalline domains, *i.e.* patches of particles with similar color, transform during the simulation. Crucially, no single crystalline domain survives throughout the entire simulations, meaning that these domains are transient in nature, as assumed in the cybotactic theory.

Movie M4.2 - dynamics_with_substrate.a2.64_f0.02_T0.0100.mp4

The video shows the out-of-equilibrium dynamic of the system on a type I substrate, with parameters $a = 2.64$ Å and $f = 0.02$. The simulation is performed at constant temperature, equal to $T = 0.0100$. Blue and red circle represent *Si* and *O* particles, respectively, and their positions is averaged over several frames, as in movie M3.2, to reduce the effect of thermal fluctuations. The video shows the crystallization of the system and some rearrangements that occur within the crystal.

Movie M4.3 - dynamics_with_substrate.a2.76_f0.03_T0.0100.mp4

The video shows the equilibrium dynamic of the system on a type II substrate, with parameters $a = 2.76$ Å and $f = 0.03$. For this interaction strength f, the overlayer is weakly affected by the substrate. The simulation is performed at constant temperature, equal to $T = 0.0100$. Blue and red circle represent *Si* and *O* particles, respectively, and their positions is averaged over several frames, as in movie M3.2, to reduce the effect of thermal fluctuations.

Movie M4.4 - dynamics_with_substrate.a2.76_f0.05_T0.0100.mp4

The video shows the equilibrium dynamic of the system on a type II substrate, with parameters $a = 2.76$ Å and $f = 0.05$. For this interaction strength f, the overlayer is moderately affected by the substrate. The simulation is performed at constant temperature, equal to $T = 0.0100$. Blue and red circle represent *Si* and *O* particles, respectively, and their positions is averaged over several frames, as in movie M3.2, to reduce the effect of thermal fluctuations.

Movie M4.5 - dynamics_with_substrate.a2.76_f0.08_T0.0100.mp4

The video shows the equilibrium dynamic of the system on a type II substrate, with parameters $a = 2.76$ Å and $f = 0.08$. For this interaction strength f, the overlayer is strongly affected by the substrate. The simulation is performed at constant temperature, equal to $T = 0.0100$. Blue and red circle represent *Si* and *O* particles, respectively, and their positions is averaged over several frames, as in movie M3.2, to reduce the effect of thermal fluctuations.

Movie M4.6 - dynamics_with_substrate.a2.11_f0.08_T0.0100.mp4

The video shows the equilibrium dynamic of the system on a type III substrate, with parameters $a = 2.11$ Å and $f = 0.08$. The simulation is performed at constant temperature, equal to $T = 0.0100$. Blue and red circle represent *Si* and *O* particles, respectively, and their positions is averaged over several frames, as in movie M3.2, to reduce the effect of thermal fluctuations.

Movie M4.7 - dynamics_with_substrate.a3.52_f0.08_T0.0100.mp4

The video shows the equilibrium dynamic of the system on a type IV substrate, with parameters $a = 3.52$ Å and $f = 0.08$. The simulation is performed at constant temperature, equal to $T = 0.0100$. Blue and red circle represent *Si* and *O* particles, respectively, and their positions is averaged over several frames, as in movie M3.2, to reduce the effect of thermal fluctuations.

Figure F5.1 - structure_polymorphs.T0H2.rigid_flexible_model.jpg

This figure shows two structures of the T_0H_2 polymorphs produced using the *rigid* and *flexible* models, along with their respective energy-strain curves. Blue and red lines refer to the *rigid* and *flexible* models, respectively. White and red circles represent boron and oxygen atoms, respectively.

Figure F5.2 - structure_polymorphs.T0H4.T5H3.pdf

This figure shows the relaxed atomic models and the simulated STM images of the T_0H_4 and T_5H_3 polymorphs. Each panel is 50 Å$\times$ 20 Å. White and red circles represent boron and oxygen atoms, respectively.

Movie M5.1 - b2o3.bands_strain.mp4

This video shows the evolution of the band structure of the free-standing T_0H_2 polymorph as a function of the strain a/a_{max} for the *flexible* model. The path in reciprocal space is the same as in Fig. 5.7, and the structure of the system is shown in the inset, with white and red circles representing boron and oxygen atoms, respectively.

Figure F7.1 - structure.b2o3.amorphous_sample.pdf

This figure is the enlarged version of Fig. 7.6 (c). It presents the network structure observed in an amorphous B_2O_3 sample. The pores with 4, 5, 6, 7, 8, 9 and 10 or more sides are colored in orange, red, green, blue, purple, yellow and pink, respectively.

Bibliography

(1) C. Klein, A. Philpotts, *Earth Materials: Introduction to Mineralogy and Petrology*, Second edition; Cambridge University Press: 2016, DOI: 10.1017/9781316652909.

(2) O. W. Flörke, H. A. Graetsch, et al. In *Ullmann's Encyclopedia of Industrial Chemistry*; John Wiley & Sons, Ltd: 2008, DOI: 10.1002/14356007.a23_583.pub3.

(3) J. C. Dyre "*Colloquium: The glass transition and elastic models of glass-forming liquids*". *Rev. Mod. Phys.* **2006**, *78*, 953–972, DOI: 10.1103/RevModPhys.78.953.

(4) J.-Q. Zhong, H.-J. Freund "*Two-Dimensional Ultrathin Silica Films*". *Chem. Rev.* **2022**, *122*, 11172–11246, DOI: 10.1021/acs.chemrev.1c00995.

(5) R. Shi, H. Tanaka "*Impact of local symmetry breaking on the physical properties of tetrahedral liquids*". *Proceedings of the National Academy of Sciences* **2018**, *115*, 1980–1985, DOI: 10.1073/pnas.1717233115.

(6) M. S. Shell, P. G. Debenedetti, A. Z. Panagiotopoulos "*Molecular structural order and anomalies in liquid silica*". *Phys. Rev. E* **2002**, *66*, 011202, DOI: 10.1103/PhysRevE.66.011202.

(7) I. Saika-Voivod, F. Sciortino, T. Grande, P. H. Poole "*Phase diagram of silica from computer simulation*". *Phys. Rev. E* **2004**, *70*, 061507, DOI: 10.1103/PhysRevE.70.061507.

(8) I. Saika-Voivod, F. Sciortino, P. H. Poole "*Computer simulations of liquid silica: Equation of state and liquid–liquid phase transition*". *Phys. Rev. E* **2000**, *63*, 011202, DOI: 10.1103/PhysRevE.63.011202.

(9) J. Horbach, W. Kob "*Static and dynamic properties of a viscous silica melt*". *Phys. Rev. B* **1999**, *60*, 3169–3181, DOI: 10.1103/PhysRevB.60.3169.

(10) J. R. G. Da Silva, D. G. Pinatti, C. E. Anderson, M. L. Rudee "*A refinement of the structure of vitreous silica*". *The Philosophical Magazine: A Journal of Theoretical Experimental and Applied Physics* **1975**, *31*, 713–717, DOI: 10.1080/14786437508226549.

(11) A. C. Wright "*Silicate glass structure: towards a working hypothesis for the 21st century*". *Physics and Chemistry of Glasses - European Journal of Glass Science andTechnology Part B* **2020**, *61*, 57–76, DOI: 10.13036/17533562.61.2.02.

(12) L. Lichtenstein, M. Heyde, H.-J. Freund "*Atomic Arrangement in Two-Dimensional Silica: From Crystalline to Vitreous Structures*". *J. Phys. Chem. C* **2012**, *116*, 20426–20432, DOI: 10.1021/jp3062866.

(13) D. Kuhness, H. J. Yang, et al. "*A Two-Dimensional 'Zigzag' Silica Polymorph on a Metal Support*". *J. Am. Chem. Soc.* **2018**, *140*, 6164–6168, DOI: 10.1021/jacs.8b02905.

(14) G. Wang, G. C. Loh, R. Pandey, S. P. Karna "*Novel Two-Dimensional Silica Monolayers with Tetrahedral and Octahedral Configurations*". *J. Phys. Chem. C* **2015**, *119*, 15654–15660, DOI: 10.1021/acs.jpcc.5b01646.

(15) J. Weissenrieder, S. Kaya, J.-L. Lu, H.-J. Gao, S. Shaikhutdinov, H.-J. Freund, M. Sierka, T. K. Todorova, J. Sauer "*Atomic Structure of a Thin Silica Film on a Mo(112) Substrate: A Two-Dimensional Network of $\{\mathrm{SiO}\}_{4}$ Tetrahedra*". *Phys. Rev. Lett.* **2005**, *95*, 076103, DOI: 10.1103/PhysRevLett.95.076103.

(16) S. Shaikhutdinov, H.-J. Freund "*Ultra-thin silicate films on metals*". *J. Phys.: Condens. Matter* **2015**, *27*, 443001, DOI: 10.1088/0953-8984/27/44/443001.

(17) D. Löffler, J. J. Uhlrich, et al. "*Growth and Structure of Crystalline Silica Sheet on Ru(0001)*". *Phys. Rev. Lett.* **2010**, *105*, 146104, DOI: 10.1103/PhysRevLett.105.146104.

(18) P. Y. Huang, S. Kurasch, et al. "*Direct Imaging of a Two-Dimensional Silica Glass on Graphene*". *Nano Lett.* **2012**, *12*, 1081–1086, DOI: 10.1021/nl204423x.

(19) M. Heyde, S. Shaikhutdinov, H. J. Freund "*Two-dimensional silica: Crystalline and vitreous*". *Chemical Physics Letters* **2012**, *550*, 1–7, DOI: 10.1016/j.cplett.2012.08.063.

(20) C. Büchner, M. Heyde "*Two-dimensional silica opens new perspectives*". *Progress in Surface Science* **2017**, *92*, 341–374, DOI: 10.1016/j.progsurf.2017.09.001.

(21) C. Büchner, Z.-J. Wang, K. M. Burson, M.-G. Willinger, M. Heyde, R. Schlögl, H.-J. Freund "*A Large-Area Transferable Wide Band Gap 2D Silicon Dioxide Layer*". *ACS Nano* **2016**, *10*, 7982–7989, DOI: 10.1021/acsnano.6b03929.

(22) L. Lichtenstein, C. Büchner, B. Yang, S. Shaikhutdinov, M. Heyde, M. Sierka, R. Włodarczyk, J. Sauer, H.-J. Freund "*The Atomic Structure of a Metal-Supported Vitreous Thin Silica Film*". *Angewandte Chemie International Edition* **2012**, *51*, 404–407, DOI: 10.1002/anie.201107097.

(23) X. Yu, B. Yang, J. Anibal Boscoboinik, S. Shaikhutdinov, H.-J. Freund "*Support effects on the atomic structure of ultrathin silica films on metals*". *Applied Physics Letters* **2012**, *100*, 151608, DOI: 10.1063/1.3703609.

(24) E. I. Altman, J. Götzen, N. Samudrala, U. D. Schwarz "*Growth and Characterization of Crystalline Silica Films on Pd(100)*". *J. Phys. Chem. C* **2013**, *117*, 26144–26155, DOI: 10.1021/jp4101152.

(25) G. S. Hutchings, J.-H. Jhang, C. Zhou, D. Hynek, U. D. Schwarz, E. I. Altman "*Epitaxial NixPd1–x (111) Alloy Substrates with Continuously Tunable Lattice Constants for 2D Materials Growth*". *ACS Appl. Mater. Interfaces* **2017**, *9*, 11266–11271, DOI: 10.1021/acsami.7b01369.

(26) P. Y. Huang, S. Kurasch, J. S. Alden, A. Shekhawat, A. A. Alemi, P. L. McEuen, J. P. Sethna, U. Kaiser, D. A. Muller "*Imaging Atomic Rearrangements in Two-Dimensional Silica Glass: Watching Silica's Dance*". *Science* **2013**, *342*, 224–227, DOI: 10.1126/science.1242248.

(27) L. Gura, Y.-F. Chen, M. Sierka, M. Heyde, Z. Yang, H.-J. Freund "*Low-Temperature Transformations in Amorphous Silica Bilayers on Ru(0001) After Crystal-Glass Transition: Closer Look*". *Chemistry – A European Journal* **2025**, *n/a*, e02669, DOI: 10.1002/chem.202502669.

(28) A. L. Lewandowski, S. Tosoni, et al. "*Growth and Atomic-Scale Characterization of Ultrathin Silica and Germania Films: The Crucial Role of the Metal Support*". *Chemistry – A European Journal* **2021**, *27*, 1870–1885, DOI: 10.1002/chem.202001806.

(29) V. L. Solozhenko, O. O. Kurakevych, Y. Le Godec, V. V. Brazhkin "*Thermodynamically Consistent p–T Phase Diagram of Boron Oxide B2O3 by in Situ Probing and Thermodynamic Analysis*". *J. Phys. Chem. C* **2015**, *119*, 20600–20605, DOI: 10.1021/acs.jpcc.5b07088.

(30) A. C. Wright "*The structural chemistry of B2O3*". *Physics and Chemistry of Glasses - European Journal of Glass Science andTechnology Part B* **2018**, *59*, 65–87, DOI: 10.13036/17533562.59.2.034.

(31) A. C. Wright "*My Borate Life: An Enigmatic Journey*". *International Journal of Applied Glass Science* **2015**, *6*, 45–63, DOI: 10.1111/ijag.12113.

(32) F. C. Kracek, G. W. Morey, H. E. Merwin "*The system water-boron oxide*". **1938**, *35A*, 143–171.

(33) D. R. Uhlmann, J. F. Hays, D. Turnbull "*The Effect of High Pressure On B2O3 Crystallization, densification and the Crystallization Anomaly*". **1966**.

(34) M. J. Aziz, E. Nygren, J. F. Hays, D. Turnbull "*Crystal growth kinetics of boron oxide under pressure*". *Journal of Applied Physics* **1985**, *57*, 2233–2242, DOI: 10.1063/1.334368.

(35) G. Ferlat, A. P. Seitsonen, M. Lazzeri, F. Mauri "*Hidden polymorphs drive vitrification in B2O3*". *Nature Mater* **2012**, *11*, 925–929, DOI: 10.1038/nmat3416.

(36) G. E. Walrafen, S. R. Samanta, P. N. Krishnan "*Raman investigation of vitreous and molten boric oxide*". *J. Chem. Phys.* **1980**, *72*, 113–120, DOI: 10.1063/1.438894.

(37) J. Goubeau, H. Keller "*RAMAN-Spektren und Struktur von Boroxol-Verbindungen*". *Zeitschrift für anorganische und allgemeine Chemie* **1953**, *272*, 303–312, DOI: 10.1002/zaac.19532720510.

(38) P. A. V. Johnson, A. C. Wright, R. N. Sinclair "*A neutron diffraction investigation of the structure of vitreous boron trioxide*". *Journal of Non-Crystalline Solids* **1982**, *50*, 281–311, DOI: 10.1016/0022-3093(82)90092-8.

(39) A. C. Wright, G. Dalba, F. Rocca, N. M. Vedishcheva "*Borate versus silicate glasses: why are they so different?*" *Physics and Chemistry of Glasses - European Journal of Glass Science andTechnology Part B* **2010**, *51*, 233–265.

(40) F. Claeyssens, J. N. Hart, N. C. Norman, N. L. Allan "*Ultra-Flexible Boron-Oxygen 3D Solid-State Networks*". *Advanced Functional Materials* **2013**, *23*, 5887–5892, DOI: 10.1002/adfm.201300172.

(41) G. Ferlat, M. Hellgren, F.-X. Coudert, H. Hay, F. Mauri, M. Casula "*van der Waals forces stabilize low-energy polymorphism in ${\mathrm{B}}_{2}{\mathrm{O}}_{3}$: Implications for the crystallization anomaly*". *Phys. Rev. Mater.* **2019**, *3*, 063603, DOI: 10.1103/PhysRevMaterials.3.063603.

(42) M. Stredansky, A. Sala, T. Fontanot, R. Costantini, C. Africh, G. Comelli, L. Floreano, A. Morgante, A. Cossaro "*On-surface synthesis of a 2D boroxine framework: a route to a novel 2D material?*" *Chem. Commun.* **2018**, *54*, 3971–3973, DOI: 10.1039/C8CC01372A.

(43) T. Zio, M. Dirindin, et al. "*Two-dimensional diboron trioxide crystal composed by boroxol groups*". *Science* **2025**, *390*, 95–99, DOI: 10.1126/science.adv2582.

(44) T. Zio "*Synthesis of two-dimensional B2O3 and characterization of its crystalline and vitreous phases*", en, Ph.D. Thesis, Trieste, 2025.

(45) M Micoulaut, L Cormier, G. S. Henderson "*The structure of amorphous, crystalline and liquid GeO2*". *J. Phys.: Condens. Matter* **2006**, *18*, R753, DOI: 10.1088/0953-8984/18/45/R01.

(46) A. L. Lewandowski, P. Schlexer, C. Büchner, E. M. Davis, H. Burrall, K. M. Burson, W.-D. Schneider, M. Heyde, G. Pacchioni, H.-J. Freund "*Atomic structure of a metal-supported two-dimensional germania film*". *Phys. Rev. B* **2018**, *97*, 115406, DOI: 10.1103/PhysRevB.97.115406.

(47) A. L. Lewandowski, S. Tosoni, L. Gura, P. Schlexer, P. Marschalik, W.-D. Schneider, M. Heyde, G. Pacchioni, H.-J. Freund "*From Crystalline to Amorphous Germania Bilayer Films at the Atomic Scale: Preparation and Characterization*". *Angewandte Chemie International Edition* **2019**, *58*, 10903–10908, DOI: 10.1002/anie.201903922.

(48) A. Malashevich, S. Ismail-Beigi, E. I. Altman "*Directing the Structure of Two-Dimensional Silica and Silicates*". *J. Phys. Chem. C* **2016**, *120*, 26770–26781, DOI: 10.1021/acs.jpcc.6b07008.

(49) J. Liebig "*Uber einige Stickstoff - Verbindungen*". *Annalen der Pharmacie* **1834**, *10*, 1–47, DOI: 10.1002/jlac.18340100102.

(50) T. S. Miller, A. B. Jorge, T. M. Suter, A. Sella, F. Corà, P. F. McMillan "*Carbon nitrides: synthesis and characterization of a new class of functional materials*". *Phys. Chem. Chem. Phys.* **2017**, *19*, 15613–15638, DOI: 10.1039/C7CP02711G.

(51) S. Kumar, V. R. Battula, K. Kailasam "*Single molecular precursors for CxNy materials- Blending of carbon and nitrogen beyond g-C3N4*". *Carbon* **2021**, *183*, 332–354, DOI: 10.1016/j.carbon.2021.07.025.

(52) M. Chen, H. Zhang, H. Li, Z. Zhao, K. Wang, Y. Zhou, X. Zhao, D. P. Dubal "*CxNy-based materials as gas sensors: Structure, performance, mechanism and perspective*". *Coordination Chemistry Reviews* **2024**, *503*, 215653, DOI: 10.1016/j.ccr.2023.215653.

(53) B. Zhu, B. Cheng, L. Zhang, J. Yu "*Review on DFT calculation of s-triazine-based carbon nitride*". *Carbon Energy* **2019**, *1*, 32–56, DOI: 10.1002/cey2.1.

(54) F. Cucchiaro, M. Peressi, N. Seriani, M. Dirindin "*Numerical simulations of 2D carbon nitride based polymorphs: composition, structure, stability, reactivity*", en, MA thesis, Trieste, 2025.

(55) F. Besharat, F. Ahmadpoor, Z. Nezafat, M. Nasrollahzadeh, N. R. Manwar, P. Fornasiero, M. B. Gawande "*Advances in Carbon Nitride-Based Materials and Their Electrocatalytic Applications*". *ACS Catal.* **2022**, *12*, 5605–5660, DOI: 10.1021/acscatal.1c05728.

(56) S. Mazzanti, G. Manfredi, A. J. Barker, M. Antonietti, A. Savateev, P. Giusto "*Carbon Nitride Thin Films as All-In-One Technology for Photocatalysis*". *ACS Catal.* **2021**, *11*, 11109–11116, DOI: 10.1021/acscatal.1c02909.

(57) D. Cruz, S. Żółtowska, O. Savateev, M. Antonietti, P. Giusto "*Carbon nitride caught in the act of artificial photosynthesis*". *Nat Commun* **2025**, *16*, 374, DOI: 10.1038/s41467-024-55518-x.

(58) P. Giusto, D. Cruz, T. Heil, H. Arazoe, P. Lova, T. Aida, D. Comoretto, M. Patrini, M. Antonietti "*Shine Bright Like a Diamond: New Light on an Old Polymeric Semiconductor*". *Advanced Materials* **2020**, *32*, 1908140, DOI: 10.1002/adma.201908140.

(59) X. Yuan, X. Hu, Q. Lin, S. Zhang "*Progress of charge carrier dynamics and regulation strategies in 2D CxNy-based heterojunctions*". *Chem. Commun.* **2024**, *60*, 2283–2300, DOI: 10.1039/D3CC05976F.

(60) D. Bhanderi, P. Lakhani, C. K. Modi "*Graphitic carbon nitride (g-C 3 N 4) as an emerging photocatalyst for sustainable environmental applications: a comprehensive review*". *RSC Sustainability* **2024**, *2*, 265–287, DOI: 10.1039/D3SU00382E.

(61) D. Liang, T. Jing, Y. Ma, J. Hao, G. Sun, M. Deng "*Photocatalytic Properties of g-C6N6/g-C3N4 Heterostructure: A Theoretical Study*". *J. Phys. Chem. C* **2016**, *120*, 24023–24029, DOI: 10.1021/acs.jpcc.6b08699.

(62) B. Zhu, L. Zhang, B. Cheng, J. Yu "*First-principle calculation study of tri-s-triazine-based g-C3N4: A review*". *Applied Catalysis B: Environmental* **2018**, *224*, 983–999, DOI: 10.1016/j.apcatb.2017.11.025.

(63) H. Zhang, G. Xu, Y. Yu "*Co single-atom C2N3 activates peroxymonosulfate for efficient degradation of sulfamethoxazole at 4 °C: A combined experimental and density functional theory study*". *Chemical Engineering Journal* **2023**, *476*, 146721, DOI: 10.1016/j.cej.2023.146721.

(64) J. Gracia, P. Kroll "*Corrugated layered heptazine-based carbon nitride: the lowest energy modifications of C3N4 ground state*". *J. Mater. Chem.* **2009**, *19*, 3013–3019, DOI: 10.1039/B821568E.

(65) E. Kroke, M. Schwarz, E. Horath-Bordon, P. Kroll, B. Noll, A. D. Norman "*Tri-s-triazine derivatives. Part I. From trichloro-tri-s-triazine to graphitic C3N4 structures*". *New J. Chem.* **2002**, *26*, 508–512, DOI: 10.1039/B111062B.

(66) J. Kouvetakis, M. Todd, B. Wilkens, A. Bandari, N. Cave "*Novel Synthetic Routes to Carbon-Nitrogen Thin Films*". *Chem. Mater.* **1994**, *6*, 811–814, DOI: 10.1021/cm00042a018.

(67) G. Algara-Siller, N. Severin, et al. "*Triazine-Based Graphitic Carbon Nitride: a Two-Dimensional Semiconductor*". *Angewandte Chemie International Edition* **2014**, *53*, 7450–7455, DOI: 10.1002/anie.201402191.

(68) Z. Song, J. Hou, E. Raguin, A. Pedersen, E. O. Eren, E. Senokos, N. V. Tarakina, P. Giusto, M. Antonietti "*Triazine-Based Graphitic Carbon Nitride Thin Film as a Homogeneous Interphase for Lithium Storage*". *ACS Nano* **2024**, *18*, 2066–2076, DOI: 10.1021/acsnano.3c08771.

(69) A. Cavagna "*Supercooled liquids for pedestrians*". *Physics Reports* **2009**, *476*, 51–124, DOI: 10.1016/j.physrep.2009.03.003.

(70) L. Berthier, M. D. Ediger "*Facets of glass physics*". *Physics Today* **2016**, *69*, 40–46, DOI: 10.1063/PT.3.3052.

(71) P. G. Debenedetti, F. H. Stillinger "*Supercooled liquids and the glass transition*". *Nature* **2001**, *410*, 259–267, DOI: 10.1038/35065704.

(72) W. Kob, H. C. Andersen "*Scaling Behavior in the $\ensuremath{\beta}$-Relaxation Regime of a Supercooled Lennard-Jones Mixture*". *Phys. Rev. Lett.* **1994**, *73*, 1376–1379, DOI: 10.1103/PhysRevLett.73.1376.

(73) C. A. Angell "*Structural instability and relaxation in liquid and glassy phases near the fragile liquid limit*". *Journal of Non-Crystalline Solids* **1988**, *102*, 205–221, DOI: 10.1016/0022-3093(88)90133-0.

(74) L. Berthier, G. Biroli "*Theoretical perspective on the glass transition and amorphous materials*". *Rev. Mod. Phys.* **2011**, *83*, 587–645, DOI: 10.1103/RevModPhys.83.587.

(75) A. Saksaengwijit "*Origin of the Fragile-to-Strong Crossover in Liquid Silica as Expressed by its Potential-Energy Landscape*". *Phys. Rev. Lett.* **2004**, *93*, DOI: 10.1103/PhysRevLett.93.235701.

(76) I. Saika-Voivod, P. H. Poole, F. Sciortino "*Fragile-to-strong transition and polyamorphism in the energy landscape of liquid silica*". *Nature* **2001**, *412*, 514–517, DOI: 10.1038/35087524.

(77) I. Saika-Voivod, F. Sciortino, P. H. Poole "*Free energy and configurational entropy of liquid silica: Fragile-to-strong crossover and polyamorphism*". *Phys. Rev. E* **2004**, *69*, DOI: 10.1103/PhysRevE.69.041503.

(78) A. C. Wright "*Crystalline-like ordering in melt-quenched network glasses?*" *Journal of Non-Crystalline Solids* **2014**, *401*, 4–26, DOI: 10.1016/j.jnoncrysol.2013.12.012.

(79) A. C. Wright "*The Great Crystallite Versus Random Network Controversy: A Personal Perspective*". *International Journal of Applied Glass Science* **2014**, *5*, 31–56, DOI: 10.1111/ijag.12039.

(80) M. L. Frankenheim, *Die Lehre von der Cohäsion: umfassend die Elasticität der Gase, die Elasticität und Cohärenz der flüssigen und festen Körper und die Krystallkunde, nebst vielen neuen Tabellen über alle Theile der Cohäsionslehre, in's besondere über die Elasticität und die Festigkeit*; bei August Schulz und Comp.: Breslau, 1835.

(81) A. A. Lebedev "*O Polimorfizme i Otzhige Stekla (On the Polymorphism and Annealing of Glass)*". **1921**, *50*, 57–76.

(82) J. T. Randall, H. P. Rooksby, B. S. Cooper "*Atomic Physics and Related Subjects.: Communications to Nature.: The Diffraction of X-Rays by Vitreous Solids and its Bearing on their Constitution*". *Nature* **1930**, *125*, 458–458, DOI: 10.1038/125458a0.

(83) J. T. Randall, H. P. Rooksby, B. S. Cooper "*13. X-ray Diffraction and the Structure of Vitreous Solids — I*". *Zeitschrift für Kristallographie - Crystalline Materials* **1930**, *75*, 196–214, DOI: 10.1515/zkri-1930-0114.

(84) J. T. Randall, H. P. Rooksby, B. S. Cooper "*The Structure of Glasses; The Evidence of X-Ray Diffraction*". **1930**, *14*, 219–229.

(85) W. H. Zachariasen "*The atomic arrangement in glass*". *J. Am. Chem. Soc.* **1932**, *54*, 3841–3851, DOI: 10.1021/ja01349a006.

(86) W. Rosenhain "*The Structure and Constitution of Glas*". **1927**, *11*, 77–97.

(87) B. E. Warren "*X-Ray Diffraction of Vitreous Silica*". *Zeitschrift für Kristallographie - Crystalline Materials* **1933**, *86*, 349–358, DOI: 10.1524/zkri.1933.86.1.349.

(88) J. T. Randall, H. P. Rooksby "*X-Ray Diffraction and the Structure of Glasses*". **1933**, *17*, 287–295.

(89) A. C. Wright "*Density fluctuations in vitreous SiO2 and GeO2*". *Physics and Chemistry of Glasses - European Journal of Glass Science andTechnology Part B* **2019**, *60*, 33–48, DOI: 10.13036/17533562.60.2.001.

(90) G. W. Stewart, R. M. Morrow "*X-Ray Diffraction in Liquids: Primary Normal Alcohols*". *Phys. Rev.* **1927**, *30*, 232–244, DOI: 10.1103/PhysRev.30.232.

(91) G. W. Stewart "*X-Ray Diffraction in Liquids*". *Rev. Mod. Phys.* **1930**, *2*, 116–122, DOI: 10.1103/RevModPhys.2.116.

(92) N. Valenkov, E. Poray-Koshitz "*X-ray Investigation of the Glassy State*". *Zeitschrift für Kristallographie - Crystalline Materials* **1936**, *95*, 195–229, DOI: 10.1524/zkri.1936.95.1.195.

(93) S. Urnes In *Modern Aspects of the Vitreous State*; Butterworths: 1960, pp 10–37.

(94) G. N. Greaves "*EXAFS and the structure of glass*". *Journal of Non-Crystalline Solids* **1985**, *71*, 203–217, DOI: 10.1016/0022-3093(85)90289-3.

(95) R. J. Bell, P. Dean "*Properties of Vitreous Silica: Analysis of Random Network Models*". *Nature* **1966**, *212*, 1354–1356, DOI: 10.1038/2121354a0.

(96) F. Wooten, K. Winer, D. Weaire "*Computer Generation of Structural Models of Amorphous Si and Ge*". *Phys. Rev. Lett.* **1985**, *54*, 1392–1395, DOI: 10.1103/PhysRevLett.54.1392.

(97) A. C. Wright, M. F. Thorpe "*Eighty years of random networks*". *Physica Status Solidi (b)* **2013**, *250*, 931–936, DOI: 10.1002/pssb.201248500.

(98) J. M. Gibson, M. M. J. Treacy, T. Sun, N. J. Zaluzec "*Substantial Crystalline Topology in Amorphous Silicon*". *Phys. Rev. Lett.* **2010**, *105*, 125504, DOI: 10.1103/PhysRevLett.105.125504.

(99) N. D. Mermin, H. Wagner "*Absence of Ferromagnetism or Antiferromagnetism in One- or Two-Dimensional Isotropic Heisenberg Models*". *Phys. Rev. Lett.* **1966**, *17*, 1133–1136, DOI: 10.1103/PhysRevLett.17.1133.

(100) P. C. Hohenberg "*Existence of Long-Range Order in One and Two Dimensions*". *Phys. Rev.* **1967**, *158*, 383–386, DOI: 10.1103/PhysRev.158.383.

(101) N. D. Mermin "*Crystalline Order in Two Dimensions*". *Phys. Rev.* **1968**, *176*, 250–254, DOI: 10.1103/PhysRev.176.250.

(102) E. Bernard "*Algorithms and applications of the Monte Carlo method : Two-dimensional melting and perfect sampling*", en, Ph.D. Thesis, Université Pierre et Marie Curie - Paris VI, 2011.

(103) H. Shiba, P. Keim, T. Kawasaki "*Isolating long-wavelength fluctuation from structural relaxation in two-dimensional glass: cage-relative displacement*". *J. Phys.: Condens. Matter* **2018**, *30*, 094004, DOI: 10.1088/1361-648X/aaa8b8.

(104) N. W. Ashcroft, N. D. Mermin, *Solid State Physics*; Cengage Learning: 2011.

(105) H. Shiba, Y. Yamada, T. Kawasaki, K. Kim "*Unveiling Dimensionality Dependence of Glassy Dynamics: 2D Infinite Fluctuation Eclipses Inherent Structural Relaxation*". *Phys. Rev. Lett.* **2016**, *117*, 245701, DOI: 10.1103/PhysRevLett.117.245701.

(106) E. Flenner, G. Szamel "*Fundamental differences between glassy dynamics in two and three dimensions*". *Nat Commun* **2015**, *6*, 7392, DOI: 10.1038/ncomms8392.

(107) A. S. Keys, L. O. Hedges, J. P. Garrahan, S. C. Glotzer, D. Chandler "*Excitations Are Localized and Relaxation Is Hierarchical in Glass-Forming Liquids*". *Phys. Rev. X* **2011**, *1*, 021013, DOI: 10.1103/PhysRevX.1.021013.

(108) G. Tarjus "*Glass transitions may be similar in two and three dimensions, after all*". *Proceedings of the National Academy of Sciences* **2017**, *114*, 2440–2442, DOI: 10.1073/pnas.1700193114.

(109) H. Shiba, T. Kawasaki, K. Kim "*Local Density Fluctuation Governs the Divergence of Viscosity Underlying Elastic and Hydrodynamic Anomalies in a 2D Glass-Forming Liquid*". *Phys. Rev. Lett.* **2019**, *123*, 265501, DOI: 10.1103/PhysRevLett.123.265501.

(110) B. Illing, S. Fritschi, H. Kaiser, C. L. Klix, G. Maret, P. Keim "*Mermin–Wagner fluctuations in 2D amorphous solids*". *Proceedings of the National Academy of Sciences* **2017**, *114*, 1856–1861, DOI: 10.1073/pnas.1612964114.

(111) S. Vivek, C. P. Kelleher, P. M. Chaikin, E. R. Weeks "*Long-wavelength fluctuations and the glass transition in two dimensions and three dimensions*". *Proceedings of the National Academy of Sciences* **2017**, *114*, 1850–1855, DOI: 10.1073/pnas.1607226113.

(112) J. M. Kosterlitz, D. J. Thouless "*Ordering, metastability and phase transitions in two-dimensional systems*". *J. Phys. C: Solid State Phys.* **1973**, *6*, 1181, DOI: 10.1088/0022-3719/6/7/010.

(113) J. M. Kosterlitz "*The critical properties of the two-dimensional xy model*". *J. Phys. C: Solid State Phys.* **1974**, *7*, 1046, DOI: 10.1088/0022-3719/7/6/005.

(114) D. R. Nelson, B. I. Halperin "*Dislocation-mediated melting in two dimensions*". *Phys. Rev. B* **1979**, *19*, 2457–2484, DOI: 10.1103/PhysRevB.19.2457.

(115) B. I. Halperin, D. R. Nelson "*Theory of Two-Dimensional Melting*". *Phys. Rev. Lett.* **1978**, *41*, 121–124, DOI: 10.1103/PhysRevLett.41.121.

(116) A. P. Young "*Melting and the vector Coulomb gas in two dimensions*". *Phys. Rev. B* **1979**, *19*, 1855–1866, DOI: 10.1103/PhysRevB.19.1855.

(117) V. L. Berezinskit "*Destruction of Long-Range Order in One-Dimensional and Two-Dimensional Systems Having a Continuous Symmetry Group I. Classical Systems*". **1971**.

(118) V. L. Berezinskit "*Destruction of Long-Range Order in One-Dimensional and Two-Dimensional Systems Possessing a Continuous Symmetry Group II. Quantum Systems*". **1972**.

(119) D. R. Nelson, *Defects and Geometry in Condensed Matter Physics*; Cambridge University Press: 2002.

(120) J. M. Kosterlitz "*Nobel Lecture: Topological defects and phase transitions*". *Rev. Mod. Phys.* **2017**, *89*, 040501, DOI: 10.1103/RevModPhys.89.040501.

(121) H. S. Seung, D. R. Nelson "*Defects in flexible membranes with crystalline order*". *Phys. Rev. A* **1988**, *38*, 1005–1018, DOI: 10.1103/PhysRevA.38.1005.

(122) E. P. Bernard, W. Krauth "*Two-Step Melting in Two Dimensions: First-Order Liquid-Hexatic Transition*". *Phys. Rev. Lett.* **2011**, *107*, 155704, DOI: 10.1103/PhysRevLett.107.155704.

(123) S. C. Kapfer, W. Krauth "*Two-Dimensional Melting: From Liquid-Hexatic Coexistence to Continuous Transitions*". *Phys. Rev. Lett.* **2015**, *114*, 035702, DOI: 10.1103/PhysRevLett.114.035702.

(124) A. L. Thorneywork, J. L. Abbott, D. G. Aarts, R. P. Dullens "*Two-Dimensional Melting of Colloidal Hard Spheres*". *Phys. Rev. Lett.* **2017**, *118*, 158001, DOI: 10.1103/PhysRevLett.118.158001.

(125) J. Russo, N. B. Wilding "*Disappearance of the Hexatic Phase in a Binary Mixture of Hard Disks*". *Phys. Rev. Lett.* **2017**, *119*, 115702, DOI: 10.1103/PhysRevLett.119.115702.

(126) M. Dirindin, D. Coslovich "*Glassy Dynamics and Local Crystalline Order in Two-Dimensional Amorphous Silica*". *J. Phys. Chem. B* **2025**, *129*, 1095–1108, DOI: 10.1021/acs.jpcb.4c06881.

(127) J. Zhang "*Phase-dependent mechanical properties of two-dimensional silica films: A molecular dynamics study*". *Computational Materials Science* **2018**, *142*, 7–13, DOI: 10.1016/j.commatsci.2017.10.005.

(128) T. Björkman, S. Kurasch, O. Lehtinen, J. Kotakoski, O. V. Yazyev, A. Srivastava, V. Skakalova, J. H. Smet, U. Kaiser, A. V. Krasheninnikov "*Defects in bilayer silica and graphene: common trends in diverse hexagonal two-dimensional systems*". *Sci Rep* **2013**, *3*, 3482, DOI: 10.1038/srep03482.

(129) F. Font-Clos, M. Zanchi, S. Hiemer, S. Bonfanti, R. Guerra, M. Zaiser, S. Zapperi "*Predicting the failure of two-dimensional silica glasses*". *Nat Commun* **2022**, *13*, 2820, DOI: 10.1038/s41467-022-30530-1.

(130) M. Wilson, A. Kumar, D. Sherrington, M. F. Thorpe "*Modeling vitreous silica bilayers*". *Phys. Rev. B* **2013**, *87*, 214108, DOI: 10.1103/PhysRevB.87.214108.

(131) M. Sadjadi, B. Bhattarai, D. A. Drabold, M. F. Thorpe, M. Wilson "*Refining glass structure in two dimensions*". *Phys. Rev. B* **2017**, *96*, 201405, DOI: 10.1103/PhysRevB.96.201405.

(132) B. W. H. van Beest, G. J. Kramer, R. A. van Santen "*Force fields for silicas and aluminophosphates based on ab initio calculations*". *Phys. Rev. Lett.* **1990**, *64*, 1955–1958, DOI: 10.1103/PhysRevLett.64.1955.

(133) P. K. Roy, M. Heyde, A. Heuer "*Modelling the atomic arrangement of amorphous 2D silica: a network analysis*". *Phys. Chem. Chem. Phys.* **2018**, *20*, 14725–14739, DOI: 10.1039/C8CP01313F.

(134) P. K. Roy, A. Heuer "*Influence of the coordination defects on the dynamics and the potential energy landscape of two-dimensional silica*". *The Journal of Chemical Physics* **2022**, *157*, 174506, DOI: 10.1063/5.0118797.

(135) D. Coslovich, G. Pastore "*Dynamics and energy landscape in a tetrahedral network glass-former: direct comparison with models of fragile liquids*". *J. Phys.: Condens. Matter* **2009**, *21*, 285107, DOI: 10.1088/0953-8984/21/28/285107.

(136) N. Bailey, T. Ingebrigtsen, et al. "*RUMD: A general purpose molecular dynamics package optimized to utilize GPU hardware down to a few thousand particles*". *SciPost Phys.* **2017**, *3*, 038, DOI: 10.21468/SciPostPhys.3.6.038.

(137) S. F. Swallen, K. L. Kearns, M. K. Mapes, Y. S. Kim, R. J. McMahon, M. D. Ediger, T. Wu, L. Yu, S. Satija "*Organic Glasses with Exceptional Thermodynamic and Kinetic Stability*". *Science* **2007**, DOI: 10.1126/science.1135795.

(138) M. P. Allen, D. J. Tildesley, *Computer simulation of liquids*, Second edition; Oxford University Press: Oxford, United Kingdom, 2017.

(139) M. Newville, T. Stensitzki, D. B. Allen, A. Ingargiola `LMFIT: Non-Linear Least-Square Minimization and Curve-Fitting for Python`, 2014, DOI: 10.5281/zenodo.11813, https://zenodo.org/records/11813.

(140) S. Le Roux, P. Jund "*Ring statistics analysis of topological networks: New approach and application to amorphous GeS2 and SiO2 systems*". *Computational Materials Science* **2010**, *49*, 70–83, DOI: 10.1016/j.commatsci.2010.04.023.

(141) D. A Aboav "*The arrangement of grains in a polycrystal*". *Metallography* **1970**, *3*, 383–390, DOI: 10.1016/0026-0800(70)90038-8.

(142) A. Kumar, D. Sherrington, M. Wilson, M. F. Thorpe "*Ring statistics of silica bilayers*". *J. Phys.: Condens. Matter* **2014**, *26*, 395401, DOI: 10.1088/0953-8984/26/39/395401.

(143) F. Ebrahem, F. Bamer, B. Markert "*Vitreous 2D silica under tension: From brittle to ductile behaviour*". *Materials Science and Engineering: A* **2020**, *780*, 139189, DOI: 10.1016/j.msea.2020.139189.

(144) D. Weaire, N. Rivier "*Soap, cells and statistics—random patterns in two dimensions*". *Contemporary Physics* **1984**, *25*, 59–99, DOI: 10.1080/00107518408210979.

(145) D. Ormrod Morley, A. L. Thorneywork, R. P. A. Dullens, M. Wilson "*Generalized network theory of physical two-dimensional systems*". *Phys. Rev. E* **2020**, *101*, 042309, DOI: 10.1103/PhysRevE.101.042309.

(146) M. E. J. Newman, *Networks*, Second edition; Oxford University Press: 2018.

(147) H. Tanaka "*Roles of liquid structural ordering in glass transition, crystallization, and water's anomalies*". *Journal of Non-Crystalline Solids: X* **2022**, *13*, 100076, DOI: 10.1016/j.nocx.2021.100076.

(148) A. Heuer "*Exploring the potential energy landscape of glass-forming systems: from inherent structures via metabasins to macroscopic transport*". *J. Phys.: Condens. Matter* **2008**, *20*, 373101, DOI: 10.1088/0953-8984/20/37/373101.

(149) F. H. Stillinger, T. A. Weber "*Hidden structure in liquids*". *Phys. Rev. A* **1982**, *25*, 978–989, DOI: 10.1103/PhysRevA.25.978.

(150) D. C. Liu, J. Nocedal "*On the limited memory BFGS method for large scale optimization*". *Mathematical Programming* **1989**, *45*, 503–528, DOI: 10.1007/BF01589116.

(151) D. Coslovich `atooms: A python framework for simulations of interacting particles`, 2018, DOI: 10.5281/zenodo.1183302, https://zenodo.org/records/1183302.

(152) S. Sastry, P. G. Debenedetti, F. H. Stillinger "*Signatures of distinct dynamical regimes in the energy landscape of a glass-forming liquid*". *Nature* **1998**, *393*, 554–557, DOI: 10.1038/31189.

(153) A. Heuer, S. Büchner "*Why is the density of inherent structures of a Lennard-Jones-type system Gaussian?*" *J. Phys.: Condens. Matter* **2000**, *12*, 6535, DOI: 10.1088/0953-8984/12/29/325.

(154) A. Saksaengwijit, A. Heuer "*Finite-size effects in silica: a landscape perspective*". *J. Phys.: Condens. Matter* **2007**, *19*, 205143, DOI: 10.1088/0953-8984/19/20/205143.

(155) C. Scalliet, B. Guiselin, L. Berthier "*Thirty Milliseconds in the Life of a Supercooled Liquid*". *Phys. Rev. X* **2022**, *12*, 041028, DOI: 10.1103/PhysRevX.12.041028.

(156) B. Doliwa, A. Heuer "*Energy barriers and activated dynamics in a supercooled Lennard-Jones liquid*". *Phys. Rev. E* **2003**, *67*, 031506, DOI: 10.1103/PhysRevE.67.031506.

(157) M. Pica Ciamarra, W. Ji, M. Wyart "*Local vs. cooperative: Unraveling glass transition mechanisms with SEER*". *Proceedings of the National Academy of Sciences* **2024**, *121*, e2400611121, DOI: 10.1073/pnas.2400611121.

(158) L. Ortlieb, T. S. Ingebrigtsen, J. E. Hallett, F. Turci, C. P. Royall `Relaxation mechanisms in supercooled liquids past the Mode-Coupling Crossover: Cooperatively Re-arranging Regions vs Excitations`, 2021, DOI: 10.48550/arXiv.2103.08060, http://arxiv.org/abs/2103.08060.

(159) G. T. Barkema, N. Mousseau "*Identification of Relaxation and Diffusion Mechanisms in Amorphous Silicon*". *Phys. Rev. Lett.* **1998**, *81*, 1865–1868, DOI: 10.1103/PhysRevLett.81.1865.

(160) C. Donati, J. F. Douglas, W. Kob, S. J. Plimpton, P. H. Poole, S. C. Glotzer "*Stringlike Cooperative Motion in a Supercooled Liquid*". *Phys. Rev. Lett.* **1998**, *80*, 2338–2341, DOI: 10.1103/PhysRevLett.80.2338.

(161) R. L. C. Vink "*A finite-temperature Monte Carlo algorithm for network forming materials*". *The Journal of Chemical Physics* **2014**, *140*, 104509, DOI: 10.1063/1.4867897.

(162) F. Banhart, J. Kotakoski, A. V. Krasheninnikov "*Structural Defects in Graphene*". *ACS Nano* **2011**, *5*, 26–41, DOI: 10.1021/nn102598m.

(163) H. W. Klemm, M. J. Prieto, F. Xiong, G. B. Hassine, M. Heyde, D. Menzel, M. Sierka, T. Schmidt, H.-J. Freund "*A Silica Bilayer Supported on Ru(0001): Following the Crystalline-to Vitreous Transformation in Real Time with Spectromicroscopy*". *Angewandte Chemie International Edition* **2020**, *59*, 10587–10593, DOI: 10.1002/anie.202002514.

(164) J. P. Garrahan, D. Chandler "*Coarse-grained microscopic model of glass formers*". *Proceedings of the National Academy of Sciences* **2003**, *100*, 9710–9714, DOI: 10.1073/pnas.1233719100.

(165) H. Tanaka "*Two-order-parameter description of liquids. I. A general model of glass transition covering its strong to fragile limit*". *J. Chem. Phys.* **1999**, *111*, 3163–3174, DOI: 10.1063/1.479596.

(166) H. Tanaka "*Structural Origin of Dynamic Heterogeneity in Supercooled Liquids*". *J. Phys. Chem. B* **2025**, *129*, 789–813, DOI: 10.1021/acs.jpcb.4c06392.

(167) D. Coslovich, L. Galliano, L. Costigliola "*Freezing, melting, and the onset of glassiness in binary mixtures*". *The Journal of Chemical Physics* **2025**, *162*, 061102, DOI: 10.1063/5.0252877.

(168) J. Horbach, W. Kob "*Relaxation dynamics of a viscous silica melt: The intermediate scattering functions*". *Phys. Rev. E* **2001**, *64*, 041503, DOI: 10.1103/PhysRevE.64.041503.

(169) J. M. Kosterlitz "*Kosterlitz–Thouless physics: a review of key issues*". *Rep. Prog. Phys.* **2016**, *79*, 026001, DOI: 10.1088/0034-4885/79/2/026001.

(170) V. Drouin-Touchette `The Kosterlitz-Thouless phase transition: an introduction for the intrepid student`, 2022, DOI: 10.48550/arXiv.2207.13748, http://arxiv.org/abs/2207.13748.

(171) W.-K. Qi, S.-M. Qin, X.-Y. Zhao, Y. Chen "*Coexistence of hexatic and isotropic phases in two-dimensional Yukawa systems*". *J. Phys.: Condens. Matter* **2008**, *20*, 245102, DOI: 10.1088/0953-8984/20/24/245102.

(172) H. Shiba, A. Onuki, T. Araki "*Structural and dynamical heterogeneities in two-dimensional melting*". *EPL* **2009**, *86*, 66004, DOI: 10.1209/0295-5075/86/66004.

(173) L. Lichtenstein, M. Heyde, H.-J. Freund "*Crystalline-Vitreous Interface in Two Dimensional Silica*". *Phys. Rev. Lett.* **2012**, *109*, 106101, DOI: 10.1103/PhysRevLett.109.106101.

(174) J. Russo, H. Tanaka "*Assessing the role of static length scales behind glassy dynamics in polydisperse hard disks*". *Proceedings of the National Academy of Sciences* **2015**, *112*, 6920–6924, DOI: 10.1073/pnas.1501911112.

(175) D. R. Nelson, M. Rubinstein, F. Spaepen "*Order in two-dimensional binary random arrays*". *Philosophical Magazine A* **1982**, *46*, 105–126, DOI: 10.1080/01418618208236211.

(176) E. Flenner, G. Szamel "*Dynamic Heterogeneity in a Glass Forming Fluid: Susceptibility, Structure Factor, and Correlation Length*". *Phys. Rev. Lett.* **2010**, *105*, 217801, DOI: 10.1103/PhysRevLett.105.217801.

(177) H. Tong, H. Tanaka "*Revealing Hidden Structural Order Controlling Both Fast and Slow Glassy Dynamics in Supercooled Liquids*". *Phys. Rev. X* **2018**, *8*, 011041, DOI: 10.1103/PhysRevX.8.011041.

(178) L. Berthier "*Revisiting the slow dynamics of a silica melt using Monte Carlo simulations*". *Phys. Rev. E* **2007**, *76*, 011507, DOI: 10.1103/PhysRevE.76.011507.

(179) A. Widmer-Cooper, P. Harrowell, H. Fynewever "*How Reproducible Are Dynamic Heterogeneities in a Supercooled Liquid?*" *Phys. Rev. Lett.* **2004**, *93*, 135701, DOI: 10.1103/PhysRevLett.93.135701.

(180) A. Sharma, C. Liu, M. Ozawa, D. Coslovich `Interpretability of linear regression models of glassy dynamics`, 2025, DOI: 10.48550/arXiv.2508.15933, http://arxiv.org/abs/2508.15933.

(181) J. L. Rodgers, W. A. Nicewander "*Thirteen Ways to Look at the Correlation Coefficient*". *Am. Stat.* **1988**, *42*, 59–66, DOI: https://doi.org/10.1080/00031305.1988.10475524.

(182) G. James, D. Witten, T. Hastie, R. Tibshirani, *An Introduction to Statistical Learning*; Springer Texts in Statistics, Vol. 103; Springer: New York, NY, 2013, DOI: 10.1007/978-1-4614-7138-7.

(183) G. Jung, R. M. Alkemade, et al. "*Roadmap on machine learning glassy dynamics*". *Nat Rev Phys* **2025**, *7*, 91–104, DOI: 10.1038/s42254-024-00791-4.

(184) Y. Li, F. Inam, A. Kumar, M. F. Thorpe, D. A. Drabold "*Pentagonal puckering in a sheet of amorphous graphene*". *physica status solidi (b)* **2011**, *248*, 2082–2086, DOI: 10.1002/pssb.201147195.

(185) A. Kumar, M. Wilson, M. F. Thorpe "*Amorphous graphene: a realization of Zachariasen's glass*". *J. Phys.: Condens. Matter* **2012**, *24*, 485003, DOI: 10.1088/0953-8984/24/48/485003.

(186) J. Tian, W. Kob, J.-L. Barrat "*Are strongly confined colloids good models for two dimensional liquids?*" *The Journal of Chemical Physics* **2022**, *156*, 164903, DOI: 10.1063/5.0086749.

(187) R. C. Roberts, J. C. Palmer, J. C. Conrad "*Long-Wavelength Fluctuations in Quasi-2D Supercooled Liquids*". *J. Phys. Chem. B* **2023**, *127*, 961–969, DOI: 10.1021/acs.jpcb.2c07417.

(188) J. S. Hansen, J. C. Dyre, P. J. Daivis, B. D. Todd, H. Bruus "*Nanoflow hydrodynamics*". *Phys. Rev. E* **2011**, *84*, 036311, DOI: 10.1103/PhysRevE.84.036311.

(189) E. Flenner, L. Berthier, P. Charbonneau, C. J. Fullerton "*Front-Mediated Melting of Isotropic Ultrastable Glasses*". *Phys. Rev. Lett.* **2019**, *123*, 175501, DOI: 10.1103/PhysRevLett.123.175501.

(190) J. Yang, Y.-W. Li, M. P. Ciamarra "*Long-wavelength fluctuations and dimensionality crossover in confined liquids*". *Phys. Rev. Res.* **2021**, *3*, 033172, DOI: 10.1103/PhysRevResearch.3.033172.

(191) R. Shi, J. Russo, H. Tanaka "*Origin of the emergent fragile-to-strong transition in supercooled water*". *Proceedings of the National Academy of Sciences* **2018**, *115*, 9444–9449, DOI: 10.1073/pnas.1807821115.

(192) G Tarjus, S. A. Kivelson, Z Nussinov, P Viot "*The frustration-based approach of supercooled liquids and the glass transition: a review and critical assessment*". *J. Phys.: Condens. Matter* **2005**, *17*, R1143, DOI: 10.1088/0953-8984/17/50/R01.

(193) D. Coslovich, G. Pastore "*Understanding fragility in supercooled Lennard-Jones mixtures. I. Locally preferred structures*". *J. Chem. Phys.* **2007**, *127*, 124504, DOI: 10.1063/1.2773716.

(194) F. C. Frank "*Supercooling of liquids*". *Proc. R. Soc. A* **1952**, *215*, 43–46, DOI: 10.1098/rspa.1952.0194.

(195) H. Tong, H. Tanaka "*Structural order as a genuine control parameter of dynamics in simple glass formers*". *Nat Commun* **2019**, *10*, 5596, DOI: 10.1038/s41467-019-13606-3.

(196) H. Tanaka, T. Kawasaki, H. Shintani, K. Watanabe "*Critical-like behaviour of glass-forming liquids*". *Nature Mater* **2010**, *9*, 324–331, DOI: 10.1038/nmat2634.

(197) H. Tanaka "*A new scenario of the apparent fragile-to-strong transition in tetrahedral liquids: water as an example*". *J. Phys.: Condens. Matter* **2003**, *15*, L703, DOI: 10.1088/0953-8984/15/45/L03.

(198) P. Giannozzi, S. Baroni, et al. "*QUANTUM ESPRESSO: a modular and open-source software project for quantum simulations of materials*". *J. Phys.: Condens. Matter* **2009**, *21*, 395502, DOI: 10.1088/0953-8984/21/39/395502.

(199) P. Giannozzi, O. Andreussi, et al. "*Advanced capabilities for materials modelling with Quantum ESPRESSO*". *J. Phys.: Condens. Matter* **2017**, *29*, 465901, DOI: 10.1088/1361-648X/aa8f79.

(200) I. V. Lebedeva, A. S. Minkin, A. M. Popov, A. A. Knizhnik "*Elastic constants of graphene: Comparison of empirical potentials and DFT calculations*". *Physica E: Low-dimensional Systems and Nanostructures* **2019**, *108*, 326–338, DOI: 10.1016/j.physe.2018.11.025.

(201) F. Memarian, A. Fereidoon, M. Darvish Ganji "*Graphene Young's modulus: Molecular mechanics and DFT treatments*". *Superlattices and Microstructures* **2015**, *85*, 348–356, DOI: 10.1016/j.spmi.2015.06.001.

(202) C. Lee, X. Wei, J. W. Kysar, J. Hone "*Measurement of the Elastic Properties and Intrinsic Strength of Monolayer Graphene*". *Science* **2008**, *321*, 385–388, DOI: 10.1126/science.1157996.

(203) K. N. Kudin, G. E. Scuseria, B. I. Yakobson "*C2F, BN, and C nanoshell elasticity from ab initio computations*". *Phys. Rev. B* **2001**, *64*, DOI: 10.1103/PhysRevB.64.235406.

(204) L. Song, L. Ci, et al. "*Large Scale Growth and Characterization of Atomic Hexagonal Boron Nitride Layers*". *Nano Lett.* **2010**, *10*, 3209–3215, DOI: 10.1021/nl1022139.

(205) C. Androulidakis, K. Zhang, M. Robertson, S. Tawfick "*Tailoring the mechanical properties of 2D materials and heterostructures*". *2D Mater.* **2018**, *5*, 032005, DOI: 10.1088/2053-1583/aac764.

(206) A. H. Castro Neto, F. Guinea, N. M. R. Peres, K. S. Novoselov, A. K. Geim "*The electronic properties of graphene*". *Rev. Mod. Phys.* **2009**, *81*, 109–162, DOI: 10.1103/RevModPhys.81.109.

(207) M. F. Thorpe "*Continuous deformations in random networks*". *Journal of Non-Crystalline Solids* **1983**, *57*, 355–370, DOI: 10.1016/0022-3093(83)90424-6.

(208) K. Park, G. H. Kim, S. Jeong "*Atomistic processes of boron and nitrogen near the Pt(111) surface*". *Applied Surface Science* **2021**, *537*, 147901, DOI: 10.1016/j.apsusc.2020.147901.

(209) J. Tersoff, D. R. Hamann "*Theory of the scanning tunneling microscope*". *Phys. Rev. B* **1985**, *31*, 805–813, DOI: 10.1103/PhysRevB.31.805.

(210) V. Popescu, A. Zunger "*Extracting E versus $\stackrel{P\vec}{k}$ effective band structure from supercell calculations on alloys and impurities*". *Phys. Rev. B* **2012**, *85*, 085201, DOI: 10.1103/PhysRevB.85.085201.

(211) P. Bonfà `unfold-x`, https://bitbucket.org/bonfus/unfold-x/src/master/.

(212) S. Lin, J. Gu, H. Zhang, Y. Wang, Z. Chen "*Porous hexagonal boron oxide monolayer with robust wide band gap: A computational study*". *FlatChem* **2018**, *9*, 27–32, DOI: 10.1016/j.flatc.2018.05.002.

(213) S. Ullah, P. A. Denis, F. Sato "*Theoretical investigation of various aspects of two dimensional holey boroxine, B_3O_3*". *RSC Adv.* **2019**, *9*, 37526–37536, DOI: 10.1039/C9RA07338H.

(214) J. R. H. Ross, *Contemporary Catalysis: Fundamentals and Current Applications*; Elsevier: 2018.

(215) F. L. Thiemann, C. Scalliet, E. A. Müller, A. Michaelides "*Defects induce phase transition from dynamic to static rippling in graphene*". *Proceedings of the National Academy of Sciences* **2025**, *122*, e2416932122, DOI: 10.1073/pnas.2416932122.

(216) C. Bertolini, G. Comelli, T. Zio, M. Dirindin "*Atomic-scale study of the crystalline-vitreous transition of two-dimensional boron oxide*", it, bachelor's thesis, Trieste, 2025.

(217) C. Wang, H. Li, Z. Hao, X. Li, C. Zou, P. Cai, Y. Wang, Y.-Z. You, H. Zhai "*Machine learning identification of impurities in the STM images**". *Chinese Phys. B* **2020**, *29*, 116805, DOI: 10.1088/1674-1056/abc0d5.

(218) L. Fu, H. Yu, X. Li, C. P. Przybyla, S. Wang "*Deep Learning for Object Detection in Materials-Science Images: A tutorial*". *IEEE Signal Processing Magazine* **2022**, *39*, 78–88, DOI: 10.1109/MSP.2021.3121558.

(219) A. Rohatgi `WebPlotDigitizer`, https://apps.automeris.io/wpd4/.

(220) W. H. Press, S. A. Teukolsky, W. T. Vetterling, B. P. Flannery, *Numerical Recipes in C*, Second Edition; Cambridge University Press: New York, 1992.

(221) B. Delaunay "*Sur la sphère vide*". **1934**, *6*, 793–800.

(222) D. T. Lee, B. J. Schachter "*Two algorithms for constructing a Delaunay triangulation*". *International Journal of Computer and Information Sciences* **1980**, *9*, 219–242, DOI: 10.1007/BF00977785.

(223) `SciPy`, https://scipy.org/.

(224) J. P. Perdew, K. Burke, M. Ernzerhof "*Generalized Gradient Approximation Made Simple*". *Phys. Rev. Lett.* **1996**, *77*, 3865–3868, DOI: 10.1103/PhysRevLett.77.3865.

(225) K. F. Garrity, J. W. Bennett, K. M. Rabe, D. Vanderbilt "*Pseudopotentials for high-throughput DFT calculations*". *Computational Materials Science* **2014**, *81*, 446–452, DOI: 10.1016/j.commatsci.2013.08.053.

(226) A. Dal Corso "*Pseudopotentials periodic table: From H to Pu*". *Computational Materials Science* **2014**, *95*, 337–350, DOI: 10.1016/j.commatsci.2014.07.043.

(227) N. Marzari, D. Vanderbilt, A. De Vita, M. C. Payne "*Thermal Contraction and Disordering of the Al(110) Surface*". *Phys. Rev. Lett.* **1999**, *82*, 3296–3299, DOI: 10.1103/PhysRevLett.82.3296.

(228) S. Grimme, J. Antony, S. Ehrlich, H. Krieg "*A consistent and accurate ab initio parametrization of density functional dispersion correction (DFT-D) for the 94 elements H-Pu*". *J. Chem. Phys.* **2010**, *132*, 154104, DOI: 10.1063/1.3382344.

(229) P. E. Blöchl "*Projector augmented-wave method*". *Phys. Rev. B* **1994**, *50*, 17953–17979, DOI: 10.1103/PhysRevB.50.17953.

(230) L. Guttman "*Ring structure of the crystalline and amorphous forms of silicon dioxide*". *Journal of Non-Crystalline Solids* **1990**, *116*, 145–147, DOI: 10.1016/0022-3093(90)90686-G.

(231) S. V. King "*Ring Configurations in a Random Network Model of Vitreous Silica*". *Nature* **1967**, *213*, 1112–1113, DOI: 10.1038/2131112a0.

(232) D. S. Franzblau "*Computation of ring statistics for network models of solids*". *Phys. Rev. B* **1991**, *44*, 4925–4930, DOI: 10.1103/PhysRevB.44.4925.

(233) K. Goetzke, H. J. Klein "*Properties and efficient algorithmic determination of different classes of rings in finite and infinite polyhedral networks*". *Journal of Non-Crystalline Solids* **1991**, *127*, 215–220, DOI: 10.1016/0022-3093(91)90145-V.

(234) F. Wooten "*Structure, odd lines and topological entropy of disorder of amorphous silicon*". *Acta Cryst A* **2002**, *58*, 346–351, DOI: 10.1107/S0108767302006669.

(235) X. Yuan, A. N. Cormack "*Efficient algorithm for primitive ring statistics in topological networks*". *Computational Materials Science* **2002**, *24*, 343–360, DOI: 10.1016/S0927-0256(01)00256-7.

(236) A. Tirelli, K. Nakano "*Topological Data Analysis for Revealing the Structural Origin of Density Anomalies in Silica Glass*". *J. Phys. Chem. B* **2023**, *127*, 3302–3311, DOI: 10.1021/acs.jpcb.2c09009.

(237) R. J. Trudeau, *Introduction to graph theory*, Second edition; Dover books on advanced mathematics; Dover Publications: New York, NY, 1993.

(238) M. Dirindin `12dr`, 2024, DOI: 10.5281/zenodo.13913245, https://zenodo.org/records/13913245.

UNIVERSITÀ
DEGLI STUDI
DI TRIESTE

La borsa di dottorato è cofinanziata con risorse dell'Unione europea, NextGeneration EU - Piano Nazionale di Ripresa e Resilienza, Missione 4 – Componente 2 – Investimento 1.4 CUP J93C22000540006